

# **Automated Construction and Structural Behavior of 3D Printed Concrete Tunnel Linings**

**Yaxin Tao**

Doctoral dissertation submitted to obtain the academic degree of  
Doctor of Civil Engineering

## **Supervisors**

Prof. Geert De Schutter, PhD\* - Prof. Kim Van Tittelboom, PhD\* - Prof. Yong Yuan, PhD\*\*

\* Department of Structural Engineering and Building Materials  
Faculty of Engineering and Architecture, Ghent University

\*\* Department of Geotechnical Engineering  
College of Civil Engineering, Tongji University, China

November 2021



**GHENT  
UNIVERSITY**





## **Automated Construction and Structural Behavior of 3D Printed Concrete Tunnel Linings**

**Yaxin Tao**

Doctoral dissertation submitted to obtain the academic degree of  
Doctor of Civil Engineering

### **Supervisors**

Prof. Geert De Schutter, PhD\* - Prof. Kim Van Tittelboom, PhD\* - Prof. Yong Yuan, PhD\*\*

\* Department of Structural Engineering and Building Materials  
Faculty of Engineering and Architecture, Ghent University

\*\* Department of Geotechnical Engineering  
College of Civil Engineering, Tongji University, China

November 2021



ISBN 978-94-6355-542-5

NUR 956, 971

Wettelijk depot: D/2021/10.500/90

## **Members of the Examination Board**

### **Chair**

Prof. Em. Luc Taerwe, PhD, Ghent University

### **Other members entitled to vote**

Prof. Eddie Koenders, PhD, Technische Universität Darmstadt, Germany

Karel Lesage, PhD, Ghent University

Prof. Stijn Matthys, PhD, Ghent University

Prof. Jian Yang, PhD, Shanghai Jiao Tong University, China

### **Supervisors**

Prof. Geert De Schutter, PhD, Ghent University

Prof. Kim Van Tittelboom, PhD, Ghent University

Prof. Yong Yuan, PhD, Tongji University, China



To my family.





# Preface

This thesis is submitted for the degree of Doctor of Civil Engineering at Ghent University. The research was conducted under the supervision of Prof. Geert De Schutter and Prof. Kim Van Tittelboom in the Department of Structural Engineering and Building Materials, Ghent University, and Prof. Yong Yuan in the Department of Geotechnical Engineering, Tongji University.

This work is original to the best of my knowledge, except for the parts where references are made to previous work. Neither this, substantially similar thesis has been or is being submitted for any other degree, diploma, or other qualification at any other university.

The basis of this research originally stemmed from the passion for extending extrusion-based 3D concrete printing for the construction of hard rock tunnel linings. It is the first time that 3D concrete printing has been used for hard rock tunnels. In addition, under this framework, a stiffening-control system named twin-pipe pumping has been developed, which might have the fastest printing speed around the world, to the best of my knowledge. In truth, I could not have achieved my current level of success without strong support.

Foremost, I would like to express my sincere gratitude to my supervisors Prof. Geert De Schutter and Prof. Kim Van Tittelboom for their patience, motivation, enthusiasm, and immense knowledge. The discussions with them always help me shape those vague ideas and thoughts into something concrete. I am also grateful from bottom of my heart to my co-supervisor Prof. Yong Yuan for enlightening me at the first glance of research and encouraging me on my research progress. I could not have imagined having better supervisors for my doctoral study.

Besides my supervisors, I would like to thank all the members of the examination committee: Prof. Luc Taerwe, Prof. Stijn Matthys, Prof. Eddie Koenders, Prof. Jian Yang, and Dr. Karel Lesage. Many thanks for their valuable insights and comments, which contribute to a significant improvement to this thesis.

My sincere thanks also go to my (former) colleagues in the group of 3D concrete printing: Jolien, Karel, Mahzad, Manu, Michiel, Rahul, and Sebastiaan. The daily interesting discussions with you inspire me a lot. A special thanks to Dr. Karel Lesage and Dr. A.V. Rahul for sharing your valuable knowledge and experience

with me. I would like to thank my (former) officemates: Chizya, Dengwu, Fanghui, Hasson, Metwally, Qiang, Robin, Serder, and Xiaoyun. I would like to express my sincere thanks to Xiaoyun for helping me develop the first version of the inline mixing system with a dynamic mixer. Special thanks to Robin for the collaboration of numerical simulation and Metwally for helping me with the dynamic lighting scattering measurements. I would like to thank all other colleagues from our lab for experimental support: Bart, Brenda, Dennis, Dieter, Eric, Nathan, Marc, Sandra, Stefan, Peter (PL), Peter (PVDB), Tom, Tommy, and for administrative help from our lab secretaries: Jens, Christel, and Marijke. An extra thanks to Dieter for deeply involving the 3D printing activities and saving the broken system every time.

From the non-technical aspects, thanks also to my friends I met during my time in Ghent: Heng & Jia, Weixi & Yiran, Ke (KS) & Miao, Changyuan & Jinluan, Bijon & Natalia, Kai & Xiujiao, Xuejiao, Yu, Puput, Beibei, Sumei, Tianlong, Jingbin, Qiang, Luchuan, Roberto, Luiza, Xiaodi, Yubo, Zhiyuan, Yifan, Ke (KX), Zhenmin, Sisi, Yingxing, Lingyan, Haitang, Yangfeng, Ji, Ren, Yongyuan, Min, et al. A special thanks for Chef Qiang for cooking nice dishes during his stay in Ghent. Thanks to Weixi for the basketball time and 20,000-shot practice during the first lockdown. Thank you very much to all of you for your friendship.

Last but not least, I would like to give my deepest gratitude to my family. To my parents, I love you both a lot and appreciate your effort and love in bringing me up to be a better individual. I owe you everything and have no way to fully reply to you. To my sister, you take good care of me for as long as I can remember. The least I can do is to thank you for your unconditional love and support. Also, thank you for being such a wonderful sister. To my wife, it is my privilege to thank you, for your constant encouragement. I know I can never thank you enough for that, especially when we were six thousand miles apart. The love of long-distance will never be easy. It was your courage that saw me through these hard times. Thank you for always being there when I need you. I will try my best to make all of you proud and return to you for the rest of my life.

Yaxin Tao

May 2021

Ghent, Belgium

## Summary

Shotcrete has been widely used for the construction of hard rock tunnel linings with many beneficial characteristics such as high flexibility and no requirement of formwork. However, irregular sprayed surfaces and a high amount of rebound cannot be avoided due to the discontinuity of sprayed materials and the pneumatic impact. Different from shotcrete with a high spraying speed, extrusion-based 3D concrete printing adopts a much smaller extrusion speed. As such, the rebound can be avoided and the surface quality is guaranteed due to the presence of a steady flow and a precise printing path. Different from other applications with layers printed on top of each other in a vertical direction, printed materials used for hard rock tunnel linings are placed against the excavated rock wall with different surface inclinations. In these conditions, practical applications are still limited due to constraints of the fabrication process and material performance. Based on this, this thesis mainly focuses on two general aspects, which relate to two potential failures of layers printed on the rock wall. One is the shear of printed materials due to the punching of loose rock. Another is that printed materials fail at the material-to-substrate interface due to the lack of adhesion.

To avoid the first type of failure (i.e. the shear of printed materials), a very high early strength development (i.e. a high stiffening rate) allows printed materials to be printed in a stable way against the surrounding rocks. However, high fluidity and a sufficient open time without early setting or hardening (i.e. a low stiffening rate) are required for the pumping process. To meet these conflicting requirements regarding the stiffening rate, an inline-mixing system named twin-pipe pumping is developed. A cement-based flow (without accelerator) and a limestone powder-based flow (with a high dosage of accelerator) are pumped from two separate pipes into a motionless helical static mixer, which is placed at the end of the pumping process. As the flows move through the helical static mixer, the non-moving baffles inside the static mixer continuously blend the two flows. As a result, the accelerator contained in the limestone powder-based flow reacts with the cement or other mineral substitutions in the cement-based flow instantaneously, leading to a sharp change in the stiffness. The influence of the number of mixing baffles on the pumping pressure and the mixing homogeneity is studied. Results indicate that a high number of mixing baffles is beneficial to achieve a good homogeneity, however results in a high pumping pressure in the meantime.

As a follow-up, the mechanical behaviors and microstructural properties of the elements printed by the twin-pipe pumping system are investigated. Samples are cut out from different locations in printed elements and subjected to compressive, flexural, and tensile tests. Microstructural investigations are carried out using mercury intrusion porosimetry (MIP) and scanning electron microscopy (SEM) in combination with image analysis. Results indicate that the helical static mixer introduces striations in the printed layers due to the flow division pattern. Although the mechanical strength of 3D printed samples is lower than that of mold cast samples, the reduction is still within an acceptable range due to ion migration between the striations of the cement-based mixture and the limestone powder-based mixture.

To avoid the second type of failure (i.e. detachment at the interface), the influence of surface inclination, substrate properties, and polymer modification of printed materials on the adhesion are discussed respectively. First, two representative surface inclinations are chosen including the inclination of  $180^\circ$  (i.e. the overhead position) and the inclination of  $90^\circ$  (i.e. the side position). The adhesion of the fresh materials at these two positions is quantified by performing a tack test and a shear test, respectively. Two series of large-scale 3D concrete printing tests are further performed including printing at the bottom surface of a horizontally supported concrete slab and printing against an upright concrete slab. The stress state analysis of the fresh materials at these two positions is given. Results indicate that the adhesion at the overhead position is limited by both the shear resistance of fresh materials and the property of the material-to-substrate interface, while the adhesion at the side position is mainly defined by the shear resistance of fresh materials, rather than the substrate properties. As such, more layers can be printed at the side position, especially for the mixture with a solid-like behavior.

The influence of the substrate surface roughness and moisture content on the tensile adhesion of the printed materials at the overhead position is studied. Concrete substrates with different surface roughness levels and moisture contents are prepared, as a replacement for the excavated rock wall. Results indicate that the macro surface textures of the rough substrate cannot be filled by stiff materials extruded from the outlet, resulting in a limited adhesion both in the fresh and hardened state. Such a limitation can be minimized by coating the rough substrate before placing layers. On the other hand, compared to a dry substrate surface, a pre-wetted substrate surface leads to higher tensile adhesion in the fresh state due to the dragging force provided by the trapped water in the macro textures.

The influence of polymer modification including redispersible polymer powders and cellulose ethers on the tensile adhesion of printed materials is investigated. Seven mixtures modified with different dosages of redispersible polymer powder and cellulose ether are formulated. A tack test with a loading control mode is performed where stepwise increasing loads are applied to mimic the 3D printing

process. A stress growth test is further performed to measure the shear resistance of fresh materials for a better understanding of the adhesion performance. Results show that cellulose ethers enhance the adhesion in the fresh state, but reduce the tensile bond strength after hardening. Adversely, redispersible polymer powders present no significant effect on the adhesion in the fresh state, while the tensile bond strength of hardened samples can be improved due to the film formation of redispersible polymer powders.

In order to combine the previously mentioned general aspects, including stiffening control and adhesion, the interaction of the accelerator for the stiffening control purpose and the cellulose ether for the adhesion purpose is studied. Four types of cellulose ethers with different viscosity levels and pure aluminum sulfate octadecahydrate are used. The viscosifying property of cellulose ether in aqueous solutions with varying concentrations and temperatures is examined. Afterwards, the hydrodynamic diameter and concentration of the cellulose ether in the extracted pore solutions of fresh materials is measured by the dynamic lighting scattering (DLS) test and by the total organic carbon (TOC) test, respectively. This is followed by the evaluation of the adhesion performance of the fresh materials. Results indicate that the addition of aluminum sulfate improves the shear resistance of fresh materials, while it compromises the migration of water towards the substrate. Moreover, the effect of cellulose ether on adhesion is limited with the presence of aluminum sulfate, especially for the cellulose ethers with high viscosity levels. The limitation can be attributed to the constraint of the mobility of cellulose ether within contracted pore sizes.





## Samenvatting

Spuitsbeton wordt op grote schaal gebruikt voor de bouw van tunnelbekledingen tegen harde rotssteen, met als voordeel de hoge flexibiliteit en het vermijden van een bekisting. Echter, onregelmatige gespoten oppervlakken en een grote hoeveelheid terugslag kunnen niet worden vermeden wegens de discontinuïteit in de stroom van het gespoten materiaal en de pneumatische impact. Anders dan bij spuitbeton met een hoge spuitsnelheid, is bij 3D-betonprinten met behulp van extrusie een veel lagere extrusiesnelheid vereist. Hierdoor kan terugslag worden vermeden en is de oppervlaktekwaliteit gegarandeerd dankzij een gestage materiaalstroom en een nauwkeurig printpad. In tegenstelling tot andere toepassingen waarbij lagen in verticale richting op elkaar worden geprint, worden geprinte materialen voor tunnelbekledingen tegen de uitgegraven rotswand geplaatst met verschillende hellingshoeken van het oppervlak. Voor dergelijke omstandigheden zijn praktische toepassingen nog steeds beperkt door beperkingen inzake fabricageproces en materiaalprestaties. Op basis hiervan worden in dit proefschrift voornamelijk twee algemene aspecten besproken, die betrekking hebben op twee potentiële bezwijkmechanismen van lagen die tegen de rotswand worden geprint. Eén daarvan is de afschuiving van geprinte materialen als gevolg van het effect van los gesteente. Een ander is het loskomen van de geprinte materialen in de overgangszone met het substraat als gevolg van het gebrek aan adhesie.

Om het eerste type falen te vermijden (d.w.z. de afschuiving van geprinte materialen), zorgt een zeer hoge vroege sterkteontwikkeling (d.w.z. een hoge verstijvingssnelheid) ervoor dat geprinte lagen het omringend gesteente kunnen vasthouden. Een hoge vloeibaarheid en een voldoende open tijd zonder vroegtijdige verharding (d.w.z. een lage verstijvingssnelheid) zijn echter vereist voor het voorafgaande pompproces. Om aan deze conflicterende eisen betreffende de verstijvingssnelheid te voldoen, wordt een *inline*-mengsysteem met de naam *twin pipe pumping* ontwikkeld. Een cementgebonden stroom (zonder versneller) en een kalksteenpoeder-gebaseerde stroom (met een hoge dosis versneller) worden via twee afzonderlijke pijpen gepompt in een spiraalvormige statische menger, die aan het einde van het pompproces is geplaatst. Terwijl de twee materiaalstromen door de spiraalvormige statische menger bewegen, mengen de niet-bewegende schotten binnenin de statische menger de materialen voortdurend. Het resultaat is dat de versneller in de kalksteenpoeder-stroom onmiddellijk reageert met het cement of met andere minerale substituten in de cement-stroom, wat leidt tot een

snelle verandering in de stijfheid. De invloed van het aantal mengschotten op de pompdruk en de menghomogeniteit wordt bestudeerd. De resultaten geven aan dat een hoog aantal mengschotten gunstig is voor het bereiken van een goede homogeniteit, maar ondertussen resulteert in een hoge pompdruk.

Als vervolg hierop worden het mechanisch gedrag en de microstructureigenschappen onderzocht van elementen geprint met behulp van *twin pipe pumping*. Er worden monsters ontnomen op verschillende plaatsen in de geprinte elementen en onderworpen aan druk-, buig- en trekproeven. De microstructuur wordt onderzocht met behulp van kwikporosimetrie (MIP) en scanning-elektronenmicroscopie (SEM) in combinatie met beeldanalyse. Resultaten tonen aan dat het stromingsverdelingspatroon van de statische menger laagjes introduceert in de geprinte lagen. Hoewel de mechanische sterkte van 3D-geprinte monsters lager is dan die van bekiste monsters, is de reductie nog steeds binnen een aanvaardbaar bereik als gevolg van de ionenmigratie tussen de laagjes van het cement-gebaseerde mengsel en het kalksteenpoeder-gebaseerde mengsel.

Om het tweede type falen (d.w.z. loslaten aan de interface) te vermijden, worden de invloed van de hellingshoek van het oppervlak, de eigenschappen van het substraat en polymeermodificatie van de geprinte materialen op de adhesie besproken. Eerst worden twee representatieve oppervlakte-oriëntaties gekozen, waaronder een hoek van  $180^\circ$  (d.w.z. de bovenliggende positie) en een hoek van  $90^\circ$  (d.w.z. de zijdelingse positie). De hechting van de verse materialen in deze twee posities wordt gekwantificeerd door het uitvoeren van een *tack test* en een afschuifproef. Twee reeksen grootschalige 3D-betonprintproeven worden verder uitgevoerd, waaronder het printen aan de onderzijde van een horizontaal ondersteunde betonplaat en het zijdelings printen tegen een rechtopstaande betonplaat. De spanningstoestand van de verse materialen in deze twee posities wordt geanalyseerd. De resultaten tonen aan dat de adhesie in de bovenliggende positie beperkt wordt door zowel de schuifweerstand van de verse materialen als de eigenschappen van de overgangszone tussen materiaal en substraat, terwijl de adhesie in de zijdelingse positie hoofdzakelijk bepaald wordt door de schuifweerstand van de verse materialen, eerder dan door de eigenschappen van het substraat. Zodoende kunnen meer lagen worden geprint op de zijdelingse positie, vooral voor het mengsel met een stijver gedrag.

De invloed van de oppervlakteruwheid van het substraat en het vochtgehalte op de hechtsterkte van de geprinte materialen in de bovenliggende positie worden bestudeerd. Betonnen substraten met verschillende oppervlakteruwheden en vochtgehalten worden voorbereid, als vervanging voor de uitgegraven rotswand. De resultaten tonen aan dat de macro-oppervlaktetexturen van het ruwe substraat niet kunnen worden opgevuld door geëxtrudeerde stijve materialen, wat resulteert in een beperkte hechting zowel in verse als in uitgeharde toestand. Een dergelijke beperking kan worden geminimaliseerd door het ruwe substraat te coaten alvorens

de lagen te printen. Anderzijds, in vergelijking met een droog substraatooppervlak, leidt een vooraf bevochtigd substraatooppervlak tot een hogere trekhechting in de verse toestand als gevolg van de trekkracht die wordt geleverd door het ingesloten water in de macrostructuren.

De invloed van polymeermodificatie met inbegrip van herdispergeerbare polymeerpoeders en cellulose-ethers op de aanhechting van geprinte materialen wordt onderzocht. Zeven mengsels gemodificeerd met verschillende doseringen van herdispergeerbare polymeerpoeders en cellulose-ethers zijn geformuleerd. Er wordt een hechtingsproef uitgevoerd met een belastingscontrole waarbij de toenemende belasting stapsgewijze wordt aangebracht om het 3D-printproces na te bootsen. Een spanningsgroei-test wordt verder uitgevoerd om de afschuifweerstand van de verse materialen te meten voor een beter begrip van de adhesieprestaties. De resultaten tonen aan dat cellulose-ethers de adhesie in verse toestand verbeteren, maar de hechtsterkte verminderen na uitharding. Daarentegen hebben herdispergeerbare polymeerpoeders geen significant effect op de adhesie in verse toestand, terwijl de hechtsterkte van uitgeharde monsters kan worden verbeterd door de filmvorming van herdispergeerbare polymeerpoeders.

Om de twee bovengenoemde algemene aspecten, waaronder verstijvingsbeheersing en adhesie, samen in overweging te nemen, wordt de interactie van de versneller voor de verstijvingsbeheersing en de cellulose-ethers voor de adhesie bestudeerd. Vier soorten cellulose-ethers met verschillende viscositeitsniveaus en zuiver aluminiumsulfaat worden gebruikt. De viscositeitsverhogende eigenschap van cellulose-ethers in waterige oplossingen met variërende concentraties en temperaturen wordt onderzocht. Daarna wordt de hydrodynamische diameter van cellulose-ethers in de geëxtraheerde porieoplossingen van verse materialen gemeten door dynamische lichtverstrooiing (DLS) en door bepaling van het totaal organisch koolstofgehalte (TOC-gehalte). Dit wordt gevolgd door de evaluatie van de adhesieprestaties van het verse materiaal. Uit de resultaten blijkt dat de toevoeging van aluminiumsulfaat de schuifweerstand van vers materiaal verbetert, terwijl de migratie van water naar het substraat wordt belemmerd. Bovendien is het effect van cellulose-ethers op de adhesie beperkt door de aanwezigheid van aluminiumsulfaat, vooral voor de cellulose-ethers met een hoge viscositeit. Deze beperking kan worden toegeschreven aan de beperking van de mobiliteit van cellulose-ethers in gecontracteerde poriën.



# Table of Contents

<b>Preface.....</b>	<b>i</b>
<b>Summary .....</b>	<b>iii</b>
<b>Samenvatting .....</b>	<b>vii</b>
<b>Table of Contents.....</b>	<b>xi</b>
<b>Nomenclature.....</b>	<b>xv</b>
<b>1 General introduction .....</b>	<b>1</b>
1.1 Motivation .....	1
1.2 Objectives .....	5
1.3 Strategies .....	7
1.4 Outline .....	8
<b>2 State of the art.....</b>	<b>11</b>
2.1 Introduction .....	11
2.2 Terminology in extrusion-based 3D concrete printing .....	11
2.2.1 Pumpability.....	11
2.2.2 Extrudability .....	12
2.2.3 Buildability .....	13
2.3 Classification of accelerators and hydration mechanism .....	14
2.3.1 Setting versus hardening.....	14
2.3.2 Inorganic versus organic salts.....	15
2.3.3 Chemical versus physical actions .....	18
2.3.4 Normal concrete versus shotcrete .....	19
2.4 Inline mixing strategies with accelerator .....	21
2.4.1 Two-fluid grouting .....	21
2.4.2 Shotcrete and spray-based 3D concrete printing .....	22
2.4.3 Extrusion-based 3D concrete printing .....	25
2.5 Issues and challenges in using accelerators .....	30
2.5.1 Mixing homogeneity.....	30
2.5.2 Effect on mechanical performance .....	32
2.5.3 Effect on durability .....	34
2.6 Adhesion mechanism.....	35
2.6.1 Basic notions of adhesion .....	35
2.6.2 Adhesion theories .....	35
2.6.3 Circumstantial effects .....	37
2.7 Influence of concrete surface characteristics on adhesion .....	39

2.7.1	Roughness .....	40
2.7.2	Moisture content .....	40
2.7.3	Bonding agents .....	40
<b>3</b>	<b>Materials and methods .....</b>	<b>43</b>
3.1	Introduction .....	43
3.2	Material properties .....	43
3.2.1	Cement .....	43
3.2.2	Limestone powder .....	44
3.2.3	Silica Sand .....	44
3.2.4	Superplasticizer .....	45
3.2.5	Cellulose ether .....	45
3.2.6	Redispersible polymer powder .....	47
3.2.7	Accelerator .....	47
3.3	Substrate properties .....	49
3.3.1	Compositions .....	49
3.3.2	Roughness .....	50
3.3.3	Moisture content .....	52
3.4	Analytical techniques .....	53
3.4.1	Flow curve test .....	53
3.4.2	Stress growth test .....	54
3.4.3	Tack test .....	55
3.4.4	Shear test .....	58
3.4.5	Viscosity measurement .....	59
3.4.6	Flow table .....	60
3.4.7	Calorimeter test .....	60
3.4.8	Penetration test .....	60
3.4.9	3D concrete printing test (twin-pipe pumping) .....	61
3.4.10	3D concrete printing test (sag resistance) .....	64
3.4.11	Compression test .....	67
3.4.12	Flexural test .....	68
3.4.13	Pull-off test (interlayer) .....	70
3.4.14	Pull-off test (overlay-to-substrate) .....	72
3.4.15	Mercury intrusion porosimetry (MIP) .....	74
3.4.16	Scanning electron microscopy (SEM) .....	75
3.4.17	Static filtration test .....	76
3.4.18	Dynamic light scattering (DLS) .....	76
3.4.19	Total organic carbon (TOC) .....	76
<b>4</b>	<b>Combined mixture design for twin-pipe pumping .....</b>	<b>77</b>
4.1	Introduction .....	77
4.2	Experimental program .....	78
4.3	Results and discussion .....	80
4.3.1	Effect of limestone powder substitution rates .....	80
4.3.2	Effect of accelerator dosages .....	82



4.4	Summaries .....	85
<b>5</b>	<b>Phase transition from transportation to fabrication .....</b>	<b>87</b>
5.1	Introduction .....	87
5.2	Experimental program .....	87
5.3	Results and discussion .....	88
5.3.1	Flow diameter .....	88
5.3.2	Rheological parameters .....	90
5.3.3	Open time .....	91
5.3.4	Mixing homogeneity.....	93
5.3.5	Pumping pressure .....	96
5.3.6	Buildability verification.....	98
5.4	Summaries .....	98
<b>6</b>	<b>Mechanical and microstructural properties in twin-pipe pumping... 101</b>	
6.1	Introduction .....	101
6.2	Experimental program .....	101
6.3	Results and discussion .....	102
6.3.1	Compressive strength .....	102
6.3.2	Flexural strength .....	104
6.3.3	Tensile bond strength.....	106
6.3.4	Porosity and microstructure morphology .....	108
6.4	Summaries .....	115
<b>7</b>	<b>Influence of surface inclination on adhesion .....</b>	<b>117</b>
7.1	Introduction .....	117
7.2	Experimental program .....	117
7.3	Results and discussion .....	118
7.3.1	Adhesion in the tension state .....	118
7.3.2	Adhesion in the shear state .....	123
7.3.3	3D printing test results.....	127
7.3.4	Stress state analysis .....	131
7.4	Summaries .....	134
<b>8</b>	<b>Influence of substrate properties on adhesion .....</b>	<b>135</b>
8.1	Introduction .....	135
8.2	Experimental program .....	135
8.3	Results and discussion .....	136
8.3.1	Normal force versus displacement curves .....	136
8.3.2	Sag resistance of printed layers .....	142
8.3.3	Tensile bond of hardened samples .....	144
8.3.4	Analysis of adhesion mechanism.....	146
8.4	Summaries .....	148
<b>9</b>	<b>Influence of polymer modification on adhesion .....</b>	<b>151</b>
9.1	Introduction .....	151
9.2	Experimental program .....	151

9.3	Results and discussion .....	152
9.3.1	Normal force versus displacement curves .....	152
9.3.2	Flow resistance .....	158
9.3.3	Sag resistance of printed layers .....	162
9.3.4	Tensile bond of hardened samples.....	166
9.4	Summaries .....	167
<b>10</b>	<b>Interaction between stiffening control and adhesion .....</b>	<b>169</b>
10.1	Introduction .....	169
10.2	Experimental program .....	169
10.3	Results and discussion.....	170
10.3.1	Viscosifying property .....	170
10.3.2	Mobility of cellulose ether under pressure .....	173
10.3.3	Adhesion in the fresh state .....	177
10.4	Summaries .....	182
<b>11</b>	<b>Conclusions and perspectives .....</b>	<b>183</b>
11.1	General conclusions .....	183
11.2	Main contributions .....	185
11.3	Perspectives .....	185
	<b>List of Figures .....</b>	<b>189</b>
	<b>List of Tables .....</b>	<b>197</b>
	<b>References .....</b>	<b>199</b>
	<b>Curriculum vitae .....</b>	<b>217</b>

# Nomenclature

These lists give a non-exhaustive overview of the symbols and abbreviations used throughout the thesis.

## Latin symbols

$A$	Plate area	(m <sup>2</sup> )
$A_c$	Cross-sectional area of cubic sample	(m <sup>2</sup> )
$A_t$	Cross-sectional area of sample	(m <sup>2</sup> )
$b$	Width of prismatic sample	(m)
$b_{p1}$	Width of one side of prismatic sample	(m)
$b_{p2}$	Width of another side of prismatic sample	(m)
$d$	Diameter of concrete cylindrical sample	(m)
$D$	Pipe diameter	(m)
$e_{LL}$	Thickness of lubricating layer	(m)
$E$	Elastic modulus	(Pa)
$F$	Normal force	(N)
$F_c$	Compressive load at failure	(N)
$F_f$	Flexural load at failure	(N)
$F_t$	Tensile load at failure	(N)
$g$	Gravitational constant	(m/s <sup>2</sup> )
$G_0$	Initial elastic shear modulus	(Pa)
$h_0$	Thickness of one individual layer	(m)
$h_b$	Height of blade	(m)
$h_p$	Height of prismatic sample	(m)
$h_{p1}$	Height of one side of prismatic sample	(m)
$h_{p2}$	Height of another side of prismatic sample	(m)
$H$	Final object height	(m)
$H_c$	Critical height	(m)
$I$	Quadratic moment of inertia	(m <sup>4</sup> )
$k$	Applied loading rate	(N/s)
$l$	Constant path length of each layer	(m)
$l_t$	Length of sample	(m)
$L$	The initial gap in tack test	(m)
$L_s$	Length of supporting span	(m)

$m$	Number of printed layers at side position	(-)
$m_{ACC}$	Mass of accelerator	(kg)
$m_{LP}$	Mass of limestone powder	(kg)
$m_{PC}$	Mass of Portland cement	(kg)
$m_S$	Mass of sand	(kg)
$m_{S1}$	Mass of sand in cement-based mixture	(kg)
$m_{SP}$	Mass of superplasticizer	(kg)
$m_{SP1}$	Mass of superplasticizer in cement-based mixture	(kg)
$m_{VMA}$	Mass of viscosity modifying admixture	(kg)
$m_W$	Mass of water	(kg)
$m_{W1}$	Mass of water in cement-based mixture	(kg)
$n$	Number of printed layers at overhead position	(-)
$N$	Number of measurements	(-)
$P$	Pumping pressure	(Pa)
$P_t$	Total porosity	(-)
$Q$	Flow rate	(m <sup>3</sup> /h)
$r_{0.5}$	Mean distribution radius	(m)
$R_b$	Radius of blade	(m)
$Re$	Reynolds number	(-)
$R_q$	Root mean square deviation	(m)
$t_0$	Break time between two layers	(s)
$t_{min}$	Lower limit of open window	(s)
$t_{max}$	Upper limit of open window	(s)
$T$	Torque	(N·m)
$T_{max}$	Maximum torque	(N·m)
$v$	Pumping speed	(m/s)
$v_0$	Printing speed	(m/s)
$V_{COM}$	Volume of combined mixture	(m <sup>3</sup> )
$V_{LP}$	Volume of limestone powder-based mixture	(m <sup>3</sup> )
$V_{PC}$	Volume of cement-based mixture	(m <sup>3</sup> )
$V_r$	Volume ratio	(-)
$w_t$	Width of sample	(m)
$Z_i$	Amplitude measured on rough substrate	(m)

### Greek symbols

$\dot{\gamma}$	Shear rate	(1/s)
$\delta_{tol}$	Tolerable deformation after deposition	(-)
$\Delta F$	Load increment	(N)
$\Delta L$	Displacement of concrete cylindrical sample	(m)
$\Delta t$	Duration of one loading step	(s)
$\varepsilon_t$	Tensile strain	(-)

$\mu$	Plastic viscosity	(Pa·s)
$\mu_{P,B}$	Plastic viscosity of concrete	(Pa·s)
$\mu_{P,LL}$	Plastic viscosity of lubricating layer	(Pa·s)
$\rho$	Density	(kg/m <sup>3</sup> )
$\rho_{ACC}$	Density of accelerator	(kg/m <sup>3</sup> )
$\rho_{LP}$	Density of limestone powder	(kg/m <sup>3</sup> )
$\rho_{PC}$	Density of Portland cement	(kg/m <sup>3</sup> )
$\rho_S$	Density of sand	(kg/m <sup>3</sup> )
$\rho_{SP}$	Density of superplasticizer	(kg/m <sup>3</sup> )
$\rho_{VMA}$	Density of viscosity modifying admixture	(kg/m <sup>3</sup> )
$\rho_W$	Density of water	(kg/m <sup>3</sup> )
$\sigma_0$	Normal stress	(Pa)
$\sigma_c$	Compressive strength	(Pa)
$\sigma_f$	Flexural strength	(Pa)
$\sigma_t$	Tensile stress	(Pa)
$\sigma_{tb}$	Tensile bond strength	(Pa)
$\sigma_y$	Stress along longitudinal direction	(Pa)
$\sigma_z$	Vertical stress	(Pa)
$\tau$	Shear stress	(Pa)
$\tau_0$	Yield stress	(Pa)
$\tau_{0,B}$	Yield stress of concrete	(Pa)
$\tau_{0,LL}$	Yield stress of lubricating layer	(Pa)
$\tau_{0,t}$	Yield stress of bottom layer	(Pa)
$\tau_s$	Shear stress measured in shear test	(Pa)
$\tau_y$	Maximum shear stress in stress growth test	(Pa)
$\tau_{yz}$	Shear stress at yz plane	(Pa)

## Abbreviations

3DCP	3D concrete printing
ACC	Accelerator
ALM	Automated laser measurement
BSE	Backscattered electron
CCD	Charge-coupled device
CE	Cellulose ether
COV	Coefficient of variation
DLS	Dynamic lighting scattering
EDX	Energy dispersive X-ray
EVA	Poly (ethylene-vinyl acetate)
HEC	Hydroxyethyl cellulose
HEMC	Hydroxyethyl methyl cellulose
HPMC	Hydroxypropyl methyl cellulose

LL	Lubrication layer
LOI	Loss on ignition
LP	Limestone powder
MC	Methyl cellulose
MIP	Mercury intrusion porosimetry
NATM	New Austrian Tunneling Method
PAE	Polyacrylic ester
PC	Portland cement
PCE	Polycarboxylate ether
RDP	Redispersible polymer powder
RSD	Relative standard deviation
SAE	Poly (styrene-acrylic ester)
SC3DP	Shotcrete 3D printing
SE	Secondary electron
SEM	Scanning electron microscopy
SP	Superplasticizer
SSD	Saturated surface dry
TBM	Tunnel Boring Machine
TPP	Twin-pipe pumping
VMA	Viscosity modifying admixture
XRD	X-ray diffractogram

### Abbreviations of cement chemistry

$\text{Al}^{3+}$	Aluminum ion
$\text{Al}(\text{OH})_3$	Aluminum hydroxide
$\text{Al}_2(\text{SO}_4)_3$	Aluminum sulfate
AFt	Ettringite
$\text{Ca}^{2+}$	Calcium ion
$\text{Cl}^-$	Chloride ion
$\text{CaCO}_3$	Calcium carbonate
$\text{CaCl}_2$	Calcium chloride
$\text{Ca}(\text{NO}_3)_2$	Calcium nitrate
$\text{Ca}(\text{OH})_2$	Calcium hydroxide
$\text{Ca}(\text{NO}_2)_2$	Calcium nitrite
$\text{Ca}(\text{SCN})_2$	Calcium thiocyanate
$\text{CaSiO}_3$	Calcium silicate
$\text{Ca}(\text{HCOO})_2$	Calcium formate
$\text{CaSO}_4 \cdot 2\text{H}_2\text{O}$	Gypsum
$\text{C}_3\text{A}$	Tricalcium aluminate
$\text{C}_3\text{S}$	Tricalcium silicate
$\text{C}_2\text{S}$	Dicalcium silicate
C-A-H	Calcium aluminate hydrate



C-S-H	Calcium silicate hydrate
$C_{12}A_7$	Dodecacalcium hepta-aluminate
$HCOO^-$	Formate ion
$KAl(OH)_4$	Potassium aluminate
$K_2CO_3$	Potassium carbonate
KOH	Potassium hydroxide
KSCN	Potassium thiocyanate
$NO_2^-$	Nitrite ion
$NO_3^-$	Nitrate ion
$Na_2CO_3$	Sodium carbonate
$NaAlO_2$	Sodium aluminate
$Na_2SiO_3$	Sodium silicate
NaSCN	Sodium thiocyanate
NaOH	Sodium hydroxide
$Na_2O$	Sodium oxide
$SiO_2$	Silicon dioxide
$SO_4^{2-}$	Sulfate ion
TEA	Triethanolamine



## General introduction

### 1.1 Motivation

This thesis aims at extending extrusion-based 3D concrete printing (3DCP) for the construction of hard rock tunnel linings.

Due to the advantages of high flexibility, convenience, and no requirement of formwork, shotcrete has been widely used in situations where access is difficult, concrete casting is impossible, and rapid setting is required (e.g. structural repairs, soil stabilization, avoidance of water penetration, and slope protection). Among all these practical applications, the support of rock in mines and tunnels is probably the most important application of shotcrete, as shown in Figure 1.1. Shotcrete is used to hold the surrounding rock, enhance the stability, and prevent oxidation, deterioration, and softening [1, 2]. Specifically, the New Austrian Tunneling Method (NATM), developed in the 1960s, explored more possibilities of shotcrete for hard rock tunnel linings. This method employs sophisticated monitoring to optimize various wall reinforcement techniques based on the type of rock encountered as tunneling progresses. The most significant advantage is that the original strength of surrounding rocks is preserved and the loads are supported by both tunnel linings and rocks [3]. As a result, a smaller cross-section is needed, leading to a lower depth of rock excavation. Around the same time, the Tunnel Boring Machine (TBM) was developed and widely used for the construction of tunnel linings. Modern TBMs typically consist of the rotating cutting wheel, called a cutter head, followed by a main bearing, a thrust system and trailing support mechanisms. In hard rock, either shielded or open-type TBMs can be used. TBMs have the advantages of limiting the disturbance to surrounding ground and producing a smooth tunnel wall. Moreover, with the employment of concrete segments, the tunneling progress is sped up significantly [4]. However, difficult geometries and complex (e.g. fractured and highly auriferous) bodies of rocks still require the use of shotcrete.

In addition, because of unpredictable disasters (e.g. earthquake, blast, and fire), tunnel linings might suffer severe damage and need urgent repairs. An example of a broken tunnel lining structure after fire exposure is shown in Figure 1.2. In this

situation, shotcrete is particularly useful for the rehabilitation of damaged tunnel structures, especially for confined construction places such as metro tunnels [5].



Figure 1.1 The application of shotcrete in tunnels, taken from [6].



Figure 1.2 Fire damage of the tunnel lining, taken from [7].

Unfortunately, several drawbacks appear during the shotcrete process including the low dimensional accuracy of the sprayed profile, pollutions such as wastewater and dust, and most of all a high amount of rebound [8]. Compared to the amount of rebound of around 30-40% during a dry-mix shotcrete process for tunnel lining construction, a wet-mix shotcrete process can reduce the amount of rebound to 5-15%. However, the rebound cannot be eliminated due to the presence of pneumatic components for projecting and compacting shotcrete. Rebound materials, comprising mainly of large aggregates that do not adhere to the excavated rock wall and fall, lead to economic problems (e.g. increased production costs) and changes in the composition (e.g. paste/aggregate ratio). Several factors which

affect the amount of rebound include the nozzle angle to the substrate, the accelerator dosage, the nozzle distance to the substrate, and the application area in the tunnel, as portrayed in Figure 1.3. It's vital to keep a distance of 1-2 m between the nozzle and the surface. A short distance would result in a large amount of rebound, while an excessive distance would prevent the shotcrete from compacting. The nozzle angle also plays an important role. The nozzle direction must be perpendicular to the surface, and the shotcrete must be applied in slow circular movements to guarantee a homogeneous overlay. Other factors such as the thickness of the applied layer and the speed of projection are also important. This caustic demand requires skilled and experienced technicians, which is the determining factor to minimize the amount of rebound, as an improper operation can cause a large loss of material, and even compromise the safety of all personnel on-site.

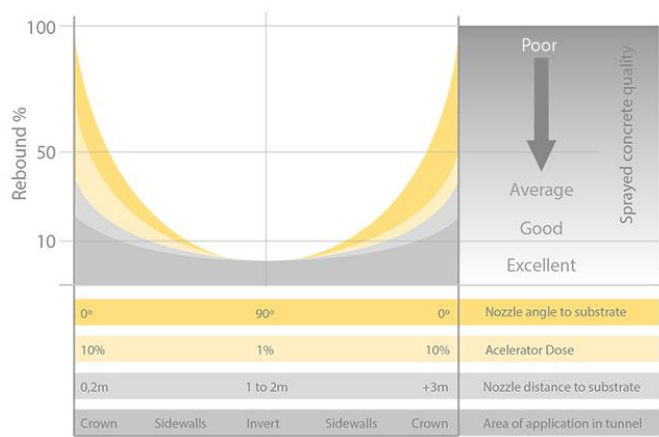


Figure 1.3 Factors influencing the amount of rebound, taken from [9].

Based on the shotcrete technology, a shotcrete 3D printing (SC3DP) technique, i.e. spray-based 3D concrete printing, has been developed [10-12]. By using the spray-based 3D concrete printing technique for the construction of hard rock tunnel linings, the degree of automation and precision can be optimized. Unfortunately, the rebound cannot be avoided due to the presence of a high-speed spraying process. Alternatively, extrusion-based 3D concrete printing is one of the most popular innovative construction methods from the past two decades [13]. The advantages of 3D concrete printing include a high construction speed, no need for formwork, less intensive labor, and an increase of freedom to design [14]. Given these advantages, extrusion-based 3D concrete printing shows the potential to be applied for the construction of hard rock tunnel linings, as shown in Figure 1.4.

With the precise control of the printing path and a high steady flow rate, the surface quality of 3D printed structures can be guaranteed, when compared to that of shotcrete or spray-based 3D concrete printing. Instead of spraying concrete with a

high speed, 3D printed materials can be slowly extruded onto the rock wall, which is beneficial for the avoidance of rebound. Moreover, there is no need for skilled and experienced workers in the 3D concrete printing process, since the direction and movement of the printing nozzle can be controlled automatically. Particularly, 3D concrete printing can be treated as an environmentally friendly process without any wastewater or dust when compared to shotcrete. The comparison between the dry-mix shotcrete process, the wet-mix shotcrete process, the spray-based 3D concrete printing process [11], and the extrusion-based 3D concrete printing process are listed in Table 1.1. It should be noted that discharging speed refers to the speed of material projected from the outlet. In the case of shotcrete, due to the presence of pneumatic components, a high spraying speed is achieved (30-40 m/s), while the flow is not continuous along the pipeline direction. Different from shotcrete, the discharging speed of 3D printed concrete is equal to the moving speed of the nozzle (0-1 m/s), while a continuous flow can be obtained. On the other hand, the flow rates of shotcrete and 3D printed concrete are the same (0-6 m<sup>3</sup>/h), which depend on the capacity of the used pump. More details can be found in Chapter 2.



Figure 1.4 Schematic view of extending 3D concrete printing to hard rock tunnel linings.

Table 1.1 Comparison between dry-mix shotcrete process, wet-mix shotcrete process, spray-based 3D concrete printing, and extrusion-based 3D concrete printing.

	Dry-mix process	Wet-mix process	Spray-based 3DCP	Extrusion-based 3DCP
Creation	1910s	1950s	2010s	2000s
Formwork	No	No	No	No
Air compressor	Yes	Yes	Yes	No
Rebound	30-40%	5-15%	5-15%	0%
Discharging speed (m/s)	30-40	30-40	30-40	0-1
Flow rate (m <sup>3</sup> /h)	0-1.5	0-6	0-6	0-6
Pollution	Heavy	No	No	No
Skilled laborers	Yes	Yes	No	No

## 1.2 Objectives

The research objectives of this thesis are set based on the necessity to introduce 3D concrete printing technology for the construction of hard rock tunnel linings. Two basic types of failure modes should be avoided, which commonly occur during a spraying process. One type is that applied materials fall with a low shear resistance due to the punching of loose rock, as shown in Figure 1.5 (a). Another one is that materials detach due to the lack of adhesion at the material-to-substrate interface, as portrayed in Figure 1.5 (b) and Figure 1.5 (c).

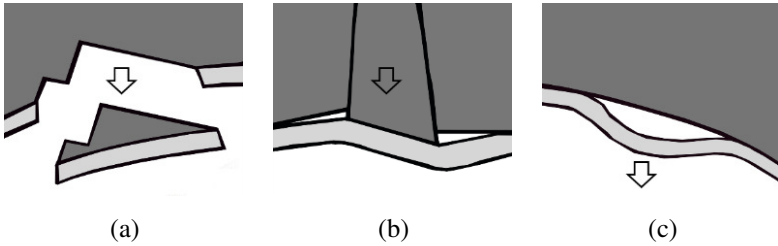


Figure 1.5 Basic types of failure modes of tunnel linings including (a) shearing of materials in the loose rock area, (b) detaching at the interface in the loose rock area, and (c) detaching at the interface under self-weight.

To avoid the punching failure, a high stiffening rate of the printed material is required after extrusion. However, high fluidity and a sufficient open time combined with a low stiffening rate are required for the pumping process to easily convey fresh materials from a reservoir or a mixer to a printing nozzle. The most common approach consists of finding a compromise between these contradictory

requirements of the fluidity and stiffening rate. Unfortunately, without any accelerating process, the maximum stiffening rate that can be achieved is very limited [15].

Interventions that are effective for active control of concrete properties have been summarized by De Schutter and Lesage [16] including mechanical [17], thermal, hydro, pressure, magnetic [18], electric (via heating due to resistivity), and microwave (via heating due to internal dipolar vibration) approaches. While mechanical, hydro, and pressure interventions show a limited effect, the drawback of heating concrete (i.e. thermal, electric, and microwave) is that elevated temperature curing requires high energy input and emits greenhouse gases that create environmental degradation. Moreover, such a curing process leads to unevenly distributed hydration products, resulting in a reduced ultimate strength [19, 20] and increased porosity [21, 22]. In addition, an innovative concept ‘Smartcast’ applying magnetic fields to achieve active stiffening control and active rheology control has been proposed by De Schutter et al. [14]. The goal is the active control of concrete rheology from pumping to casting, and the active triggering of early stiffening of the concrete, as well as to guarantee the formwork tightness after the concrete placement. It is shown by Jiao et al. [18] that magnetic intervention has a significant effect on the structural-build-up of fresh cement-based materials. However, the practical application of this idea requires further development. Chemical interventions are most widely used to modify the performance of cement-based materials. Potential admixtures used for 3D concrete printing such as accelerators (ACC), viscosity modifying admixtures (VMA), and clays are discussed by Marchon et al. [23]. Many trials based on the idea of stiffening control by introducing chemical admixtures have been performed. For example, a system in which the dormant period of cement was modified with sucrose and calcium hydroxide was developed by Reiter et al. [24]. Among all these admixtures, the accelerator is probably the most effective admixture to accelerate the stiffening process. The hydration and strength build-up kinetics of two formulated accelerators for 3D printable concrete are investigated by Szabo et al. [25]. It is found that the rate of yield stress evolution could be customized by using different dosages of accelerators. The accelerators can either be mixed with water and dry materials during the pre-mixing process or can be injected into the fresh concrete during or immediately after the pumping process. In the first case, the fresh concrete containing an accelerator would obtain high yield stress [26] and a fast stiffening rate, which will introduce severe pumping problems and could ruin the whole pumping system once some unexpected interruptions happen. In the second case, the risk of pipe blocking would be reduced as the accelerator is not mixed in advance. [27, 28]. However, in such cases, a huge challenge still remains in dosing accelerator into fresh cement-based materials. Therefore, the first objective of this thesis is to develop an inline mixing system that can dose accelerator into fresh cement-based materials at the nozzle position. The hydration mechanism of the accelerator used in the inline mixing system and the phase



transition of the cement-based materials also need to be studied. In addition, the influence of such an inline mixing process on the mechanical and microstructural properties of 3D printed elements is worthy of studying.

The second objective of this thesis is to develop a 3D printable mixture with good adhesion properties both in the fresh and hardened state. Thus the detaching failure where the printed layers fail at the interface can be avoided. However, different from shotcrete where fresh materials are sprayed onto the rock surface at a high speed, such a compacting effect is very limited when fresh materials are extruded from the outlet with a much lower speed. As such, fresh materials printed on the rock surface would face more risks to drop down. Unfortunately, very limited studies focus on this topic, especially on the adhesion performance of freshly printed cement-based materials onto the rock. In the context of 3D printed hard rock tunnel linings, it is necessary to systematically investigate the adhesion performance of 3D printed materials and the influencing factors such as the surface inclination, the substrate properties, and the influence of polymers in 3D printed materials.

### **1.3 Strategies**

To achieve the first objective, an innovative strategy, namely twin-pipe pumping, is proposed. The accelerator is used for the stiffening control right before extrusion, where a motionless helical static mixer without any moving components is used. Instead of injecting a liquid accelerator into fresh cement-based materials directly, an inert filler suspension (e.g. limestone powder-based suspension) works as an admixture carrier, able to carry all “thickening” admixtures including accelerators and viscosity modifying admixtures for prompting the stiffening process. All types of admixtures can be added, whether they are liquids or powders. During the printing process, the cement-based mixture is pumped from one pipe while the inert filler-based mixture is pumped from another pipe. Afterwards, these two mixtures are incorporated into the static mixer before extrusion. During the inline mixing process, the accelerator and viscosity modifying admixture in the inert filler-based mixture would soon take effect within the cement-based mixture, resulting in a fast stiffening process and a prompt phase transition from a liquid form to a solid form. The twin-pipe pumping system is shown in Figure 1.6.

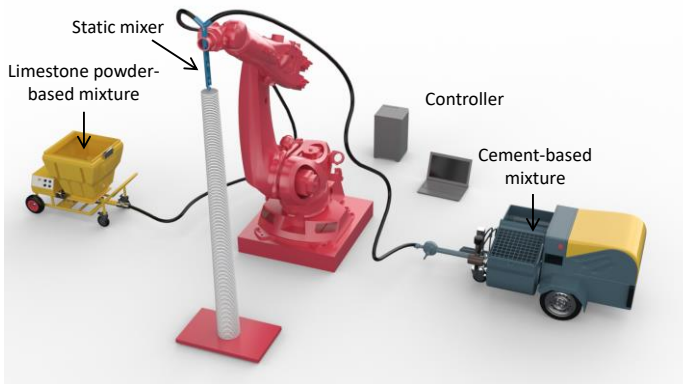


Figure 1.6 Schematic view of the twin-pipe pumping system.

In this thesis, limestone powder is used as the carrier material for the accelerator. The combined mixture is developed in the first step. The substitution rate of limestone powder and the accelerator dosage are determined. Then the combined mixture is divided into two separate mixtures, including a cement-based mixture and a limestone powder-based mixture. The fresh properties and the pumping process are studied. Afterwards, the influence of the inline mixing system on the mechanical and microstructural properties of the hardened elements is investigated.

To achieve the second objective, concrete substrates are used to replace the excavated rock wall. The adhesion properties of fresh cement-based materials are considered on two scales including a small scale for investigating the adhesion mechanism (the tack test) and a large scale for validation (the 3D concrete printing test). Different from other 3D concrete printing tests where fresh materials are deposited layer by layer vertically, the fresh cement-based materials in this study are printed against the lower surface of a supported concrete slab (overhead position of the tunnel lining) or the surface of an upright concrete slab (side position of the tunnel lining). Based on this, the influence of substrate surface inclination on the adhesion is investigated. In addition, different concrete surface treatment technologies including polishing, gritblasting, hammering, and water-jetting are used to prepare a series of concrete substrates with different roughness levels. The influence of substrate properties on the adhesion is then studied. Further, different types of polymers are adopted including cellulose ethers and redispersible polymer powders to modify the adhesion. Mold cast samples are also prepared and adhesion properties of the 3D printed samples are compared to that of mold cast samples.

## 1.4 Outline

The thesis consists of 11 chapters, divided into four main parts.

The first part gives a general overview of this thesis. In Chapter 1, an introduction is given including the motivation, research objectives, and research strategies to replace shotcrete with extrusion-based 3D concrete printing for the construction of hard rock tunnel linings. Chapter 2 gives a state of the art about the basic concepts and terminologies with regard to 3D concrete printing, stiffening control using accelerators in inline mixing processes, and adhesion mechanisms. In Chapter 3, materials and testing methods are presented.

The second part focuses on the development of the twin-pipe pumping system, aiming at achieving easy pumping during transportation and fast setting after extrusion. This part starts from Chapter 4 and ends with Chapter 6. In Chapter 4, the combined mixture used in the twin-pipe pumping system is developed. Chapter 5 presents the phase transition of printed materials from the pumping process to the fabrication process. Chapter 6 further investigates the mechanical and microstructural properties of the hardened elements printed via the twin-pipe pumping system.

The third part focuses on the adhesion behaviors of the printed materials for hard rock tunnel linings, including Chapter 7, Chapter 8, and Chapter 9. Chapter 7 presents the adhesion of fresh materials for different surface inclinations in a hard rock tunnel. In Chapter 8, substrate properties (i.e. surface roughness level and moisture content) on the adhesion in the fresh and hardened states are explored. Chapter 9 investigates the effect of polymer modification including redispersible polymer powders and cellulose ethers on adhesion performance.

The last part includes Chapter 10 and Chapter 11. Chapter 10 discusses the interaction effect of the accelerator (for stiffening control) and cellulose ether (for adhesion). In conclusion, Chapter 11 offers the main findings of this thesis and perspectives for future research.

The thesis outline is shown in Figure 1.7.

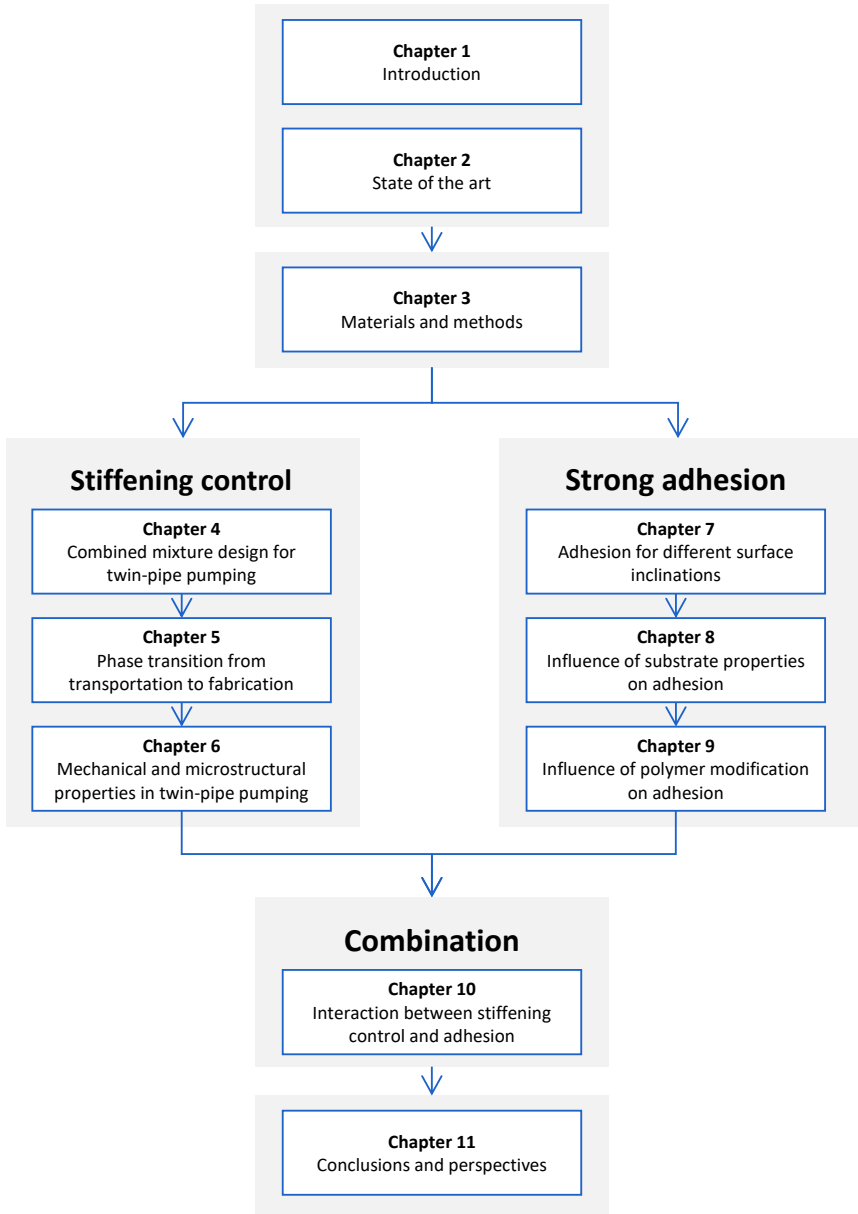


Figure 1.7 Thesis outline.

## State of the art

### 2.1 Introduction

To meet the two requirements including stiffening control and strong adhesion as introduced in Chapter 1, this chapter gives a state of the art regarding these aspects, as well as some general concepts in the context of extrusion-based 3D concrete printing. This chapter begins with the terminology used in 3D concrete printing including pumpability, extrudability, and buildability. Afterwards, for the first requirement, the classifications of accelerators and hydration mechanisms are given, which is vital to determine when and where to inject the accelerator. This is followed by a detailed discussion on the inline mixing process of accelerators as a reference for the stiffening control system developed in this thesis. Further, the problems and challenges of using accelerators in these applications will be pointed out. For the second requirement of strong adhesion, basic notions including adhesion and cohesion are distinguished. Moreover, typical adhesion theories and some circumstantial effects are introduced to better understand the performance of 3D printable concrete for hard rock tunnel linings. Afterwards, the influence of concrete surface characteristics such as roughness, moisture content, and the application of bonding agents is discussed.

### 2.2 Terminology in extrusion-based 3D concrete printing

#### 2.2.1 Pumpability

Pumping is an indispensable part of extrusion-based 3D concrete printing. This is a process that pushes fresh materials through a pipe by adopting progressive cavity pumps or positive displacement piston pumps [29]. The pumpability can be characterized by pressure losses. However, the pumping pressure calculated by using the Buckingham-Reiner equation for laminar flow of fresh concrete can be overestimated up to 5 times due to neglect of the lubrication layer (LL) [30]. It is well recognized that the formation of the lubrication layer originates from shear-induced particle migration. Normally, the yield stress and plastic viscosity of the lubrication layer are significantly lower than that of the bulk material, respectively [31]. The shear stress, shear rate, and velocity profiles of the pumped concrete are shown in Figure 2.1. It can be observed that the values of the shear stress and shear

rate are zero at the center of the pipe cross-section and reach a maximum value at the pipe wall. As such, shearing inside the bulk concrete occurs when the shear stress exceeds the yield stress. The analytical models for predicting the concrete pumping pressure using rheological parameters including the shear stress and plastic viscosity of the bulk and lubrication layer are given by Kaplan et al. [32].

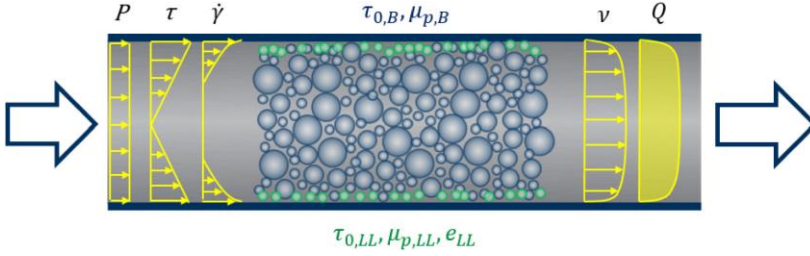


Figure 2.1 Pressure  $P$  (Pa), shear stress  $\tau$  (Pa), shear rate  $\dot{\gamma}$  ( $\text{s}^{-1}$ ), velocity  $v$  (m/s), and flowrate  $Q$  ( $\text{m}^3/\text{s}$ ) profiles of a concrete flow inside a pumping pipeline. The yield stress and plastic viscosity of concrete are  $\tau_{0,B}$  (Pa) and  $\mu_{p,B}$  (Pa·s), whereas the yield stress, plastic viscosity and the thickness of the lubrication layer are  $\tau_{0,LL}$  (Pa),  $\mu_{p,LL}$  (Pa·s), and  $e_{LL}$  (m), taken from [29].

With regard to the pumpability of 3D printable concrete, pumping fresh concrete with high yield stress or accelerated concrete may not be an optimal solution, especially for a long-distance pumping process. For example, major difficulties in resuming pumping operations might appear after short interruptions due to the significant effect of internal structural build-up [30]. Alternatively, pumping fresh concrete with low yield stress and low plastic viscosity and activating it right before extrusion would be a more suitable approach for 3D concrete printing, which will be introduced in the following sections and chapters.

However, determining the rheological parameters of the bulk and lubrication layer, and predicting the pumping pressure are still considerable challenges. Compared to the empirical designs counting on a slump or spread parameter, advanced testing approaches and prediction models have been developed recently [33]. Unfortunately, most of these approaches are not suitable to quantify the rheological properties (e.g. high yield stress) of stiff materials for 3D concrete printing [34]. Moreover, the influence of the activation process at the printing head on the pumping behavior of fresh concrete is very limited studied at this stage.

### 2.2.2 Extrudability

The extrusion process can be considered as the action of conferring the shape of the cross-section to deposited layers [29]. Several aspects should be considered in this regard. For example, the flow rate, as well as the velocity profile, plays an important role in the proper placement and the cross-section of printed layers. In addition, the design of the nozzle (e.g. the geometric reduction of the outlet, the

use of side trowels, and the rotation of the nozzle) is important for the extrusion process.

Another interesting point to be discussed is extrusion-induced segregation. Such a behavior can be treated as a competition between the extrusion time and the characteristic drainage time due to the pressure difference. Segregation would occur when the extrusion time is longer than the characteristic drainage time. This phenomenon has been reported in literature, including water migration in frictional plastic materials under a ram extrusion force [35]. Such behavior would induce surface defects such as cracks or even blockage. A potential solution is to add additional energy such as vibration to ease the flow [36]. However, such an energy-based approach to extrude has not been widely studied. Some studies were only carried out in an axisymmetric case where a vibration needle is immersed in concrete [37]. For 3D concrete printing, one challenge is to precisely determine the vibrated area since the action of vibration might compromise the structural build-up of the deposited layers.

### 2.2.3 Buildability

The buildability requirements include individual strength-based layer stability, collective strength-based layer stability, individual layer geometry control, collective geometry control, and collective buckling failure prevention [38, 39].

The first issue to be discussed is the strength-based layer stability, where the shear stress inside fresh concrete is dominated by gravity-induced stress. For the individual layer, the initial yield stress should meet the following requirement:

$$\tau_0 > \rho gh \quad (2.1)$$

where  $\tau_0$  is the initial yield stress (Pa),  $\rho$  is the density of fresh concrete ( $\text{kg/m}^3$ ),  $g$  is the gravitational constant ( $\text{m/s}^2$ ), and  $h$  is the thickness of one individual layer (m).

Regarding the collective stability, where plastic collapse is not expected, the yield stress of the bottom layer should meet the following requirement:

$$\tau_{0,t} > \frac{\rho g H}{(\sqrt{3})} \quad (2.2)$$

where  $\tau_{0,t}$  is the yield stress at the bottom layer (Pa), and  $H$  is the final object height (m).

The second issue to be discussed is geometry control (i.e. the individual layer geometry control and the collective geometry control) [38]. As for an individual

layer, the geometry control requires that the initial elastic shear modulus follows the following requirement:

$$G_0 > \frac{\rho gh}{\delta_{tol}} \quad (2.3)$$

where  $G_0$  is the initial elastic shear modulus (Pa),  $\delta_{tol}$  is a tolerable deformation right after deposition (-).

There are no specific requirements for the collective geometry control since the elastic shear modulus increases with time and the critical shear strain (i.e. the tolerable deformation) decreases with time.

The third issue to be discussed is the collective buckling failure [38, 40]. This type of failure does not occur at the bottom layer of the printed object, but is caused by a loss of stability. The critical height, for which self-buckling is expected to occur in a vertical structure submitted only to its weight writes:

$$H_c = \left( \frac{8EI}{\rho g A} \right)^{\frac{1}{3}} \quad (2.4)$$

where  $H_c$  is the critical height (m),  $E$  is the elastic modulus of the material (Pa),  $I$  is the quadratic moment of inertia (m<sup>4</sup>), and  $A$  is the horizontal rectangular cross-sectional area (m<sup>2</sup>).

## 2.3 Classification of accelerators and hydration mechanism

Accelerators can be classified into different categories and can be used for different purposes. For example, accelerators can be classified by the effect (enhancing setting or hardening), the composition (inorganic or organic salts), the action (physical action or chemical action), and also on the type of application (e.g. shotcrete and normal concrete accelerator).

### 2.3.1 Setting versus hardening

To better understand the reaction mechanism of accelerators, the difference between setting and hardening is given first. According to the standard BS EN 934-2 [41], a distinction is made whether the effect of the accelerator is an enhancement in setting or in hardening properties. Setting accelerators shorten the transition time from a plastic state to a rigid state, while hardening accelerators increase the strength at early age, with or without influencing the setting time [42].

The setting and hardening type accelerators can be distinguished by which mineral phase they affect. Setting accelerators mainly affect the tricalcium aluminate (C<sub>3</sub>A) phase with the promotion of silica and alumina dissolution and interference



of the  $C_3A$ -gypsum ( $CaSO_4 \cdot 2H_2O$ ) reaction. Hardening accelerators mainly affect the tricalcium silicate ( $C_3S$ ) phase, resulting in C-S-H gel formation [43, 44].

The effect on setting is normally described by the setting times - the initial setting time (the time when the concrete starts losing its plasticity) and the final setting time (the time when the concrete completely loses its plasticity) - which are measured by a penetration test [45]. The effect on hardening is commonly characterized by measuring the mechanical strength development of young concrete samples [46]. Setting and hardening can also be assessed by the rate of hydration, which is generally measured by a calorimeter test. An earlier increase in the cumulative heat production (J/g) or temperature ( $^{\circ}C$ ) generated from the hydration reactions indicates an accelerated setting performance while a faster heat production rate (J/gh) indicates an accelerated hardening performance [42, 47, 48], as shown in Figure 2.2.

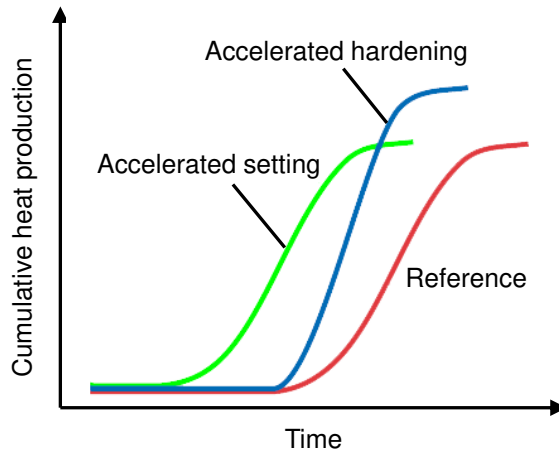


Figure 2.2 Setting or hardening effect represented by cumulative heat production [42].

The reference represents the mixture without any accelerator. Adding a setting accelerator leads to an earlier heat release with a parallel slope compared to the curve obtained for the reference sample. Adding a hardening accelerator results in a higher heat release rate (i.e. a steeper slope) but with the heat release starting at the same time as the reference.

### 2.3.2 Inorganic versus organic salts

It is also common to distinguish accelerators as either inorganic or organic salts. Inorganic salts typically include alkali and alkali earth salts of chlorides (as well as other halogens such as bromides and fluorides), nitrates, nitrites, thiocyanates, thiosulfates, silicates, aluminates, carbonates, and alkaline hydroxides [42]. From

a general point of view, the accelerating function of anions relates to the identity of the associated counterion with the divalent and trivalent cations (e.g. calcium, magnesium, and aluminum) showing superior performance compared to monovalent ions (e.g. sodium, potassium, and ammonium) [44]. Specifically, the accelerating effect of different anions and cations on  $C_3S$  hydration in decreasing order is as follows:

Anions:  $Br^- \approx Cl^- > SCN^- > I^- > NO_3^- > ClO_4^-$

Cations:  $Ca^{2+} > Sr^{2+} > Ba^{2+} > Li^+ > K^+ > Na^+ \approx Cs^+ > Rb^+$

Among all these inorganic salts, calcium chloride ( $CaCl_2$ ) has proven to be the most efficient and one of the most low-cost accelerators [49-52].  $CaCl_2$  can accelerate both the setting and hardening of Portland cement [53]. The mechanism of  $CaCl_2$  mainly relates to the nucleation and dissolution kinetics [52, 53]. Firstly,  $CaCl_2$  can accelerate the  $C_3A$ -gypsum reaction resulting in a decreased setting time [54]. Also,  $CaCl_2$  can enhance C-S-H nucleation and results in the formation of a more penetrable C-S-H gel to accelerate the iron diffusion in the induction period [49, 51].  $CaCl_2$  can also accelerate the hydration of dicalcium silicate ( $C_2S$ ) and lowers the alkalinity of the pore solution to promote hydration [55-57]. However, it has to be mentioned that the use of chloride-based admixtures is forbidden by several standards due to the risk of reinforcement corrosion.

Sodium and calcium salts of nitrate ( $NO_3^-$ ) and nitrite ( $NO_2^-$ ) are commonly used as accelerators in traditional concrete. The accelerating effect of  $NO_3^-$  is less than that of  $Cl^-$  [52], leading to a less effective accelerating effect of calcium nitrate ( $Ca(NO_3)_2$ ), compared to that of  $CaCl_2$ , as indicated in the isothermal conduction calorimeter curves shown in Figure 2.3 [52]. The mechanism of  $Ca(NO_3)_2$  to accelerate the setting is similar to that of  $CaCl_2$  [58-60]. Firstly, a lower sulfate concentration would decrease the formation of ettringite and shorten the onset of  $C_3A$  hydration. Another mechanism is that  $Ca(NO_3)_2$  increases the calcium ( $Ca^{2+}$ ) concentration and the supersaturation degree of calcium hydroxide ( $Ca(OH)_2$ ), thereby shortening the time needed for initial crystallization and the renewal of  $C_3S$  hydration. Calcium nitrite ( $Ca(NO_2)_2$ ) has probably been the most popular non-chloride setting accelerator since the late 1960s [52].  $Ca(NO_2)_2$  is widely used in antifreeze admixtures. Despite this widespread use, reports describing the mode of action and mechanisms involved in cement paste settings are lacking. However, it can be predicted that the hydration mechanism of  $Ca(NO_2)_2$  is similar to that of  $Ca(NO_3)_2$  to some extent [42].

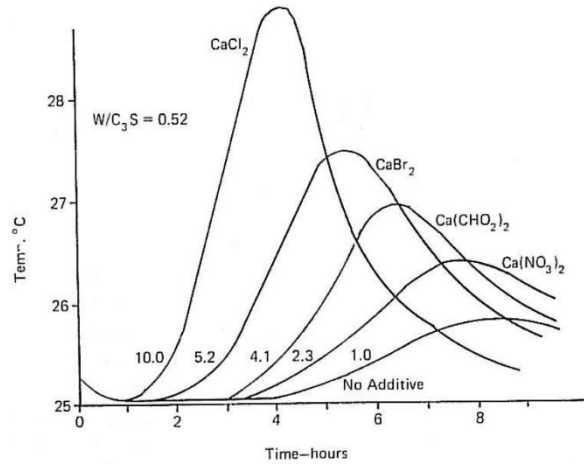


Figure 2.3 Isothermal conduction calorimeter curves for  $C_3S$  with various calcium salts. Dosage is 2% anhydrous salt by weight of  $C_3S$ , taken from [52].

Unlike nitrates and nitrites, alkali, and calcium salts of thiocyanic acid only affect the hardening process, without affecting the setting [61]. Calcium thiocyanate ( $Ca(SCN)_2$ ) is the most effective to promote strength development, as compared to sodium thiocyanate ( $NaSCN$ ) and potassium thiocyanate ( $KSCN$ ). Compared to  $CaCl_2$ , the addition of thiocyanate can promote the formation of  $Ca(OH)_2$  and accordingly, the hydration of  $C_3S$  [62].

Silicates and aluminates show quick setting or flash setting properties, which have been widely used in shotcrete, as well as in 3D concrete printing applications [11, 63, 64]. Silicates (e.g. sodium silicate ( $Na_2SiO_3$ )) can lead to a rapid setting by forming insoluble calcium silicates ( $CaSiO_3$ ) [65, 66]. Aluminates (e.g. sodium aluminate ( $NaAlO_2$ )) consumes  $Ca^{2+}$  and sulfate ions ( $SO_4^{2-}$ ) quickly, leading to an earlier gypsum depletion and the subsequent  $C_3A$  hydration in an under-sulfated system. Therefore, the main aluminate hydrates would be ettringite, monosulfoaluminate, and C-A-H. Because the solubility of a surface layer of monosulfoaluminate and C-A-H is lower than that of  $C_3S$ , the dissolution of  $C_3S$  would be blocked, and further hydration would be inhibited [47]. Different from  $NaAlO_2$ , aluminum sulfate ( $Al_2(SO_4)_3$ ) is more commonly used in recent years to avoid problems caused by the alkaline accelerators. Because of the presence of  $SO_4^{2-}$  in the accelerator, the main hydrate formed is ettringite. Because the gypsum depletion rate is lower and enough sulfate can remain for controlling  $C_3A$  hydration, there will be the normal progress of  $C_3S$  hydration [47, 67, 68]. In addition,  $Al_2(SO_4)_3$  can react with lime and produce aluminum hydroxide ( $Al(OH)_3$ ), which is also known as an accelerator [69, 70].

To some extent, carbonates such as potassium carbonate ( $K_2CO_3$ ) and sodium carbonate ( $Na_2CO_3$ ) have also been used to accelerate the setting. However, the

effect of carbonates largely depends on the added dosage. In case that a high dosage of  $K_2CO_3$  is used, a fast setting can be reached because of the promotion of  $C_3A$  hydration. While a low dosage of  $K_2CO_3$  would lead to a retarding effect [51]. Therefore, it is difficult to regulate the setting time by adding carbonates.

Apart from the inorganic accelerators listed above, organic salts are also used to promote stiffening. Carboxylic and hydroxycarboxylic acids and their salts; and alkanolamines are two main types of organic salts. Accelerators of carboxylic and hydroxycarboxylic acids and their salts include monocarboxylic, dicarboxylic, and hydroxycarboxylic types. Calcium formate ( $Ca(HCOO)_2$ ), which belongs to the monocarboxylic type, is the most commonly used accelerator in the carboxylic acid group [51, 53, 71].  $Ca(HCOO)_2$  can accelerate setting and increase the strength at an early age as well [52]. This is because the formate ion ( $HCOO^-$ ) can promote the dissolution of  $Ca^{2+}$  [72]. However,  $Ca(HCOO)_2$  is less effective than  $Ca(NO_3)_2$  and  $CaCl_2$ , which relates to their anion size ( $HCOO^-$  - 0.45 nm,  $NO_3^-$  - 0.34 nm, and  $Cl^-$  - 0.27 nm). The large anion size of  $HCOO^-$  would lead to more difficulties to penetrate hydrated layers covering  $C_3S$  grains [72-74]. In addition, because of the low solubility,  $Ca(HCOO)_2$  is always used in a powdery form.

Alkanolamines are amines containing different hydroxyalkyl groups, among which triethanolamine (TEA) is the most widely used alkanolamine. The effect of TEA can be either acceleration or retardation of hydration, which relates to the TEA dosage. At a low dosage, the  $C_3A$ -gypsum reaction is accelerated by TEA. In addition, TEA can also accelerate the subsequent transition from ettringite to monosulphate. On the other hand, TEA retards the hydration of  $C_3S$  when used at a high dosage [75-78]. It can be seen that with the increase of the TEA dosage, a higher value is obtained for the first peak which relates to the hydration of  $C_3A$ . While the inhibition of TEA on  $C_3S$  is represented by the postponement of the second peak, which relates to the hydration of  $C_3S$  [79]. Therefore, alkanolamines must be used with caution since their performance is strongly related to the type and dosage used.

### **2.3.3 Chemical versus physical actions**

Acceleration of cement hydration is achieved in different ways, which can also be divided into physical and chemical actions [23]. All the admixtures described in the previous sections perform based on chemical actions. Since they act chemically, their performance is closely related to the cement characteristics and other additives added to the mixture [80, 81]. For example, when limestone filler is added as an additive in a Portland cement system containing an accelerator, the limestone would react with aluminum ions ( $Al^{3+}$ ) supplied from the accelerator, forming hemi and monocarboaluminate [48]. Moreover, as cement is diluted by the filler addition, more space is available for the precipitation of hydrates, which

can further enhance the early age hydration promoted by the accelerator and contribute to reducing the setting time [82].

Another category relates to accelerators with only physical actions such as portlandite and C-S-H seeds. It should be noted that portlandite itself does accelerate the hydration process. In some specific cases, sucrose, acting as a retarder, absorbs onto the surface of cement particles. With the addition of portlandite, the sucrose prefers to absorb onto the surface of portlandite, rather than the surface of cement particles [23, 83] resulting again in an acceleration of the hydration process. The second type of accelerator with physical action is C-S-H seeds [84]. Introducing C-S-H seeds can increase the hydration surface significantly [85]. Therefore, the setting time can be reduced and the early age strength can be improved considerably [86-89].

#### **2.3.4 Normal concrete versus shotcrete**

From a more practical point of view, accelerators are sometimes classified simply according to the type of concrete in which they are used: accelerator for normal concrete is commonly added during the mixing of the concrete at the concrete plant; shotcrete accelerator for sprayed concrete is added in the nozzle of the equipment during spraying [42]. From the chemical point of view, the accelerator used for normal concrete commonly reacts with  $C_3S$ , while the accelerator used for shotcrete commonly reacts with  $C_3A$ . It is therefore, almost the same as the classification method of setting versus hardening.

A summary of the reaction mechanism of different accelerators is shown in Table 2.1.

Table 2.1 Summary of the mechanism and effect of different accelerators.

Type	Mechanism	Effect	reference
CaCl <sub>2</sub>	accelerate the C <sub>3</sub> A-gypsum reaction enhance C-S-H nucleation form a more penetrable C-S-H gel	accelerate setting and hardening	[49-57]
Ca(NO <sub>3</sub> ) <sub>2</sub>	accelerate the C <sub>3</sub> A-gypsum reaction enhance C-S-H nucleation form a more penetrable C-S-H gel	accelerate setting and hardening	[52, 58-60]
Ca(SCN) <sub>2</sub>	produce more Ca(OH) <sub>2</sub> and promote C <sub>3</sub> S hydration	hardly affect the setting, only accelerate hardening	[61, 62]
Na <sub>2</sub> SiO <sub>3</sub>	react with Ca <sup>2+</sup> in the cement to form insoluble CaSiO <sub>3</sub>	rapid setting	[11, 63, 65, 66]
NaAlO <sub>2</sub>	consume Ca <sup>2+</sup> and SO <sub>4</sub> <sup>2-</sup> quickly lead to an earlier gypsum depletion and further C <sub>3</sub> A hydration in undersulfated systems block the dissolution of C <sub>3</sub> S	rapid setting	[56, 90-92]
Al <sub>2</sub> (SO <sub>4</sub> ) <sub>3</sub>	provide SO <sub>4</sub> <sup>2-</sup> form more ettringite react with lime and produces Al(OH) <sub>3</sub>	rapid setting	[47, 67-70]
K <sub>2</sub> CO <sub>3</sub>	promote the hydration of C <sub>3</sub> A	accelerate setting at high dosages, retard setting at low dosages	[51]
Ca(HCOO) <sub>2</sub>	promote the dissolution of Ca <sup>2+</sup> from the cement compounds the penetrating effect into hydrated layers of HCOO <sup>-</sup> is less than Cl <sup>-</sup> and NO <sub>3</sub> <sup>-</sup>	setting and hardening	[51-53, 71-74]
TEA	accelerate C <sub>3</sub> A hydration retard C <sub>3</sub> S hydration	accelerate setting at low dosages, retard setting at high dosages	[75-79]
Portlandite	retarder tends to absorb on portlandite rather than cement	counteract retarding	[23, 83]
C-S-H seed	increase the hydration surface	accelerate setting and hardening	[84-89]

## 2.4 Inline mixing strategies with accelerator

### 2.4.1 Two-fluid grouting

The inline mixing strategy of concrete can be traced back to the 1900s when grouting was invented for sealing or strengthening soil to prevent water entrance and support foundations after excavation [93]. Several grouting materials have been developed such as sodium silicate solutions [94]. In recent years, there has been an increase in the use of fast-setting grouting methods to prevent dilution and displacement by moving water [95, 96]. Some accelerators such as chlorides, sulfates, and organic amines are used for fast-setting grouting [97]. Among all the fast-setting grouting materials, cement-sodium silicate grouting is becoming one of the most popular methods because of the short gel time, high early strength, and sufficient sealing efficiency [98, 99].

Because of the very fast hydration kinetics, almost all fast-setting grouting methods adopt the two-pipe injecting system (e.g. one pipe for cement slurry and another pipe for sodium silicate solution, commonly called water glass). A schematic representation of the two-fluid grouting system is shown in Figure 2.4.

During the grouting process, the cement paste and sodium silicate solution are pumped from two pipes separately. Afterwards, these two streams are combined in a Y-shaped pipe right before injection into soils or rocks. Normally, non-return valves are placed in the two inlets of the Y-shape pipe to avoid backflow of either cement paste or sodium silicate solution which can be observed in the insert in Figure 2.4. The advantages of two-fluid grouting are: easy installation and maneuverability. In a two-fluid grouting system, a controlled range of propagation into the rock or soil guarantees the construction quality and accuracy, which are commonly characterized by the setting time of grouted slurry [100, 101]. The setting time of the grouts can be regulated by adjusting the proportion of cement-based slurry and sodium silicate solution or changing the  $\text{SiO}_2/\text{Na}_2\text{O}$  ratio of sodium silicate solutions.

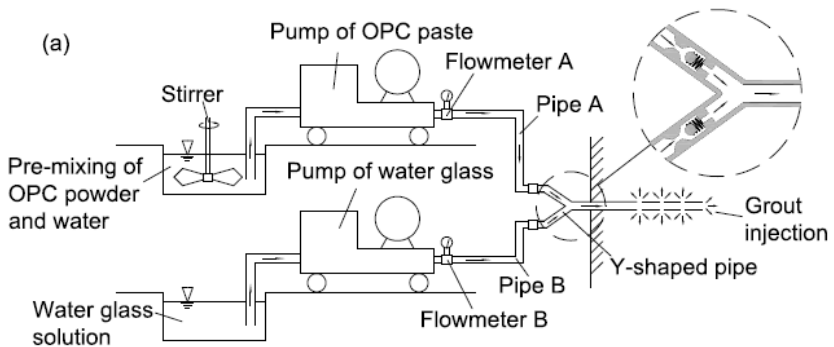


Figure 2.4 Schematic view of the two-fluid grouting system, taken from [102].

### 2.4.2 Shotcrete and spray-based 3D concrete printing

From the chemical point of view, the accelerators used for traditional concrete commonly react with  $C_3S$ , while the accelerators used for shotcrete commonly react with  $C_3A$ . Although to some extent it is too arbitrary to say this because commercial accelerators contain a mixture of many chemical components. For example, commercial alkali shotcrete accelerators are reported to include  $Na_2SiO_3$ , alkali aluminates, alkali carbonates (e.g.  $Na_2CO_3$  and  $K_2CO_3$ ), alkali hydroxides (e.g.  $NaOH$  and  $KOH$ ), and TEA. Almost all commercial alkali-free accelerators contain  $Al_2(SO_4)_3$  and other components such as diethanolamine, fluorides, organic acids, and inorganic acid [42, 103, 104].

Due to the very fast setting process, the accelerators for shotcrete should be added in an inline mixing system. Normally, shotcrete can be divided into dry-mix and wet-mix shotcrete processes. The dry-mix shotcrete process was first invented in the 1910s [64]. In the 1960s, an alternative method called the wet-mix shotcrete process was developed [105]. The dry-mix and wet-mix shotcrete processes are shown in Figure 2.5. In the dry-mix shotcrete process, water is added at the nozzle of a delivering hose to the flow of a pre-mixed mixture (aggregates, binders, and powdery admixtures). In the wet-mix shotcrete process, constitutive materials (aggregates, binders, and water) are mixed in advance and pumped to the nozzle, then mixed with a liquid accelerator and sprayed against the substrate with high-pressure air [106].

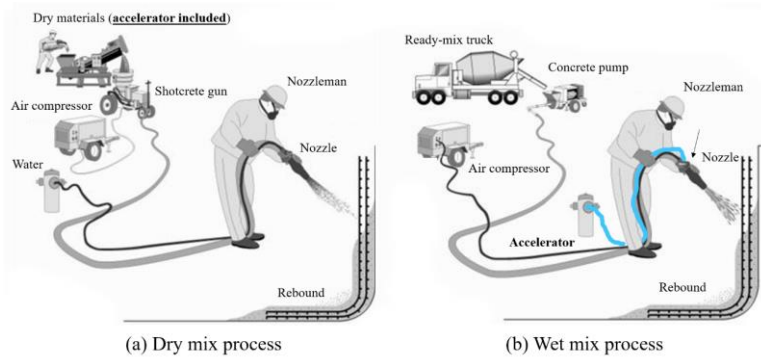
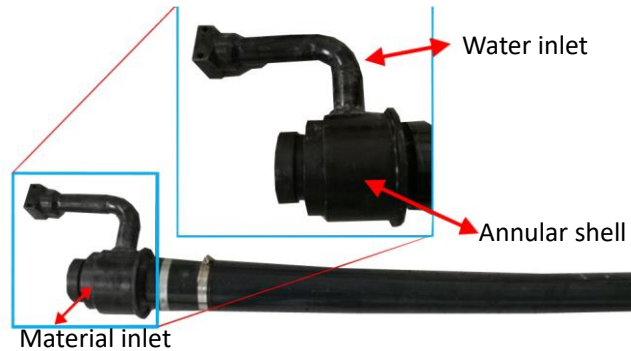


Figure 2.5 Representation of the shotcrete process with accelerators: (a) dry-mix shotcrete process, (b) wet-mix shotcrete process [107].

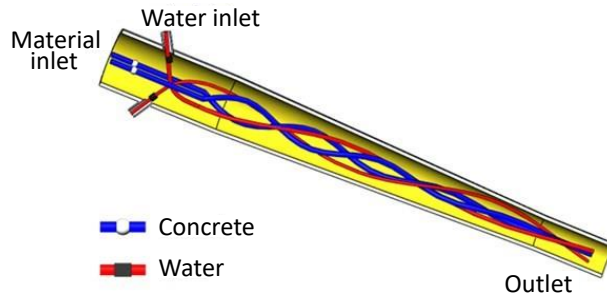
The different mixing procedures of the dry-mix shotcrete process and the wet-mix shotcrete process can also be reflected by the design of the nozzle, as shown in Figure 2.6 and Figure 2.7, respectively. It can be observed that there is an annular shell applied around the water inlet in the nozzle used for the dry-mix shotcrete process. During spraying, dry materials are pushed by high-pressure air to arrive at the material inlet, afterwards, water enters into the nozzle through the water inlet



and is combined with the dry materials from the annular shell. Then all the components are mixed via collisions at a high speed. Liu et al. [108] pointed out that more water inlets result in a better mixing homogeneity. The nozzle used for wet-mix shotcrete processes contains two (i.e. wet-mix material and air) or three inlets (i.e. wet-mix material, air, and liquid accelerator). It must be noted that both the dry-mix and the wet-mix shotcrete process require the use of compressed air. In the former, compressed air is used to pump the dry ingredients to the nozzle where it is mixed with water. In the latter, although the wet concrete mixture is pumped using a conventional concrete pump, compressed air is introduced at the nozzle along with the liquid accelerator as it is essential for ensuring mixing homogeneity between the wet concrete mixture and the liquid accelerator.



(a)



(b)

Figure 2.6 Nozzle used for the dry-mix shotcrete process, (a) nozzle structure, and (b) working principle of the nozzle used for the dry-mix shotcrete process, taken from [108].

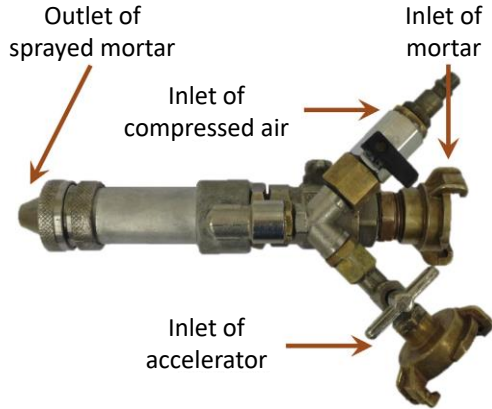


Figure 2.7 Spray gun used for the wet-mix shotcrete process, taken from [109].

Moreover, a spray-based 3D concrete printing technique named shotcrete 3D printing (SC3DP) has been developed in TU Braunschweig [11, 110-113], as shown in Figure 2.8. Due to the varying nozzle angle from  $0^\circ$  to  $180^\circ$ , a full three-dimensional deposition is achievable. The resulting geometry of the print path can be controlled by different process parameters such as nozzle distance and print velocity. Similar to the wet-mix shotcrete process of shotcrete, compressed air is applied at the nozzle to spray the pumped concrete with high kinetic energy. As discussed earlier, the introduction of compressed air is useful to provide a higher mixing homogeneity. During the traditional shotcrete process, experienced technicians are needed because the nozzle position and angle should be controlled precisely to decrease the amount of rebound. Compared to the traditional process, in SC3DP the nozzle position and angle can be arranged via an automated system. Therefore, manpower can be saved, and the construction process can be speeded up.

However, rebound still exists because of the presence of the pneumatic component. Pan et al. [114] pointed out that the amount of rebound can be decreased by limiting the coarse aggregate proportion, increasing the amount of accelerator and tackifier, and decreasing the amount of water reducing agent. In addition, the low dimensional accuracy of the sprayed profile is another problem. Although some efforts have been made to limit the splash width and assure uniform material distribution with the addition of fly ash and air-entraining agent [10], the low surface quality of the structure is still a shortcoming for techniques like shotcrete and spray-based 3D concrete printing.



Figure 2.8 Example of spray-based 3D concrete printing, taken from [113].

### 2.4.3 Extrusion-based 3D concrete printing

Compared to other digital fabrication methods, extrusion-based 3D concrete printing is the most widely developed technology in the context of digital fabrication [29]. Compared to SC3DP, the surface quality of printed elements made by extrusion-based 3D concrete printing is higher [115]. However, without the support of formwork, the printed structures are exposed to the danger of collapse during printing. The fresh materials need a fast stiffening rate (i.e. high hydration kinetics) once they are extruded out of the nozzle to fulfill a high construction rate [116]. This can be achieved by the use of accelerators. However, adding accelerators shortens the open time dramatically, leading to pumping problems such as high pumping pressure and blockages. It is therefore not ideal to add the accelerator too early during the printing process. Therefore, many researchers proposed different inline mixing strategies, using either a dynamic mixer or a motionless static mixer. A dynamic mixer is a device with one or multiple shafts powered with electric motors [117]. A static mixer is a device for the continuous mixing of liquid material, with a series of fixed baffles rather than moving components [118]. For 3D concrete printing, the innovative idea of injecting an accelerator at the position of the nozzle during the extrusion process was proposed by Gosselin et al. [119], as shown in Figure 2.9. The printing system consists of a dynamic mixer mounted on the robot as well as two peristaltic pumps, one for the pre-mixed fresh material and one for the accelerator. Unfortunately, the design details of the print head and more information about the type of accelerator are not reported.

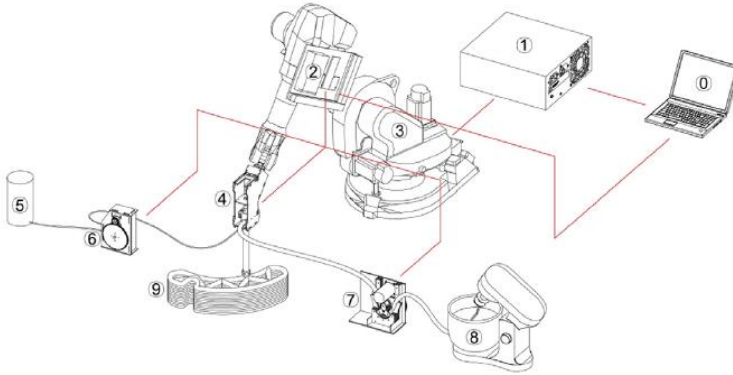


Figure 2.9 Schematic overview of a 3D printing setup: (0) System command, (1) Robot controller, (2) Printing controller, (3) Robotic arm, (4) Print head, (5) Accelerator, (6) Peristaltic pump for accelerator, (7) Peristaltic pump for premix, (8) Premix mixer, (9) 3D printed object, taken from [119].

A similar system was designed by Esnault et al. [120] where an accelerator is injected near the nozzle, to modify both the rheology and the hydration kinetics in a short time frame. In their method, a self-leveling mortar is conveyed through a pump and a piping system. A secondary pump conveys the liquid accelerator (low alkalinity shotcrete accelerator, Sika 40 AF) to a dynamic mixing device where it is mixed together with the self-leveling mortar using a rotating blade. Unfortunately, no more details about the printing system were given. A nozzle with an incorporated inline mixing chamber was designed in ETH Zurich [121-123], as shown in Figure 2.10. It consists of rotating pins for mixing the fresh cement-based materials and the liquid accelerator brought into the chamber from two separate lines. One of the accelerators used in the system is X-SEED 100 (from BASF), which consists of a suspension of synthetic crystal nuclei that favors the growth of calcium silicate hydrate (C-S-H) particles. A dynamic mixer was designed by Yuan et al. [124] consisting of blades and a screw system that allows for both material mixing and extrusion, as shown in Figure 2.11. The accelerator used in the system is an alkali-free shotcrete accelerator, but the injection point of the accelerator got easily blocked resulting in erroneous results.

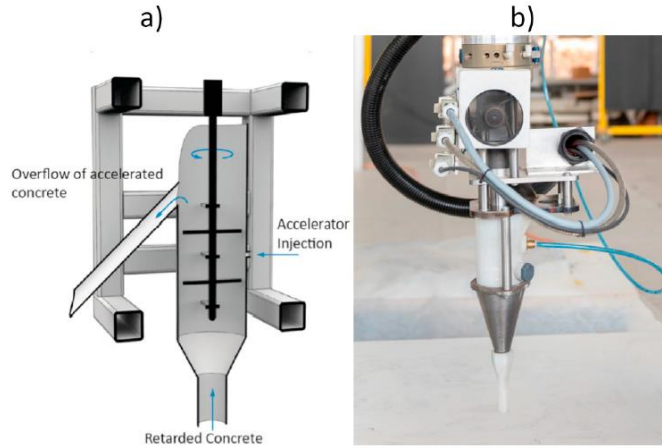


Figure 2.10 Mixing chamber used in ETH Zurich: a) a mixing reactor with a pin mixer type tool for smart dynamic casting; b) a mixing reactor with a pin mixer type tool for extrusion-based 3D printing, taken from [121].

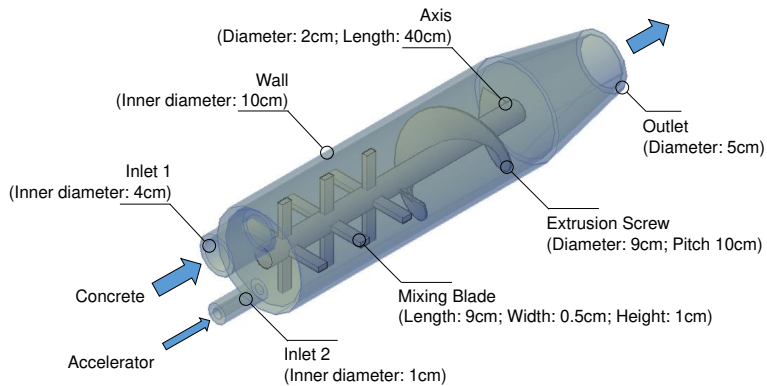


Figure 2.11 A dynamic mixer consisting of blades and screw system, taken from [124].

In the context of digital fabrication, some patent applications have also been submitted for inline mixing strategies. For example, a patent for a dynamic mixer was filed by Kuhn et al. [125] and it is indicated that homogenization is best achieved by active mechanical mixing in a chamber and by positioning the mixing chamber close to where concrete is placed.

However, the adoption of a dynamic mixer consists of complicated components and thus leads to difficulties in maintenance and operation. Moreover, the performance of the dynamic mixer depends on the design of the blade. The dead zone is another common problem [126]. Because the magnitude of fluid velocity

is quite different inside the dynamic mixer, especially for some areas where the velocity is nearly zero, dead zones can form and blockages are more likely to occur.

Instead of using a dynamic mixer, a motionless static mixer is also a potential choice. For example, a rudimentary static mixing system, where the diameter of the inlet is the same as that of the nozzle, made by placing metal pins through a mortar tube after the additive injection point was designed [63], as shown in Figure 2.12. Also, it must be noted that different types of static mixers can be used for materials with different properties, as listed in Figure 2.13. However, further research is required to examine the suitability of these different types and their effect on mixing homogeneity and pumping pressure for cement-based materials.

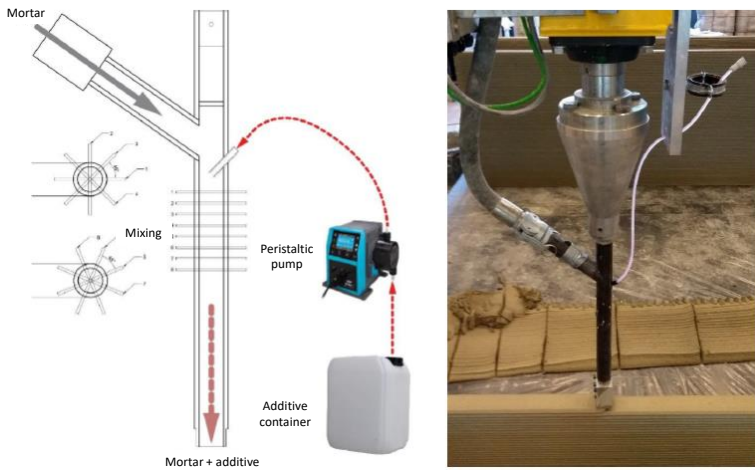
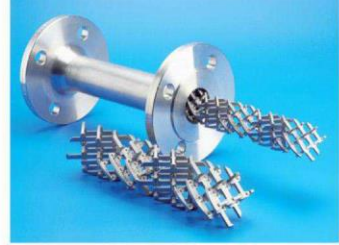


Figure 2.12 Liquid additive injection device. Left: schematic drawing. Right: overview image of accelerator injection during printing, taken from [63].



KMX-V (Chemineer, Inc.)



SMX (Sulzer, Inc.)



Custody Transfer (Komax Systems, Inc.)



Standard LPD (Ross Engineering, Inc.)



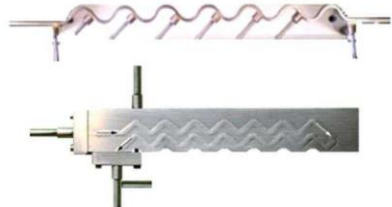
Kenics KM (Chemineer, Inc.)



ZT-MX (ZelenTech, Ltd)



SMI (Sulzer, Inc.)



Corrugated channel reactors  
(Laboratory pilots)

Figure 2.13 Commercially available in-line static mixers, taken from [127].

To give a summary, the advantages and disadvantages of different inline mixing systems are listed in Table 2.2.

Table 2.2 Summary of recent studies on inline mixing systems.

Application	Type	Advantages	Disadvantages	References
Two-fluid grouting	No mixing tool	Easy installation and maneuverability	Limited application  Without aggregates	[93-102]
Shotcrete	Dry-mix	Easy operation	Bad sprayed profiles  Waste manpower High rebound	[64, 107, 108]
	Wet-mix	Less rebound than dry- mix	Bad sprayed profiles  Waste manpower	
Extrusion-based 3D printing	Dynamic mixer	Low pumping pressure	Hard to maintain  Hard to design  Dead zone	[119, 121-126]
	Static mixer	No dead zone  easy maintenance	High pumping pressure	

## 2.5 Issues and challenges in using accelerators

### 2.5.1 Mixing homogeneity

It should be noted that the mixing homogeneity of accelerators is the most important aspect of the inline mixing method as discussed in the previous section. The mixing homogeneity of accelerators is more emphasized in the area of 3D concrete printing. Van Der Meijde et al. [63] pointed out that the best mixing grade was achieved by injecting the additive such as an accelerator in the center of the mortar tube and placing all 8 mixing pins, as shown in Figure 2.12. However, the printed samples still present visible color differences, indicating that the final design did not yet achieve a high mixing grade, as shown in Figure 2.14.





Figure 2.14 Insufficient mixing homogeneity, taken from [63].

Wangler et al. [122] measured the residence time distribution to assess the homogeneity of the mixing process in a dynamic mixer. In their study, a pigment suspension of 15% w/w chromium oxide (Colortherm Green GN-M from Harold Scholz & Co. GmbH) was firstly blended with a  $\text{Ca}(\text{NO}_3)_2$  based accelerator in a liquid form. The accelerator was used at a dosage of 8% w/w binder and then injected into the fresh concrete via a dynamic mixer. After hardening, the samples were sliced at various positions, and the concentration of pigment was analyzed by SEM/EDX analysis [118, 129, 130]. Detecting methods to define the mixing homogeneity can also be adopted from the chemical industries. For example, two main methods, namely intrusive and non-intrusive methods have been developed [131]. By using the intrusive methods, parameters such as fluorescence density, temperature, pH, and conductivity can be obtained. However, to measure these parameters, some intrusive probes need to be placed inside the reactor, resulting in some disruption of the mixing pattern. On the other hand, non-intrusive methods can provide comprehensive data without disturbing the flow regime, such as acid-base neutralization, where a transparent vessel is only needed. Another example is based on collecting images of the mixing process by a Charge-coupled device (CCD) camera and then analyzing it to assess the mixing homogeneity [131]. However, the method is not adopted for fresh concrete since no images can be made inside the mixer. As for the intrusive techniques, putting the detecting probes inside the concrete inline mixer and choosing which parameter to monitor for assessing the mixing homogeneity requires further research before it can be employed.

Nevertheless, achieving a high mixing homogeneity remains a bottleneck regarding the inline mixing system for 3D concrete printing. Apart from the influence of process parameters, the material properties also play an important role in an inline mixer. Previous researches on Newtonian fluids have pointed out that a high mixing homogeneity is expected if the viscosity difference is not too high

[118, 127]. Taking this point into consideration, instead of injecting the accelerator into fresh concrete directly, an inert filler-based mixture can be used as a carrier for the accelerator. As such, mixing a cement-based mixture and an inert filler-based mixture (with accelerator) would be an easier option. Moreover, in the case of Bingham fluids (e.g. concrete suspensions), the effect of yield stress difference between the two fluids may also influence the mixing homogeneity and further research may be required in this regard.

### **2.5.2 Effect on mechanical performance**

In specific applications such as 3D concrete printing, it is essential to consider the effect of the accelerator on the interlayer bond strength. The addition of the accelerator would result in a higher structural build-up rate and avoidance of collapse. However, the addition of an accelerator would also lead to limited mechanical interlocking, as shown in Figure 2.15. Previous studies have shown that the interlayer bond strength depends on various print parameters such as the time interval between layers, the print speed, and the nozzle standoff distance during deposition [132-136]. Also, the reduction in strength becomes more pronounced for samples that were left uncovered during the interval time, susceptible to drying before the subsequent layer was printed [133, 137, 138]. If the surface is dry, it does not have the workability (or malleability) for the bond to develop. With the addition of accelerator, free water on the interlayer position will be consumed. Therefore, the addition of an accelerator is likely to reduce the interlayer bond strength. Dressler et al. [113] examined the effect of alkali-free setting accelerator (0-6 % of the binder content) on the interlayer strength of shotcrete 3D printed elements. The interlayer strength was characterized based on a 3-point bending test such that the load is applied parallel to the direction of the layer orientation, and the maximum bending stress occurs at the layer interface. The flexural strength was observed to decrease with an increase in the interlayer time interval (0-5 minutes). The reduction in bond strength was, however, found to be independent of the accelerator dosage used in the mixture. Kloft et al. [11] compared the interlayer strength based on a similar 3-point bending test of prismatic elements made with extrusion and spray-based 3D printing, both with the same mixture composition. The flexural strength was found to be much lower for prisms made by extrusion-based 3D printing. Further, with an increase in the interlayer time interval, the decrease in the flexural strength was found to be much more pronounced in the case of extruded prismatic elements. The comparatively better interlayer strength for elements made by the shotcrete process can be attributed to the higher impact exerted during the placement of each layer as compared to the extrusion-based process.

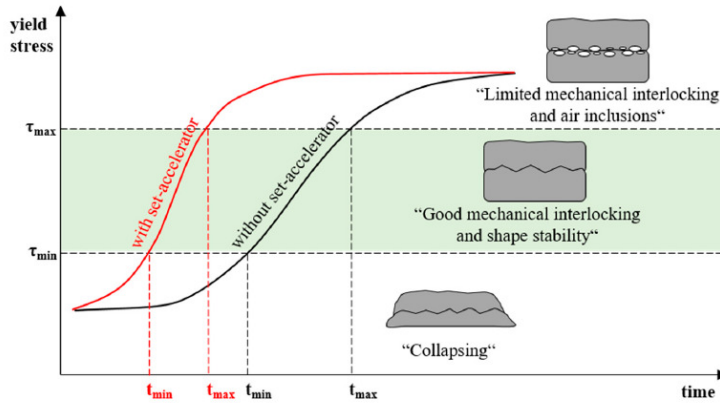


Figure 2.15 Principle of yield stress development over time with and without accelerator (alkali-free shotcrete accelerator) as well as the open window indicated by  $t_{min}$  and  $t_{max}$ , taken from [113].

To mitigate the interlayer strength loss due to the use of accelerators in extrusion-based 3D printing, researchers have suggested various methods. This includes chemical means such as the application of adhesive agents (cement paste or polymer-based materials) between the layers [139-143], the addition of superabsorbent polymers to the mixture which can help to mitigate the rapid moisture loss from the surface [144-146], or the addition of redispersible polymer powder that enhances the bond via film formation [147]. Wang et al. [143] showed that the use of epoxy resin and chloroprene latex-modified mortars as interlayer adhesive agents can improve the interlayer bond strength of 3D printed elements. The bond improvement is due to the electrostatic interaction between the resin and the calcium ion of the C-S-H gel. Mechanical methods are based on either forming mechanical interlocks between the layers [148] or techniques like wire brushing that can enhance the roughness of the bottom layer resulting in better interlayer strength [138].

Another aspect that needs to be pointed out is the modification in the hydration kinetics brought by the introduction of the accelerator and its likely effect on the long-term strength development of concrete. Accelerators based on sodium aluminate rapidly deplete sulfate ions from the liquid phase and lead to accelerated and under-sulfated C<sub>3</sub>A reactions, which inhibit further C<sub>3</sub>S hydration and lead to a decreased strength [47, 149]. While for the alkali-free accelerators used for shotcrete, higher ultimate strength and improved mechanical properties can be reached when the  $Al_2O_3/SO_4^{2-}$  ratio in alkali-free accelerators ranges between 0.38 and 0.60 [105, 109]. However, it must be noted that an excessive increase in hydration rate may lead to air-entraining during spraying and an improper consolidation of sprayed layers. Because of that, increases in porosity and

reductions of around 20 % in compressive strength at 28 days have been reported in sprayed concrete when compared to conventional concrete [81, 105, 150].

### 2.5.3 Effect on durability

The type and the amount of accelerator used in the concrete mixture can also influence its long-term performance. The change in the hydration kinetics by accelerators can alter the microstructure of the hardened concrete at later ages which, in turn, influences the resistance to chloride and carbon dioxide penetration. For instance, Park et al. [151] evaluated the chloride permeability of shotcrete mixture compositions made with silicate, aluminate, and a  $C_{12}A_7$  mineral-based accelerator. Their performance was compared with respect to a plain shotcrete mixture containing no accelerator. While the mixtures containing silicate and aluminate accelerators showed a relatively higher permeability, the mixture with  $C_{12}A_7$  accelerator showed a slightly reduced permeability compared to the plain shotcrete mixture. A similar improvement in permeability with the use of  $C_{12}A_7$  accelerator was also observed in the study by Won et al. [152]. The authors attributed this improvement to the dense web structure of ettringite formed at initial ages when the  $C_{12}A_7$  accelerator is used.

Another aspect that needs discussion is the alteration of the aluminate/sulphate balance in the pore solution with the addition of setting accelerators, and its influence on sulfate attack. The effect of aqueous calcium nitrate on sodium sulfate attack was examined by Lee et al. [153]. The accelerator was found to enhance the formation of ettringite and thaumasite which can be attributed to the reaction between the  $Ca^{2+}$  ions supplied from the accelerator with the externally supplied sulfate ions. The continuous presence of the sulfate ions in the cement matrix also decreases the local pH of the system which destabilized the C-S-H gel and led to its decalcification. The negative effect on sulfate attack has also been reported with the use of other alkali-free accelerators such as aluminum sulfate and alkaline accelerators such as  $KAl(OH)_4$  aqueous solution [68, 154]. The increased alkali content in concrete containing alkaline accelerators has also been found to increase the potential for leaching of hydrate phases [67] and also promote alkali-aggregate reaction if reactive aggregates are present in the system [41, 46].

A few researchers have indicated that the addition of an accelerator may influence the durability because of crack formation. The causes for crack formation can be attributed to several aspects including the thermal effect, autogenous shrinkage, and drying shrinkage [155]. As the hydration reaction progresses, the concrete would expand because of the heat development. If local parts are restrained or as the temperature subsequently decreases, cracks could be formed, especially for massive structures [156-159]. Several factors affect the thermal expansion such as the thermophysical properties of concrete, the hydration heat release, and the interaction between the concrete and the environment [158, 160, 161]. Due to the presence of accelerators in the concrete, the heat release performance would be

different along the hydration process, therefore leading to a different thermal response. In the meantime, the addition of accelerators would also have the potential to increase autogenous deformation and subsequent cracking in concrete [162-166]. In addition, the use of alkaline accelerators has also been found to enhance drying shrinkage since the addition of these admixtures resulted in a coarser microstructure with higher porosity at later ages, which would harm the durability [167].

Finally, in the case of layered printed concrete, the influence of interlayer permeability on ionic-transport-related durability issues must be pointed out. Although no literature could be found on the effect of the accelerator on interlayer permeability, the addition of the accelerator is likely to result in a weaker interlayer bond with higher permeability. Recent studies have indicated that this can result in sudden water uptake by capillary absorption through interfaces which may increase the rate of deterioration in the printed concrete [145, 168-170]. However, to gain further understanding in this regard, more studies are needed that examine the effect of accelerators on the interlayer permeability and its implications on the transport properties.

## 2.6 Adhesion mechanism

### 2.6.1 Basic notions of adhesion

To have a better understanding of adhesion, two basic notions, i.e. cohesion and adhesion, should be distinguished. Cohesion refers to the internal strength as a result of the interactions within the material, while adhesion refers to the interaction between two different materials, e.g. an adhesive to a substrate [171]. The cohesion and adhesion forces existing inside an adhesive and between an adhesive and a substrate, are illustrated in Figure 2.16.

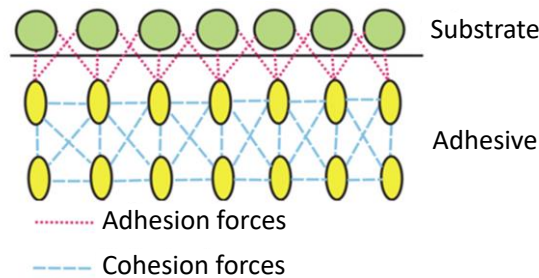


Figure 2.16 Cohesion forces and adhesion forces.

### 2.6.2 Adhesion theories

To explain adhesion, several theories have been proposed including the physical adsorption theory, chemisorption theory, diffusion theory, electrostatic theory, and

mechanical interlocking theory. However, there is no unanimity regarding the comprehensive theory that can describe all adhesion phenomena.

### **2.6.2.1 Physical adsorption theory**

Physical adsorption is also known as dispersive adhesion, where the adhesion is formed by van der Waals forces, which is the attraction between two molecules with a region of slight positive and negative charges. Therefore, such molecules are polar for average charge density. These positive and negative poles might be permanent, which is known as Keesom forces. While in some other cases, a transient effect may occur due to the random movement of electrons leading to a temporary concentration of electrons in a specific region, which is known as London forces [172]. These are the weakest forces that contribute to the adhesive bonding but they are quite sufficient to make strong joints.

### **2.6.2.2 Chemisorption theory**

The chemisorption theory is applied when a compound forms at the interface, which is attributed to the formation of either ionic, covalent, or hydrogen bonds. To be specific, the adhesion generates by swapping electrons (ionic bonding), sharing electrons (covalent bonding) or as hydrogen atoms are attracted to an atom of nitrogen, fluorine, or oxygen (hydrogen bonding) [171].

That is to say, two materials can be held together as long as the molecules at the interface can bond. This principle is quite straightforward, while it still needs to be noted that the chemical bond only works over a tiny distance such as less than one nanometer. Therefore, two materials should be brought as close as possible, aiming at forming strong chemical adhesion [173].

### **2.6.2.3 Diffusion theory**

Diffusive bonding may occur when the molecules of both materials are soluble and mobile in each other. For example, this theory is applicable for the sintering of metal or ceramic, where the atoms would diffuse from one particle to another, and the bond forms between two particles. Another particular example is a polymeric material where the polymer molecules diffuse between two materials and intertwine both sides. The diffusive force at polymer-to-polymer surfaces is determined by the mobility of polymers, which is further influenced by the contact time, the temperature, the molecular weight of polymers, and the physical form. The mobility of two different types of polymers including an uncross-linked type and a cross-linked type is shown in Figure 2.17. Compared to the cross-linked polymers, the uncross-linked polymers have more freedom of movement to wander into another surface by penetrating tails and loops across the interface. As such, the adhesion would be quite strong with the formation of a large network of these bonds [174].

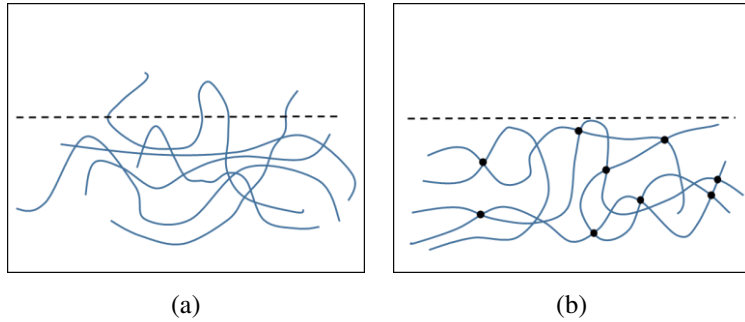


Figure 2.17 (a) Uncross-linked polymers are somewhat free to diffuse across the interface, and (b) cross-linked polymers are not free enough to diffuse, where the dashed line indicates the interface.

#### 2.6.2.4 Electrostatic theory

Electrostatic adhesion theory indicates the electrons transfer from one material to another material when a difference in electrical charge forms and an electrical double layer appears at the contact surface. This contributes to the attraction force and the separation resistance between two materials. It should be noted that the electrostatic theory is not applicable in the case that insulators appear [173].

#### 2.6.2.5 Mechanical interlocking theory

The mechanical interlocking theory indicates that the adhesion forms in the case that fresh materials penetrate the open pores and textures on the substrate, and lock mechanically to the substrate. Based on this theory, strong adhesion is expected when fresh materials have proper rheological properties to penetrate the open pores and textures at a certain time. Moreover, a rough surface is beneficial to increase the contact area, leading to increased surface energy. As a result, the adhesion at the interface is improved [175]. However, it should be noted that the increased substrate surface roughness might compromise the contact when fresh materials fail to penetrate the macro textures and micro pores on the rough surface [171].

### 2.6.3 Circumstantial effects

Apart from the primary surface forces described above, several circumstantial effects also play important roles, especially for the overall strength.

#### 2.6.3.1 Wettability

Some effects on the functionality of adhesives can be characterized by the theory of interfacial tension and surface energy. The surface free energy of a substrate determines its ability to be wetted by a liquid, which contributes to increasing the

contact surface and the effective forces [176]. On the other hand, the interfacial tension directly relates to the liquid's wettability. It can also be extrapolated that non-wetting liquids have higher cohesion while wetting liquids have lower cohesion.

In a typical solid-liquid-gas system such as a drop of liquid on a solid surrounded by air, the contact angle is commonly adopted to evaluate the adhesion. Generally, cases with high adhesion have lower contact angles and vice versa. The contact angle of the three-phase system depends not only on dispersive adhesion (interaction between the molecules in the liquid and the molecules in the solid) but also cohesion (interaction between the liquid molecules themselves). Strong adhesion and weak cohesion lead to a high degree of wetting, i.e. low contact angles. Conversely, weak adhesion and strong cohesion result in a low degree of wetting, i.e. high contact angles. In the case of a small contact angle, fresh materials spread uniformly on the substrate, while a high contact angle results in no spreading of fresh materials over the substrate, as illustrated in Figure 2.18.

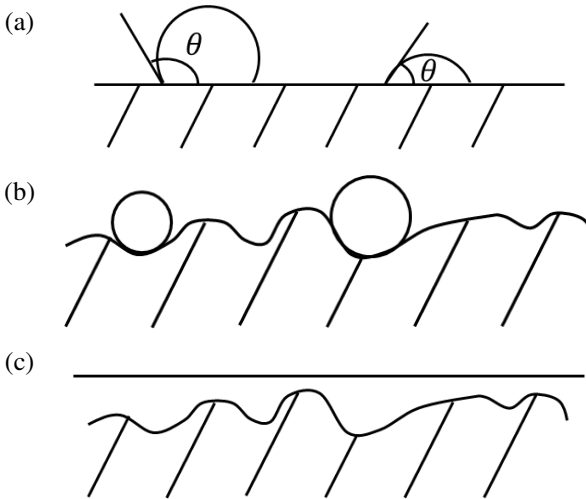


Figure 2.18 (a) Liquid droplets with a high and low contact angle on a flat substrate, (b) no spreading of liquid on the substrate with a high contact angle, and (c) complete contact of liquid with a low contact angle, adapted from [171].

### 2.6.3.2 Stringing

Stringing might be the most crucial one among these circumstantial effects. Stringing refers to the bridging of molecules across the gap, rather than cracking when two surfaces are separated. As a result, the initiation and propagation of cracks can be restricted by providing some flexibility. In this regard, the stress at the interface is spread out rather than concentrated, leading to less possibility of overwhelming the total adhesion force between two surfaces [177]. In some cases



such as the detaching process of a viscoelastic adhesive agent, stringing can be observed by a gradual process called “fingering” [178]. This phenomenon is also observed during the tack test, which will be introduced in the following chapters.

### **2.6.3.3 Hysteresis**

Hysteresis refers to the restructuring of the adhesive interface over some period. As a result, the work needed to separate two surfaces is more than the work to bring these two surfaces together. For the most part, this effect relates to the diffusive bonding. The adhesion would be stronger if more time is given for surfaces exhibiting diffusive bonding to restructure.

Hysteresis can be observed when performing “stop-start” measurements. In these experiments, one surface slides against another surface continuously and is occasionally stopped for some periods. Results on polymer-to-polymer surfaces show that the resumption of smooth sliding is easy if the stopping time is short while an initial increase of resistance to movement appears when the stopping period exceeds some limit [174]. With regard to cementitious materials, hysteresis relates to the structural build-up, where the network of colloidal interactions and C-S-H bonds forms [179].

### **2.6.3.4 Lateral adhesion**

Lateral adhesion indicates the situation that one object slides on a substrate. In the case that both the object and the substrate are solids, the lateral adhesion can be described as friction. On the other hand, when the object is liquid such as a drop, the behavior of lateral adhesion is very different from the friction between solids [180, 181]. In this thesis, printing against the sidewalls of hard rock can be treated as a case of lateral adhesion.

## **2.7 Influence of concrete surface characteristics on adhesion**

In the context of applying 3D concrete printing to the construction of hard rock tunnel linings for adhesion purposes, the printed materials must meet the requirements of wetting concrete substrates, adhering to concrete substrates, gaining enough strength after placing and remaining stable. The adhesive qualities are therefore determined by the characteristics of concrete substrate surfaces, such as the mechanical integrity, roughness, moisture content, cleanliness, contamination, and the placement of bonding agents. Among all these characteristics, this section only introduces several items that fit the scope of this thesis. Other aspects can be found in the literature [176]. It should also be noted that only the influence on the adhesion in the hardened state is given, as very limited literature relating to the adhesion of fresh cement-based materials can be found.

### **2.7.1 Roughness**

Substrate surface roughness is considered to have a major influence on the bond between overlays and concrete substrates, as mechanical interlocking is generally recognized as one of the crucial factors. A wide spectrum of substrate surface roughnesses can be obtained by adopting a variety of surface treatments such as gritblasting, hammering, and water-jetting [182]. Various reported studies indicate that the bond strength improves but reaches a threshold value with the increase of substrate roughness [183, 184]. The influence of substrate surface roughness on bond strength also depends on a range of other parameters such as the effective surface area and the material strength. In some cases, an increase in roughness may result in a bad substrate mechanical integrity, which would compromise the bond capacity accordingly [185]. The cross-influence of substrate surface roughness and mechanical integrity upon concrete repair bond was studied by Bissonnette et al. [186] and the results showed that the pull-off strength values were significantly lower when using a hammered substrate. A quantitative analysis of the cross-influence of substrate surface roughness and macrocracking performed by Courard et al. further proved such a complex interaction [187].

### **2.7.2 Moisture content**

The substrate moisture content may have an important influence on the bond characteristics of the overlay. In some cases, the presence of moisture is required, while the substrate surface needs to be dry in some other cases such as the placement of epoxy-based materials. It is well recognized that a dry substrate surface may absorb water from the overlay and result in a weak structure at the interface area. Adversely, a very wet surface tends to dilute the material at the interface and increase the water-to-cement ratio, leading to a limited adhesive strength. In addition, the water in open pores further does harm to the mechanical interlocking effect. In practice, a saturated surface dry (SSD) condition of the substrate before the application of the overlay is always recommended [188]. Nevertheless, various investigations conclude that different substrate surface moisture contents are required for different substrates and overlays. Unfortunately, there is no suitable method to accurately find out the optimum moisture content when specific types of substrates and overlays are used [176].

### **2.7.3 Bonding agents**

The use of bond agents has been a common solution to ensure a sufficient bond between the substrate and the overlay. A variety of materials have been applied including cement grout and mortar, latex and other polymeric materials, latex-modified grout and mortar, and epoxy resins [176]. The intention of applying bonding agents lies in a more uniform and reliable bond over the surface, rather than increasing the bond strength significantly. In some situations that the overlay fails to wet the irregular surface of the substrate adequately due to relatively low

workability, the presence of bonding agents is beneficial to fill the profile valleys and penetrate the surface porosity. However, bonding agents may perform as a bond breaker in some improperly used cases [189]. The most likely cause is the introduction of a third material and a second interface, which increases the risks of compatibility.

The use of bonding agents is not strictly required for cement-based materials due to the availability of surface preparation and placement technologies. Moreover, with the development of vibration placement processes, a satisfactory bond can be achieved as the vibration decreases the voids at the interface area and facilitates the penetration of applied materials to substrates.



## Materials and methods

### 3.1 Introduction

This chapter gives a summary of the material properties and testing methods. First, the properties of the cement, limestone powder, silica sand, superplasticizer, cellulose ether, redispersible polymer powder, and accelerator used within this thesis are introduced. Further, the characteristics of the concrete substrates used to replace excavated rock walls at a lab-scale are given. Finally, the analytical techniques that have been applied for this thesis are presented.

### 3.2 Material properties

#### 3.2.1 Cement

Cement is a hydraulic binder, which contributes a lot to the strength of cement-based materials both in the fresh and hardened state. In this work, Type I Portland cement (PC) was obtained from Holcim. The physical properties and chemical composition are provided by the supplier and summarized in Table 3.1 and Table 3.2, respectively. The particle size distribution of the Portland cement was determined by laser diffraction analysis, as shown in Figure 3.1.

Table 3.1 Physical properties of cement.

Water requirement (%)	Setting time		Stability (mm)	Blaine specific surface area (m <sup>2</sup> /kg)	Apparent density (kg/m <sup>3</sup> )	Sieve residue 200 $\mu$ m (%)
	Initial	Final				
29	3h25min	4h14min	<1	408	3160	<0.5

Table 3.2 Chemical composition and loss on ignition (LOI) of cement (%).

CaO	SiO <sub>2</sub>	Al <sub>2</sub> O <sub>3</sub>	Fe <sub>2</sub> O <sub>3</sub>	MgO	Na <sub>2</sub> O	K <sub>2</sub> O	SO <sub>3</sub>	Cl <sup>-</sup>	Insoluble	LOI
64.3	18.3	5.2	4.0	1.4	0.32	0.43	3.5	0.06	0.4	2.3

### 3.2.2 Limestone powder

Limestone powder (LP) is one of the alternatives for cement. In this thesis, limestone powder obtained from Carmeuse is mainly used as an inert carrier for the accelerator in the twin-pipe pumping system. The chemical composition is provided by the supplier and listed in Table 3.3. The particle size distribution of limestone powder was determined by laser diffraction analysis, as shown in Figure 3.1.

Table 3.3 Chemical composition and loss on ignition (LOI) of limestone powder (%).

CaO	SiO <sub>2</sub>	Al <sub>2</sub> O <sub>3</sub>	Fe <sub>2</sub> O <sub>3</sub>	MgO	Na <sub>2</sub> O	K <sub>2</sub> O	SO <sub>3</sub>	Cl <sup>-</sup>	Insoluble	LOI
48.85	8.15	1.28	0.88	1.41	1.25	0.28	0.05	-	0.4	37.29

### 3.2.3 Silica Sand

Sand gives volume, stability, resistance to wear or erosion, and other desired properties. In the context of 3D concrete printing, fine aggregates are always used to facilitate the pumping and extrusion process [190]. In this thesis, silica sand obtained from Vanderveelde NV (specific gravity 2650 kg/m<sup>3</sup>, maximum particle size 2 mm, fineness modulus 2.05) was used. The particle size was determined by sieving, as shown in Figure 3.1.

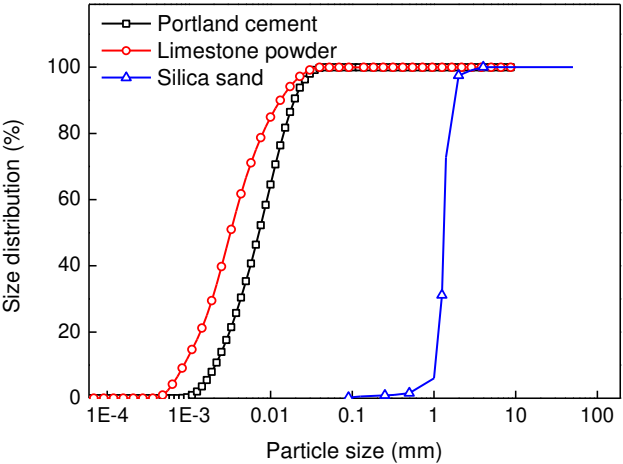


Figure 3.1 Particle size distribution of Portland cement, limestone powder, and silica sand.

### 3.2.4 Superplasticizer

Superplasticizers, also known as high range water reducers, are additives used for increasing the fluidity of fresh concrete or making high-strength concrete. The effect of superplasticizers comes from introducing a repulsive inter-particle force that reduces the overall attractive force between cement particles and consequently leads to a high fluidity [49]. In this work, polycarboxylate ether (PCE) provided by BASF was used as superplasticizer (SP). The product data is listed in Table 3.4.

Table 3.4 Product data of superplasticizer.

Property	Description
Brand type	Master Glenium 51
Appearance	Brown liquid
Concentration	35%
Specific gravity @ 20 °C	$1.10 \pm 0.03 \text{ g/cm}^3$
pH-value	$7.0 \pm 1$
Alkali content (%)	$\leq 5.00$ by mass
Chloride content (%)	$\leq 0.10$ by mass

### 3.2.5 Cellulose ether

Cellulose ethers (CE) are commonly used in repair materials to obtain some of the required properties such as reducing the absorption of water into the porous substrate and increasing the cement hydration and mechanical strength of the repair materials [49]. Cellulose ethers are generated from wood fibers or refined short cotton fibers as the main raw materials, after chemical treatment, and by the reaction with etherifying agents [191]. Among the wide variety of existing cellulose ethers, four types of cellulose ethers are commonly used including methyl cellulose (MC), hydroxypropyl methyl cellulose (HPMC), hydroxyethyl methyl cellulose (HEMC), and hydroxyethyl cellulose (HEC) [192, 193]. It should be noted that the properties of cellulose ether depend on both the molecular weight of the polymer and on the degree of etherification. However, such information is generally not provided and considered confidential by the manufacturer. Still, it has been demonstrated that the average molecular weight of the polymer is linked to its solution viscosity when it is dissolved in water at a set concentration and a set temperature [192].

In total 6 types of cellulose ethers were provided by SE Tylose GmbH & Co. KG and used for the work in this thesis. The brand types include MH300P2, MH6000YP4, MH15000YP4, MH30000YP4, MOT60000YP4, and MB60000P2. The use of “MH” within the product name reflects the incorporation of only methyl and hydroxyethyl in the substituents for the hydroxyl groups (i.e. hydroxyethyl

methyl cellulose), while the use of “MOT” indicates the incorporation of methyl and hydroxypropyl groups (i.e. hydroxypropyl methyl cellulose). The use of “Y” indicates a delayed solubility. In addition, the use of “P2” refers to products with a powder size less than 180  $\mu\text{m}$  while “P4” refers to products with a size less than 125  $\mu\text{m}$ . The product data of cellulose ethers are shown in Table 3.5.

Table 3.5 Product data of cellulose ether.

Property	Description
Brand type	Shin-Etsu
Appearance	White powder
Density @ 20 °C	1.1-1.5 g/cm <sup>3</sup>
Solubility @ 20 °C	> 10g/l
NaCl content	Max. 1.5%
Moisture, as packed	Max. 7%

The viscosity levels of these cellulose ethers are shown in Table 3.6. The Höppler viscosity (mPa·s) was measured by using a 2% solution with 5% moisture content, 20 °C, 20 °dH, while the Brookfield viscosity (mPa·s) was measured by using a 1.9% solution with 5% moisture content, 20 °C, 20 °dH.

Table 3.6 Viscosity levels of cellulose ethers.

	Product name	Höppler viscosity (mPa·s)	Brookfield viscosity (mPa·s)
CE1	MH300P2	300	400
CE2	MH6000YP4	6000	7000
CE3	MH15000YP4	15000	13000
CE4	MH30000YP4	30000	24000
CE5	MOT60000YP4	60000	30000
CE6	MB60000P2	60000	30000

In this thesis, CE5 (MOT60000YP4) is used in Chapter 4, Chapter 5, and Chapter 6 as a viscosity modifying admixture (VMA). In Chapter 7 and Chapter 8, CE6 (MB60000P2) is used to increase the adhesion of the fresh material. In Chapter 9, CE1 (MH300P2) and CE6 (MB60000P2) are used to investigate the polymer modification on the adhesion performance of printed materials. In Chapter 10, aiming at exploring the interaction between accelerator and cellulose ether, four types of cellulose ethers including CE1 (MH300P2), CE2 (MH6000YP4), CE3(MH15000YP4), and CE4 (MH30000YP4) are used.



### 3.2.6 Redispersible polymer powder

Redispersible polymer powders (RDP) are polymer emulsions that have been commonly used in dry-mix mortars, specifically suited for tile adhesives and render mortars. When mixed with water, these polymer powders can redisperse in water, forming new emulsions with essentially identical properties to the original copolymer emulsions. The addition of redispersible polymer powders can improve the cohesion and flexibility of the material. Further, it can improve the water retention of mortar and form a film to reduce the evaporation of water. In addition, it can improve the bond strength of repair mortars [194]. Commonly-used redispersible polymer powders include elastomeric powders such as styrene-butadiene rubber, and thermoplastic powders such as poly (ethylene-vinyl acetate) (EVA), poly (styrene-acrylic ester) (SAE), and polyacrylic ester (PAE) [195]. In this thesis, as one potential to increase the adhesion of printed materials, one type of redispersible polymer based on a hard copolymer of ethylene-vinyl acetate was provided by Wacker. The brand type is VINNAPAS® 5010N with a neutral effect on rheology. The product data is shown in Table 3.7.

Table 3.7 Product data of redispersible polymer powder.

Property	Description
Brand type	VINNAPAS® 5010N
Appearance	White to light beige powder
Bulk density	0.49-0.59 g/cm <sup>3</sup>
Ash content (1000 °C)	Max. 13%
Particle size (> 400 µm)	Max. 4%
Solid content	Min. 98%
Minimum film forming temperature	4 °C
Protective colloid/ emulsifier system	Polyvinyl alcohol

### 3.2.7 Accelerator

As already discussed in Chapter 2, adding accelerator (ACC) in shotcrete benefits the adherence and strength gain of sprayed materials. Moreover, using accelerators is one of the most effective methods to increase the stiffening rate of 3D printed materials. In this thesis, two types of accelerators are used. The first one is an alkali-free shotcrete accelerator based on different aluminum salts, in particular aluminum sulfate, which was provided by Sika. The product data is shown in Table 3.8.

Table 3.8 Product data of shotcrete accelerator.

Property	Description
Brand type	Sigunit 49-AF
Appearance	Beige powder
Bulk density	$1.10 \pm 0.1 \text{ g/cm}^3$
Total chloride ion content (%)	$\leq 0.1$
Equivalent sodium oxide (%)	$\leq 1.0$

The X-ray diffractogram (XRD) of the alkali-free shotcrete accelerator is shown in Figure 3.2. The accelerator mainly consists of calcite (PDF# 05-0586), ye'elimite (PDF# 33-0256), and alunogen (PDF# 33-0311). The other type accelerator used within this thesis is aluminum sulfate octadecahydrate provided by VWR. The composition of the material can vary between 16-18 hydrates. The product data is shown in Table 3.9. During the development of the twin-pipe pumping system, the commercial shotcrete accelerator was used due to the comparatively low cost. While in Chapter 10, pure aluminum sulfate was used to avoid possible influences of the organic components in the commercial shotcrete accelerator.

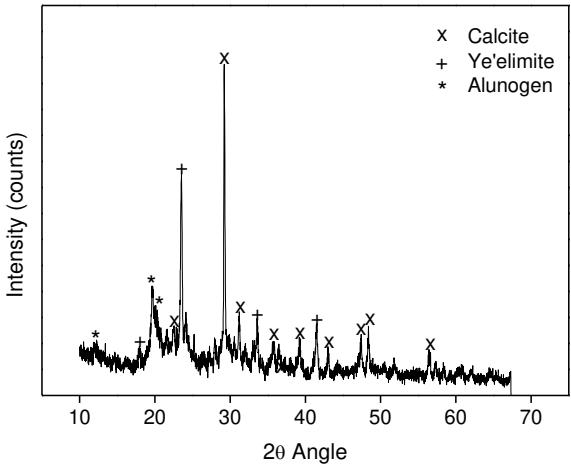


Figure 3.2 X-ray diffractogram of the shotcrete accelerator.

Table 3.9 Product data of aluminum sulfate octadecahydrate.

Property	Description
Assay (calculated as $\text{Al}_2(\text{SO}_4)_3$ )	51.0-59.0%
Density (20°C)	1.69 g/cm <sup>3</sup>
Solution (20°C, water)	Clear colorless liquid
pH (20°C, 2%)	2.5-4.0
Alkali and alkaline-earth metals	Max. 0.4%
Heavy metals (as Pb)	Max. 20 ppm
Cl (Chloride)	Max. 50 ppm
$\text{NH}_4^+$ (Ammonium)	Max. 100 ppm
Fe (Iron)	Max. 50 ppm

### 3.3 Substrate properties

#### 3.3.1 Compositions

In this study, the composition of the substrate will not be considered. Instead, the influence of surface inclinations, substrate properties (surface roughness and moisture content), and the addition of admixtures (polymers and accelerators) in the printed material on the adhesion will be discussed. As such, concrete slabs, which are more frequently used, can be used to replace excavated rock wall. Two concrete mixtures of micro-concrete and crushed stone concrete were used to make the substrates [182]. The mixture design and characteristics are shown in Table 3.10. Superplasticizer was added to the system until the slump reached between 100 and 150 mm. To determine the compressive strength of the substrate, 3 cubes (150×150×150 mm<sup>3</sup>) for each mixture were tested at the age of 28 days according to NEN-EN 12390-3 (2009) [196]. Moreover, the direct surface tensile test (three tests for each mixture) was performed directly on the troweled face of the concrete slabs (300×300×100 mm<sup>3</sup>) at the age of 28 days [182], which was according to NBN EN 1542 (1999) [197].

Table 3.10 Mixture design and characteristics for concrete substrates.

Materials	Micro-concrete	Crushed stone concrete
CEM I 52.5 N (kg/m <sup>3</sup> )	470	340
Water (kg/m <sup>3</sup> )	188	153
Sand (kg/m <sup>3</sup> )	750	604
Gravel 2/8 (kg/m <sup>3</sup> )	946	
Crushed limestone 2/6.3 (kg/m <sup>3</sup> )		336
Crushed limestone 6.3/20 (kg/m <sup>3</sup> )		967
Superplasticizer Glenium 27	*	
Superplasticizer Viscocrete 1020X		*
W/C	0.4	0.45
Tensile strength (N/mm <sup>2</sup> )	3.6	3.3
Compressive strength (N/mm <sup>2</sup> )	35.3	37.0

### 3.3.2 Roughness

To remove the near-to-surface layer and offer a new surface to the substrate before the application of tunnel linings or repair materials, various surface treatment methods are adopted such as gritblasting, hammering, and chiseling [176]. In this study, two types of micro concrete slabs treated by polishing (Flex, Le 12-3 100 wet, 3 minutes for each step with rotational speeds of 1200, 1700, 2250, 2700, 3250, and 3700 rpm, R1-A and R1-B) and gritblasting (pressure 0.7 MPa, R2-A and R2-B) were prepared. Another two types of crushed stone concrete slabs treated by hammering (Air Hammer model 29062, 3000 strokes per min, R3-A and R3-B) and water jetting (high pressure of 130 MPa, R4-A and R4-B) were prepared. Two cylindrical samples (diameter 50 mm) were drilled from each type of slab and in total eight cylindrical samples were prepared, as shown in Figure 3.3. The treated surface of each concrete cylindrical sample was scanned by using automated laser measurements (ALM) with a high precision laser sensor (ILD 1800-50, Micro-epsilon mess-tech GmbH, resolution 5  $\mu\text{m}$ ) [138, 182]. The treated surface profile of each concrete cylindrical sample was scanned four times along different diametric scanning paths and the profile height along with the evaluation position was recorded, as shown in Figure 3.4. The roughness levels of the lower surfaces were characterized by the root mean square deviation  $R_q$  (mm), which was in accordance with BS 1134 [198], as follows:

$$R_q = \sqrt{\frac{1}{N} \sum_{i=1}^n Z_i^2} \quad (3.1)$$

where  $N$  is the number of measurements and  $Z_i$  is the amplitude of each test  $i$  (mm) [199].

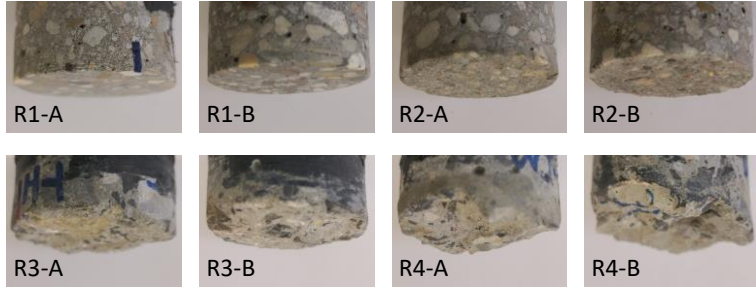


Figure 3.3 Concrete cylindrical samples with different roughness levels: R1-A and R1-B: polished surface; R2-A and R2-B: gritblasted surface; R3-A and R3-B: hammered surface; R4-A and R4-B: water-jetted surface.

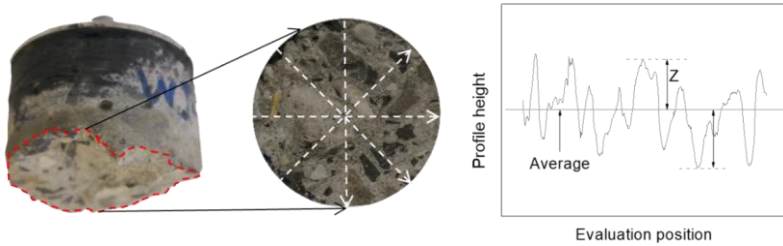


Figure 3.4 Example of a concrete cylindrical sample glued to a steel plate (left), the bottom surface and scanning paths (middle), and profile height along with evaluation position (right).

The  $R_q$  values of the treated surfaces of the eight concrete cylindrical samples are shown in Figure 3.5. It was shown that the  $R_q$  values of the cylindrical samples varied from an average value of almost 0 (polished samples) to around 2.5 mm (water-jetted samples). Similar results were reported by other researchers. For example, Yazdi et al. [182] indicated that gritblasting was not comparable to aggressive techniques such as water-jetting, which was able to remove concrete core or matrix. However, the cracks caused by the removal techniques would have an influence on the bond in the hardened state. For example, Yazdi et al. [182] pointed out that the bond strength reduced significantly when the jack-hammered substrates were used. Nevertheless, in the tack test and the shear test (see the following sections) where substrates treated by different removal technologies were used, merely the adhesion properties in the fresh state were investigated. Although some microstructural damage might appear, the strength of the substrate is still considerably higher when compared to the fresh cement-based material. Therefore, the influence of potential microstructural damage of the substrates will not be considered in the current study.

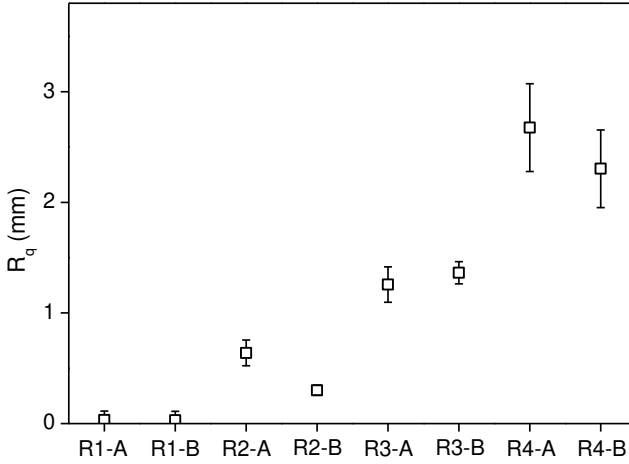


Figure 3.5 Root mean square deviation ( $R_q$ ) of the lower surface of concrete cylindrical samples (error bars represent the standard error,  $n=4$ ).

### 3.3.3 Moisture content

Five surface moisture contents were selected to resemble practice on construction sites, as well as to provide extreme situations of very moist and very dry substrates [188]. Due to the limited number of cylindrical samples and concrete strokes, which will be further introduced in the following sections, after each measurement, the substrates (either the cylindrical sample or the concrete stroke) was cleaned by a water gun and remained in a laboratory environment (temperature 20 °C, relative humidity 65%) for 7 days. As such, the substrate condition is treated as an initial state and the influence of the earlier performed tests on the latter can be ignored. The substrate surface moisture contents are described as follows:

(1) Oven-dried surface (M1). The substrate in the initial state was exposed to oven drying for a period of 24 hours at a temperature of 40 °C. After removal from the oven, the substrate was left in the laboratory to cool down for approximately 30 minutes before testing. This substrate surface was considered to represent the case of a completely dry condition.

(2) Air-dried surface (M2). The substrate in the initial state was kept in the laboratory environment (temperature 20 °C, relative humidity 65%) for 7 days. This substrate surface was considered representative of conditions in practice where no surface pre-conditioning is performed.

(3) Saturated-surface-dry surface (M3). The substrate in the initial state was submerged in a water tank for 24 hours and subsequently left to dry until a saturated-surface-dry state was obtained (10 minutes). This substrate surface represented the commonly recommended site practice.

(4) Wet surface (M4). The substrate in the initial state was submerged in a water tank for 2 hours and subsequently used for tests without any surface drying. This substrate surface represented a wet situation.

(5) Over-wet surface (M5). The substrate in the initial state was submerged in a water tank for 24 hours and subsequently used for tests without any surface drying. This substrate surface represented an extremely wet situation.

### 3.4 Analytical techniques

#### 3.4.1 Flow curve test

A stress-controlled rotary rheometer (Anton Paar, MCR 52) was employed to determine the Bingham rheological parameters of the mixtures developed in Chapter 5. A 4-blade vane rotor and a building material cell were used. 24 vertical ribs (1 mm width) are uniformly placed at the inner surface of the building material cell to prevent wall slippage. The fresh material was placed inside the cell to make sure that the blades were covered. The setup and dimensions are shown in Figure 3.6.

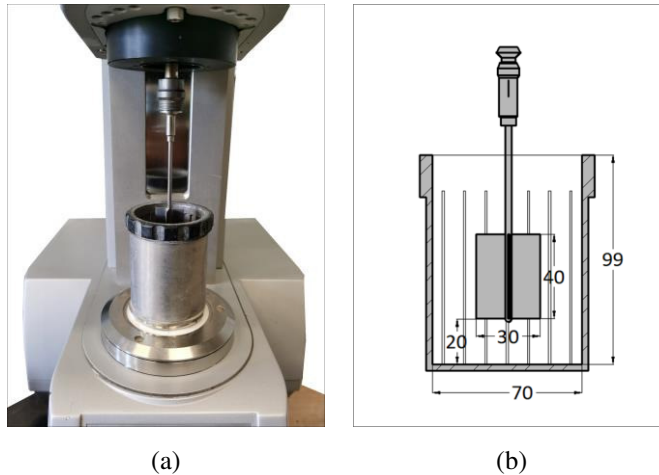


Figure 3.6 (a) Setup equipped with the building material cell and the 4-blade vane rotor for the flow curve measurement, and (b) dimensions (mm).

A test protocol consisting of a pre-shear and a stepwise increase and decrease of the shear strain rate was adopted, as shown in Figure 3.7. The average of the last five points in each decreasing step was then used to compute the average shear stress. The test was repeated twice for each mixture.

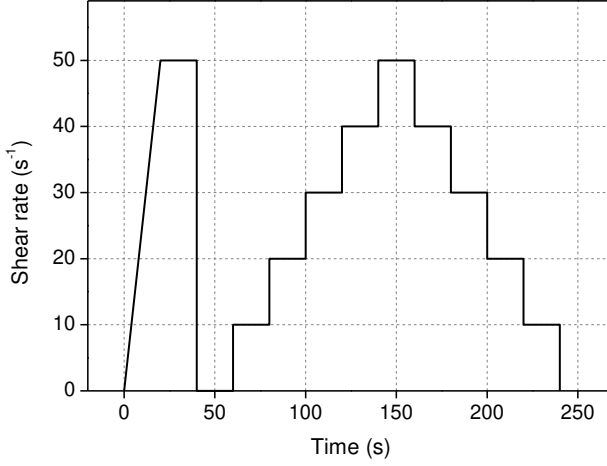


Figure 3.7 Shearing regime in flow curve tests.

### 3.4.2 Stress growth test

To measure the yield stress of stiff materials, a 6-blade vane rotor with a relatively small blade size was adopted to enlarge the capacity of the rheometer. A stress-controlled rotary rheometer (Anton Paar, MCR 52) was employed to perform the stress growth test. The building material cell and the 6-blade vane rotor were used. The fresh material was placed inside the cell to make sure that the blades were covered. After that, the blades were sheared at a constant rotational speed with a maximum period of 200 s and the rotational torque values were recorded. A schematic view of the building materials cell and the vane rotor is shown in Figure 3.8.

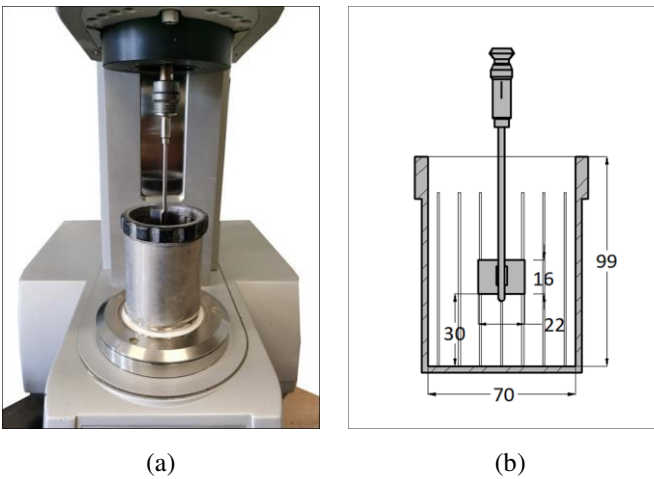


Figure 3.8 (a) Setup equipped with the building materials cell and the 6-blade vane rotor for the stress growth test, and (b) dimensions (mm).



For the mixtures described in Chapter 7, the rotational speed was set as 0.1 rpm and the test was repeated twice for each mixture, while for the mixtures described in Chapter 9, the rotational speed was set as 0.2 rpm and the test was repeated 5 times. Since the rotational speeds (either 0.1 rpm or 0.2 rpm) are very small, it can be assumed that the tested materials were sheared in a static condition. The maximum shear stress  $\tau_y$  (Pa) was calculated as follows:

$$\tau_y = \frac{T_{max}}{2\pi R_b^2 h_b} \quad (3.2)$$

where  $T_{max}$  is the maximum torque (N·m),  $R_b$  is the radius of the blade geometry (m),  $h_b$  is the height of the blades (m).

### 3.4.3 Tack test

The adhesive properties of cement-based materials are mostly measured after the final setting and only a few test methods focus on the adhesive properties of fresh materials. The tack test provides one way for measuring the adhesive properties of fresh materials. During a tack test, two solid surfaces, between which the fresh material is inserted, are pulled away at a fixed velocity or loading rate after a certain duration. The force versus separating displacement (or time) curves is then recorded.

In this thesis, a rheometer (Anton Paar, MCR 102) with a parallel-plate geometry (diameter 50 mm) was used for the tack test. Then, the concrete cylindrical samples described in Section 3.3.2 were glued to the top plate. Circular sandpaper with the same diameter as the plates (root mean square deviation  $R_q$  0.18 mm) was glued onto the bottom plate of the rheometer to avoid slippage. The tack test was performed using the following steps: (1) placing a plastic circular mold (inner diameter 50 mm, height 20 mm) on the bottom plate and fixing it by hand, (2) putting the fresh material in the plastic circular mold and flattening the sample surface, as indicated in Figure 3.10 (a), (3) removing the circular plastic mold, as indicated in Figure 3.10 (b), (4) optionally, the lower surface of the concrete cylindrical sample was coated by smearing with a trowel until the macro textures were filled with fresh material, (5) moving the concrete cylindrical sample (uncoated or coated) downwards until the gap between the lower surface of the concrete sample and the bottom plate reached 10 mm, which is equal to the thickness of one printed layer, as indicated in Figure 3.10 (c), (6) pulling off the concrete cylindrical sample either in a displacement control mode or a load control mode, as indicated in Figure 3.10 (d). The normal force versus displacement curves were then recorded. The setup for the tack test and the schematic views of coated and uncoated cylindrical samples are shown in Figure 3.9. A schematic view of the testing procedure for the tack test is shown in Figure 3.10.

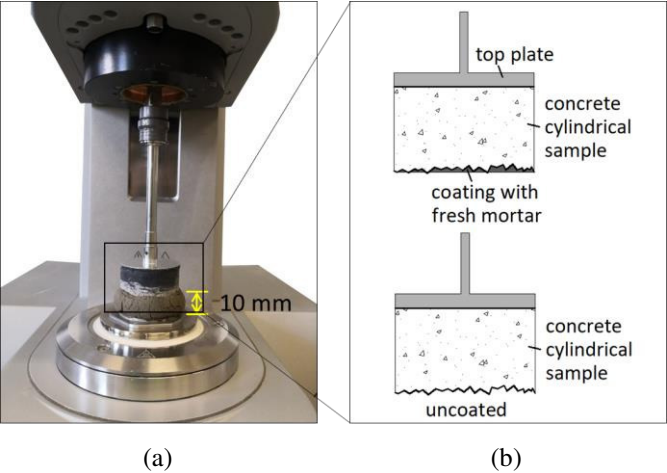


Figure 3.9 (a) Setup equipped with the parallel plate geometry and the concrete cylindrical sample for the tack test, and (b) schematic view of the coated and uncoated concrete cylindrical sample.

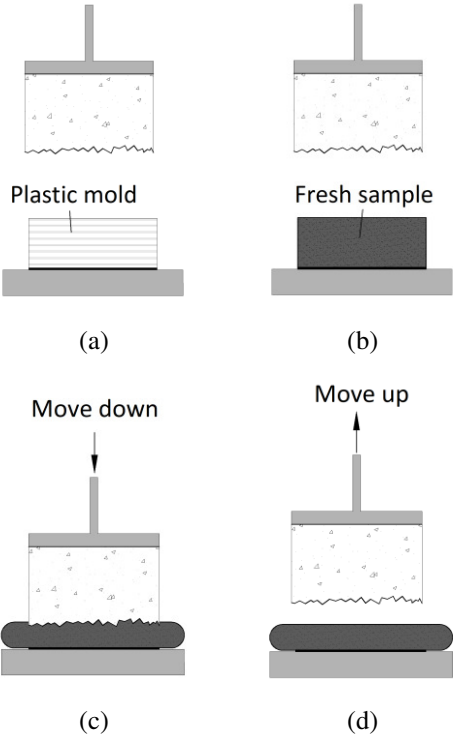


Figure 3.10 Testing procedure of the tack test including (a) molding, (b) demolding, (c) squeezing, and (d) pulling off.

Two types of tack tests were performed including a test in displacement control mode and a test in load control mode. In the displacement control mode, the concrete cylindrical sample was pulled off at a constant speed of  $50 \mu\text{m/s}$  for a maximum period of 500 s. In the load control mode, linearly increasing loads were applied to mimic the stepwise increasing loads of the 3D printing process, as shown in Figure 3.11. The duration of one loading step  $\Delta t$  (s) is expressed as follows:

$$\Delta t = \frac{l}{v_0} + t_0 \quad (3.3)$$

where  $l$  is the constant path length of each layer (m),  $v_0$  is the printing speed (m/s), and  $t_0$  is the break time (s) between two layers without the extrusion of material. Therefore, the applied loading rate  $k$  (N/s) in the tack test equals force over time and is expressed as follows:

$$k = \frac{\Delta F}{\Delta t} = \frac{\rho g A h}{\left(\frac{l}{v_0} + t_0\right)} \quad (3.4)$$

where  $\Delta F$  is the load increment (N),  $\rho$  is the density ( $\text{kg/m}^3$ ), taken as  $2000 \text{ kg/m}^3$ ,  $g$  is the gravitational constant, taken as  $9.81 \text{ m/s}^2$ ,  $A$  is the plate area ( $\text{m}^2$ ), and  $h$  is the layer thickness (m), taken as  $0.01 \text{ m}$ .

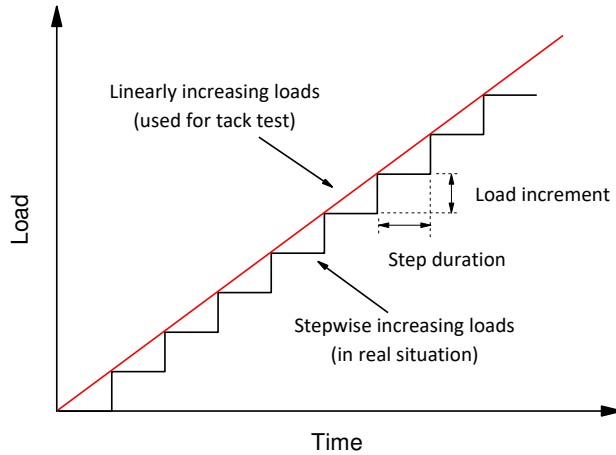


Figure 3.11 Linearly increasing loads during the tack test.

The tensile stress  $\sigma_t$  (Pa) and strain  $\varepsilon_t$  (-) can also be derived from the recorded normal force and displacement. This can be down as follows:

$$\sigma_t = \frac{4F}{\pi d^2} \quad (3.5)$$

$$\varepsilon_t = \frac{\Delta L}{L} \quad (3.6)$$

where  $F$  is the normal force (N),  $d$  is the diameter of the concrete cylindrical sample (m),  $\Delta L$  is the displacement of the concrete cylindrical sample (m), and  $L$  is the initial distance between the lower surface of the concrete sample and the bottom plate (m).

The tests with a displacement control mode were repeated twice while the tests with the load control mode were repeated 5 times for each series with a new molding procedure. An overview of the test conditions for the tack test is shown in Table 3.11.

Table 3.11 An overview of the test conditions for the tack test.

Chapter	Surface roughness (see Section 3.3.2)	Surface moisture content (see Section 3.3.3)	Testing mode	coating
Chapter 7	R1-A, R1-B, R2-A, R2-B, R3-A, R3-B, R4-A, R4-B	M3	Displacement control	No
Chapter 8	R1-A, R2-A, R3-A, R4-B	M1, M2, M3, M4, M5	Displacement control	Yes/ No
Chapter 9	R2-A	M3	Load control	Yes
Chapter 10	R2-A	M3	Displacement control	No

#### 3.4.4 Shear test

The shear test was performed with the rheometer used for the flow curve and stress growth test (Anton Paar, MCR 52). The shear test was performed using the following steps: (1) fixing a plastic circular container (inner diameter 100 mm, height 25 mm) on the bottom module of the rheometer, (2) putting the fresh material in the plastic circular container and flattening the sample surface, (3) moving down the concrete cylindrical sample, which was glued on the top part of the rheometer, until the lower surface was submerged inside the fresh material to a depth of 10 mm, (4) rotating the shaft with a constant rotational speed of 0.1 rpm for a total period of 100 s and recording the torque values. Then, the lower surface of the concrete cylindrical sample was cleaned and the experiment was repeated twice for each mixture. This test was used to evaluate the adhesion of the mixture

described in Chapter 7. The setup for the shear test and its dimensions are shown in Figure 3.12.

Under the assumption that the fresh material reaches the yield point in the whole circular plane, the shear stress  $\tau_s$  (Pa) is given as [200]:

$$\tau_s = \frac{12T}{\pi d^3} \quad (3.7)$$

where  $T$  is the torque value (N·m) and  $d$  is the diameter of the concrete cylindrical sample (m).

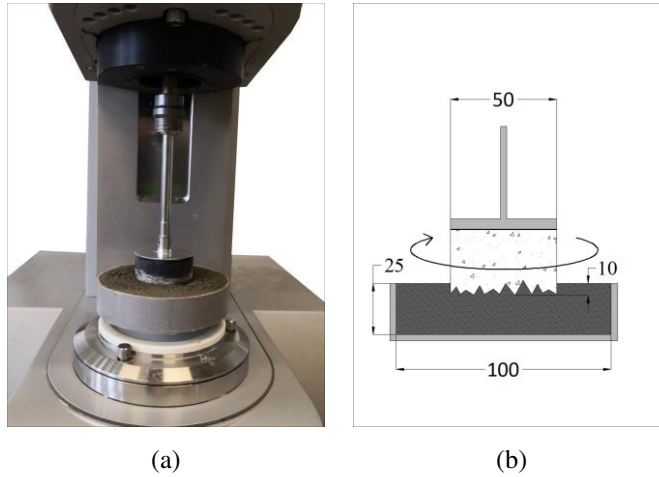


Figure 3.12 (a) Setup equipped with the concrete cylindrical sample for the shear test and (b) dimensions (mm).

### 3.4.5 Viscosity measurement

The viscosity of cellulose ether solutions was measured by using a stress-controlled rheometer (Anton Paar, MCR 102) equipped with coaxial cylinders. The aqueous solutions of cellulose ether were prepared using deionized water as solvent. The polymer was dissolved in water by agitation for a period of 80 s with a handheld mixer (rotational speed 1000 rpm). After that, the solution was centrifuged for 15 min (Thermo Scientific, LABOFUGE 400, rotational speed 2500 rpm) to obtain a homogeneous solution without any entrained air bubbles. A polymer solution sample of 20 ml was poured into the cup container (inner diameter 28 mm, depth 70 mm) before the spindle cylinder (diameter 26.6 mm) was set into position (10 mm from the bottom). After pre-shearing for 15 s and resting for another 15 s, a constant rotational speed (5 rpm) was set with a period of 60 s. The temperatures were set from 20 °C to 60 °C. The data was recorded every second. Each test was repeated twice with the same sample. This test was

used to measure the viscosity of the aqueous solutions of cellulose ether described in Chapter 10. The setup used for the viscosity measurements and dimensions are shown in Figure 3.13.

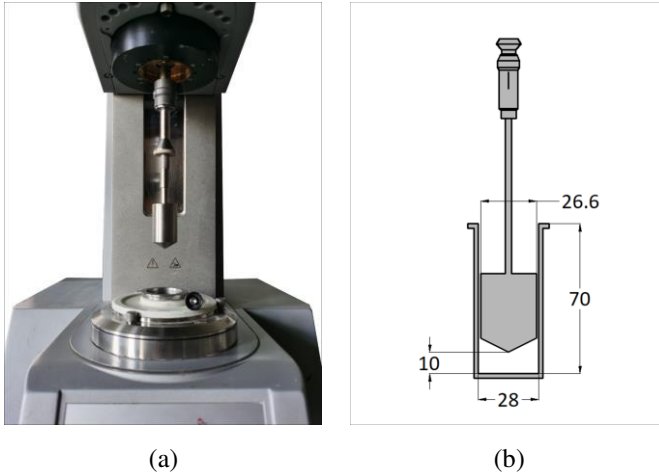


Figure 3.13 (a) Setup equipped with coaxial cylinders for the viscosity measurement of aqueous solutions, and (b) dimensions (mm).

### 3.4.6 Flow table

The fluidity of the printable mortar was evaluated by a flow table test following NBN EN 1015-3 [201]. The test was performed 5 minutes after contact between water and cement. The fresh material was poured into the mold in two layers and each layer was tamped 20 times. After that, the fresh materials were flatted by a trowel and the mold was moved. Then, the diameter was measured after 25 drops of the flow table. The test was repeated twice for each mixture. This test was used to evaluate the fluidity of mixtures described in Chapter 5.

### 3.4.7 Calorimeter test

The rate of hydration was studied by using an isothermal calorimeter (TAM AIR), following EN196-9 [202]. About 10 g of the paste sample was placed in a cylindrical container. Then the sample was placed in an isothermal condition at 20 °C and the heat release was monitored for 72 h. The tests were repeated twice. This test was used to evaluate the hydration process of the combined mixtures described in Chapter 4.

### 3.4.8 Penetration test

The setting time of mixtures was measured by a penetration resistance test following ASTM C403 [203]. Two cubic samples ( $150 \times 150 \times 150 \text{ mm}^3$ ) were cast

for each mixture. The area of the penetration needle and the force provided by the penetrometer was recorded for calculating the pressure. The setting time was determined using the criteria of 3.5 and 27.6 MPa for the initial and final setting. This test was used to evaluate the open time of the mixtures described in Chapter 4 and Chapter 5.

### 3.4.9 3D concrete printing test (twin-pipe pumping)

Two flow rate controlled pumps were used including Putzmeister SP 11 pump and Rudolf STROBOT 407 pump, both delivered by MMB Belgium. The technical data is shown in Table 3.12. One robotic arm (ABB IRB 6650) is adopted for dominating the nozzle position and the technical data is shown in Table 3.13. The helical static mixer consisted of multiple pieces which were used in different combinations. The pieces used within this study are shown in Figure 3.14. Two adjacent mixing baffles have opposite rotational directions and the technical data of the static mixer are shown in Table 3.14. The pieces (i.e. parts A, B, C, and D) can be combined by screw joints. The combinations of the helical static mixer pieces are shown in Table 3.15. Two separate pipes (diameter 25.4 mm, length 5 m) were connected to the pumps and delivered fresh materials to the helical static mixer. Custom-made 3D printed plastic nozzles (material: standard PLA, printer: Ultimaker 2+) were printed. The whole system is shown in Figure 3.15.

Table 3.12 Technical data of the pumps used for the 3D concrete printing test.

Pump	Rudolf STROBOT 407	Putzmeister SP 11
Type	Worm pump	Worm pump
Working pressure	Up to 30 bar	Up to 35 bar
Flow rate	2-29 l/min	5-60 l/min
pumping height (h)	Up to 30 m	Up to 60 m
pumping distance (l)	Up to 48 m	Up to 120 m
Max. grain size	4 mm	6 mm, optional 8 mm
Funnel	70 l	220 L
Weight Approx.	85 kg	900 kg
Length	1300 mm	3924 mm
Width	580 mm	1420 mm
Filling height	770 mm	1160 mm

Note: the pumping height and pumping distance depend on the material properties.

Table 3.13 Technical data of the robotic arm.

Property	Description
Axis	6
Robot version	IRB 6650 125/ 3.2
Reach	3.2 m
Handling capacity	125 kg
Center of gravity	360 mm

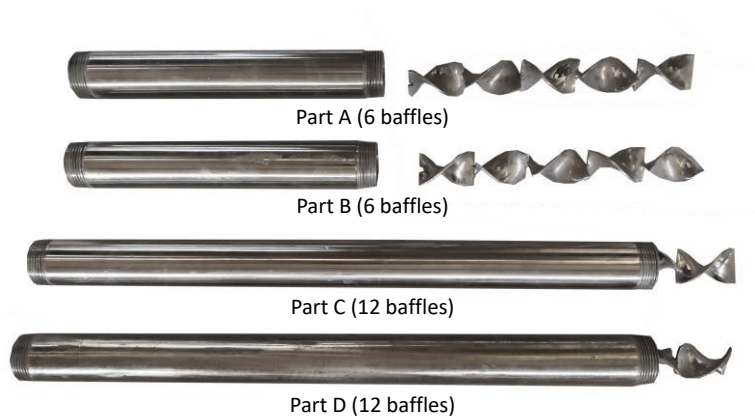


Figure 3.14 Four parts of static mixer.

Table 3.14 Technical data of the helical static mixer.

Property	Part A & Part B	Part C & Part D
Number of baffles	6	12
Inner diameter	32 mm	32 mm
Thickness of each baffle	2 mm	2 mm
Length of each baffle	45 mm	45 mm
Length of the tube	300 mm	570

Table 3.15 Combinations of static mixer parts.

No.	Combination	Mixing baffles
1	A, C and D	30
2	A, B and C	24
3	A and C	18
4	A and B	12
5	A	6
6	None	0



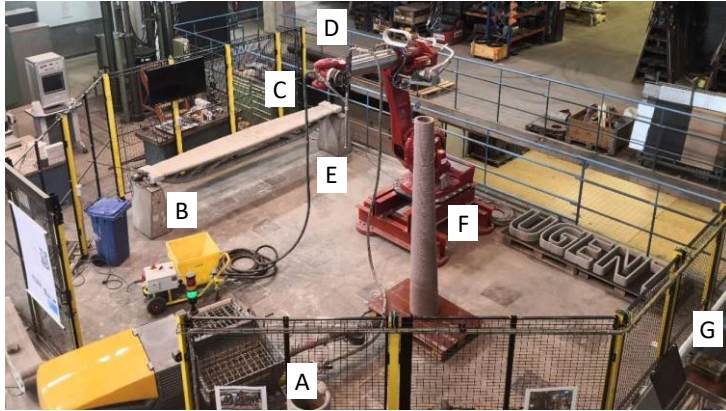


Figure 3.15 Twin-pipe pumping system: A is the pump for the cement-based mixture, B is the pump for the limestone powder-based mixture, C and D are valves, E is the helical static mixer, F is the printed element, G is the controlling system.

Several elements were printed by the twin-pipe pumping system including a column and several straight walls, as listed in Table 3.16. The straight walls described in Chapter 5 were used to study the influence of the number of mixing baffles on the mixing homogeneity, while the straight walls described in Chapter 6 were used to evaluate the mechanical and microstructure properties of the hardened samples. The hollow column described in Chapter 5 was printed to verify the buildability of the combined mixture.

Table 3.16 Details of the printed elements.

Shape	Straight wall (Chapter 5)	Hollow column (Chapter 5)	Straight wall (Chapter 6)
Number of baffles	0, 6, 12, 18, 24, 30	18	18
Nozzle shape	Circular	Circular	Rectangular
Nozzle size	Diameter 32 mm	Diameter 25.4 mm	40×10 mm
Layer thickness	10 mm	10 mm	10 mm
Layer width	40 mm	30 mm	40 mm
Printing speed	250 mm/s	400 mm/s	200 mm/s
Element size	Length 600 mm, height 70 mm	Bottom diameter 400 mm, top diameter 200 mm, height 3 m	Length 1 m, height 160 mm
Gap between each layer	2 s	Less than 1 s	2 s
Lateral trowels	No	No	Yes (height 10 mm)

### 3.4.10 3D concrete printing test (sag resistance)

A 6-axis robotic arm (ABB IBR 6650) was used to control the nozzle position, and a worm pump (Rodulf STROBOT 407) with a pumping pipe (diameter 25.4 mm, length 3 m) was used for material extrusion. Custom-made 3D printed plastic nozzles with a trowel (material: standard PLA, printer: Ultimaker 2+) were printed for surface smoothing.

The first aim is to study the influence of the surface inclination on the adhesion performance of fresh materials. On this basis, two series of 3D concrete printing tests were performed at two representative surface inclinations including the inclination of  $180^\circ$  (overhead position) and the inclination of  $90^\circ$  (side position), as shown in Figure 3.16. When printing at the overhead position, the slab was supported horizontally at two lateral sides with the treated surfaces (either polished or gritblasted surface) facing downwards. The layers were printed against the lower surface of the slab. To mimic printing at the side position, the slab was placed vertically, as well as the printed layers. A digital camera was used to record the whole printing process.

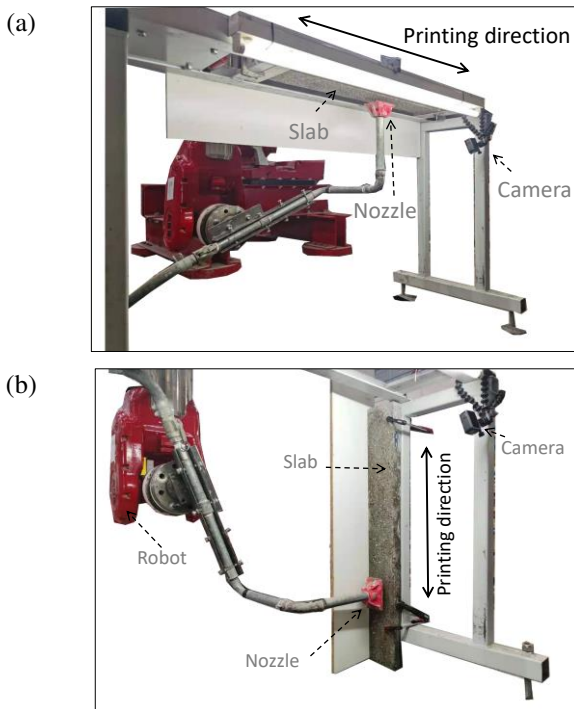


Figure 3.16 3D concrete printing setup: (a) printing at the overhead position and (b) printing at the side position.

As a follow-up, the influence of substrate properties including surface roughness and moisture content (in Chapter 8), and the polymer modification of the overlay (in Chapter 9) on the adhesion at the overhead position were explored. Two different printing paths were used including a continuous path and an one-way printing path, as shown in Figure 3.17. In Chapter 7, printing paths (a) and (c) were used. In Chapter 8, only printing path (a) was used. In Chapter 9, printing path (b) was used. The printing speed was 100 mm/s for all series. The width of extruded layers was 60 mm and the thickness was 10 mm for all series. For the printing paths (a) and (c), the length of the printed layer was kept constant as 600 mm, while for the printing path (b), the length of the first layer was 600 mm and the length of the subsequent layers was 4 mm shorter on the two lateral sides compared to the previous layer to avoid boundary effects at the two lateral sides. The gap between two layers was 4 s in the series of the one-way printing path.

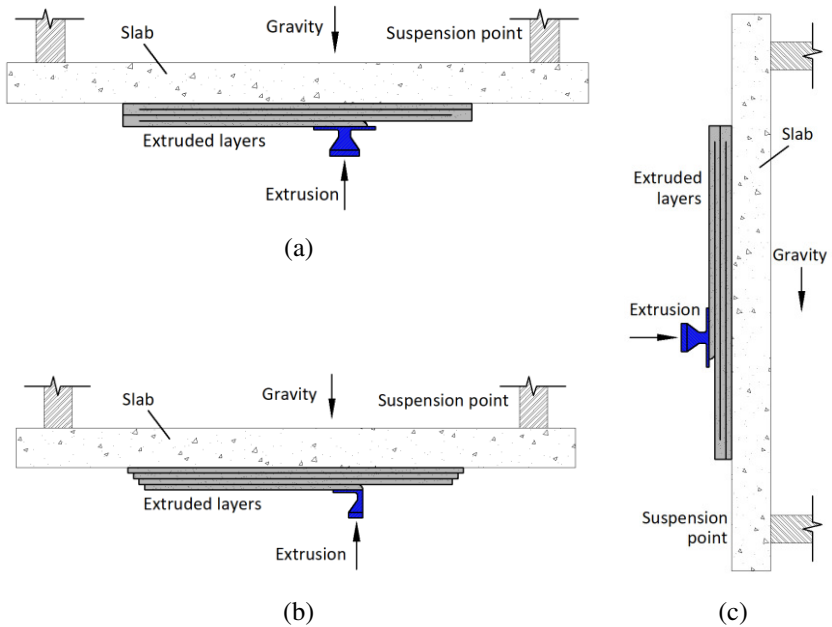


Figure 3.17 Schematic view of the printing paths: (a) continuous printing at the overhead position, (b) one-way printing at the overhead position, and (c) continuous printing at the side position.

For the continuous printing path, i.e. printing paths (a) and (c), a plastic 3D printed nozzle with trowels on both sides was designed, as shown in Figure 3.18 (a). For the one-way printing path, i.e. printing path (b), a plastic 3D printed nozzle with only one-side trowel was designed, as shown in Figure 3.18 (b).

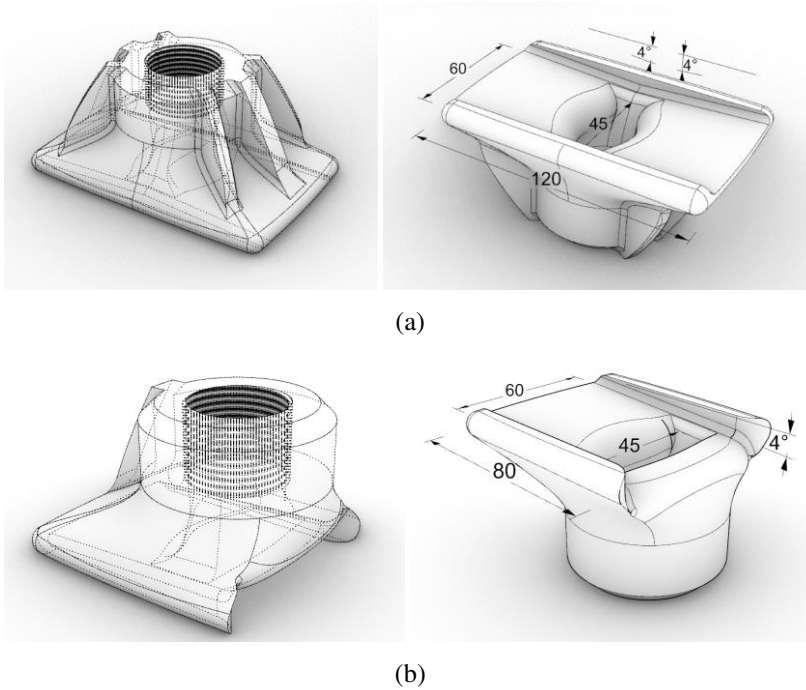


Figure 3.18 Schematic view and dimensions (mm) of nozzles, (a) for the continuous printing and (b) for the one-way printing.

In addition, similar to that in the tack test, the treated surface of the concrete slabs was coated by smearing with a trowel until the macro textures were filled with the fresh material. An overview of the test conditions for the 3D concrete printing (sag resistance) tests is listed in Table 3.17.

Table 3.17 Test conditions for the 3D concrete printing (sag resistance) test.

Chapter	Surface inclination	Stroke type	Stroke size	Printing path	Repetition	Coating
Chapter 7	90° 180°	Gritblasted	1000×12	continuously	3	No
			0×50 mm <sup>3</sup>			
Chapter 8	180°	Gritblasted	1000×12	continuously	3	Yes/ No
		Polished	0×50 mm <sup>3</sup>			
Chapter 9	180°	Gritblasted	1000×20	One way	2	Yes
			0×50 mm <sup>3</sup>			

### 3.4.11 Compression test

Mold cast samples were made by using prismatic molds ( $40 \times 40 \times 160 \text{ mm}^3$ ). After the molding procedure, a shaking table (frequency 1 Hz, period 60 s) was used to compact the fresh materials. The mold cast samples were demolded at the age of 1 day. After that, cubic samples ( $40 \times 40 \times 40 \text{ mm}^3$ ) were sawn from the demolded samples. The samples were cured in a controlled environment ( $T = 20 \text{ }^\circ\text{C}$ , R.H = 65%) until testing.

3D printed wall elements ( $1000 \times 160 \times 40 \text{ mm}^3$ ) were kept in the testing hall in the first day. After that, cubic samples ( $40 \times 40 \times 40 \text{ mm}^3$ ) were extracted by sawing from the 3D printed wall elements at the age of 1 day to measure the compressive strength, as shown in Figure 3.19. All extracted samples were cured in a controlled environment ( $T = 20 \text{ }^\circ\text{C}$ , R.H = 65%) until testing.

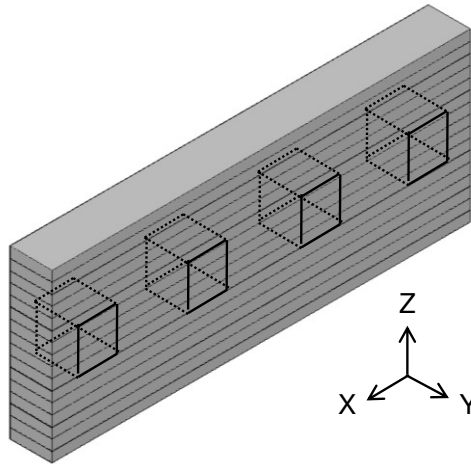


Figure 3.19 Extracting cubic samples from the printed wall element to test the compressive strength.

The compressive strength was evaluated following NEN-EN 12390-3 [196]. The compressive strength of the mold cast samples was measured 6 times for each mixture and each age. For 3D printed samples, the tests were repeated 6 times for each age and each loading direction. The loading directions of the cubes extracted from the 3D printed elements are shown in Figure 3.20. The loading directions C-1 and C-2 were parallel to the 3D printed interlayer, following the x-axis and y-axis respectively, while the loading direction C-3 was perpendicular to the 3D printed interlayer (z-axis).

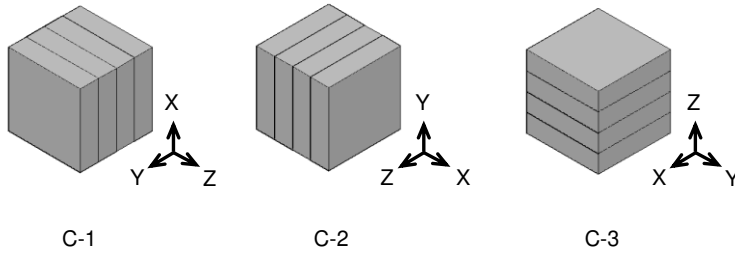


Figure 3.20 Compression test of 3D printed samples under three different loading directions including C-1, C-2, and C-3.

The compressive strength is calculated as follows:

$$\sigma_c = \frac{F_c}{A_c} \quad (3.8)$$

where  $\sigma_c$  is the compressive strength (MPa),  $F_c$  is the load at failure (N), and  $A_c$  is the cross-sectional area of the cubic sample.

#### 3.4.12 Flexural test

Mold cast samples were made by using prismatic molds ( $40 \times 40 \times 160 \text{ mm}^3$ ). After the molding procedure, a shaking table (frequency 1 Hz, period 60 s) was used to compact the fresh materials. The mold cast samples were demolded at the age of 1 day. In addition, prismatic samples ( $40 \times 40 \times 160 \text{ mm}^3$ ) were extracted in two directions (parallel and perpendicular to the printing direction) by sawing from the 3D printed wall elements ( $1000 \times 160 \times 40 \text{ mm}^3$ ) at the age of 1 day to measure the flexural strength, as shown in Figure 3.21. The same curing procedure used for the cubic samples described in Section 3.4.11 was adopted for the prismatic samples. The flexural test was performed at the age of 3, 7, and 28 days. This test was used for the samples described in Chapter 6.

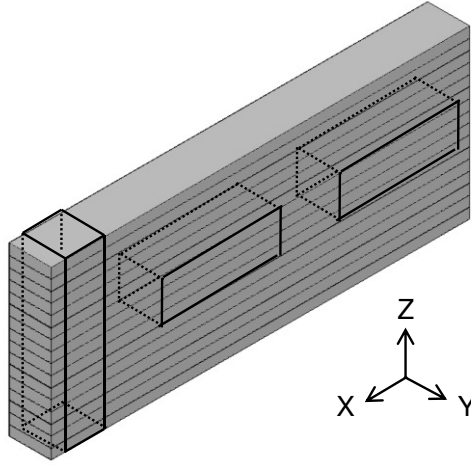


Figure 3.21 Extracting prismatic samples from the printed wall element to test the flexural strength.

The flexural strength of prismatic samples was measured by a three-point bending test, following NEN-EN 12390-5 [204]. The prismatic samples were placed on two supporting rollers with a supporting span of 100 mm. The test was repeated 3 times for each age and each loading direction. For the mold cast samples with a rectangular cross-section, the flexural strength is calculated using the following equation:

$$\sigma_f = \frac{3F_f L_s}{2bh_p^2} \quad (3.9)$$

where  $\sigma_f$  is the flexural strength (MPa),  $F_f$  is the load at the middle position of the prismatic sample (N),  $L_s$  is the supporting span (mm),  $b$  is the width of the prismatic sample (mm), and  $h_p$  is the height of the prismatic sample (mm).

For the 3D printed samples, three loading directions were applied including D-1 (along the x-axis), D-2 (along the y-axis), and D-3 (along the z-axis), as shown in Figure 3.22.

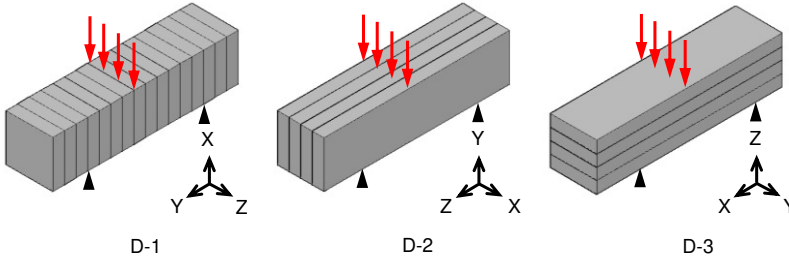


Figure 3.22 Flexural test of 3D printed samples under three loading directions including D-1, D-2, and D-3.

Since the cross-section of prismatic samples extracted from 3D printed elements might change along the length, the flexural strength of 3D printed prismatic samples is calculated using the following equation:

$$\sigma_f = \frac{12F_f L}{(b_{p1} + b_{p2})(h_{p1} + h_{p2})^2} \quad (3.10)$$

where  $b_{p1}$  and  $b_{p2}$  are the width of two sides of the prismatic sample (mm),  $h_{p1}$  and  $h_{p2}$  are the height of two sides of the prismatic sample (mm). Taking the 3D printed sample under the loading direction D-1 as an example, the dimensions of the prismatic sample are illustrated in Figure 3.23.

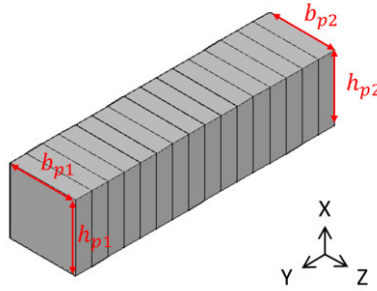


Figure 3.23 Width and height of the 3D printed prismatic sample.

#### 3.4.13 Pull-off test (interlayer)

Small prismatic samples ( $40 \times 30 \times 20 \text{ mm}^3$ ) were extracted by sawing from the 3D printed wall elements ( $1000 \times 160 \times 40 \text{ mm}^3$ ) at the age of 1 day to measure the tensile bond strength, as shown in Figure 3.24. In addition, prismatic samples of the same size ( $40 \times 30 \times 20 \text{ mm}^3$ ) were sawn from the mold cast samples ( $40$



$\times 40 \times 160 \text{ mm}^3$ ). All extracted samples were cured in a controlled environment ( $T = 20^\circ\text{C}$ ,  $R.H = 65\%$ ) until the age of 3, 7, and 28 days.

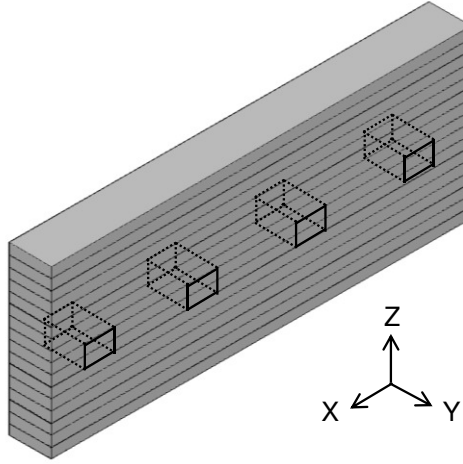


Figure 3.24 Extracting small prismatic samples from the wall element to test the tensile bond strength.

The tensile bond strength of small prismatic samples was measured by a pull-off test, following NBN EN 1542 [197]. Two steel dollies ( $20 \times 20 \times 20 \text{ mm}^3$ ) were glued on the top and bottom surface of each sample. The pull-off test was performed with an automatic bond strength device (Proceq DY-2, maximum tensile force 16 kN). The loading rate was set as 50 N/s. A schematic view of the pull-off test is shown in Figure 3.25. The test was performed 5 times for each series and the maximum force required was recorded. This test was performed on the samples described in Chapter 6.

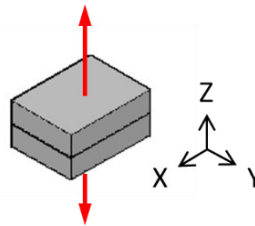


Figure 3.25 Pull-off test of 3D printed samples with an interface in the middle.

The tensile bond strength  $\sigma_{tb}$  (Pa) is calculated as follows:

$$\sigma_{tb} = \frac{F_t}{A_t} \quad (3.11)$$

where  $F_t$  is the load at failure (N), and  $A_t$  is the cross-sectional area of the sample, which equals  $1200 \text{ mm}^2$ .

#### 3.4.14 Pull-off test (overlay-to-substrate)

Two series of pull-off tests were performed to measure the bond strength at the overlay-to-substrate position in the hardened state, as shown in Figure 3.26. The first series, which will be further described in Chapter 8, was to evaluate the influence of substrate properties on the bond strength of the hardened overlays, as portrayed in Figure 3.26 (a) and (b). For 3D printed samples, three layers ( $600 \times 60 \times 30 \text{ mm}^3$ ) were printed against the lower surface of the supported concrete stroke ( $1000 \times 120 \times 50 \text{ mm}^3$ ). The samples were kept in the testing hall on the first day and cured in a controlled environment (temperature  $20^\circ\text{C}$ , humidity 65%) until the age of 28 days. In addition, a mold cast sample was made as a reference. Unfortunately, the bond of the printed layers applied on the uncoated substrate was very weak, which was easy to be destroyed during the drilling process. Therefore, the samples were sawn with a larger cross-section. To prepare the mold cast samples, two wooden boards (height 80 mm) were placed on two sides of the stroke ( $1000 \times 120 \times 50 \text{ mm}^3$ ) with the rough surface oriented upwards. The fresh material was compacted and flattened by a manual trowel after placement. The mold cast samples were placed in the same controlled environment (temperature  $20^\circ\text{C}$ , humidity 65%) immediately after casting. Afterwards, the samples were cut into 6 pieces along the longitudinal direction (length 100 mm for each piece). For mold cast samples, the overlay was further cut and the width of each piece was reduced from 120 mm to 60 mm, aiming at achieving the same contact area as that of the printed samples. Steel dollies (diameter 50 mm, thickness 10 mm) were glued onto the upper face with epoxy resin (Sika, Sikadur-30). An automatic testing machine (Proceq DY-2, maximum tensile force 16 kN, loading rate 50 N/s) was used to measure the tensile bond strength at the age of 28 days. The maximum tensile force was recorded and the fracture surface (surface A on the side of the printed layer and surface B on the side of the substrate) was observed. The test was repeated 6 times for each series. The tensile bond strength  $\sigma_t$  (MPa) is calculated as follows:

$$\sigma_t = \frac{F_t}{l_t \cdot w_t} \quad (3.12)$$

where  $F_t$  is the load at failure (N),  $l_t$  is the length of each sample (m),  $w_t$  is the width of the sample, which equals 60 mm (m).

The second aim was to evaluate the influence of the polymer modification on the bond strength of the overlays in the hardened stage, which will be further discussed in Chapter 9. Both 3D printed samples ( $600 \times 60 \times 30 \text{ mm}^3$ ) and mold cast samples ( $600 \times 80 \times 30 \text{ mm}^3$ ) were prepared, as shown in Figure 3.26 (c) and (d). In this series, the substrates ( $1000 \times 80 \times 50 \text{ mm}^3$ ) were coated beforehand by smearing

with a trowel until the macro textures were filled with the fresh material. The strokes used for 3D printed samples were supported on a steel frame with the rough surface down, while the stroke for mold cast samples was placed with the rough surface up. Due to the presence of the coating, the bond strength of hardened samples was improved. Therefore, circular drilling was adopted and the bond strength was measured at the age of 7 days. The samples were kept in the testing hall for one day and cured in a controlled environment (temperature 20 °C, relative humidity 65%) for 6 more days, the printed element was drilled to a depth of 15 mm into the concrete substrate with a core drill (diameter 50 mm) and then a dolly (diameter 50 mm, height 10 mm) was glued to the core face. The same loading rate (50 N/s) was used and the test was performed three times for each mixture. The tensile bond strength  $\sigma_t$  (MPa) is calculated as follows:

$$\sigma_t = \frac{4F_t}{\pi d^2} \quad (3.13)$$

where  $F_t$  is the load at failure (N),  $d$  is the diameter of each sample (m), which equals 50 mm (m).

An overview of the overlay-to-substrate samples used for the pull-off test is listed in Table 3.18.

Table 3.18 Test conditions for the pull-off test (overlay-to-substrate).

Chapter	Sample	Surface inclination	Stroke size	Preparation	Repetition	Age
Chapter 8	3D printed	180°	1000×120×50 mm <sup>3</sup>	Sawing	6	28
	Mold cast	0°	1000×120×50 mm <sup>3</sup>	Sawing	6	28
Chapter 9	3D printed	180°	1000×80×50 mm <sup>3</sup>	Drilling	3	7
	Mold cast	0°	1000×80×50 mm <sup>3</sup>	Drilling	3	7

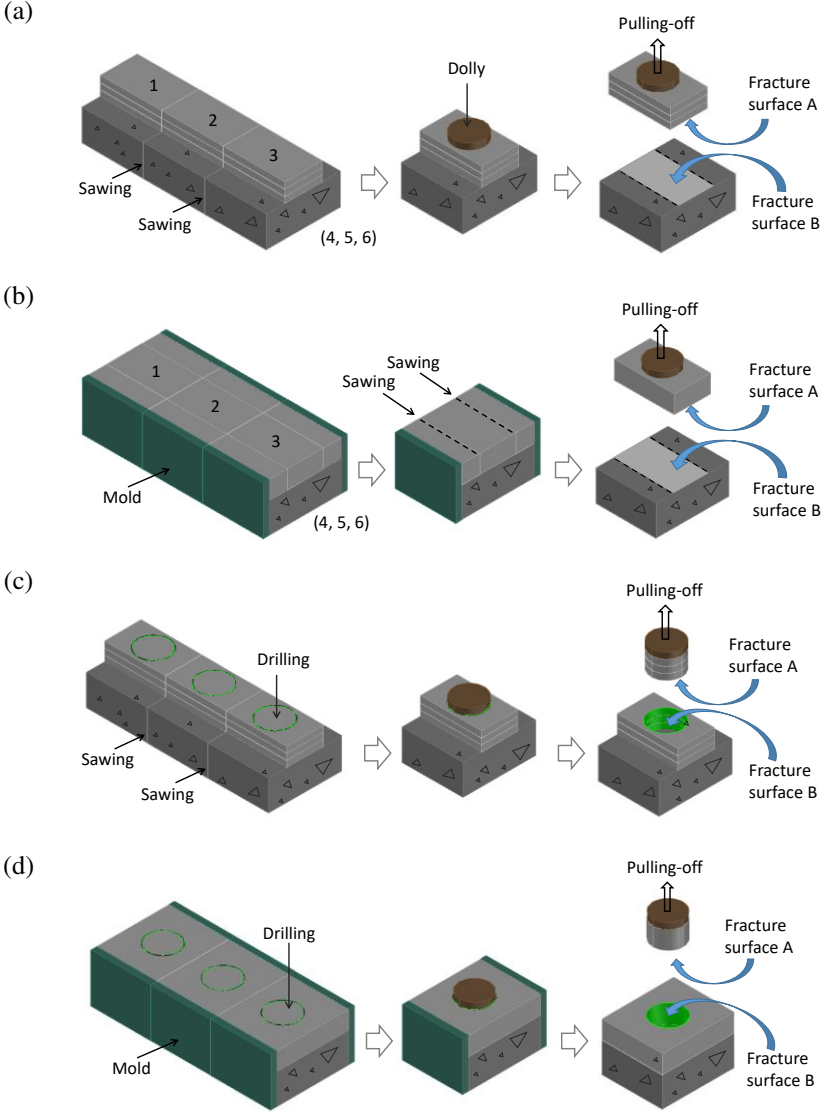


Figure 3.26 Schematic view of the pull-off test: (a) 3D printed samples on uncoated substrates and (b) mold cast samples prepared by sawing, (c) 3D printed sample on coated substrates, and (d) mold cast samples prepared by drilling.

### 3.4.15 Mercury intrusion porosimetry (MIP)

The porosity of 3D printed samples (both bulk and interface area) and mold cast samples, which will be further introduced in Chapter 6, was measured by mercury intrusion porosimetry (MIP, Thermo scientific, Pascal 140 series and 440 series)

with a pressure limitation of 420 MPa. Small cubic samples (width 10 mm) were extracted by sawing from the bulk area inside one layer (3DCP\_Bulk) and the interface between two adjacent layers (3DCP\_Interface) for microstructure assessment at the age of 1 day, as shown in Figure 3.27. In addition, small cubic samples (width 10 mm) were sawn from the mold cast samples.

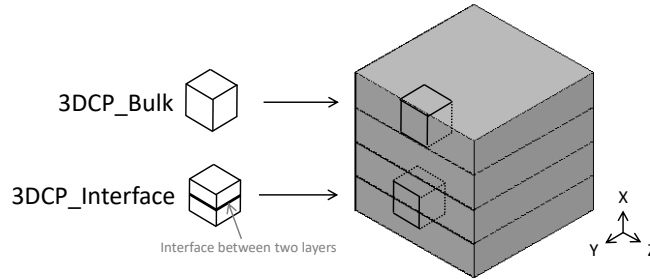


Figure 3.27 Extracting small cubic samples from the bulk area inside one layer and the interface between two adjacent layers for microstructure assessment.

The small cubic samples were sawn at the age of 1 day and cured in the same environment ( $T = 20\text{ }^{\circ}\text{C}$ ,  $R.H = 65\%$ ) until the age of 28 days. Then, the samples were immersed in 2-propanol for 24 h to stop hydration. Afterwards, the samples were oven-dried at  $40\text{ }^{\circ}\text{C}$  for 24 h and vacuum dried at  $20\text{ }^{\circ}\text{C}$  for two weeks at 0.1 bar to minimize microstructural damage during sample preparation [205]. During the measurement, the pressure was limited to 200 MPa to avoid cracking. The contact angle between the mercury and the sample surface was  $142^{\circ}$  and the surface tension was 0.482 N/m. The pore diameters were calculated from the recorded pressure according to the Washburn equation [206].

### 3.4.16 Scanning electron microscopy (SEM)

The microstructure of 3D printed samples and mold cast samples, which will be further introduced in Chapter 6, was observed by scanning electron microscopy (SEM, JEOL JSM-7400F) using secondary electrons (SE), backscattered electrons (BSE), and energy-dispersive X-ray (EDX) mode. After curing for 28 days, small cubic samples (width 10 mm) were immersed in 2-propanol for 24 h to stop hydration. After that, the samples were oven-dried at  $40\text{ }^{\circ}\text{C}$  for 24 h and vacuum dried at  $20\text{ }^{\circ}\text{C}$  for two weeks at 0.1 bar. The samples observed by BSE and EDX were further impregnated by epoxy resin (CONDOR, Conpox Resin BY 158, and Conpox Hardener HY 2996) and polished (Struers, LaboPol-5, and LaboForce-3). The polishing process including the following steps: (1) using silicon carbide (SiC) paper of 320 grit (Struers, the following as well) with running water at 300 rpm for 90 s, (2) using SiC paper of 500 grit with running water for 90 s, (3) using SiC paper of 1200 grit with running water at 300 rpm for 90 s, (4) using SiC

paper of 2400 grit with lubricant brown at 150 rpm for 90 s, (5) using MD Dac plate with 3  $\mu\text{m}$  diamond paste (DP-Paste P, the following as well) with methanol at 150 rpm for 240 s, (6) using MD Dac plate with 1  $\mu\text{m}$  diamond paste with methanol at 150 rpm for 240 s, (7) and MD Nap plate with 0.25  $\mu\text{m}$  diamond paste with methanol at 150 rpm for 90 s. The surface of the samples was cleaned with high-pressure air and soft paper after each polishing step.

#### **3.4.17 Static filtration test**

The pore solution was extracted from fresh cement pastes by using a static filtration setup (BAUER, maximum air pressure 7 bars). The test procedure was conducted as follows: (1) placing a filter paper (BAUER) at the bottom of the cell to exclude the presence of cement particles in the extracted solution, (2) pouring the homogenized cement paste (around 1200 g) into the filter cell, (3) applying a differential air pressure of 5 bars at the top of the filter cell, (4) collecting the pore solution for 5 minutes, and (5) releasing the air pressure. The preparation of the cement paste and the results will be given in Chapter 10.

#### **3.4.18 Dynamic light scattering (DLS)**

To measure the hydrodynamic diameter of the cellulose ether in the extracted pore solution, dynamic lighting scattering (DLS) measurement was performed using a Zetasizer nano series from Malvern Instrument. The wavelength of the incident light was 633 nm and the scattered light was detected at an angle of  $173^\circ$ . The temperature was set constantly at  $25^\circ\text{C}$  for all the DLS measurements. Each experiment was repeated three times with one sample. The results will be given in Chapter 10.

#### **3.4.19 Total organic carbon (TOC)**

A total organic carbon (TOC) test was performed on the pore solution extracted from fresh cement pastes by using a TOC analyzer (Shimadzu TOC-V). By acidizing the sample, the amount of total carbon (TC) and inorganic carbon (IC) can be measured. The amount of TOC is calculated by subtraction of the IC value from the TC value. The results will be given in Chapter 10.

## Combined mixture design for twin-pipe pumping

### 4.1 Introduction

Many attempts have been made to develop a dosing system for 3D concrete printing, as introduced in Chapter 2. However, the above-mentioned dynamic mixers incorporate complicated components and thus lead to difficult maintenance and operation. Another weakness is that only liquid admixtures are suitable, leading to a limited range of applications. Different from the dynamic mixers mentioned above, static mixers without any moving component provide another option for dosing accelerator (ACC). Among the different types of static mixers introduced in Chapter 2, the helical static mixer is the most commonly used, where two adjacent baffles inside the static mixer have opposite rotational directions. As separate flows go through the helical static mixer, the non-moving mixing baffles continuously blend the processed flows.

In this chapter, a twin-pipe pumping (TPP) strategy using limestone powder (LP) suspension as an admixture carrier is proposed. During the 3D printing process, one mixture (i.e. PC-based mixture) consisting of Portland cement (PC), sand, water, and superplasticizer (SP) is mixed and pumped from one pipe, while another mixture (i.e. LP-based mixture) consisting of limestone powder, sand, water, superplasticizer, accelerator, and viscosity modifying admixture (VMA) is mixed and pumped from another pipe. Two kinds of mixtures are pumped from separate pipes and incorporated in a helical static mixer at the position of the nozzle. Without the addition of an accelerator, the PC-based mixture is expected to sustain a good fluidity and a long open time. On the other hand, the accelerator contained in the LP-based mixture has little effect without the presence of cement, leading to a high open time as well for the LP-based mixture. As the PC-based mixture and LP-based mixture move through the helical static mixer, the mixing elements continuously blend the two mixtures and a combined mixture is extruded from the outlet. As a result, the accelerator in the LP-based mixture soon takes effect in contact with cement in the PC-based mixture, giving rise to a fast stiffening process and a prompt stage transition from a liquid form to a solid form. A schematic view of the cement-based mixture, the limestone powder-based mixture, and the combined mixture developed in the twin-pipe pumping system is

shown in Figure 4.1. This chapter focuses on the mixture design of the combined mixture. The substitution rate of the limestone powder and the dosage of the accelerator for the combined mixture are determined accordingly.

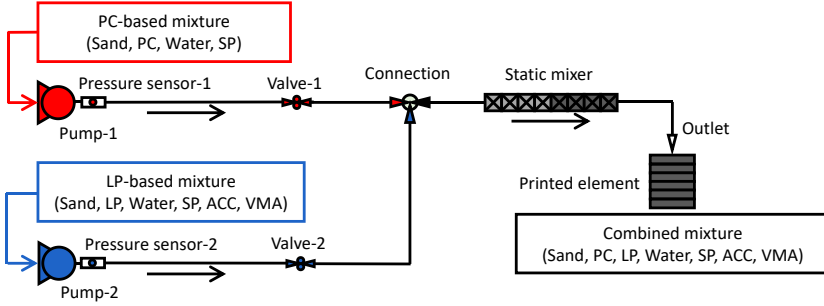


Figure 4.1 Schematic view of the cement-based mixture, the limestone powder-based mixture, and the combined mixture developed in the twin-pipe pumping system.

## 4.2 Experimental program

In the first step, a combined mixture consisting of sand, cement, limestone powder, water, superplasticizer, accelerator, and viscosity modifying admixture is developed with satisfying mechanical properties and a fast stiffening rate. After that, the combined mixture is divided into the PC-based mixture and LP-based mixture to meet the requirements of high fluidity and long open time. The PC-based mixture consists of sand, cement, water, and superplasticizer. While the LP-based mixture consists of sand, limestone powder, water, superplasticizer, accelerator, and viscosity modifying admixture.

The volume of the combined mixture  $V_{COM}$  ( $\text{m}^3$ ) is expressed as:

$$V_{COM} = \frac{m_S}{\rho_S} + \frac{m_{PC}}{\rho_{PC}} + \frac{m_{LP}}{\rho_{LP}} + \frac{m_W}{\rho_W} + \frac{m_{SP}}{\rho_{SP}} + \frac{m_{ACC}}{\rho_{ACC}} + \frac{m_{VMA}}{\rho_{VMA}} \quad (4.1)$$

Where  $m_S$ ,  $m_{PC}$ ,  $m_{LP}$ ,  $m_W$ ,  $m_{SP}$ ,  $m_{ACC}$ , and  $m_{VMA}$  (kg) are the mass of sand, cement, limestone powder, water, superplasticizer, accelerator, and viscosity modifying admixture in the combined mixture, respectively. In addition,  $\rho_S$ ,  $\rho_{PC}$ ,  $\rho_{LP}$ ,  $\rho_W$ ,  $\rho_{SP}$ ,  $\rho_{ACC}$ , and  $\rho_{VMA}$  ( $\text{kg}/\text{m}^3$ ) are the density of sand, cement, limestone powder, water, superplasticizer, accelerator, and viscosity modifying admixture, respectively.

The volume of the PC-based mixture  $V_{PC}$  ( $\text{m}^3$ ) and LP-based mixture  $V_{LP}$  ( $\text{m}^3$ ) is then expressed as:



$$V_{PC} = \frac{m_{S1}}{\rho_S} + \frac{m_{PC}}{\rho_{PC}} + \frac{m_{W1}}{\rho_W} + \frac{m_{SP1}}{\rho_{SP}} \quad (4.2)$$

$$V_{LP} = \frac{m_S - m_{S1}}{\rho_S} + \frac{m_{LP}}{\rho_{LP}} + \frac{m_W - m_{W1}}{\rho_W} + \frac{m_{SP} - m_{SP1}}{\rho_{SP}} + \frac{m_{ACC}}{\rho_{ACC}} + \frac{m_{VMA}}{\rho_{VMA}} \quad (4.3)$$

Where  $m_{S1}$  (kg) is the mass of sand in the PC-based mixture,  $m_{W1}$  (kg) is the mass of water in the PC-based mixture, and  $m_{SP1}$  (kg) is the mass of the superplasticizer in the PC-based mixture.

Then a sand ratio is defined as  $x$  and expressed as follows:

$$x = m_{S1} : m_S \quad (4.4)$$

In addition, a water ratio is defined as  $y$  and expressed as follows:

$$y = m_{W1} : m_W \quad (4.5)$$

In addition, a superplasticizer ratio is defined as  $z$  and expressed as follows:

$$z = m_{SP1} : m_{SP} \quad (4.6)$$

The volume ratio between the PC-based mixture and LP-based mixture is defined as  $v$  and expressed as follows:

$$v = V_{PC} : V_{LP} \quad (4.7)$$

The volume of superplasticizer and viscosity modifying admixture is ignored due to a very small amount compared to that of the other components. Then the following equation is reached:

$$\left[ \frac{xm_S}{\rho_S} + \frac{m_{PC}}{\rho_{PC}} + \frac{ym_W}{\rho_W} \right] : \left[ \frac{(1-x)m_S}{\rho_S} + \frac{m_{LP}}{\rho_{LP}} + \frac{(1-y)m_W}{\rho_W} + \frac{m_{ACC}}{\rho_{ACC}} \right] = v \quad (4.8)$$

Therefore, given a pre-defined volume ratio  $V_{PC} : V_{LP}$  and a sand ratio  $m_{S1} : m_S$ , the water ratio  $m_{W1} : m_W$  can thus be obtained and the volume of the combined mixture, PC-based mixture, and LP-based mixture is determined.

In this study, the sand to binder ratio of the combined mixture was kept as 1, the water-to-binder ratio of the combined mixture was kept as 0.35. Three limestone powder substitution rates were prepared including 0%, 25%, and 50% by mass of PC. Three dosages of accelerator (ACC1) were prepared including 0%, 3.5%, and 7% by mass of cement. Viscosity modifying admixture used in this Chapter was CE5 (MOT 60000 YP4).

The mix design of the combined mixtures is shown in Table 4.1.

Table 4.1 Mix design of combined mixtures (kg/m<sup>3</sup>).

Mixture	Sand	PC	LP	Water	SP	ACC	VMA
COM-LP0%-ACC0%	950.59	950.59	0	332.71	5.70	0	0.95
COM-LP25%-ACC0%	950.59	712.94	237.65	332.71	5.70	0	0.95
COM-LP50%-ACC0%	950.59	475.30	475.30	332.71	5.70	0	0.95
COM-LP25%-ACC3.5%	950.59	712.94	237.65	332.71	5.70	24.96	0.95
COM-LP25%-ACC7%	950.59	712.94	237.65	332.71	5.70	49.91	0.95

For the calorimeter test, sand was not included in the mixture. The mixture design of the cement paste is shown in Table 4.2.

Table 4.2 Mix design of cement paste mixtures (kg/m<sup>3</sup>).

Mixture	PC	LP	Water	SP	ACC	VMA
CP-LP25%-ACC0%	1238.31	412.78	577.89	9.90	0	1.65
CP-LP25%-ACC3.5%	1238.31	412.78	577.89	9.90	43.35	1.65
CP-LP25%-ACC7%	1238.31	412.78	577.89	9.90	86.69	1.65

The mixtures were prepared in a conventional planetary mixer according to the following protocol: (1) manually mixing superplasticizer with water for 10 s; (2) mixing dry powders (cement, limestone powder, and viscosity modifying admixture) at 140 rpm for 10s; (3) adding water (and superplasticizer) to the pre-mixed dry powders and rotating the paddle at 140 rpm for 30 s; (4) adding sand (if any) and rotating the paddle at 140 rpm for 30 s; (5) rotating the paddle at 285 rpm for 30 s; (6) scraping and resting for 90 s; (7) rotating the paddle at 285 rpm for 60 s; (8) adding accelerator and mixing at 140 rpm for 30 s.

### 4.3 Results and discussion

#### 4.3.1 Effect of limestone powder substitution rates

Three combined mixtures with different limestone powder substitution rates (i.e. COM-LP0%-ACC0%, COM-LP25%-ACC0%, and COM-LP50%-ACC0%) were formulated. The compressive strength after a certain period (i.e. 3 days, 7 days, and 28 days) is shown in Figure 4.2.

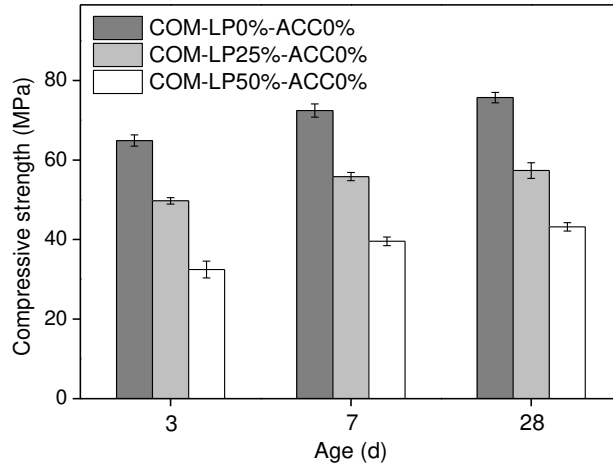


Figure 4.2 Compressive strength of mold cast samples with different limestone powder substitution rates (error bars represent the standard error,  $n=3$ ).

It can be easily seen that, regardless of curing age, there was a decrease in the compressive strength with the increase of limestone powder substitution rate. Moreover, for 28 days, compared to the reference mixture (i.e. COM-LP0%-ACC0%), decreases were 24.24% and 42.93% respectively for the replacement of 25% and 50% cement by limestone powder.

The effect of limestone powder on the compressive strength can be interpreted in terms of particle size, content, and replacement pattern. For example, it was reported by Ghafoori et al. that the compressive strength of concrete was improved with the incorporation of ultra-fine limestone powder because of the filler effect [207]. On the other hand, İnan Sezer reported that the compressive strength reduced with the increase of LP content because of the dilution effect [208]. Li and Kwan noticed that the compressive strength significantly increased because of filler and nucleation effects [209]. In the latter study, the presence of limestone powder promoted the precipitation of C-S-H and increased the hydration degree of cement due to its nucleation effect.

In this study, the decrease in compressive strength was caused by the dilution effect of limestone powder. With the increase of limestone powder content, the amount of hydration products reduced. Cement, resulting in a higher amount of hydration products, is one of the most important, even superior, parameters that affects compressive strength values. An enhancement in hydration rate was reported by Wang et al. when limestone powder substitution rates lower than 15% were used. When this level was exceeded, and the amount of cement was further reduced, a decrease in compressive strength was observed [210]. Sezer reported that the dilution effect of limestone powder was more obvious when the amount

of limestone powder surpassed 35% [208]. Nevertheless, it was noticed in this study that the combined mixture with 25% limestone powder substitution (i.e. COM-LP25%-ACC0%) achieved a compressive strength above 50 MPa at 28 days which is still sufficient for common applications of 3D concrete printing.

### 4.3.2 Effect of accelerator dosages

A fast stiffening rate of the combined mixture is essential to provide a high construction rate. The stiffening process can be driven by using a highly reactive set accelerator, which is commonly used in shotcrete applications. Therefore, it is important to investigate the effect of the accelerator on hydration kinetics, as well as mechanical properties. Firstly, a flow table test was performed to investigate the fluidity of combined mixtures with different accelerator dosages (i.e. COM-LP25%-ACC0%, COM-LP25%-ACC3.5%, and COM-LP25%-ACC7%). With the increase of accelerator dosages, the flow diameter of combined mixtures decreased gradually. The average values of the flow diameter were 300 mm, 164.26 mm, and 130.60 mm for the accelerator addition level of 0%, 3.5%, and 7%, respectively.

To go one step further, the setting time of combined mixtures was measured by the penetration test. The penetration curves are shown in Figure 4.3. The combined mixture with an accelerator addition level of 7% (i.e. COM-LP25%-ACC7%) reached the initial setting (14.21 min) and final setting (35.33 min) fastest, while the reference mixture (i.e. COM-LP25%-ACC0%) took the maximum time (an initial setting time of 304.02 min and a final setting time of 427.35 min).

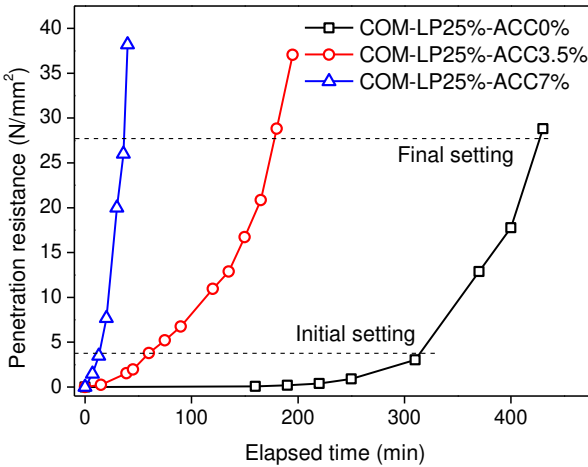


Figure 4.3 Penetration resistance with time for combined mixtures with different levels of accelerator addition (symbols represent individual measurements).

In addition, the rate of hydration was used to assess the stiffening process of combined mixtures. Figure 4.4 demonstrates the heat evolution curves of combined mixtures with different accelerator dosages measured by isothermal calorimetry. The first exothermic peak reached 18.36 J/gh in the reference mixture (i.e. CP-LP25%-ACC0%), while it reached 22.96 J/gh in the combined mixture with 7% accelerator addition (i.e. CP-LP25%-ACC7%). It was manifested that during the initial reaction period, with increasing dosage of accelerator, the heat release rate increased and the time to reach the first peak was decreased. The increased heat release rate and decreased time to arrive at the first peak were due to the promoted hydration of  $C_3A$ , forming ettringite (AFt) [47]. In addition, the aluminum sulfate in the accelerator also reacted with lime and produced AFt and aluminum hydroxide, which also acted as an accelerator [48]. The promoted hydration process of  $C_3A$  expedited the stiffening rate of the combined mixture and thus resulted in a decreased setting time and subsequent loss of fluidity. This result supports the measurements of the setting time and the flow diameters.

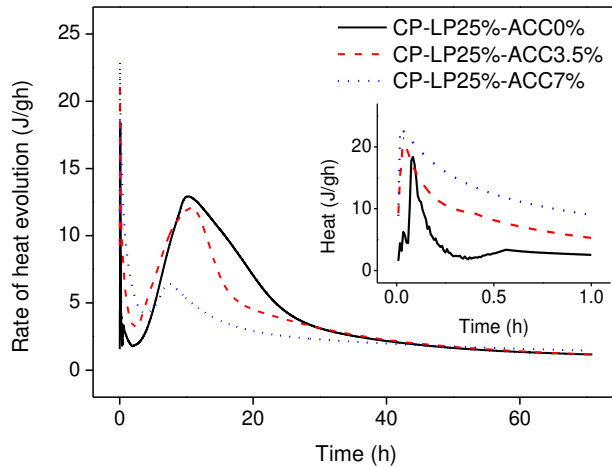


Figure 4.4 Heat flow curves of combined mixtures with different levels of accelerator addition.

The cumulative heat production during the first 72 hours is depicted in Figure 4.5. As the dosage of accelerator increased, total hydration heat increased in the first 10 hours of the hydration process and decreased after 10 hours. Such a phenomenon showed that the aluminum sulfate inhibited the hydration process of  $C_3S$ . The inhibited hydration process of  $C_3S$  can impair the quantity of C-S-H. Such effect was intensified for higher accelerator dosages [67]. The first reason for the decreased hydration of  $C_3S$  may be attributed to the increased quantity of calcium sulfoaluminate hydrate, which acted as a barrier on the surface of cement particles and hindered the transportation of ions and water [211]. Another reason

was the water binding ability of calcium sulfoaluminate hydrate, which would reduce the water content available for  $C_3S$  hydration. [212].

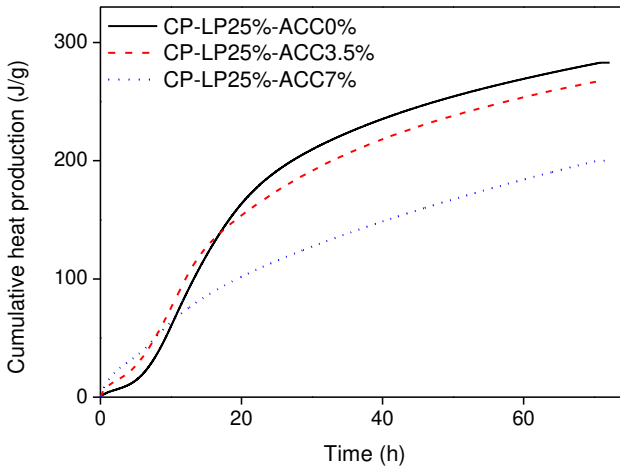


Figure 4.5 Energy released during the first 72 hours.

The compressive strength of the combined mixtures after curing for 1 day, 3 days, and 7 days were also obtained, as shown in Figure 4.6. It was observed that the addition of accelerator enhanced the concrete strength at the age of 1 day, but impaired that at later ages. The prompted early age strength was caused by the promoted hydration process of  $C_3A$ , with the formation of Aft. While the impaired later age strength was caused by the hindered hydration process of  $C_3S$ , with a reduced quantity of C-S-H. The later age strength was lowered by 21.35% for 3.5% accelerator addition and by 17.40% for 7% accelerator addition, which supports the statement that alkali-free accelerators have better later age strength than alkali accelerators (the alkali accelerators can lower concrete later age strength up to 50%) [103, 104].

Considering the practical applications of constructing rock tunnel linings, the ground temperature should be taken into consideration. For example, deep tunnel linings always pass through the high temperature environment areas with frequent geothermal activities [213]. In some extreme situations, the maximum temperature can reach more than 70 °C [214, 215]. As pointed out by Liu et al. [216], a lot of micropores were observed in shotcrete at a temperature of 60 °C. However, the printing test, which will be introduced in the following sections, was performed at room temperature. Further study focusing on the aspect of the influence of high temperature on the setting results, as well as the function of accelerator, is certainly useful.

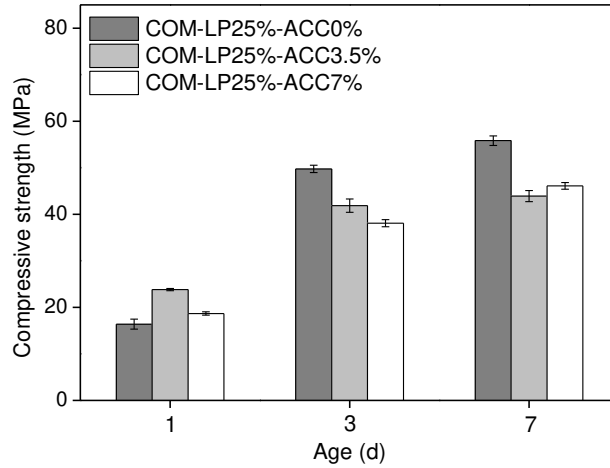


Figure 4.6 Compressive strength of mold cast samples with different accelerator dosages (error bar represents the standard error, n=3).

#### 4.4 Summaries

In this chapter, the twin-pipe pumping strategy is proposed. The limestone powder substitution rate and the accelerator dosage are determined. Based on the experimental results, the following summaries are given:

- (1) A high substitution rate of limestone powder compromises the mechanical properties because of the dilution effect. A substitution rate of 25% in the combined mixture is chosen to achieve a satisfying compressive strength which is higher than 50 MPa at the age of 28 days.
- (2) By introducing the accelerator in the static mixer, a fast strength gain can be obtained after extrusion. With a 7% addition of accelerator, the combined mixture reaches an initial setting within 15 minutes and a final setting within 35 minutes, which is essential for good shape stability and a high construction rate for hard rock tunnel linings.





## Phase transition from transportation to fabrication

### 5.1 Introduction

This chapter is a follow-up of Chapter 4. The combined mixture developed in Chapter 4 is divided into two separate mixtures including the PC-based mixture and the LP-based mixture. The fluidity and open time of the PC-based mixture, LP-based mixture, and the combined mixture is evaluated. The rheological behaviors of the PC-based mixture and the LP-based mixture are further investigated, for a better understanding of the pumping performance of these two flows. Afterwards, a twin-pipe pumping test is performed. The influence of the number of mixing baffles inside the static mixer on the pumping pressure and the mixing homogeneity of the printed elements is studied. Finally, a 3-meter high hollow column is printed to verify the buildability of the combined mixture extruded via the twin-pipe pumping system.

### 5.2 Experimental program

As concluded in Chapter 4, the limestone powder substitution rate of the combined mixture was fixed as 25% and the accelerator addition level of the combined mixture was fixed as 7%. To go one step further, for the determination of the PC-based mixture and LP-based mixture, the volume ratio  $V_{PC}:V_{LP}$  was fixed as 2, and the superplasticizer ratio  $m_{SP1}:m_{SP}$  was fixed as 2 as well. The sand ratio  $m_{S1}:m_S$  varied from 40% to 80% and the water ratio  $m_{W1}:m_W$  was determined accordingly. Therefore, a series of PC-based mixtures and LP-based mixtures were obtained, as shown in Table 5.1. Small batches were prepared following the mixing procedure described in Chapter 4.

In addition, big batches (70 liters for PC-based mixtures and 40 liters for LP-based mixtures) were prepared by a pan mixer for 3D printing experiments. Dry materials (sand, cement for PC-based mixture; sand, limestone powder, and viscosity modifying admixture for LP-based mixture) were mixed for 30 s. After contact with the dry materials with water (and superplasticizer), the paddle was rotated for 3 minutes. For LP-based mixtures, an accelerator was added in the last step and the paddle was mixed for 30 s.

Table 5.1 Mix design of PC-based mixtures and LP-based mixtures (kg/m<sup>3</sup>).

$m_{S1}:m_S$	Mixture	Sand	PC	LP	Water	SP	ACC	VMA
40%	PC-S40%	570.35	1069.41	0	449.88	5.70	0	0
	LP-S60%	1711.06	0	712.94	98.37	5.70	149.72	2.85
50%	PC-S50%	712.94	1069.41	0	396.67	5.70	0	0
	LP-S50%	1425.88	0	712.94	204.77	5.70	149.72	2.85
60%	PC-S60%	855.53	1069.41	0	343.47	5.70	0	0
	LP-S40%	1140.71	0	712.94	311.18	5.70	149.72	2.85
62%	PC-S62%	884.05	1069.41	0	332.83	5.70	0	0
	LP-S38%	1083.67	0	712.94	332.47	5.70	149.72	2.85
64%	PC-S64%	912.57	1069.41	0	322.19	5.70	0	0
	LP-S36%	1026.64	0	712.94	353.75	5.70	149.72	2.85
66%	PC-S66%	941.08	1069.41	0	311.54	5.70	0	0
	LP-S34%	969.60	0	712.94	375.03	5.70	149.72	2.85
68%	PC-S68%	969.60	1069.41	0	300.90	5.70	0	0
	LP-S32%	912.57	0	712.94	396.31	5.70	149.72	2.85
70%	PC-S70%	998.12	1069.41	0	290.26	5.70	0	0
	LP-S30%	855.53	0	712.94	417.59	5.70	149.72	2.85
80%	PC-S80%	1140.71	1069.41	0	237.06	5.70	0	0
	LP-S20%	570.35	0.	712.94	524.00	5.70	149.72	2.85

## 5.3 Results and discussion

### 5.3.1 Flow diameter

In terms of pumping issues, both the PC-based mixture and the LP-based mixture, are expected to have a high fluidity, which is beneficial to decrease the pumping pressure. The flow diameters of PC-based mixtures and LP-based mixtures measured by the flow table are shown in Figure 5.1. With the increase in the sand ratio  $m_{S1}:m_S$ , the sand to binder ratio increased and the water-to-binder ratio decreased in the PC-based mixture, leading to a decrease in flow diameter from 300 mm (the upper limit) to 100 mm (the lower limit). On the other hand, the increase in the sand ratio  $m_{S1}:m_S$  resulted in a decreased sand to binder ratio and increased water-to-binder ratio in the LP-based mixture. As a result, the flow diameter of LP-based mixtures increased from 100 mm to 300 mm. A cross point was observed in the case of a sand ratio  $m_{S1}:m_S$  between 64% and 66%, reflecting a similar fluidity.

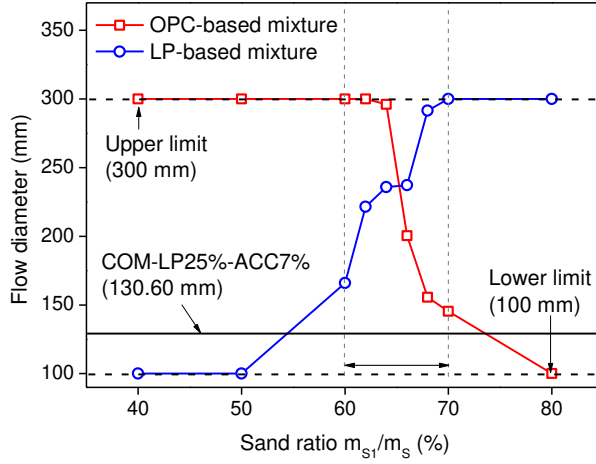


Figure 5.1 Flow diameters of PC-based mixtures and LP-based mixtures (symbols represent individual measurements).

The top view of flow diameters obtained for PC-based mixtures, LP-based mixtures, and combined mixtures are shown in Figure 5.2. It was observed that the flow diameter of the combined mixture (i.e. COM-LP25%-ACC7%) was much smaller than that of PC-based mixtures and LP-based mixtures, especially for the cases with sand ratios  $m_{s1}:m_s$  between 62% and 66%.

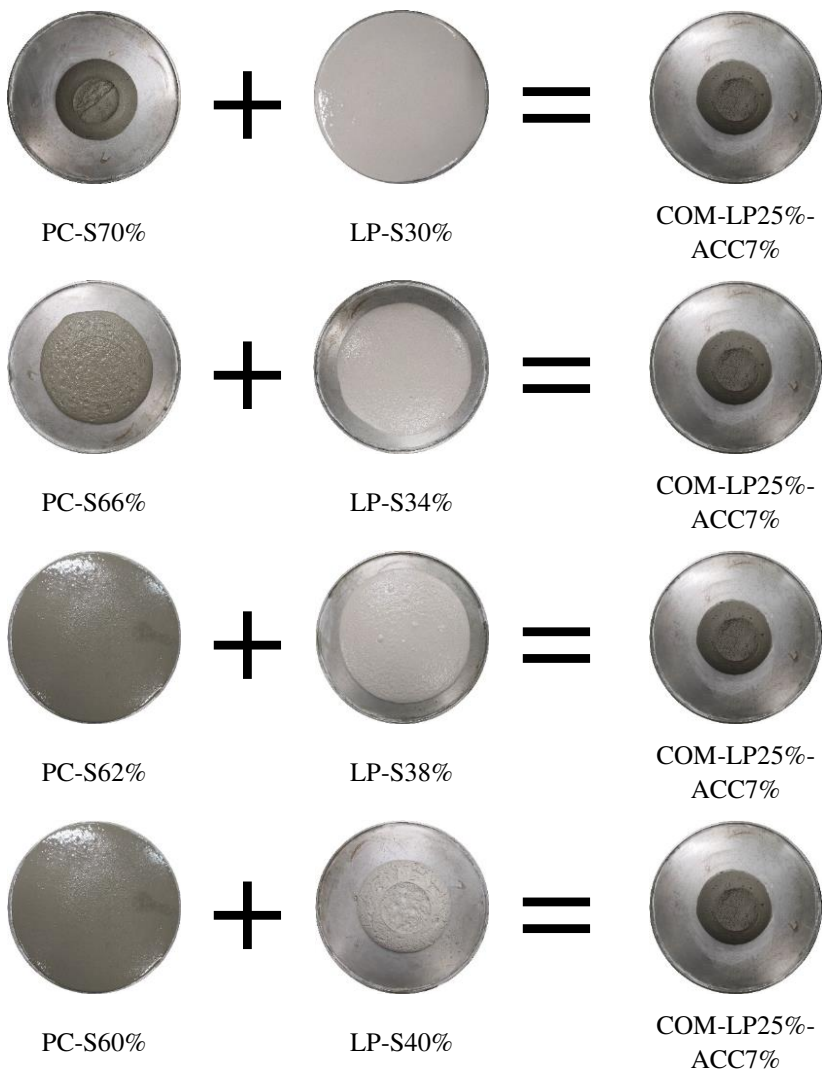


Figure 5.2 Flow diameters of PC-based mixtures, LP-based mixtures, and combined mixtures.

### 5.3.2 Rheological parameters

The results of the yield stress and viscosity measurements of PC-based mixtures and LP-based mixtures are shown in Figure 5.3 and Figure 5.4. It was shown that with the increase of the sand ratio  $m_{S1}:m_S$ , the yield stress and viscosity of PC-based mixtures increased, indicating a decreased fluidity, while the yield stress and viscosity of LP-based mixtures decreased, reflecting an increased fluidity. A

cross point was observed in the case of a sand ratio  $m_{s1}:m_s$  of 64%. The results were in consistence with the results of the flow diameter measurements.

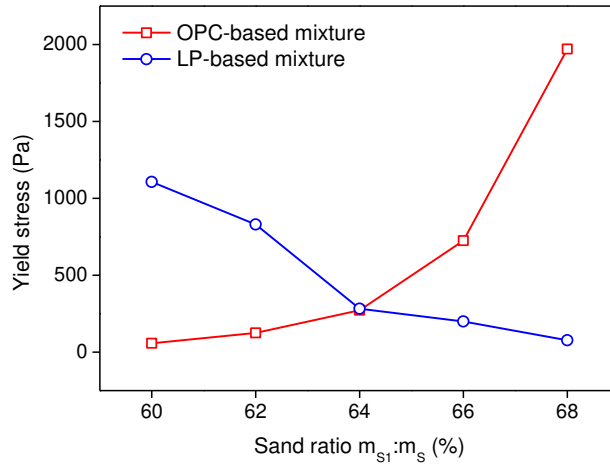


Figure 5.3 Yield stress of PC-based mixtures and LP-based mixtures (symbols represent individual measurements).

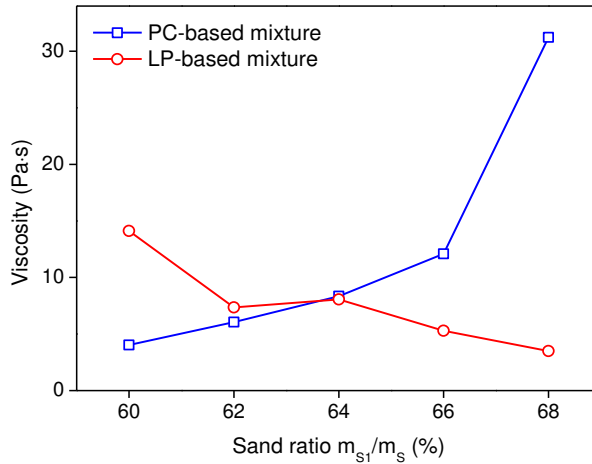


Figure 5.4 Viscosity of PC-based mixtures and LP-based mixtures (symbols represent individual measurements).

### 5.3.3 Open time

A long open time of PC-based mixtures and LP-based mixtures is beneficial for resuming pumping operations if a short interruption is experienced such as the delay of material feeding. The setting time measured by the penetration test is presented in Table 5.2.

Table 5.2 Initial and final setting times (min).

Mixture	Initial setting	Final setting
COM-LP25%-ACC7%	14.2	35.3
PC-S60%	290.6	361.0
PC-S62%	278.6	345.4
PC-S64%	265.1	334.9
PC-S66%	249.2	327.2
LP-based mixtures	> 600	> 600

As mentioned before, the combined mixture COM-LP25%-ACC7% showed an initial setting time of 14.2 min and a final setting time of 35.3 min. With such a fast stiffening rate, the combined mixture is not suitable to be transported in a long pipe, where blockage would easily happen. Different from the combined mixture, PC-based mixtures showed a much longer open time. With sand ratios varying from 60% to 66%, the initial setting time ranged from 249.2 min to 290.6 min and the final setting time ranged from 327.2 min to 361.0 min. Within 10 hours after mixing, no initial set was observed for LP-based mixtures because no hydration process existed in the LP-based mixtures.

The results can be interpreted as shown in Figure 5.5. By incorporating accelerator and viscosity modifying admixture in the flow of the LP-based mixture, the PC-based mixture was exempted from the effect of accelerator and viscosity modifying admixture. On the other side, the main component of limestone powder was calcium carbonate, and treated as an inert filler. Therefore, the accelerator, with the main component being aluminum sulfate, would not react with limestone powder and had little effect on the fluidity of LP-based mixtures. In terms of viscosity modifying admixture, the main function of viscosity modifying admixture in the LP-based mixture was to increase the apparent viscosity of the aqueous solution. While the phenomenon of bridging flocculation between limestone powder particles is much less than that between cement particles [49].

After merging inside the static mixer, the PC-based mixture and LP-based mixture are thoroughly blended and extruded. Accelerator and viscosity modifying admixture in the LP-based mixture have an immediate effect on the cement particles in the PC-based mixture. A decreased setting time and loss of fluidity are observed because of the formation of hydration products, as explained in previous sections. In addition, viscosity modifying admixture would absorb onto cement particles and physically hold them together, leading to a stronger inner structure.

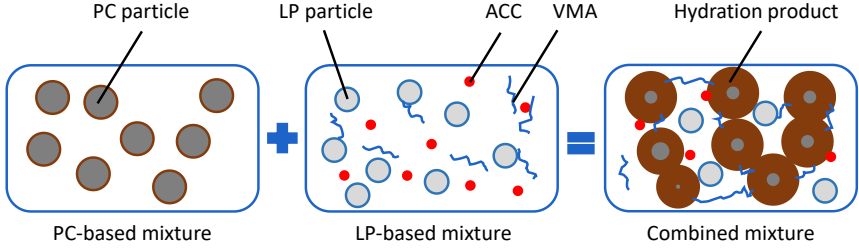


Figure 5.5 Schematic view of the mechanism in twin-pipe pumping.

### 5.3.4 Mixing homogeneity

In addition, to evaluate the mixing homogeneity of printed objects made with different mixing baffles, as indicated in Table 3.15, three cross-sections were obtained from each straight element (at both ends and the middle position), as described in Table 3.16, and the portion of the cross-section (40 mm × 30 mm, without the edges) was observed. A sand ratio  $m_{S1}:m_S$  of 64% was used for preparing the printed elements, as well as for the experiments introduced in following sections. One of the three cross-sections is shown in Figure 5.6.

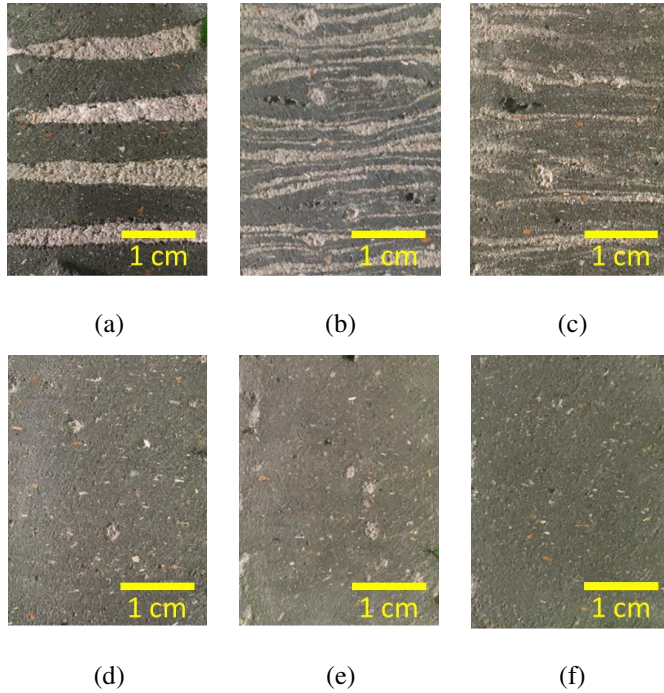


Figure 5.6 Cross-sections of hardened samples obtained by the use of a static mixer with (a) 0 baffles, (b) 6 baffles, (c) 12 baffles, (d) 18 baffles, (e) 24 baffles, and (f) 30 baffles.

Compared to the PC-based mixture or combined mixture (dark gray), the color of the LP-based mixture is relatively light. To analyze the mixing homogeneity, the original figures were transferred to a binary type. Given a threshold value of 150, the LP-based mixture was colored white and the rest was colored black, as shown in Figure 5.7.

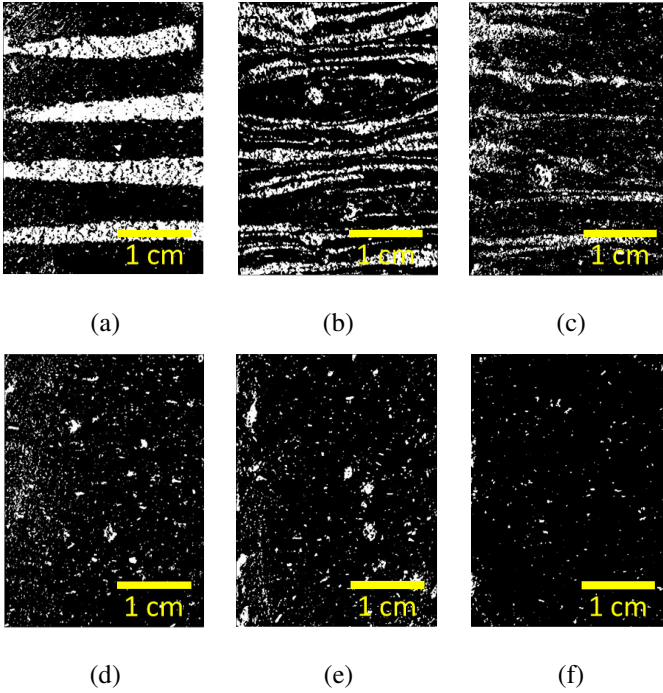


Figure 5.7 Binary images of the cross-sections of hardened samples obtained by the use of a static mixer with (a) 0 baffles, (b) 6 baffles, (c) 12 baffles, (d) 18 baffles, (e) 24 baffles, and (f) 30 baffles.

It was obvious that some striations were present at the cross-sections. The formation of these striations was related to the patterns of the static mixer. Helical mixing baffles can simultaneously produce patterns of flow division and radial mixing. Flow division refers especially to the laminar flow where materials are divided into two channels at the first mixing element and further divided at each subsequent element, leading to an exponential increase in stratification. On the other hand, radial mixing happens in either a turbulent flow or a laminar flow, which is caused by the rotational circulation of the processed flow around the hydraulic center [118].

For the cement-based materials which are treated as Bingham fluids, the Reynolds number (-) is calculated as follows [217]:



$$Re = \frac{8\rho v^2}{\tau_0 + \mu\left(\frac{8v}{D}\right)} \quad (5.1)$$

Where  $\rho$  is the density of freshly printed material, which is usually around 2500 kg/m<sup>3</sup>. An average velocity  $v$  of 0.25 m/s and a diameter  $D$  of 0.032 m was selected. Choosing a yield stress  $\tau_0$  of 300 Pa and a plastic viscosity  $\mu$  of 10 Pa·s, leads to a Reynolds number of 1.35. The Reynolds number expresses the ratio of inertial forces to viscous forces, which can be used to determine whether a flow is laminar or turbulent. For low values of the Reynolds number, the flow is laminar, while high values denote turbulent flow. A critical Reynolds number (around 2100 to 4000) is used to distinguish laminar and turbulent flow [218]. In this study, the calculated Reynolds number is considerably lower than the critical value. As such, the pattern of the mixture can be treated as a pattern for a laminar mix, which is schematically shown in Figure 5.8.

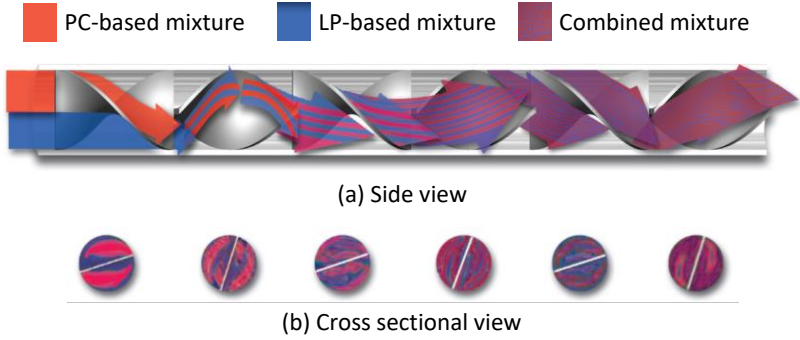


Figure 5.8 Schematic view of the striations with a division pattern, taken from [219].

It is essential to quantify the mixing homogeneity. More than 50 parameters were tabulated by Grosz-Roll [220] to evaluate the homogeneity. However, these parameters are not always clearly defined. In this study, the percentage of white in Figure 5.7 was adopted to evaluate the mixing homogeneity. A high percentage of white represented that much LP-based mixture was not mixed into the PC-based mixture, indicating a bad mixing homogeneity. The percentage of white in function of the number of mixing elements is shown in Figure 5.9.

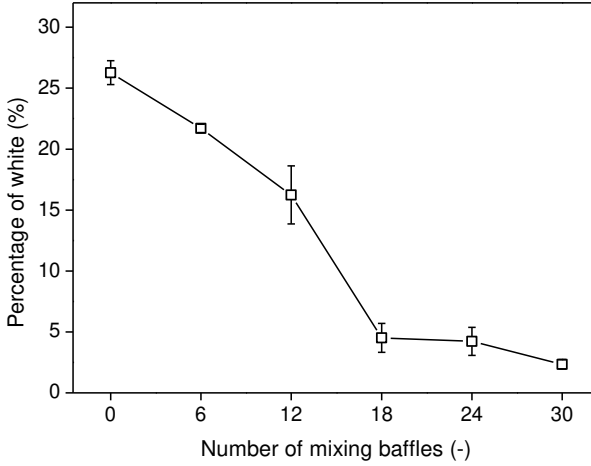


Figure 5.9 Percentage of white in function of the number of mixing baffles (error bars represent the standard error,  $n=3$ ).

It was obvious that with the increase of the number of mixing baffles, the percentage of white decreased gradually. The percentage was less than 5% when the number of mixing baffles amounted to 18, while 30 mixing baffles led to the best mixing homogeneity with a white percentage of around 2%. Indeed, a higher mixing homogeneity can be expected with more mixing baffles. Unfortunately, when we further increased the number of mixing baffles to 36, the pumping pressure became too high to pump the mixture using the current setup (pressure limit 40 bar), which will be explained in the coming section.

### 5.3.5 Pumping pressure

The pumping pressure measured by the pressure sensors of the SP11 pump (for the PC-based mixture) and the STROBOT 407 pump (for the LP-based mixture) was monitored. The pumping pressure in function of the number of mixing baffles of the static mixer is shown in Figure 5.10.

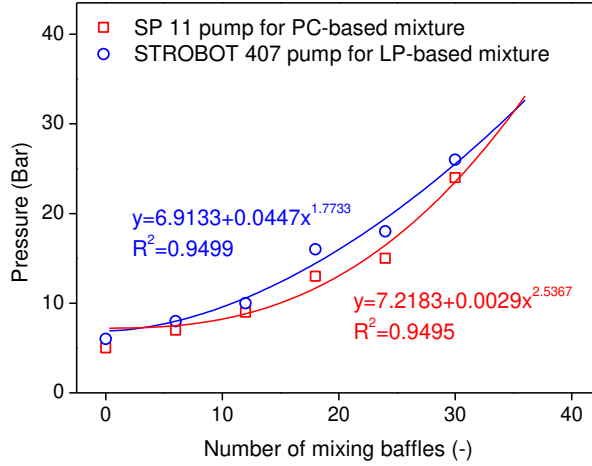


Figure 5.10 Pumping pressure in function of the number of mixing baffles.

It was shown that with the increase in the number of mixing baffles, the pumping pressure increased from around 5 bar (with 0 baffles) to around 26 bar (with 30 baffles) for each pump. It was pointed that the pressure loss caused by a static mixer is 5 or 6 times larger than that in a round pipe because of the presence of the mixing baffles [118]. In addition, as the PC-based mixture and LP-based mixture moved through the static mixer, a fast stiffening process and a prompt stage transition from a liquid form to a solid form further increased the pumping pressure.

In summary, more mixing baffles in the static mixer improved the homogeneity and accordingly enhanced the mechanical performance. However, adopting more mixing baffles led to a higher pumping pressure [221]. According to the results, a static mixer with 18 mixing baffles presented a good mixing homogeneity (the percentage of white is less than 5%) and an acceptable pumping pressure (16 bar for each pump).

Nevertheless, achieving a high mixing homogeneity remains a bottleneck regarding the inline mixing system for 3D concrete printing. Apart from the influence of material properties and process parameters, the baffles on the inner wall also play an important role in a dynamic mixer. Lu et al. [222] pointed that the insertion of the appropriate number of baffles improves the extent of flow mixing while excessive baffles would interrupt the flow mixing and decrease mixing efficiency. As for the static mixer, the mixing homogeneity can be improved by increasing the number of baffles but this also increases the pumping pressure [118]. In addition, previous researches on Newtonian fluids have pointed out that a high mixing homogeneity is expected if the viscosity difference is not too high [118, 127]. However, in the case of Bingham fluids (e.g. concrete suspensions), the effect of yield stress difference between the two fluids may also

influence the mixing homogeneity and further research may be required in this regard.

### 5.3.6 Buildability verification

The feasibility of the twin-pipe pumping process was verified by printing a 3 meters high column, as shown in Figure 5.11. A sand ratio  $m_{s1}:m_s$  of 64% was used for the column printing. The column printing was finished in 9 minutes with an average vertical construction rate of 0.34 meters per minute. It should be mentioned that 3 meters high is the limitation of the robot rather than the material. It is believed that the twin-pipe pumping strategy has even potential for a higher construction height and a faster construction rate.

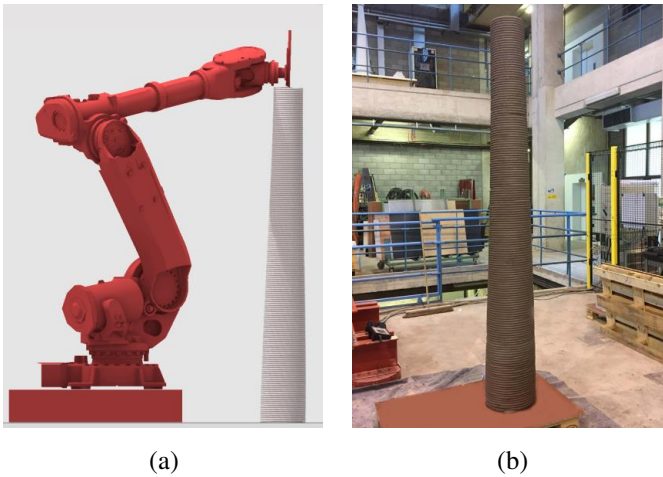


Figure 5.11 3D concrete printing of a 3 meters high column, (a) column design, and (b) the column that was just printed.

## 5.4 Summaries

In this chapter, the phase transition from two separate flows in the context of twin-pipe pumping is presented. Based on the results and discussion, the following summaries are given:

(1) Limestone powder is suitable to be used as a carrier material for powdery admixtures including an accelerator and a viscosity modifying admixture. In this way, two separate flows including a Portland cement-based mixture and a limestone powder-based mixture are pumped into the static mixer. By regulating sand and water proportions, both flows (e.g. PC-64% and LP-36%) can achieve a high fluidity (flow diameter  $> 235$  mm) and a long open time (initial setting time  $> 265$  min, final setting time  $> 334$  min for the PC-64% mixture, and indefinite setting time for the LP-36% mixture), which is beneficial for the pumping process.

(2) The static mixer is proven to be useful for mixing two separate fresh granular paste materials with a flow division pattern. A high number of mixing baffles is beneficial to achieve a good homogeneity, however, leads to a high pumping pressure (26 bar for 30 mixing baffles) in the meantime. Based on the results, a static mixer with 18 mixing baffles presents a good mixing homogeneity (the percentage of white is less than 5%) and an acceptable pumping pressure (16 bar).

(3) A column with a height of 3 meters is printed in 9 minutes (with an average vertical construction rate of 0.34 meters per minute). This indicates that the twin-pipe pumping strategy has a high potential to solve the first challenge (stiffening control) and avoid the shear failure of printed tunnel linings.



## Mechanical and microstructural properties in twin-pipe pumping

### 6.1 Introduction

3D printed structures consist of multiple layers and should exhibit a strong mechanical behavior for guaranteed structural performance. Compared to extrusion-based 3D concrete printing, spray-based printed samples present excellent mechanical performance which is mainly attributed to the enhanced interlocking of the layer interface with a high spraying speed [11]. The mechanical properties of extrusion-based 3D printed elements are more related to the printing parameters (in particular, the time gap and printing speed) and the loading directions [133, 223]. Due to the lack of mechanical integrity at the layer interfaces, extrusion-based 3D printed concrete has also been reported to show anisotropic behavior, particularly in flexural loading [132, 168]. Concerning the twin-pipe pumping system, despite the significant advantages and opportunities introduced in previous chapters, its use can also result in some negative effects. For instance, the high dosage of accelerator used in the twin-pipe pumping system may adversely influence later-age mechanical behavior. Further, the inline mixing process introduces striation patterns in the 3D printed elements, which may affect the mechanical behavior. As a follow-up to Chapter 5, a detailed mechanical and microstructural investigation of 3D printed elements fabricated using the twin-pipe pumping system is presented in this chapter. To investigate the mechanical behavior, samples are cut out from different locations in the printed elements and subjected to compressive, flexural, and tensile bond strength tests. Microstructural investigations are carried out using mercury intrusion porosimetry (MIP) and scanning electron microscopy (SEM) in combination with image analysis.

### 6.2 Experimental program

In this chapter, we only take the PC-S64% mixture and LP-S36% mixture for further exploration, which has been tested in Chapter 5. The protocol of 3D concrete printing remained the same as that in Chapter 5. The terms PC-based mixture, LP-based mixture, and combined mixture in this chapter specifically refer to mixture PC-S64%, mixture LP-S36%, and mixture COM-LP25%-ACC7%,

respectively. To make reading more convenient, the mixture compositions of these three mixtures are listed in Table 6.1.

Table 6.1 Mixture compositions of the PC-based mixture, the LP-based mixture, and the combined mixture (kg/m<sup>3</sup>).

Mixture	Sand	PC	LP	Water	SP	VMA	ACC
PC-based	969.60	1069.41	0	300.90	5.70	0	0
LP-based	912.57	0	712.94	396.31	5.70	2.85	149.72
Combined	950.59	712.94	237.65	332.71	5.70	0.95	49.91

The samples were prepared by two different procedures including 3D concrete printing and mold casting. For 3D printing experiments, 40 liters of the PC-based mixture and 20 liters of the LP-based mixture were prepared by a pan mixer in the following sequence: (1) manually mixing superplasticizer with water for 10 s, (2) mixing dry materials (sand and Portland cement for the PC-based mixture; sand and limestone powder for the LP-based mixture) for 30 s, (3) adding water with superplasticizer to dry materials and mixing for 3 min, (4) scrapping and resting for 2 min, (5) adding CE5 (MPT60000YP4) and ACC1 (shotcrete accelerator) for the LP-based mixture and mixing for 30 s. The total mixing time in the pan mixer for the PC-based mixture and LP-based mixture was 340 s and 370 s, respectively. Subsequently, both mixtures (i.e. the PC-based mixture and LP-based mixture) were combined and mixed in the static mixer during the extrusion process.

The mold cast samples, consisting of the combined mixture, were prepared in a conventional planetary mixer according to the following steps: (1) manually mixing superplasticizer with water for 10 s, (2) mixing Portland cement and limestone powder at 140 rpm for 10s, (3) adding water with superplasticizer to the pre-mixed dry powders and rotating the paddle at 140 rpm for 30 s, (4) adding sand and rotating the paddle at 140 rpm for 30 s, (5) rotating the paddle at 285 rpm for 30 s, (6) scraping and resting for 90 s, (7) adding CE5 (MPT60000YP4) and mixing the paddle at 285 rpm for 60 s, (8) adding ACC1 (shotcrete accelerator) and mixing at 285 rpm for 30 s. The total mixing time was 290 s for the mold cast samples.

### 6.3 Results and discussion

#### 6.3.1 Compressive strength

The influence of layer orientation on the compressive strength at the age of 3, 7, and 28 days is shown in Figure 6.1. Results indicated no directional dependency for the compressive strength of 3D printed samples. This is in line with the findings of other researches [132, 133, 224]. In addition, it can be seen that the compressive strength of the mold cast samples was considerably higher than that of the 3D



printed samples, especially at the age of 3 and 7 days. The reduction in compressive strength of C-1 samples was 55, 40, and 13% compared to that of mold cast samples, at the age of 3, 7, and 28 days, respectively. It should be noted that the dosage of accelerator was kept the same as 7% by the mass of binder for both the printed samples and the mold cast samples.

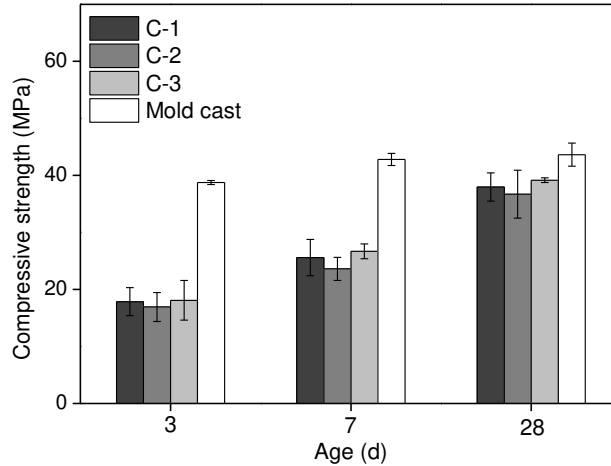


Figure 6.1 Influence of the layer orientation on compressive strength (error bars represent the standard error,  $n=6$ ).

The failure patterns and fracture planes of samples in the compression test are shown in Figure 6.2. The fracture development of C-1 and C-2 samples was approximately parallel to the loading direction while the fractures of C-3 samples showed a typical cone type failure, which was similar to the failure pattern of mold cast samples. By observing the fracture surface after compression, two distinct colors, including a dark grey color and a light grey color were observed. From previous experimental results, the PC-based mixture presented a dark grey color while the LP-based mixture presented a relatively light grey color. The fracture plane of C-1 and C-2 samples showed a light grey color over most of the area, indicating that fracture propagated inside the striation of the LP-based mixture. Different from C-1 and C-2 samples, the fracture surface of C-3 samples presented numerous dark grey and light grey striations, which were oriented parallel to the interface of adjacent layers. Compared to the fracture surface of mold cast samples with mono color, striations with color difference existed in the 3D printed samples indicating a lack of mixing homogeneity. However, as seen from Figure 6.1, no significant difference among the compressive strength of 3D printed samples under different loading directions (i.e. C-1, C-2, and C-3) was observed which indicated that the orientation and distribution of such striations in 3D printed samples had no significant influence on the compressive strength. Previously, orientation-depended failure patterns of 3D printed samples were reported by Ma et al. [225]. It was pointed that the fracture lines of C-1 and C-2 samples, where

the deposited layers were parallel to the loading direction, were derived from the layered structures. For the samples printed by the twin-pipe pumping system, another weak chain might appear inside the bulk of one layer, i.e. at the striations of LP-based mixture, rather than at the interface between the adjacent layers with a very short time gap between two adjacent layers (2 seconds only).

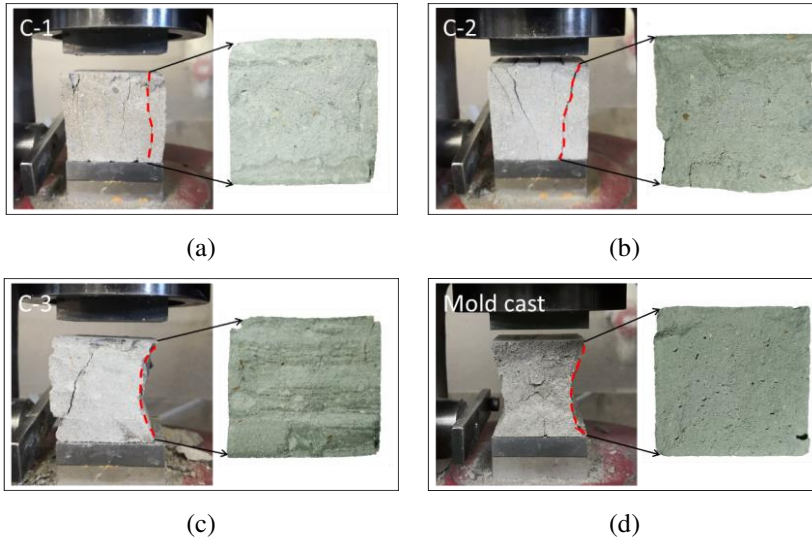


Figure 6.2 Failure patterns and fracture planes of samples in the compression test: (a) C-1, (b) C-2, (c) C-3, and (d) mold cast samples.

### 6.3.2 Flexural strength

The influence of the layer orientation on the flexural strength at the age of 3, 7, and 28 days is shown in Figure 6.3. Results showed that the flexural strength of D-1 samples was lower than that of D-2 and D-3 samples. The average value of the flexural strength corresponding to D-1 samples was 25 and 23 % lower, respectively than that of the D-2 sample and D-3 sample at the age of 28 days. In addition, the flexural strength of mold cast samples was modestly higher than the value measured for D-2 and D-3 samples. In other studies, Panda et al. [134], Ma et al. [225], and Rahul et al. [168] indicated that the flexural strength of mold cast samples was higher than the values noted for 3D printed samples loaded in the D-1 direction but lower than the values noted in the case of D-2 and D-3 directions. They held the opinion that the tensile stress at the bottom of the samples under the D-1 loading direction was perpendicular to the weak interface with higher porosity and fracture, where the failure was prone to initiate, resulting in lower flexural capacity. On the other hand, the maximum tensile stress occurred in the bulk concrete for samples under D-2 and D-3 loading directions which were more densified from the pressure exerted during the extrusion process and had a lower porosity compared to the mold cast samples. Interestingly, in the current study, no

increase in the flexural strength could be observed even when loaded along the D-2 and D-3 direction where the bulk concrete is subjected to the maximum flexural stress. This again indicated the likely formation of weak zones in the bulk concrete from the incomplete mixing homogeneity.

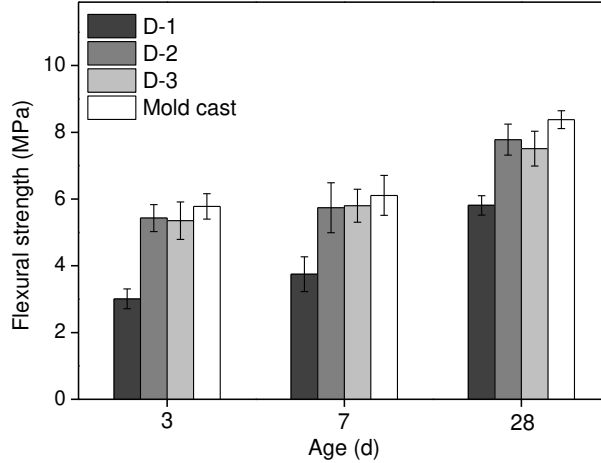


Figure 6.3 Influence of layer orientation on flexural strength (error bars represent the standard error,  $n=3$ ).

The failure patterns and fracture planes of 3D printed samples and mold cast samples under a flexural condition are shown in Figure 6.4. Similar to the fracture surface of C-1 samples loaded under compression, the fracture surface of D-1 samples presented a light grey color for the largest part. However, for D-2 samples and D-3 samples, the fracture surfaces showed evident striations with different grey colors, where the fracture surface was perpendicular to the interface between two printed layers. Different from 3D printed samples, the fracture surface of mold cast samples under a flexural condition showed a uniform distribution of components. The failure mode of 3D printed samples exposed to flexural loading was also reported by Wolfs et al. [133]. They pointed out that for 3D printed samples with small interlayer time gaps, the crack initiated at the lower surface and propagated randomly through the sample during flexural loading while a more distinct vertical crack appeared in the case of samples with a higher interlayer time gap. In the current study, 3D printed elements were prepared with a very short interlayer time gap (around 2 seconds only) due to the very high printing speed used in the twin-pipe pumping system. Despite this, a clear vertical crack can be seen in the case of all loading directions for the flexural strength tests in the current study. This indicated that well-defined fracture planes were created possibly along the weak zones of the LP-based mixture caused by the incomplete mixing homogeneity. Further, as seen from Figure 6.3, unlike the compressive strength tests, a clear anisotropic behavior can be seen in the flexural strength tests. This has also been observed by other researchers for conventional 3D printed samples

[132, 168]. This is because, in the case of the D-1 loading direction, the interlayer, as well as the striations existed perpendicular to the loading direction. As a result, vertical cracks split open more easily under the lateral bending stress developed during the flexural tests. Subsequently, flexural strength along D-1 was significantly lower than that obtained along D-2 and D-3.

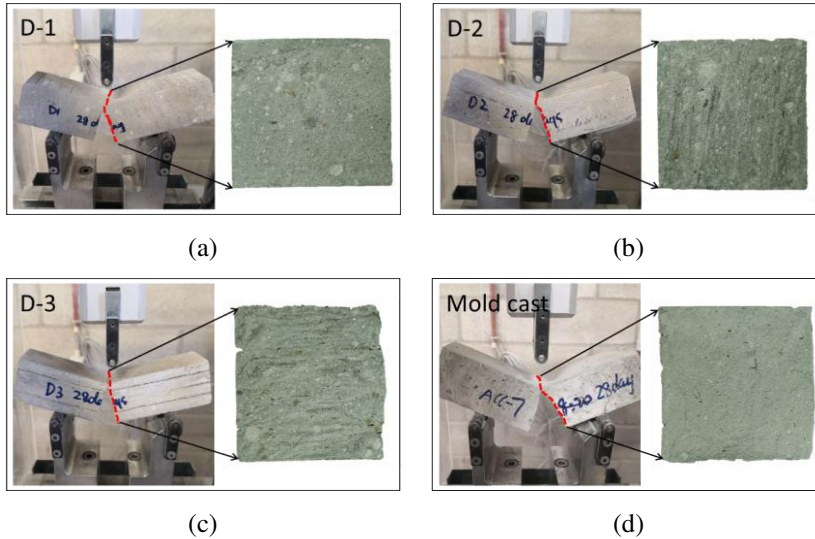


Figure 6.4 Failure patterns and fracture planes of samples in the flexural test: (a) D-1, (b) D-2, (c) D-3, and (d) mold cast samples.

### 6.3.3 Tensile bond strength

A strong interlayer bond is essential to achieve a monolithic performance for 3D printable concrete. Anisotropic behavior of 3D printed samples has already been observed in other studies, which can be partially attributed to the poor interlayer bond [132, 223]. In this study, the tensile bond strength of 3D printed samples and mold cast samples at the age of 3, 7, and 28 days was measured by a pull-off test, as shown in Figure 6.5. Results showed that the average value of the tensile bond strength of 3D printed samples was 2.23 MPa while mold cast samples reached a value of 2.73 MPa at the age of 28 days, which is 22% higher. Nematollahi et al. [226] investigated the effect of introducing polypropylene fibers into geopolymers and observed the interlayer bond strength to be in the range of 1.70 MPa to 3.10 MPa after curing for 1 day. In addition, Panda et al. [135] pointed out that the bond strength at the age of 28 days was 1.44 MPa for an interlayer time gap of 1 min. A similar conclusion was drawn by Van Der Putten et al. [227] namely that the bond strength at the age of 28 days was around 2.18 MPa with a negligible time gap in between the printing of two subsequent layers. In addition, Van Der Putten et al. [227] also mentioned a reduction of more than 50% of the bond strength of 3D printed samples, compared to that of mold cast samples. In this

study, although the tensile bond strength of 3D printed samples was relatively lower than that of mold cast samples, a strength reduction of only 22%, compared to 50% in the study of Van Der Putten et al., was observed.

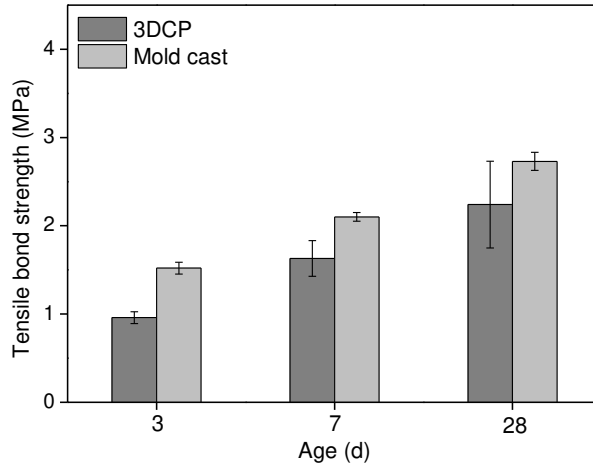


Figure 6.5 Tensile bond strength results (error bars represent the standard error,  $n=5$ ).

The failure patterns and fracture planes of 3D printed samples under a tension state are shown in Figure 6.6. Most of the fracture surfaces of 3D printed samples occurred inside the layer, rather than at the interlayer position, indicating that the interlayer was not the most vulnerable failure position for the 3D printed samples in this study. Le et al. [132] studied the failure patterns of samples under a tension state where the fracture occurred inside the bulk area of layers printed with a time gap of less than 15 min, indicating that the bond strength was larger than the tensile capacity of the printed material itself. However, an interlayer time gap of 30 min or more led to a failure occurring at the interface between two printed layers. Other studies also pointed out that the interface between two printed layers was the weak point due to insufficient interlocking when a higher interlayer time gap was used [132, 137]. In this study, most parts of the fracture surfaces occurred in the bulk area of one printed layer with a light grey color, which was identified to be the LP-based mixture. As a result, 3D printed samples represented a lower tensile bond strength, compared to the mold cast samples due to the relatively low strength of the unmixed LP-based mixture. On the other hand, all the fracture surfaces occurred near dollies for the mold cast samples, which can be explained by the high-stress concentration at the near-to-dolly area. In structural design, tensile stress that is perpendicular to the interface of printed layers is seldom. In contrast, shear stress frequently occurs such as for a composite slab in a bending state [228]. Normally, the tensile bond strength is determined by the transverse anchorage in air voids and pores, while the shear bond strength relates to the surface roughness. For different situations, varying test methods have been developed including shear

tests, torsion tests, and tension tests [176]. In this study, the pull-off test was useful to observe the weakest point in the chain being the light grey striation of the LP-based mixture in the case of 3D printed samples.

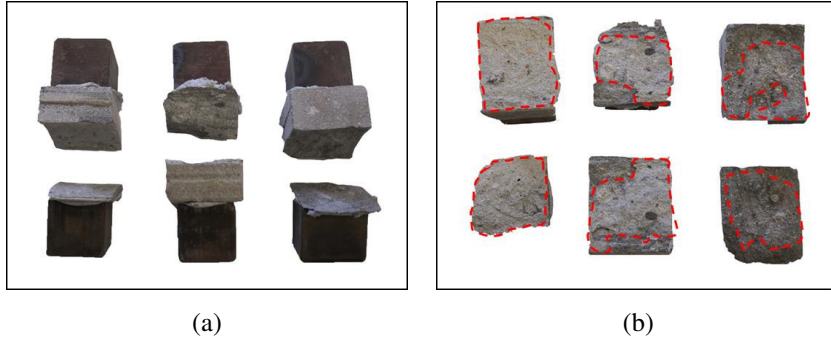


Figure 6.6 Failure patterns and fracture planes of 3D printed samples in the pull-off test: (a) side view and (b) red area indicates the light grey zone.

### 6.3.4 Porosity and microstructure morphology

From the observations discussed in the previous sections, mixing homogeneity has been pointed out as one of the most important aspects of 3D printed samples made using the twin-pipe pumping technology. Two distinguishing colors, a dark grey and a light grey color were observed on the fracture surface of 3D printed samples. The formation of the striations in the 3D printed samples was related to the flow division pattern of the helical static mixer. When the two flows, the PC-based mixture and LP-based mixture, went through the helical static mixer, the mixing baffles inside the helical static mixer continuously divided the flow into two channels and the striation numbers would grow exponentially. To better understand the microstructure of such striations, porosity and microstructure morphology were studied by using MIP and SEM as detailed in the subsequent sections.

#### 6.3.4.1 MIP measurements

Pore size distribution curves and cumulative intruded volume curves of samples at the age of 28 days measured by MIP are shown in Figure 6.7 and Figure 6.8, respectively. All three groups of samples (i.e. 3DCP\_Bulk, 3DCP\_Interface, and mold cast samples) followed a distinct unimodal pore size distribution. The critical pore size, the mean distribution radius, and total porosity by mercury intrusion, as well as their respective standard deviation, were derived from the pore size distribution curves and cumulative pore volume curves, as shown in Table 6.2. The critical pore size corresponded to the peak in the differential pore volume curves while the mean distribution radius corresponded to the pore size at 50 % volume intrusion of mercury. From Table 6.2, it can be seen that the total porosity

showed no obvious difference between the bulk area of the printed layer (3DCP\_Bulk) and the interface area between two adjacent layers (3DCP\_Interface). Interestingly, the total porosity values for the 3D printed samples were found to be lower than that for the mold cast samples. The reason for this can be better visualized through the cumulative pore size distribution curve shown in Figure 6.7. It can be seen that the mold cast sample has a much higher volume of finer pores (less than 50 nm) while the printed samples showed a higher amount of macropores. Previous studies have indicated that the creation of fine micropores in cementitious systems can be linked to the formation of hydration products such as the C-S-H gel [229-231]. For instance, Das and Kondraivendhan [230] examined the mean distribution radius for cementitious systems at different curing ages. They observed that with an increasing curing age, the mean distribution radius decreased due to the increase in the volume of the finer micropores. Similarly, Wild et al. [231] suggested that the formation of C-S-H in the cementitious system caused a pore-blocking effect which, in turn, resulted in a finer pore size distribution. Therefore, it can be inferred that even though the total porosity was higher for the mold cast compared to the 3D printed samples, as revealed from the cumulative pore size distribution curve, the higher total porosity arose from its relatively higher volume of micropores and may possibly indicate a higher amount of C-S-H gel formation.

Another important aspect to be considered is the relationship between the MIP parameters and strength values obtained for the 3D printed and mold cast samples. Apart from the total porosity, studies have shown that various other parameters derived from the pore size distribution curve can also strongly influence the compressive strength [230, 232, 233]. For instance, Das and Kondraivendhan [230] suggested an empirical relationship in which the compressive strength is proportional to  $(1-P_t)$ , where  $P_t$  indicates the total porosity and is inversely proportional to  $\sqrt{r_{0.5}}$ , where  $r_{0.5}$  is the mean distribution radius. From Table 6.2, it can be observed, even though the total porosity is marginally lower for the printed samples, they have a significantly higher  $r_{0.5}$  value due to their relatively coarser pore size distribution. Therefore, the lower strength values obtained for the 3D printed samples can be attributed to their coarser pore size distribution arising from the relatively higher amount of macropores in the 3D printed samples as compared to the mold cast samples.

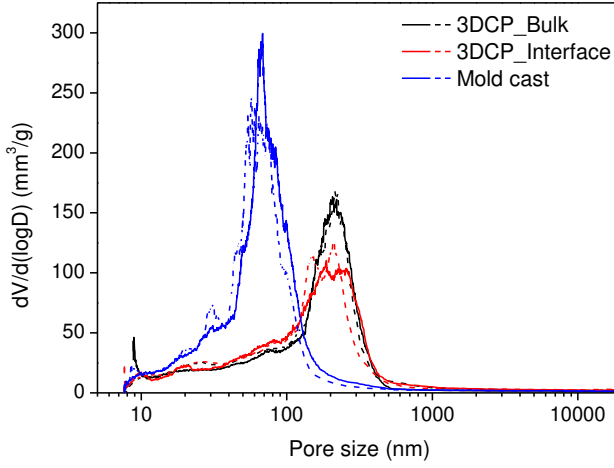


Figure 6.7 Pore size distribution of samples at the age of 28 days, measurements for each series were repeated twice (solid and dashed lines).

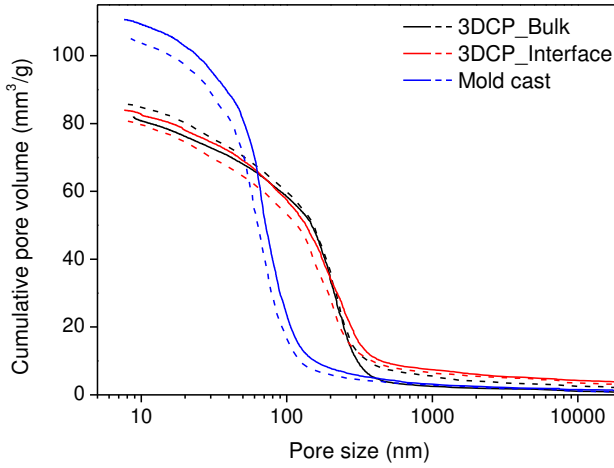


Figure 6.8 Cumulative pore volume of samples at the age of 28 days, measurements for each series were repeated twice (solid and dashed lines).

Table 6.2 Characteristics of the pore structure from mercury intrusion porosimetry.

Sample	Critical pore size (nm)	Mean distribution radius (nm)	Porosity (%)
3DCP_Bulk	$209.99 \pm 5.71$	$177.62 \pm 2.49$	$15.83 \pm 0.42$
3DCP_Interface	$197.48 \pm 14.75$	$160.25 \pm 13.26$	$16.30 \pm 0.42$
Mold cast	$62.70 \pm 7.76$	$65.16 \pm 4.59$	$19.75 \pm 0.64$



#### **6.3.4.2 SEM images**

Secondary electron (SE) images of 3D printed samples and mold cast samples were taken, as shown in Figure 6.9. From Figure 6.9 (a), an obvious contact zone was observed. Above the contact zone, irregularly shaped C-S-H gel was observed in the area of the PC-based mixture. A lot of un-hydrated particles can be seen below the contact zone, which were the particles of limestone powder from the LP-based mixture. At the contact zone between the PC-based mixture and LP-based mixture, growth of ettringite needles can be observed. After the contact between the PC-based mixture and LP-based mixture, the aluminum sulfate in the LP-based mixture soon promoted hydration of tricalcium aluminate ( $C_3A$ ) leading to ettringite formation at the contact zone between the two striations. In addition, the aluminum sulfate contained in the LP-based mixture can also react with lime from the PC-based mixture, forming ettringite and aluminum hydroxide, subsequently.

Two images taken from the LP-based mixture are shown in Figure 6.9 (b). Some unshaped C-S-H was found, as well as some ettringite needles can be observed in the pores. Theoretically, no such hydration products were expected to grow in the striations of the LP-based mixture since limestone powder performed as an inert filler. The reason that C-S-H and ettringite also grew in the striations of the LP-based mixture can be explained by the ion migration crossing two different types of striations by diffusion due to different concentrations, taking water as the carrier [234, 235]. After the contact of two mixtures, the calcium ions and hydroxyl ions migrated from the PC-based mixture to the LP-based mixture and formed ettringite in the pores in the striation of the LP-based mixture. It can be also inferred that the concentration difference caused the aluminum and sulfate ions to migrate from the LP-based region to the striation of the PC-based mixture, leading to a faster stiffening rate, as already observed during the 3D printing process. The ion migration is schematically illustrated in Figure 6.10. Such ion migration and hydration product formation in the LP-based mixture accounted for the acceptable mechanical strength of 3D printed samples (e.g. merely a tensile bond strength reduction of 22% at the age of 28 days). Nevertheless, the ion migration can be facilitated by narrowing the width of striations in 3D printed elements. As already discussed in Chapter 5, the mixing homogeneity can be improved by increasing the number of baffle elements inside the helical static mixer but this would also compromise the pumping process with increased pumping pressure. For instance, the pumping pressure amounted to approximately 17 bars for 18 mixing baffles. Toutou et al. [236] showed that cement-based materials used for extrusion exhibit both frictional and plastic behaviors, which are very sensitive to fluid filtration. When a high amount of mixing baffles was used, the stress gradient would become more pronounced and could induce migration of interstitial fluid inside the helical static mixer. Further, no calcium hydroxide was observed either in the PC-based mixture or LP-based mixture due to the consumption of calcium hydroxide by the

high dosage of accelerator (7% by mass of cement in the combined mixture) [237, 238]. Figure 6.9 (c) shows the SE images of mold cast samples. A relatively uniform distribution of limestone powder was observed compared to the 3D printed samples, which can be interpreted as the reason for its higher mechanical strength.

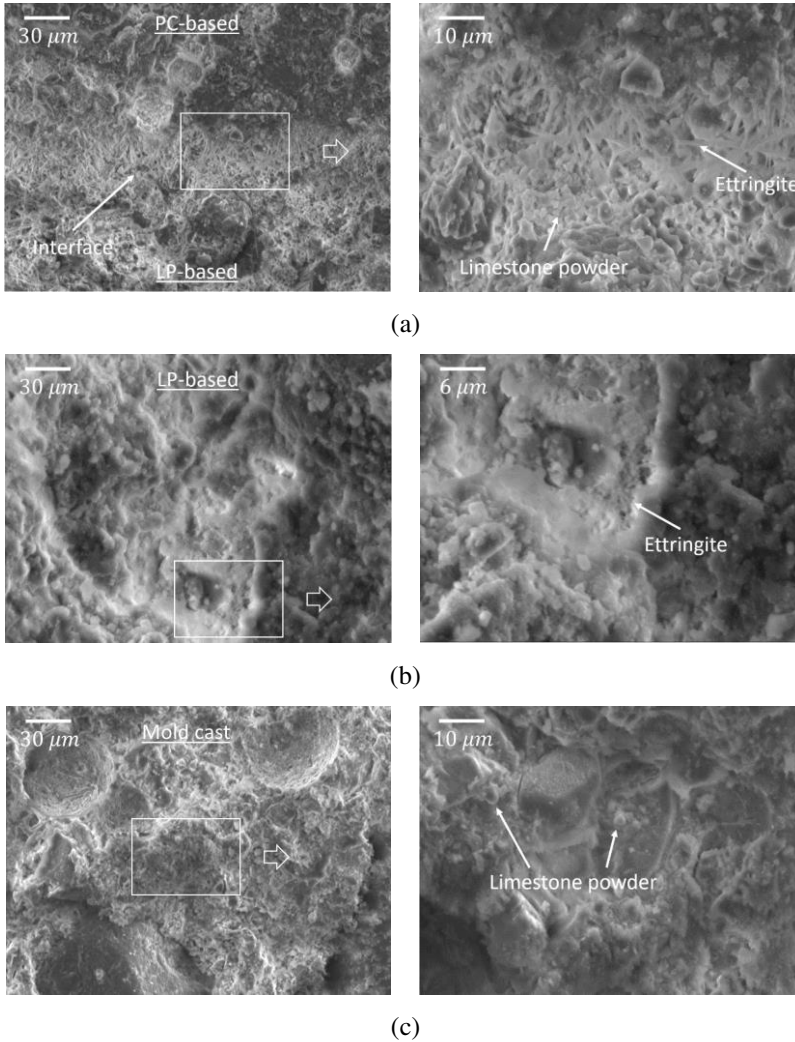


Figure 6.9 Secondary electron (SE) images of samples at the age of 28 days, (a) contact zone formation between two mixtures, (b) ettringite formation in LP-based mixture, and (c) limestone powder distribution in mold cast sample.

The microstructure of the 3D printed samples was further analyzed using the micrographs obtained in the BSE mode, as shown in Figure 6.11 (a). In the BSE images, the PC-based mixture can be distinguished from the LP-based mixture

from the difference in the grayscale intensities and this is further confirmed from the EDX analysis, as Figure 6.12 indicated calcium carbonate ( $\text{CaCO}_3$ ) in the LP-based region [239]. To characterize the difference in the porosity between the two regions, the grayscale images were binarized by implementing the overflow algorithm [240-242] using a Matlab program. The binarized images, with the white and black color, indicating the solid phase and pores, respectively are shown in Figure 6.11 (b). A higher pore area segmentation can be observed in the striation of the LP-based mixture. Previous studies showed that the porosity and mean pore diameter of concrete decreased slightly after the incorporation of limestone powder (up to 30%), while further increase in the limestone powder content reversed the trend [243]. In this study, high porosity seems reasonable in the LP-based striations when the substitution rate of cement by limestone powder amounted to 100%. Therefore, even though hydration products such as ettringite and some minor C-S-H were formed in the regions of the LP-based mixture as observed from the SE images, the regions of the LP-based mixture did not have the high densification of C-S-H formed in the regions of the PC-based mixture. This resulted in a relatively higher porosity in these regions. Finally, an important aspect to be noted was the differences in the resolution obtained from the different porosity measurement techniques. While MIP can reveal information on micropores even up to the range of a few nanometers, the resolution of the SEM images was limited to only  $3.6\ \mu\text{m}$  (in the range of macropores). Therefore, the higher porosity from BSE images in the LP-based striation is indicative of a higher volume of macropores in these regions. The results from the BSE analysis further imply that the coarser pore size distribution observed earlier from the MIP measurements for the printed sample can be attributed to the macropores in the LP-based striations.

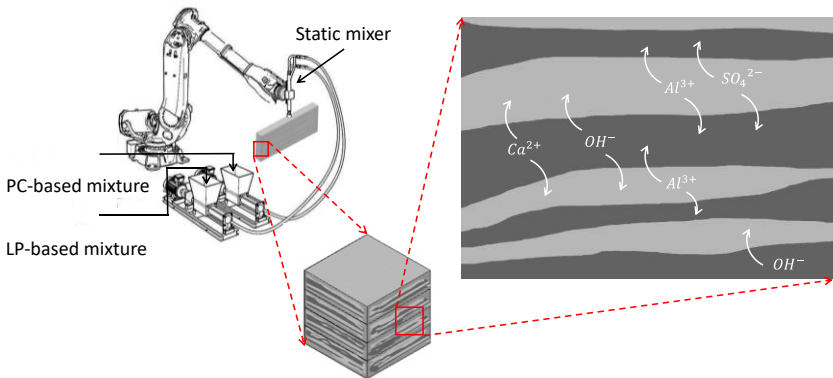


Figure 6.10 Ion migration between the striations of the PC-based mixture and the LP-based mixture.

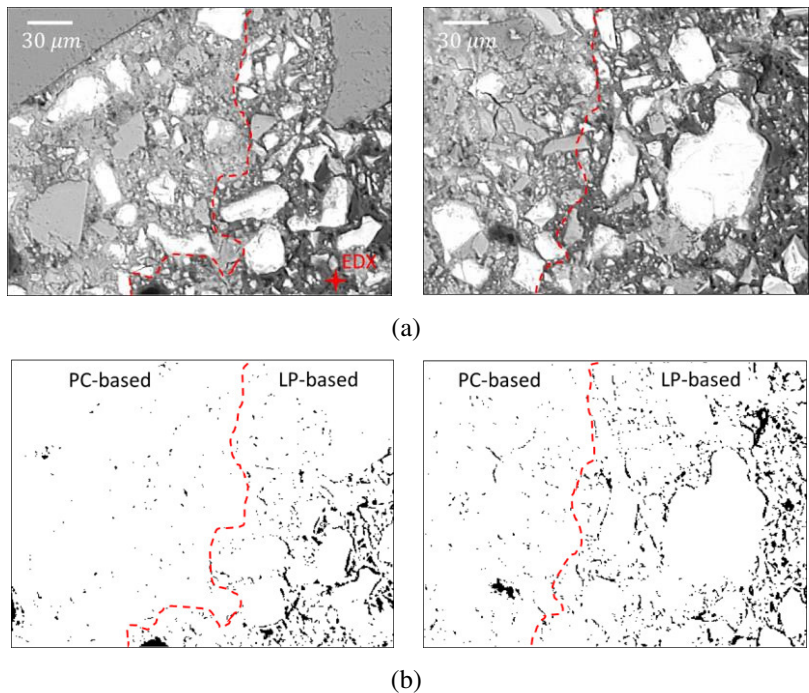


Figure 6.11 (a) Backscattered electron (BSE) images and (b) binarized images of the samples at the age of 28 days.

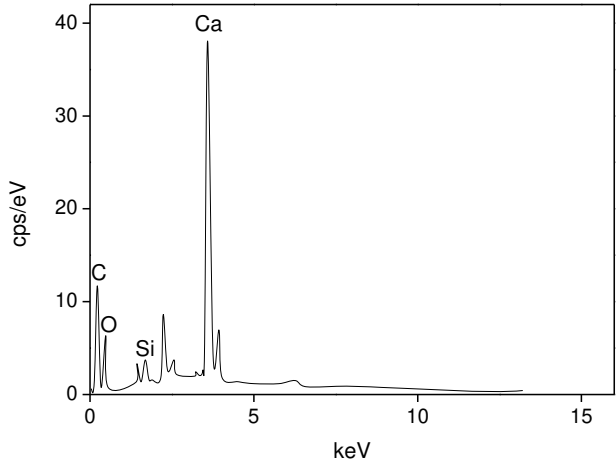


Figure 6.12 Energy dispersive X-ray (EDX) spectrum obtained from the chosen point in Figure 6.11 (a).

## **6.4 Summaries**

In this chapter, the mechanical behavior and microstructure of 3D printable concrete in the context of the twin-pipe pumping strategy are explored. According to the results and discussions, the following summaries are given:

(1) The layer orientation has no significant influence on the compressive strength of 3D printed samples, while the flexural strength of samples exposed to a loading direction parallel to the interface (D-1) is lower than that for the other two loading directions (D-2 and D-3). In addition, the tensile bond strength of 3D printed samples is lower than that of mold cast samples. Although the mechanical strength of 3D printed samples is lower than that of mold cast samples, the reduction is still within an acceptable range.

(2) When the loading direction is parallel to the striations of the cement-based (PC-based) and limestone powder-based (LP-based) mixture such as for C-1, C-2, and D-1 samples, fractures propagate inside the striation of the LP-based mixture, with a fracture surface showing light grey over most of the area. On the other hand, when the loading direction is perpendicular to the striations of the PC-based and LP-based mixture such as for C-3, D-2, and D-3 samples, a large number of PC-based and LP-based striations intertwining with each other are observed on the fracture surface. In the tensile bond strength test, most of the fracture surfaces of 3D printed samples occur inside the layer with a light grey fracture surface, further indicating that the striations of the LP-based mixture are the weakest point in the chain, rather than the interlayer position.

(3) The microstructure characterization is carried out by a multi-analytical approach using MIP and SEM. MIP analysis shows that the pore size distribution in the bulk and the interface area of printed samples are found to be similar, but distinct from that of the mold cast samples. The mold cast samples show a higher volume of finer micropores which may also possibly indicate a relatively higher volume of C-S-H gel formation. On the other hand, the printed samples show a relatively higher volume of macropores (higher than 50 nm), which is found to have a more detrimental effect on the compressive strength. Further, BSE-SEM analysis reveals that the macropores in the printed samples primarily occur in the LP-based mixture.

(4) Further, morphological observations from the micrographs show an obvious contact zone between the striations of the PC-based mixture and LP-based mixture. A mass of ettringite needles grows at the contact zone due to the promoted hydration of tricalcium aluminate ( $C_3A$ ) by aluminum sulfate. In addition, some unshaped C-S-H gel and ettringite needles are found within the pores in the striations of the LP-based mixture, indicating ion migration between two different types of striations.

(5) The ion migration inside the 3D printed elements can be facilitated by optimizing the compositions, as well as the rheological performance, of the two streams to be combined in the static mixer. The use of these strategies to promote ion migration is some direction for future research concerning the use of the twin-pipe pumping system in 3D concrete printing of hard rock tunnel linings.

## Influence of surface inclination on adhesion

### 7.1 Introduction

The influence of surface inclinations on the adhesion performance, which is an important aspect for controlling the amount of rebound of 3D printed materials was not studied previously. In this chapter, two representative surface inclinations are chosen including the inclination of  $180^\circ$  (overhead position) and the inclination of  $90^\circ$  (side position), as schematically illustrated in Figure 7.1. First, the adhesion of the fresh materials for these two surface inclinations is measured by a tack test and a shear test. Further, two series of large-scale 3D concrete printing tests are performed including printing at the lower surface of a horizontally supported slab and printing against an upright slab. Finally, the stress state of these two cases is analyzed.

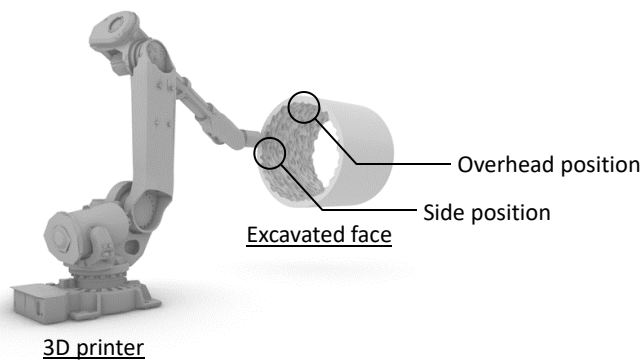


Figure 7.1 Schematic view of 3D concrete printing for hard rock tunnel linings including the overhead position and the side position.

### 7.2 Experimental program

Different surface roughness levels were considered in this chapter. Eight concrete cylindrical samples described in Figure 3.3 were used. CE6 (MB60000P2) was used for the tests in this chapter, aiming at enhancing the adhesion of the fresh material. To take the shear resistance of fresh materials into consideration in this

study, three mixtures were prepared including Mix1, Mix2, and Mix3 with the same sand to binder ratio of 1, the same water-to-binder ratio of 0.35, and the same cellulose ether dosage of 0.2% by the mass of cement. The dosages of the superplasticizer were 0.1%, 0.3%, and 0.5% by the mass of cement for the mixture Mix1, Mix2, and Mix3, respectively.

Small mixture batches (around 1.5 liters) were prepared in a conventional planetary mixer with the following mixing protocol: (1) manually mixing superplasticizer with water for 10 s, (2) adding water (and superplasticizer) to cement and rotating the paddle at 140 rpm for 30 s, (3) adding silica sand and rotating the paddle at 140 rpm for 30 s, (4) rotating the paddle at 285 rpm for 30 s, (5) scraping and resting for 90 s, (6) rotating the paddle at 285 rpm for 60 s, (7) adding CE6 and mixing at 285 rpm for 30 s.

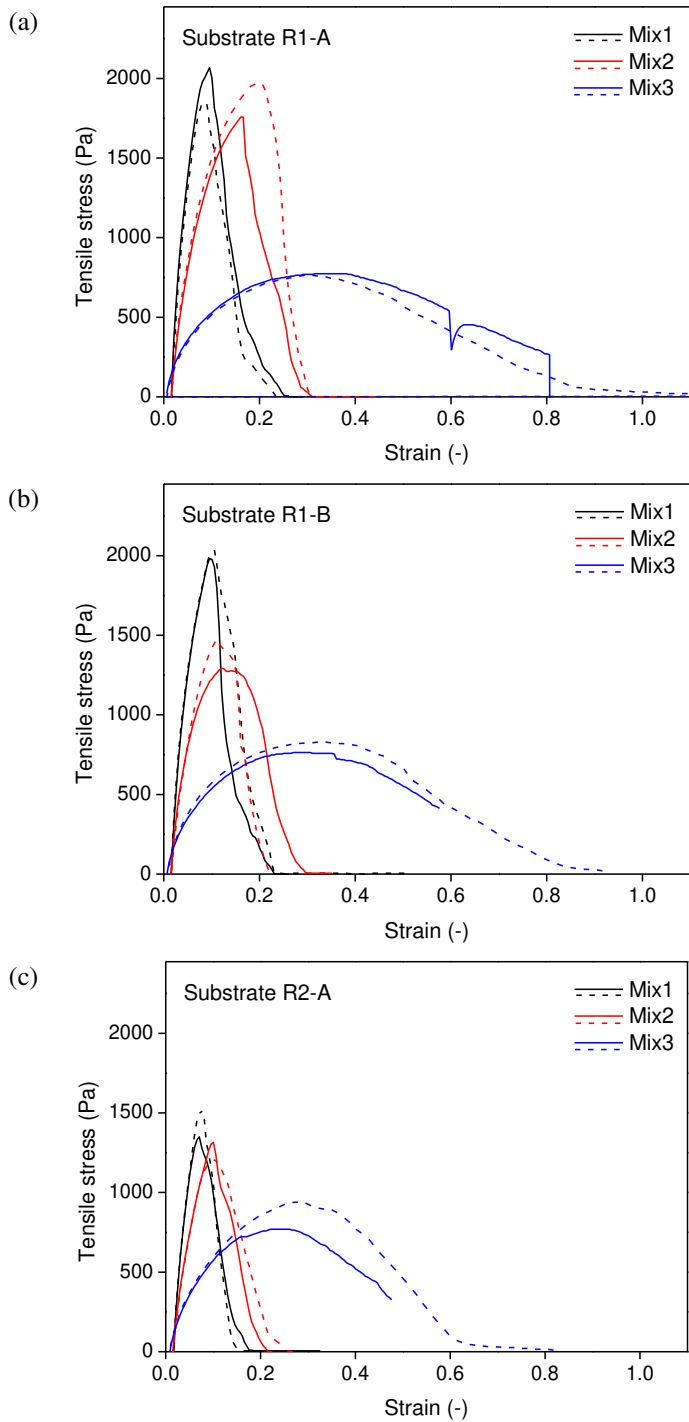
In addition, big mixture batches (around 20 liters) were prepared in a pan mixer for 3D concrete printing tests with the following mixing protocol: (1) manually mixing superplasticizer with water for 10 s, (2) mixing silica sand and cement for 30 s, (3) adding water (and superplasticizer) to the dry materials (silica sand and cement) and mixing for 180 s, (4) adding CE6 and mixing for 60 s. The total mixing period for both the small and big batches was 280 s.

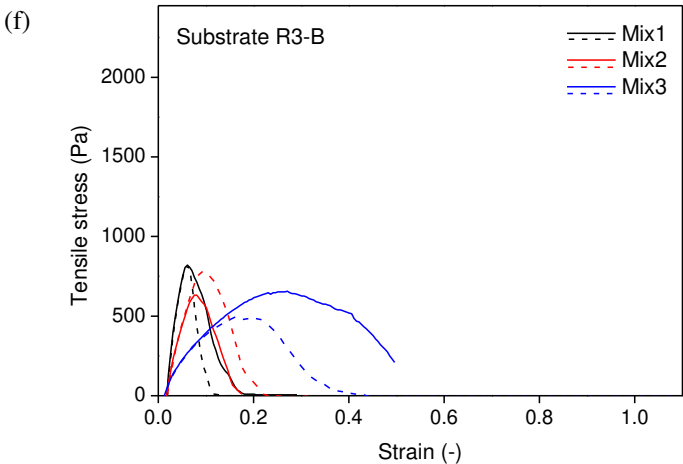
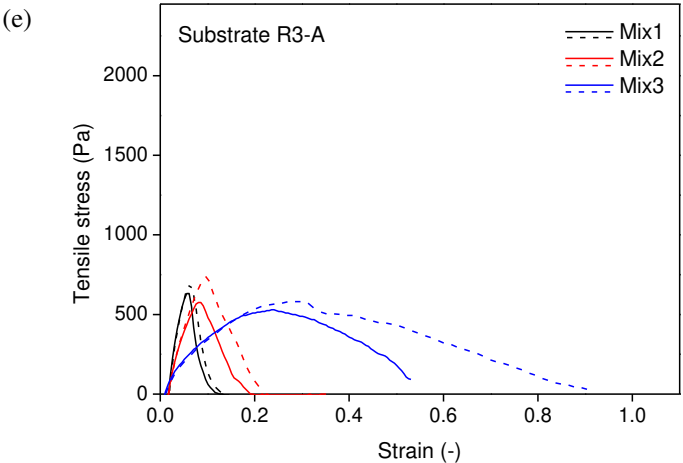
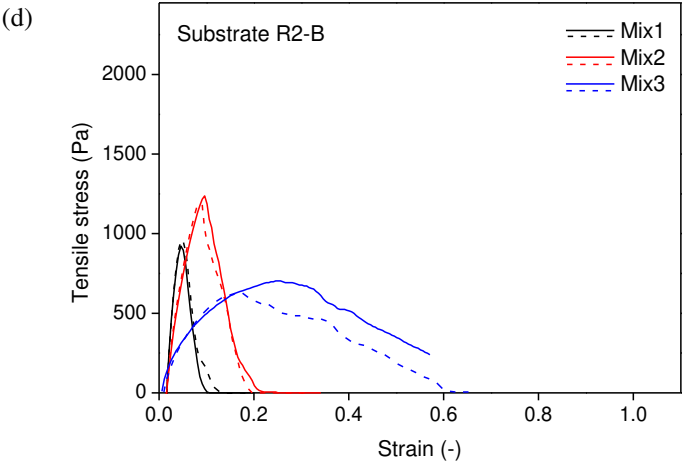
## **7.3 Results and discussion**

### **7.3.1 Adhesion in the tension state**

Tensile stress versus strain curves obtained from the tack test are shown in Figure 7.2. At the early beginning of the test, fresh materials deformed elastically and the tensile stress presented a semi-linear increase along with the increase of the displacement. After the tensile strain of the fresh material exceeded a critical value, the tensile stress decreased gradually to zero, indicating that the fresh material underwent a failure process [244, 245].







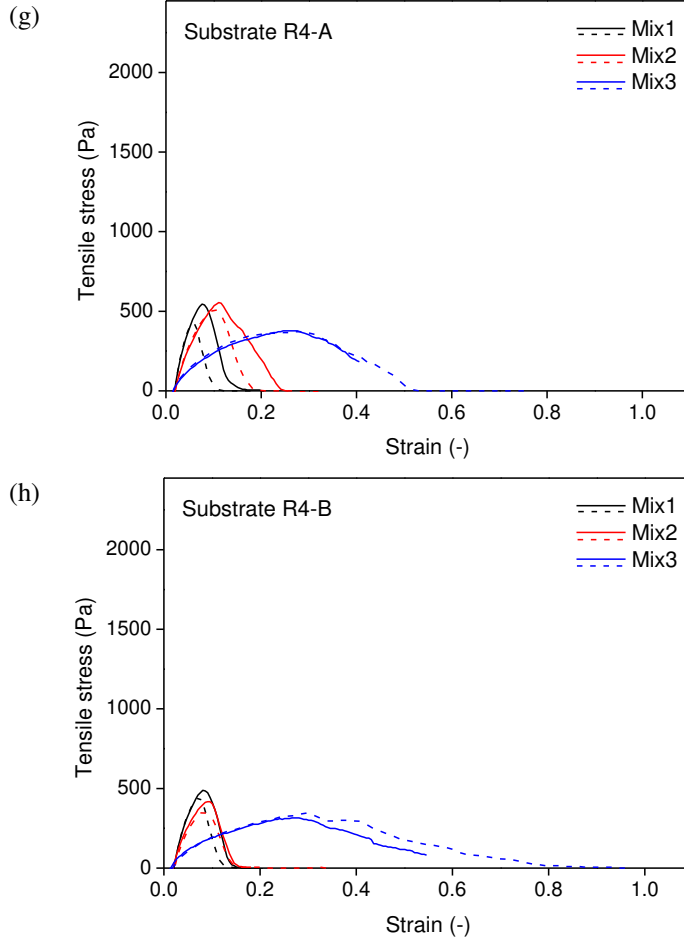


Figure 7.2 Tensile stress versus strain curves obtained in the tack test.

The peak values of the tensile stress were used to quantify the adhesive strength of the fresh material [244], as shown in Figure 7.3. It was indicated that the peak tensile stress reduced as the substrate roughness increased. Specifically, the average value of the peak tensile stress of mixture Mix1 decreased from 1960.8 Pa to 468.6 Pa as the root mean square deviation value ( $R_q$ ) increased from 0.03 to 2.68. While the average value of the tensile stress of mixture Mix3 decreased from 769.0 Pa to 331.0 Pa as the  $R_q$  value increased. Additionally, in the case of substrate R1-A, a difference of 60.8% was observed when comparing the peak tensile stress of mixture Mix1 and mixture Mix3 (1960.8 Pa and 769.0 Pa). While such a difference between the peak tensile stress of mixture Mix1 and mixture Mix3 was only 29.4% in the case of substrate R4-B. A two-way ANOVA test was conducted to examine the effect of the mixture type and the roughness level on the peak tensile stress obtained in the tack test. A p-value less than 0.05 ( $p < 0.05$ ) was considered statistically significant. According to the results, there was a

statistically significant interaction between the effects of the mixture type and the roughness level on the peak tensile stress ( $p = 0.000$ ). For the order of roughness levels, the groups were pair-wise compared with a Bonferroni test. A significant difference was observed when we pair-wise compared all three mixture types.

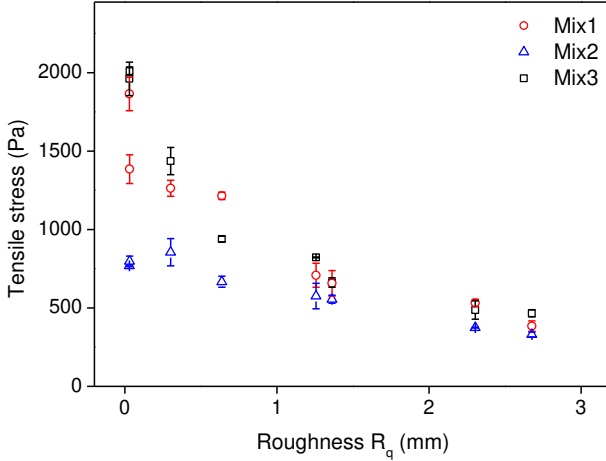


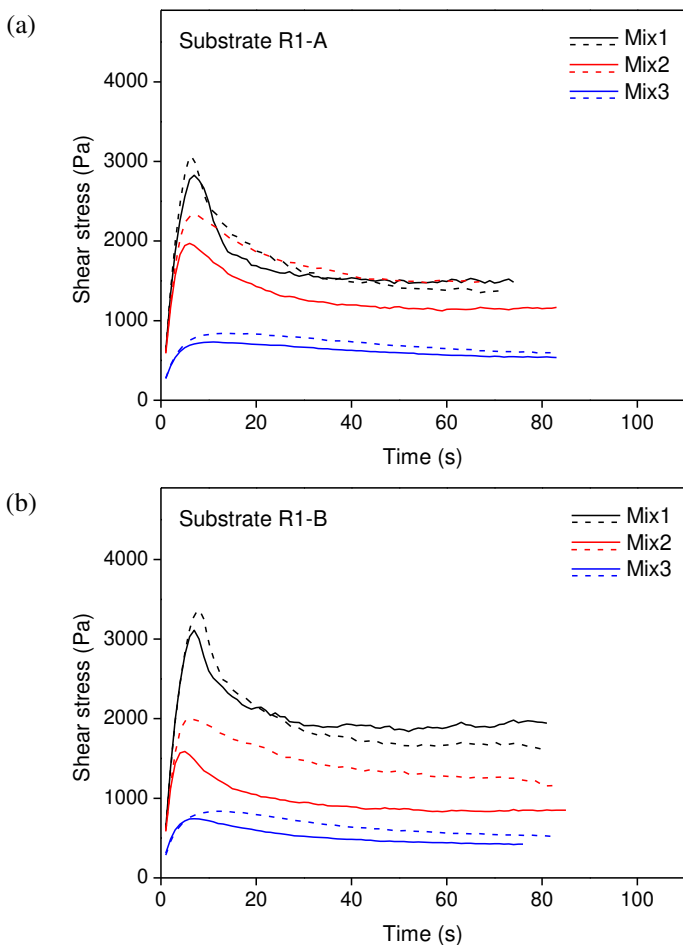
Figure 7.3 Effect of roughness levels and mixture types on peak tensile stress (error bars represent the standard error,  $n=2$ ).

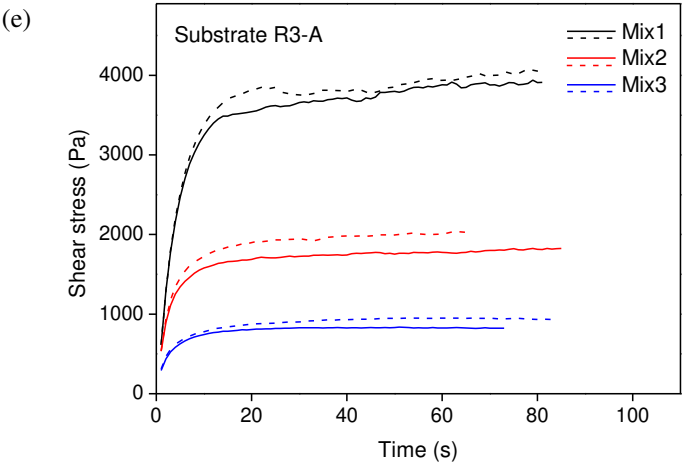
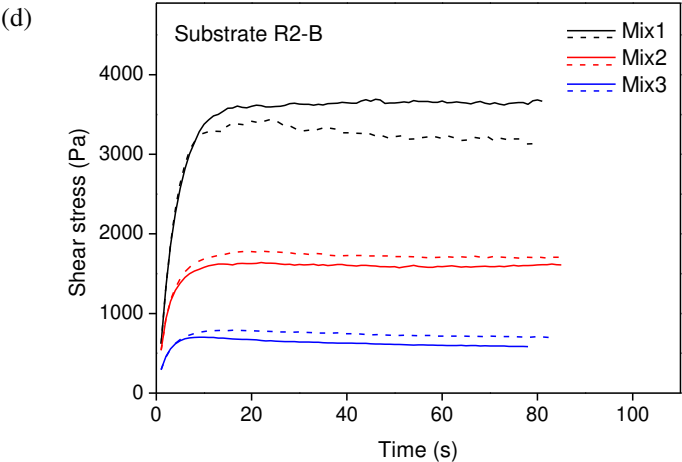
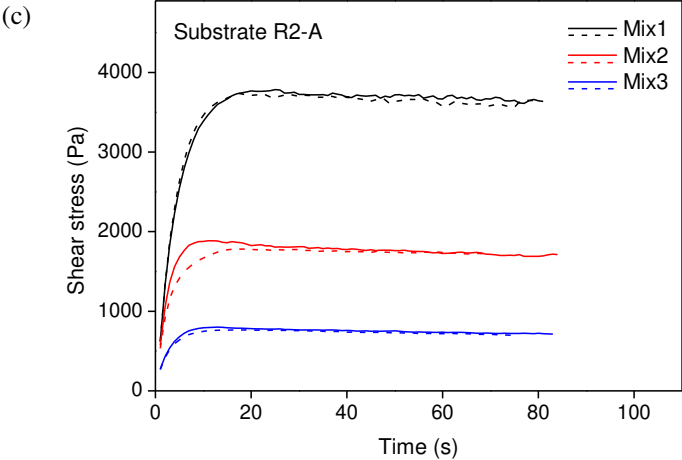
Distinguished from the adhesion of cement-based materials in the hardened state that is mainly attributed to mechanical interlocking [246, 247], the adhesion of cement-based materials in the fresh state is related to some other aspects. It was pointed out by Mohamed et al. [248] that the effort required to lift the top plate was determined by the inward flow of the fresh sample. At the early stage of the pull-off process, a short movement of the top plate would induce a significant inward flow at the air-to-sample interface. The inward flow of the fresh sample is determined by both viscous dissipation (dynamic performance) and cohesion strength (static performance). In this study, a relatively low pulling velocity ( $v = 50 \mu\text{m/s}$ ) was used and the whole testing process can be treated as a quasi-static process. Therefore, the viscous dissipation, which is related to the dynamic performance of the material, was not considered [245]. Further, such an inward flow is constrained by the friction provided by the top and bottom plates. As a result, the peak tensile stress depended on the shear resistance of the fresh sample and the sample-to-plate interface. In this study, it was assumed that the contact area at the interface was limited when using a more solid-like material such as mixture Mix1. As such, less friction confining the inward flow of the fresh material was provided at the interface and the adhesion was compromised accordingly. Reversely, for mixture Mix3 with a more liquid-like behavior, more contact between the lower surface of the concrete cylindrical sample and the fresh material was expected. However, the lower shear resistance of the mixture limited

the adhesive strength and the fracture was more likely to occur in the bulk of the fresh material, which will be further discussed in the following section.

### 7.3.2 Adhesion in the shear state

The shear stresses were recorded in the shear test, as shown in Figure 7.4. The shear stress evolution curves obtained in the shear test followed two different patterns. For the cylindrical samples with a low roughness level such as R1-A and R1-B, an obvious peak was observed, while for the rest of the cylindrical samples with higher roughness levels, it was observed that a plateau followed an increasing stage.





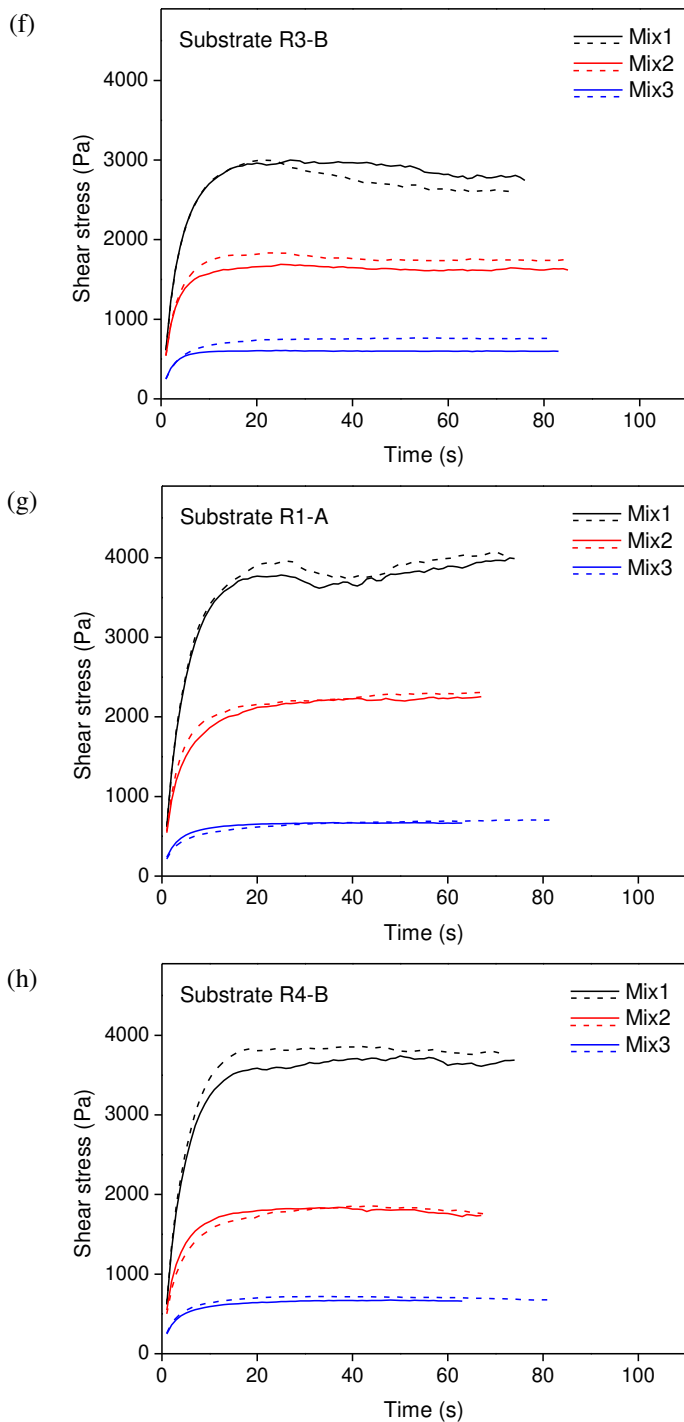


Figure 7.4 The shear stress evolution along with time obtained in the shear test.

Maximum values of shear stress derived from the shear stress evolution curves are shown in Figure 7.5. Generally, mixture Mix1 presented the highest shear stress while mixture Mix3 had the lowest shear stress value. For example, the maximum shear stress of mixture Mix1 reached an average value of 2945.0 Pa while the maximum shear stress of mixture Mix3 was merely 785.9 Pa in the context of using substrate R1-A. In addition, a two-way ANOVA test was conducted to examine the effect of the mixture type and the roughness level on the maximum shear stress obtained in the shear test. The statistical analysis followed the same procedure introduced in the previous section. Results indicated that no interaction existed between the two factors in the discrimination performance analysis, but respective differences were noted in the two dependent variables. For the mixture type, significant differences were observed when we compared different mixture types while no significant difference appeared between different substrates.

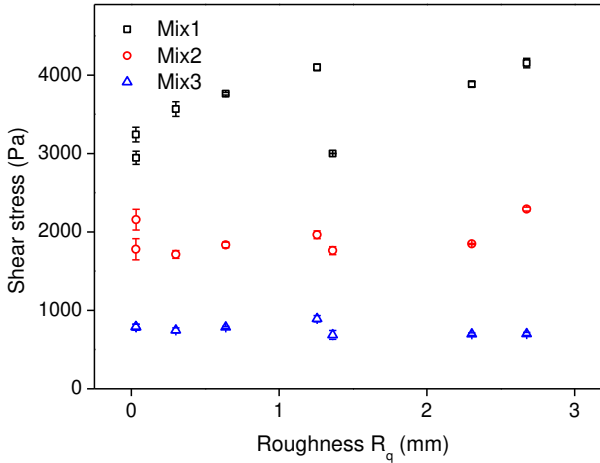


Figure 7.5 Maximum shear stress measured for different concrete substrates (error bars represent the standard error,  $n=2$ ).

Further, the maximum shear stress (i.e. yield stress) of each of the three mixtures was measured in the stress growth test. The average values were 3460.6, 2297.1, and 545.1 Pa for mixture Mix1, Mix2, and Mix3, respectively. Since no significant difference existed when comparing different substrates in the shear test, the maximum shear stress measured with the gritblasted substrate R2-A was chosen. The average values were 3762.0, 1834.2, and 783.9 Pa for mixture Mix1, Mix2, and Mix3, respectively. Afterwards, the maximum shear stress measured in the shear test ( $\tau_s$ ) and the maximum shear stress measured in the stress growth test ( $\tau_y$ ) were linearly fit, as shown in Figure 7.6. A good linear relationship ( $R^2 = 0.8885$ ) was obtained. Such a result proved that the shear resistance of the bulk of the fresh material played a decisive role in the adhesion in the shear state.



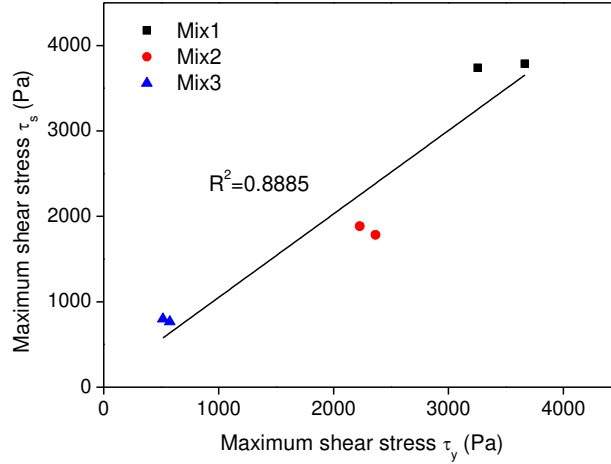


Figure 7.6 Maximum shear stress measured in the shear test and the stress growth test (dots represent individual measurements).

### 7.3.3 3D printing test results

The results of the 3D concrete printing tests at the overhead position are shown in Figure 7.7. For each mixture, one of the three representative repetitions is shown including the moment when the maximum number of layers were printed (left), the moment when the failure occurred (middle), and the moment after failure (right). As presented in Figure 7.7 (a), the maximum number of printed layers of mixture Mix1 amounted to 7, which was followed by a debonding at the interface between the lower surface of the slab and the fresh material. For mixture Mix2, 6 layers were printed before failure occurred, which was slightly less than that of mixture Mix1. An adhesive failure pattern similar to that of mixture Mix1 was observed, see Figure 7.7 (b). Different from mixture Mix1 and Mix2, the number of printed layers for mixture Mix3 was quite lower, with a maximum value of 3. During the printing of the fourth layer, the plastic nozzle invaded into the fresh material for around 10 mm, indicating a large deformation of printed layers due to the relatively low shear resistance of the fresh material. In addition, the fracture initiated and propagated inside the bulk of the first printed layer, indicating a cohesive failure of the fresh material.



(a)

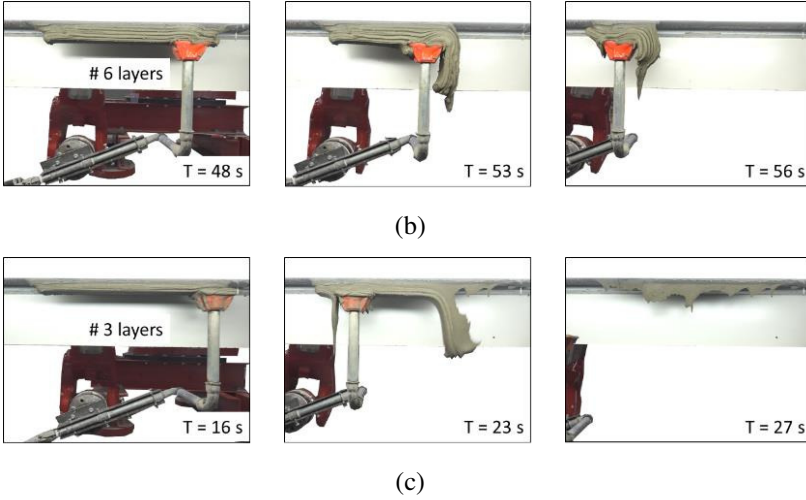
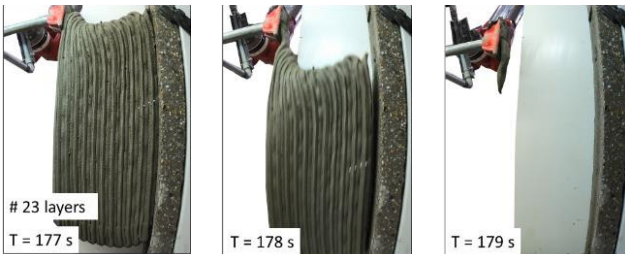


Figure 7.7 3D concrete printing at the overhead position, (a) Mix1, (b) Mix2, and (c) Mix3.

The results of 3D concrete printing tests at the side position are shown in Figure 7.8. For each mixture, one of the three representative repetitions is presented including the maximum number of 3D printed layers (left), the occurrence of failure (middle), and the moment after failure (right). The number of the printed layers reached 23, 9, and 4 for mixture Mix1, Mix2, and Mix3, respectively, demonstrating a higher adhesion towards the substrate when compared with that at the overhead position, especially for mixture Mix1. Upon visual observation, the results showed a different failure pattern of sliding under gravity. From mixture Mix1 to mixture Mix3, the deformation of printed layers became more pronounced, which can be attributed to the difference in the shear resistance of the fresh material. Moreover, in the case of mixture Mix1, a large eccentricity of the gravity center of printed elements led to a tensile stress perpendicular to the vertical substrate, resulting in a detaching from the vertical substrate. This is captured in the images of the failure moment at 178 s for mixture Mix1 and the failure moment at 105 s for mixture Mix2. As for mixture Mix3, due to a limited number of printed layers, the layers didn't undergo such a detaching process.



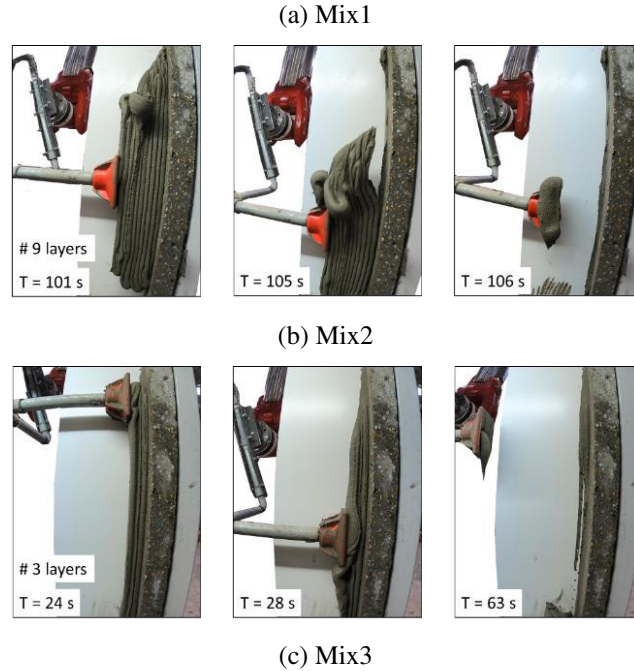


Figure 7.8 3D concrete printing at the side position.

The maximum number of 3D printed layers of each of the three mixtures (i.e. Mix1, Mix2, and Mix3) at the overhead position and the side position are shown in Figure 7.9. In both cases, with a decrease in shear resistance of the fresh material from mixture Mix1 to mixture Mix3, the maximum number of printed layers tended to decrease. Specifically, for the side position, the maximum number of printed layers decreased from an average value of 22 to 3. While a change from an average value of 8 layers to 4 layers was observed at the overhead position. It was clearly illustrated that the fresh material printed at the side position achieved more printed layers, particularly for mixture Mix1 and Mix2, indicating a stronger capacity for a thicker lining structure when compared to the overhead position. However, it should be noted that the resistance to failure at the side position faced a sharp decrease from mixture Mix1 to mixture Mix3. As a result, the printing capacity of mixture Mix3 at the side position was even slightly lower than that at the overhead position.

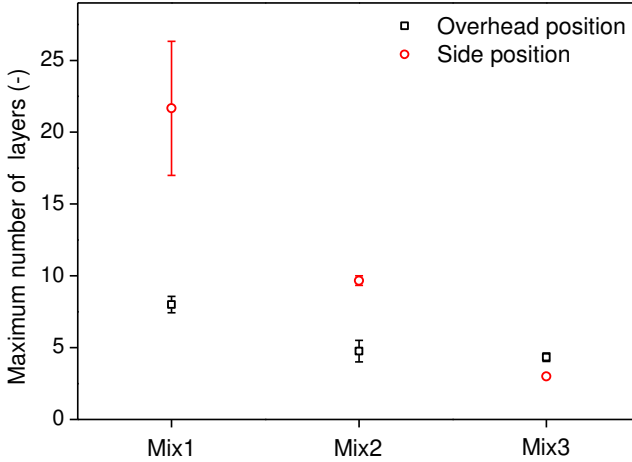


Figure 7.9 Maximum number of 3D printed layers (error bars represent the standard error,  $n=3$ ).

To better understand the significant difference between the failure modes and the capacity to print layers at the overhead position and the side position, schematic views of the contact zone and the fracture surfaces are depicted, as shown in Figure 7.10. When comparing the detaching behavior of the fresh material, the mechanism behind the failure was different in each case. For the overhead position, more macro textures and gaps can be filled with the fresh material with lower shear resistance when applying the same pressure. As a result, more contact can be achieved with mixture Mix3 while mixture Mix1 experienced a lower contact area. The difference in the contact area and the shear resistance of the fresh material further led to different failure modes. The failure occurred at the interface for mixture Mix1 and Mix2, which can be attributed to the weak adhesion at the interface and a more solid-like behavior of the fresh material. Distinctively, the fracture propagated inside the bulk of the freshly printed layers of mixture Mix3 due to the full contact at the interface and a more liquid-like behavior of the fresh material. On the other hand, the printing capacity at the side position was more related to the shear resistance of the fresh material rather than the contact at the interface. Based on the results of the shear test and the observation of the 3D printing test against the vertical slab, it can be concluded that the contact area made no difference at the side position and the shear plane initiated for each mixture in the bulk of the fresh material. Recall that the mixture type had a more significant influence on the printing capacity at the side position when compared to that at the overhead position. This indicates that the printing capacity of the fresh material at the overhead position was controlled by both the shear resistance of the fresh material and the contact at the interface, while the printing capacity at the side position was mainly determined by the shear resistance of the fresh material. As a result, only 8 layers of mixture Mix1 were printed at the overhead position while the side position was hardly affected by the contact at the interface (22 layers).

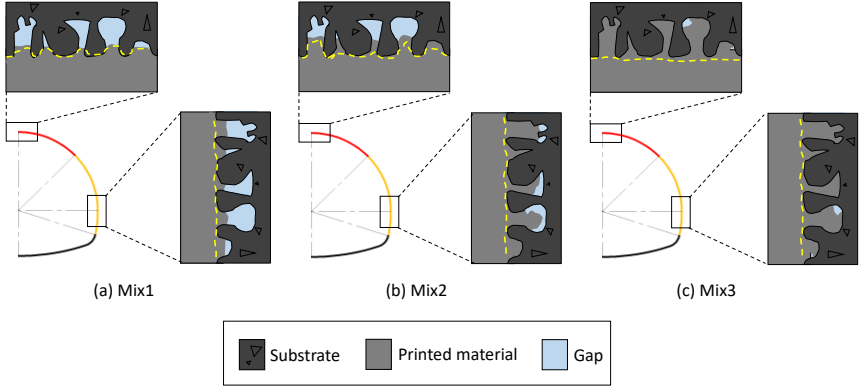


Figure 7.10 Schematic view of the contact zone with different mixtures and different surface inclinations, where dashed yellow lines indicate the failure surface.

### 7.3.4 Stress state analysis

The stress state of the first printed layer is analyzed in this section, as schematically illustrated in Figure 7.11. Several characteristic positions of the hard rock tunnel lining are depicted including the crown, shoulder, axis, knee, and invert, among which, the overhead position (i.e. crown) and the side position (i.e. axis) were specifically analyzed in this study. For the first printed layer at the overhead position, only the vertical stress  $\sigma_z$  (Pa) was applied perpendicular to the printed layer due to the self-weight of the subsequent layers, which can be calculated as follows:

$$\sigma_z = n\rho gh_0 \quad (7.1)$$

where  $n$  is the number of printed layers at the overhead position (-),  $\rho$  is the density of the fresh material ( $\text{kg/m}^3$ ), taken as  $2000 \text{ kg/m}^3$ ,  $g$  is the gravitational acceleration ( $\text{m/s}^2$ ), taken as  $9.8 \text{ m/s}^2$ , and  $h_0$  is the thickness of each printed layer (m).

Further, the stress along the longitudinal direction  $\sigma_y$  (Pa) can be calculated as follows:

$$\sigma_y = \nu \cdot \sigma_z \quad (7.2)$$

where  $\nu$  is the Poisson's ratio of the freshly printed material (-), which is commonly assumed to be 0.3 for 3D printed materials in the fresh state [40]. Nevertheless, this value would vary when modifying the mixture composition of fresh materials.

On the other hand, the stress state of the printed layer at the side position experiences a different situation, as compared to that at the overhead position. The shear stress  $\tau_{yz}$  was applied by the presence of the subsequent layers and can be assumed to be uniformly distributed along the longitudinal direction (i.e. the vertical direction), which is calculated as follows:

$$\tau_{yz} = m\rho gh_0 \quad (7.3)$$

where  $m$  is the number of printed layers at the side position (-).

In addition, the compressive effect inside the first printed layer at the side position induced the normal stress  $\sigma_z$  (Pa) in the vertical direction. In practice, the value of the normal stress  $\sigma_z$  was very limited as the first printed layer was also supported by the substrate with friction. Further, due to the eccentricity of the self-weight of the printed layers, a moment was induced, which further led to a tensile force or a compressive force in the horizontal direction against the vertical substrate. Accordingly, the normal stress  $\sigma_y$  (Pa) perpendicular to the printing direction might appear. The effect of the normal stress  $\sigma_y$  was more critical when more layers were printed and detaching on the upper part of the printed layers was observed, as shown in Figure 7.8 (a) and Figure 7.8 (b). While for printed layers with a limited number of layers, the stress  $\sigma_y$  can be ignored. For example, sliding of printed layers was only observed for mixture Mix3, as shown in Figure 7.8 (c).

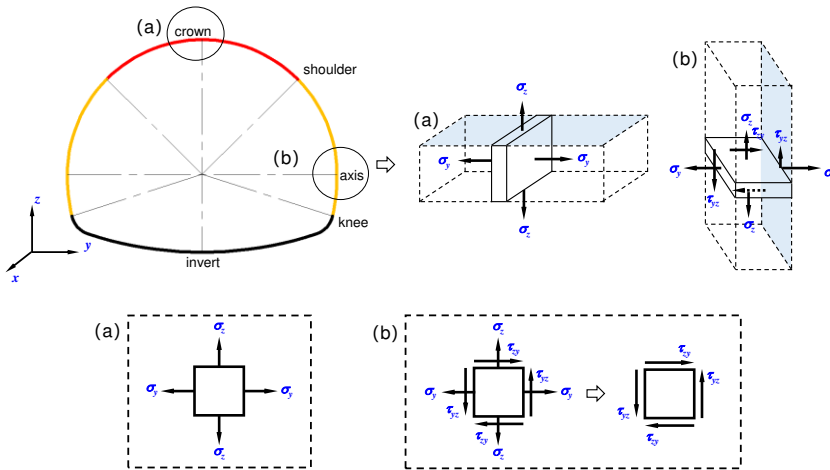


Figure 7.11 Stress state analysis of the first printed layer at the overhead position (i.e. crown), and the side position (i.e. axis) where the effect of the normal stress is ignored.

For comparison, the tensile stress obtained in the tack test and the 3D concrete printing test (overhead position) is shown in Figure 7.12 (a). In addition, the shear stress obtained in the shear test and 3D concrete printing test (side position) is

shown in Figure 7.12 (b). Results indicate that the stresses predicted from the tack test and the shear test fit very well with the stresses derived from the 3D concrete printing test. Therefore, it can be concluded that the tack test and the shear test are suitable to predict the capacity of 3D printed layers in both the overhead position and the side position. However, it should be noted that the prediction of other positions (e.g. the shoulder position and knee position shown in Figure 7.11) is still lacking. More analysis about the stress field and the failure criterion of the fresh material needs attention.

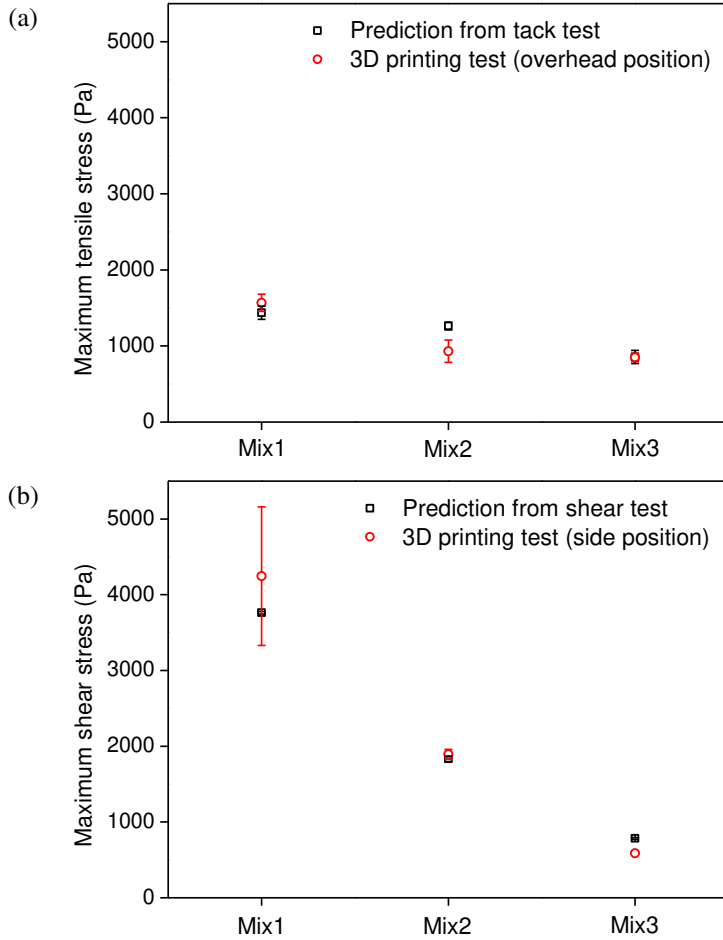


Figure 7.12 (a) Tensile stress derived from the tack test ( $\sigma_t$ ) and the 3D concrete printing test ( $\sigma_z$ ), (b) Shear stress derived from the shear test ( $\tau_s$ ) and the 3D concrete printing test ( $\tau_{yz}$ ).

## 7.4 Summaries

In this chapter, the adhesion of the fresh, 3D printable material, for two typical surface inclinations including the overhead position and the side position, are studied. Based on the experimental results and theoretical analysis, the following summaries are given:

(1) The adhesion at the overhead position is limited by both the shear resistance of the fresh material and the property of the material-to-substrate interface. For a more solid-like material, less contact at the interface is obtained, leading to less friction at the interface confining the inward flow. Consequently, the adhesion at the overhead position is compromised. For a more liquid-like material, relatively complete contact between the substrate and the fresh material is achieved.

(2) The adhesion at the side position is mainly defined by the shear resistance of the fresh material, rather than the substrate properties. More layers are printed at the side position when compared to that at the overhead position, indicating a stronger capacity for a thicker lining structure, particularly for the mixture with a solid-like behavior. As such, in the following chapters, only the overhead position is considered.

(3) The difference in the contact area and the shear resistance of the fresh material results in different failure patterns. For a more solid-like material, fracture occurs at the material-to-substrate interface which can be attributed to the weak adhesion at the interface. Adversely, for a more liquid-like material, the fracture propagates inside the bulk of the fresh material.

(4) The stress states of the printed layers at the overhead position and the side position are analyzed. The stresses measured by the tack test and the shear test fit well with the stresses derived from the maximum amount of printed layers in the 3D concrete printing test. Results indicate that the tack test and the shear test can be used to predict the capacity of 3D printed layers for the overhead position and the side position, respectively.



## **Influence of substrate properties on adhesion**

### **8.1 Introduction**

The adhesion performance of hardened samples is strongly influenced by the quality and behavior of the interface created between the substrate and the overlay [249]. The adhesion at the interface is affected by various factors, among which the substrate surface roughness and moisture content might be two of the most important parameters [176, 188, 250]. However, very limited research focused on the effect of the substrate surface roughness and moisture content on the adhesion performance of 3D printable concrete, especially the material in the fresh state. In Chapter 7, it has been shown that the printed materials at the overhead position suffer more risk of falling when compared to that at the side position. Therefore, in this chapter, only the tensile adhesion at the overhead position is considered. The influence of the substrate surface roughness and moisture content on the tensile adhesion of 3D printable concrete is studied. The effect of a possible pretreatment is also considered. First, concrete substrates with four surface roughness levels and five surface moisture contents are prepared. Subsequently, a tack test is performed and the normal force versus displacement curves are recorded to quantify the tensile adhesion of fresh concrete. Further, a large-scale 3D concrete printing test is performed to evaluate the sag resistance of freshly printed concrete. Finally, the tensile bond strength of hardened samples at the age of 28 days is measured by a pull-off test and a comparison is made between placing through printing and casting.

### **8.2 Experimental program**

Only mixture Mix1 developed in Chapter 7 was used. The mixing procedure follows the same as that described in Chapter 7. An overview of the different conditions used in the tack test, the 3D concrete printing test, and the pull-off test is shown in Table 8.1. In this chapter, R1 refers to R1-A, R2 refers to R2-A, R3 refers to R3-A, and R4 refers to R4-B. More details of R1-A, R2-A, R3-A, and R4-B can be found in Chapter 3.

Table 8.1 An overview of different conditions used in the tack test (column A), the 3D concrete printing test (column B), and the pull-off test (column C), where the star “\*” indicates that the surface condition is tested within this study.

Series	Roughness	Moisture content	Coating	A	B	C
R1-M3	Polished	Saturated-surface-dry	No	*	*	*
R2-M3	Gritblasted			*	*	*
R3-M3	Hammered			*		
R4-M3	Water-jetted			*		
R1-M3-CT	Polished	Saturated-surface-dry	Yes	*		
R2-M3-CT	Gritblasted			*	*	*
R3-M3-CT	Hammered			*		
R4-M3-CT	Water-jetted			*		
R2-M1	Gritblasted	Oven-dried	No	*		
R2-M2		Air-dried		*	*	*
R2-M4		Wet		*	*	*
R2-M5		Over-wet		*		
R2-M3-MC	Gritblasted	Saturated-surface-dry	Yes			*

### 8.3 Results and discussion

#### 8.3.1 Normal force versus displacement curves

To evaluate the influence of the substrate surface roughness and pretreatment on the tensile adhesion of the fresh material, the substrate surface moisture content was kept constant as a saturated-surface-dry condition (M3). Two groups of tack tests were performed and the normal force versus displacement curves are shown in Figure 8.1 and Figure 8.2, respectively. All curves present similar patterns with two main stages. The first stage is characterized by an increasing normal force, followed by a second stage where the normal force decreases gradually to zero. Kaci et al. [244] stated that fresh materials displayed mainly an elastic behavior or viscoelastic behavior in the beginning, and a plastic behavior after some time. During the second stage, irreversible rupture started to take over until complete detachment [248]. In this study, the fracture propagated at the contact interface between the uncoated concrete cylindrical sample and the fresh material, while for the coated concrete cylindrical samples, the failure occurred at the contact zone between the fresh coating and the fresh, squeezed sample.

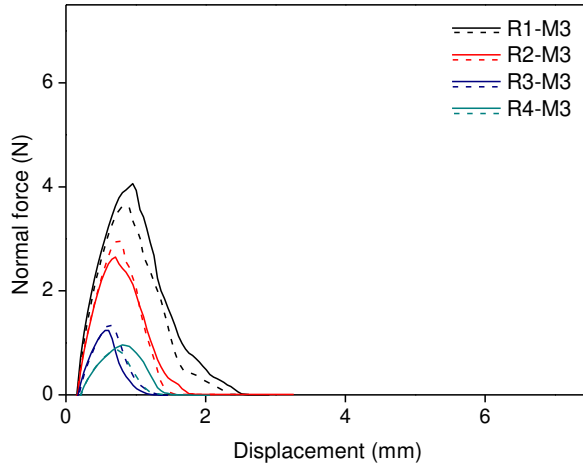


Figure 8.1 Normal force versus displacement curves for the uncoated substrates with different surface roughness levels.

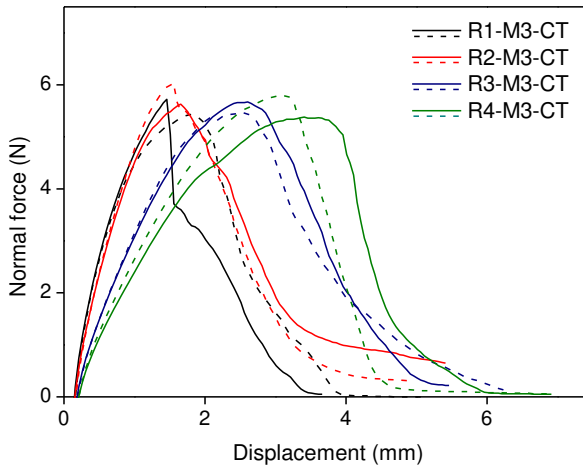
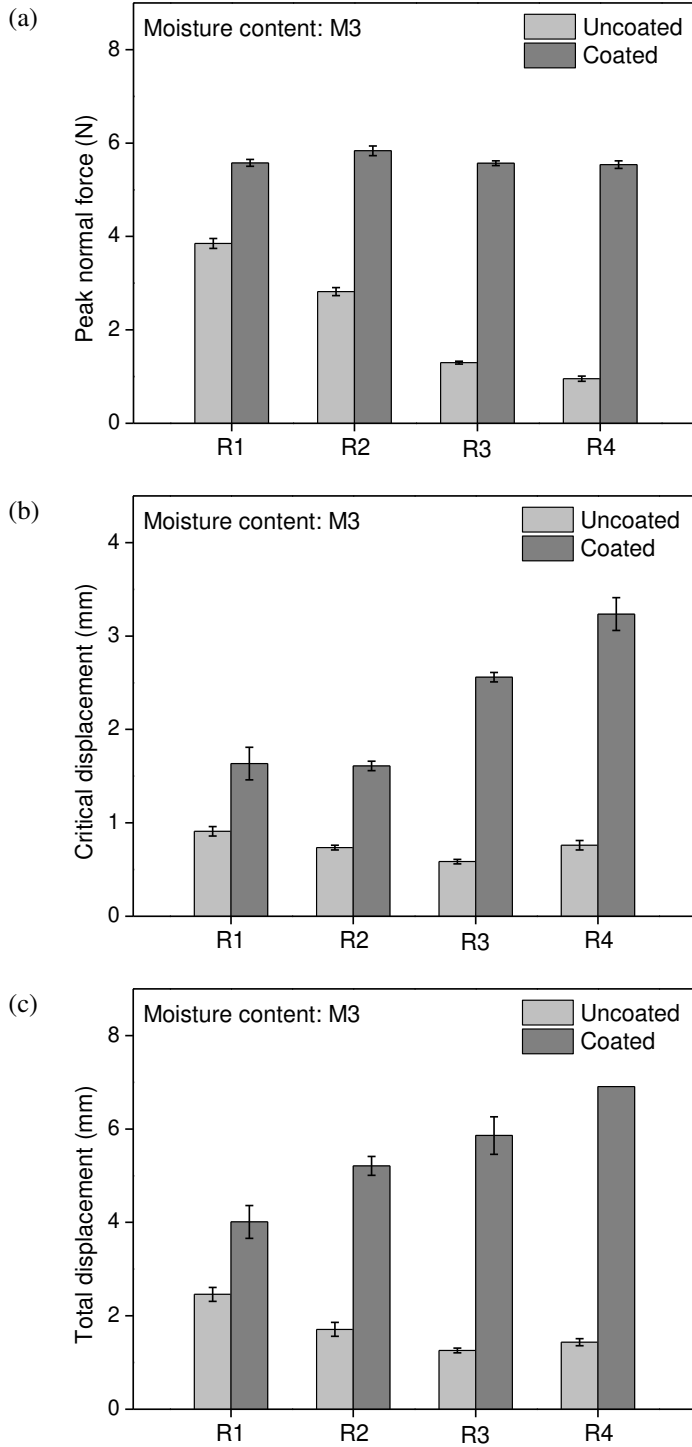


Figure 8.2 Normal force versus displacement curves for the coated substrates with different surface roughness levels.

In total four parameters can be derived from the normal force versus displacement curves including the peak normal force, the critical displacement (i.e. the displacement where the normal force reached the maximum value), the total displacement (the displacement where the normal force reduced to zero or a stable value), and the dissipated energy (the area formed by the normal force curve obtained in the test and the horizontal axis). The peak values of the normal force are presented in Figure 8.3 (a). For the uncoated cylindrical samples, the average value of peak normal force reduced gradually from 3.85 N to 0.92 N as the root mean square deviation value ( $R_q$ ) increased from 0.03 (substrate R1) to 2.68 (substrate R4), while the peak normal force remained almost the same for the

coated cylindrical samples. It was indicated that two aspects contributed to the peak normal force including the shear resistance of the fresh sample and the force at the interface between the top plate and the upper surface of the fresh sample [251, 252]. In the series with uncoated concrete cylindrical samples, the peak normal force was mainly controlled by the force at the interface. When a rough substrate was used such as substrate R4, limited contact formed at the interface, leading to a compromised tensile adhesion. As a result, the peak normal force reduced as the substrate roughness level increased. In the series of coated concrete cylindrical samples, the coating contributed remarkably to the tensile adhesion at the interface and the peak normal force was mainly controlled by the shear resistance of the fresh material. The second interesting point relates to the critical displacement, as plotted in Figure 8.3 (b). It was observed that the critical displacement reduced slightly with the increase of the substrate roughness for the series of uncoated concrete cylindrical samples. On the other hand, for the coated concrete samples, the critical displacement was increased as the substrate roughness level increased, especially for the concrete cylindrical samples R3 and R4. For example, the critical displacement measured with coated concrete sample R4 (3.24 mm) was almost twice the value measured with coated concrete sample R1 (1.64 mm). Moreover, the total displacement presented a similar trend, as shown in Figure 8.3 (c). This can be interpreted by the improved mechanical interlocking provided by the fresh coating, especially for the rough substrate. Therefore, we could conclude that the fresh material exceeded the yield point in the first stage (before reaching the peak normal force). After reaching the yield point, the fresh material with a stronger tensile adhesion at the interface (such as coated substrate R4) continued to deform, while in other cases with lower substrate roughness, failure occurred earlier. As a result, no significant difference was observed when comparing the peak normal forces in the series of coated concrete cylindrical samples due to the same yielding level, while a remarkable difference between the displacement (both the critical displacement and total displacement) was observed. The dissipated energy is shown in Figure 8.3 (d). With the increase of the substrate surface roughness, the dissipated energy tended to reduce in the uncoated condition, whereas an opposite phenomenon was observed when the concrete cylindrical samples were coated. Combining the results of the peak normal force and the displacement, the results of the dissipated energy can be inferred. In addition, it should be noted that dissipated energy measured with coated substrate R4 was around 25 times that measured with uncoated substrate R4. The great distinction indicated the prominence of applying a coating.



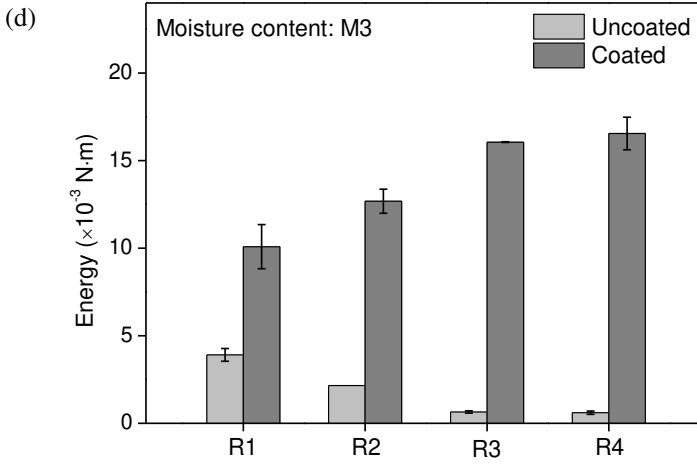


Figure 8.3 Peak normal force (a), critical displacement (b), total displacement (c), and dissipated energy (d) of fresh samples measured with the coated and uncoated substrates (error bars represent the standard error,  $n=2$ ).

To study the influence of the substrate surface moisture content on the tensile adhesion of the fresh material, the concrete cylindrical sample R2 with five different moisture contents (i.e. M1, M2, M3, M4, and M5) was used. The same tack test procedure was conducted and the normal force versus displacement curves are shown in Figure 8.4.

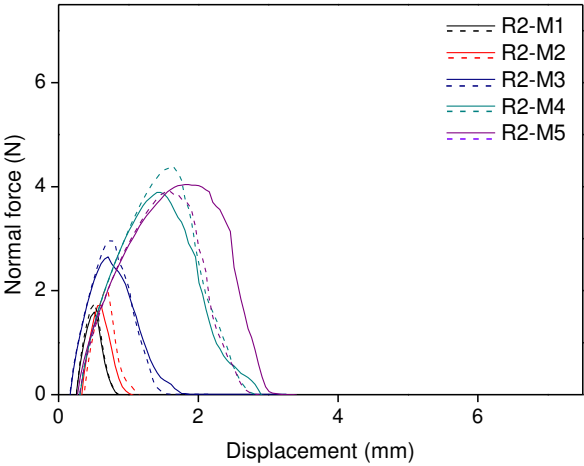
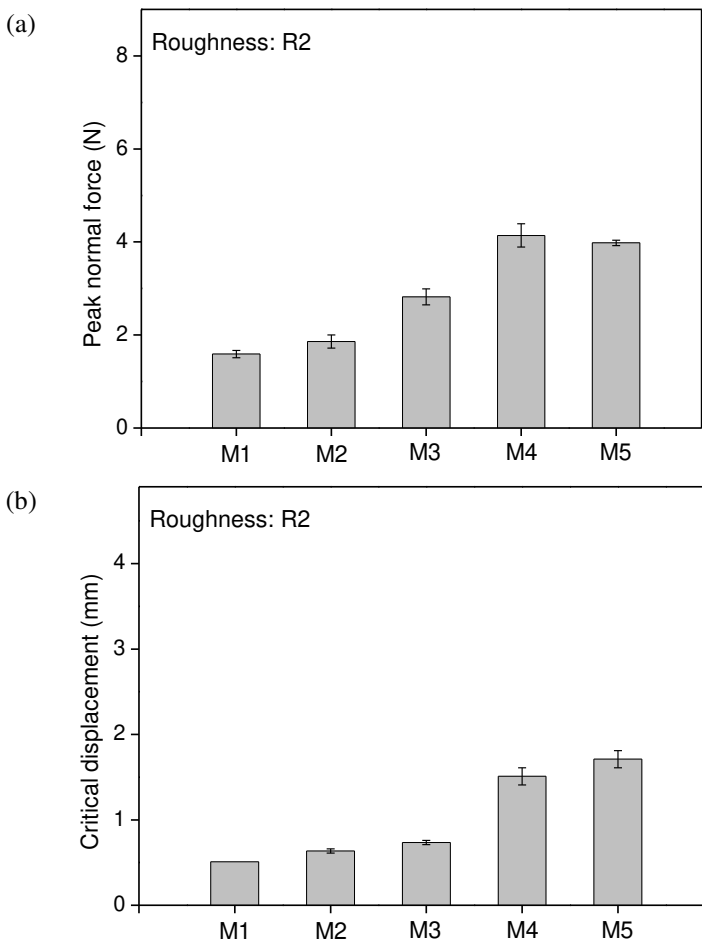


Figure 8.4 Normal force versus displacement curves for substrates with different surface moisture contents.

It was shown that the normal force evolution followed the same trend, as observed in the previous section. Similar as in the previous section, four parameters were derived from the normal force versus displacement curves including the peak

normal force, the critical displacement, the total displacement, and the dissipated energy, as plotted in Figure 8.5. Results indicate that the wet surface (M4) contributed to the highest peak normal force (average value 4.14 N) while the oven-dried surface (M1) resulted in the lowest peak normal force (average value 1.59 N). Moreover, the critical displacement and total displacement also increased as the surface moisture content increased. This can be interpreted by an enhanced tensile adhesion at the interface, where more water was present and the occurrence of the detaching failure was delayed. As a result, the energy dissipated during the lifting process was also increased. This will be further discussed in the following section.



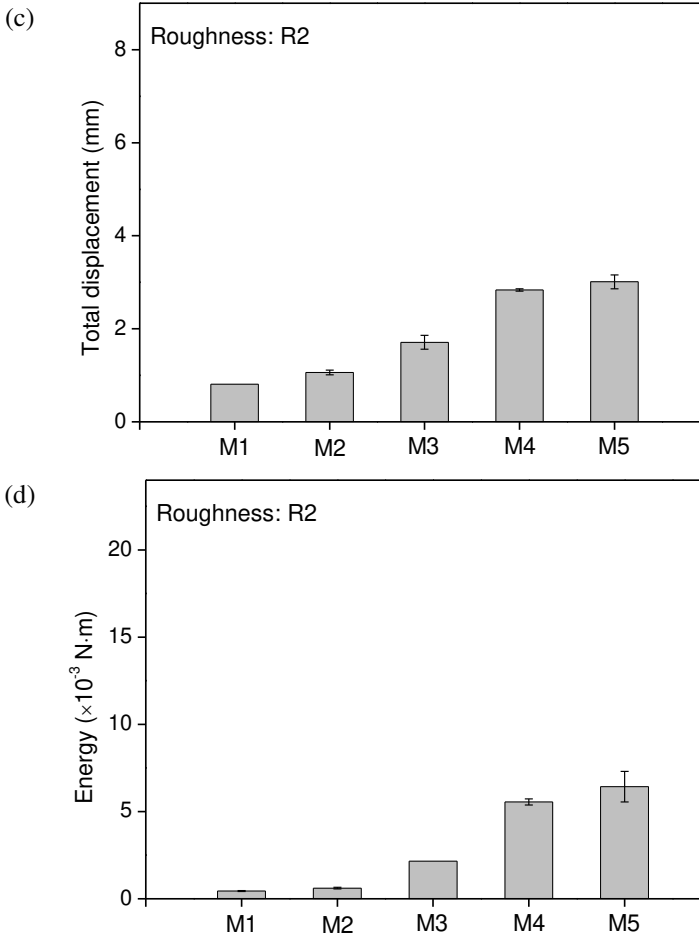


Figure 8.5 Peak normal force (a), critical displacement (b), total displacement (c), and dissipated energy (d) of fresh samples measured with different surface moisture contents (error bars represent the standard error,  $n=2$ ).

### 8.3.2 Sag resistance of printed layers

3D concrete printing tests were performed to investigate the sag resistance of 3D printed layers with different substrate conditions, as shown in Figure 8.6. It was indicated that a maximum of 8 layers can be printed before failure occurred with the uncoated substrate R2-M3, while 10 layers were reached with the coated substrate R2-M3-CT. Moreover, a different failure pattern was observed. For the uncoated substrate R2-M3, the failure occurred at the interface between the first layer and the lower surface of the concrete stroke. While the fracture propagated in the bulk of the printed layers when the coated substrate R2-M3-CT was used. The distinct failure patterns also manifested that the negative influence of the rough substrate surface on the adhesion of the fresh material could be minimized



by applying a layer of coating onto the substrate beforehand. The negative influence of the rough substrate surface in the 3D concrete printing test was following the tack test results. However, for the polished substrate R1-M3, an obvious overall slippage, i.e. all printed layers moved along the printing direction while printing another layer, was observed. As a result, only 4 layers were printed before failure occurred at the interface. It can be interpreted that the substrate surface with a lower roughness level (e.g. polished substrate R1) cannot provide enough friction against the printing direction, which would compromise the lateral adhesion in the shear direction. This was also related to the cohesion of the fresh material, which is worthy of further investigation.

On the other hand, the influence of the substrate surface moisture content on the sag resistance of 3D printed layers was analyzed with different substrate conditions including air-dried substrate (R2-M2), the saturated-surface-dry substrate (R2-M3), and the wet substrate (R2-M4). It was shown that a maximum of 6 layers was printed with the air-dried substrate, which was lower than that with the saturated-surface-dry substrate. This followed the tack test results where the saturated-surface-dry substrate (M3) led to a stronger tensile adhesion in the fresh state in comparison with the air-dried substrate (M2). However, an overall slippage of the printed layers along a horizontal direction was also observed when the wet substrate was used. This can be explained by the presence of superfluous water at the interface, leading to less friction and higher overall slippage. Further explanations will be given in the following section.

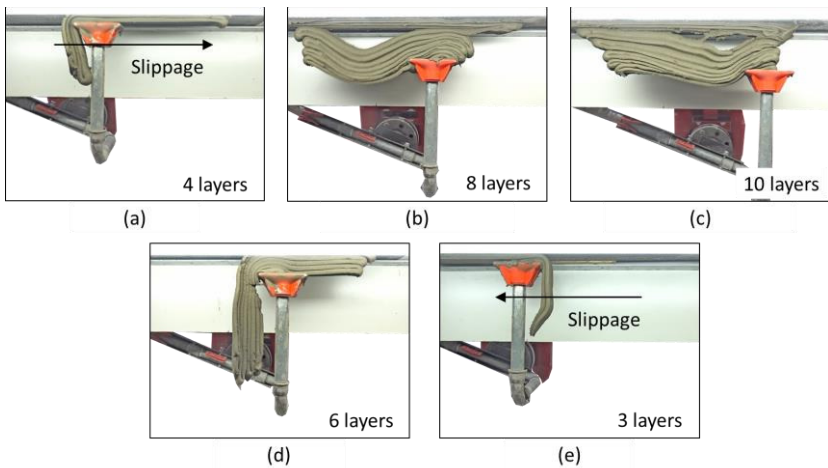


Figure 8.6 Effect of substrate surface roughness levels and moisture contents on the sag resistance of 3D printed layers, (a) R1-M3, (b) R2-M3, (c) R2-M3-CT, (d) R2-M2, and (e) R2-M4.

### 8.3.3 Tensile bond of hardened samples

In this section, the influence of the substrate surface roughness and moisture content on the tensile adhesion of 3D printed layers in the hardened state is evaluated including five types of substrates (R1-M3, R2-M3, R2-M3-CT, R2-M2, and R2-M4). For one substrate condition (R2-M3), a comparison is also made with molding casting (R2-M3-MC). The tensile bond strength at the age of 28 days was measured by the pull-off test, as shown in Figure 8.7. Results indicated that the average value of the tensile bond strength of samples printed on a polished substrate (R1-M3) was lower than that printed on a gritblasted substrate (R2-M3). Similar results about the influence of substrate surface roughness were reported in other researches. For example, Beushausen and Alexander [228] indicated that notched interfaces had higher bond strength, up to 45% higher than gritblasted surfaces and 220% higher than smooth surfaces at 28 days. Moreover, Valikhani et al. [253] pointed out that a failure load of about 80-90% of concrete monolithic samples can be obtained by increasing the surface roughness. However, the average values of the tensile bond strength with substrates R1-M3 and R2-M3 were merely 0.11 MPa and 0.47 MPa, respectively, which were lower than the Concrete Society recommended minimum bond strength of 0.8 MPa for wet-process sprayed mortar [254]. Fortunately, the tensile bond strength of hardened samples can be improved by applying a layer of coating on the substrate beforehand. In this way, the tensile bond strength of the sample applied on the coated substrate (R2-M3-CT) reached an average value of 1.08 MPa, which was more than twice the average tensile bond strength obtained with the uncoated substrate R2-M3. Further, distinguished from the printed samples, the mold cast samples placed on the gritblasted substrates (R2-M3-MC) remarkably reached an average value of 2.31 MPa. The measured values followed the published bond strength of repair materials ranging from 0.8 to 3.5 MPa [182, 254].

The tensile bond strength of samples with different substrate surface moisture content including air-dried (R2-M2), saturated-surface-dry (R2-M3), and wet (R2-M4) were 0.65, 0.47, and 0.45 MPa, respectively. Results indicated that the tensile bond strength of hardened samples reduced as the substrate surface moisture content increased. It is widely reported that the substrate surface moisture content has an important influence on the bond strength. In most cases, the presence of moisture can facilitate the bond strength due to the fact that a dry substrate surface may absorb water from the overlay and result in a weak connection at the contact area. In some other cases, a dry substrate surface is expected such as for the placement of epoxy-based materials [176]. For the cement-based material used in this study, however, pre-wetting the substrate surface may not contribute to the tensile adhesion in the hardened state [255, 256], and in some situations, negatively affects the bond [188]. This can be interpreted by the dilution effect at the interface when a very wet surface is adopted. In addition, the water in open pores can further diminish the mechanical interlocking effect [257]. For example,

Luković et al. [258] indicated that an increase in substrate surface moisture content resulted in increased porosity and a lower degree of hydration at the interfacial transition zone (ITZ). As a result, the overall effect of increasing the substrate surface moisture content appeared to be a decrease in tensile bond strength between the substrate and applied layers. Nevertheless, the tensile bond strength of these three series including R2-M2, R2-M3, and R2-M4 were significantly lower when compared with that of the mold cast samples (2.31 MPa).

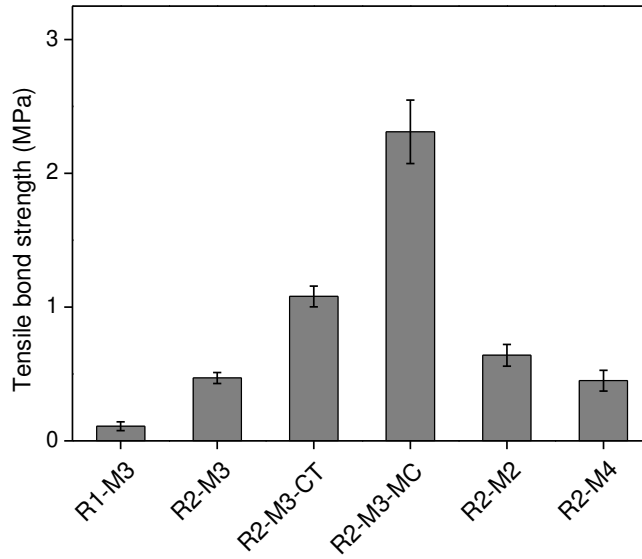


Figure 8.7 Effect of substrate surface roughness level and moisture content on tensile bond strength after curing for 28 days (error bars represent the standard error,  $n=6$ ).

The failure patterns of tested samples are shown in Figure 8.8. It was observed that the failure of the samples with a polished substrate (R1-M3) and uncoated gritblasted substrate (i.e. R2-M2, R2-M3, and R2-M4) occurred fully at the interface. While the failure of the samples with a coated substrate (R2-M3-CT) and the mold cast samples (R2-M3-MC) occurred partially inside the substrate and the overlay, which corresponded to higher tensile bond strength. It can be predicted that the printed material failed to fill the rough notches, especially for the air-dried substrate (R2-M2) where no trace was observed on the substrate surface after de-bonding. Different from the air-dried substrate, a very thin layer with a different color remained on the over-wet substrate (R2-M4), indicating that the fresh material penetrated to the wet substrate with superfluous water at the interface. However, due to the higher water-to-cement ratio, the tensile bond strength with substrate R2-M4 at 28 days was even lower when compared with R2-M2 [258].

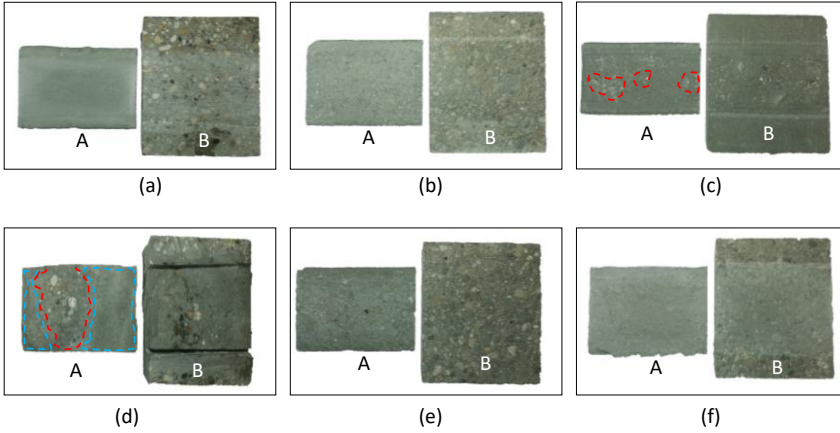


Figure 8.8 Failure patterns on fracture surface A (on the side of the printed layers) and fracture surface B (on the side of the substrate) of samples after the pull-off test (failure in red zone occurred in the substrate and failure in blue zone occurred in the printed layers), (a) R1-M3, (b) R2-M3, (c) R2-M3-CT, (d) R2-M3-MC, (e) R2-M2, and (f) R2-M4.

### 8.3.4 Analysis of adhesion mechanism

The influence of the substrate surface roughness and moisture content on the tensile adhesion is schematically illustrated in Figure 8.9. In terms of the substrate surface roughness, two levels including the macro roughness and the micro roughness can be considered [228]. The macro roughness is provided by surface textures while the micro roughness is provided by open pores and cavities. Mechanical interlocking can thus be formed when the fresh material flows into the surface textures and fills open pores and cavities. It was indicated that filling the open pores and cavities depended on the interfacial properties such as hydrophobicity. For example, Feng et al. [259] pointed out that the hydrophobicity would remarkably affect the liquid wettability of the interface. This was also found by Courard [260] that the interfacial energy can be significantly affected by the hydrophobicity of the interface. Specifically, a hydrophobic surface would generate a high contact angle and hinder the cement paste from entering the open pores and cavities, leading to the compromised tensile adhesion at the interface. Inversely, a hydrophilic surface contributed to a small contact angle and facilitates tensile adhesion [261]. Different from filling the open pores and cavities, surface textures (i.e. macro roughness) can always be filled by using a high-fluidity material or applying vibration under normal circumstances such as a concrete repairing process [176]. However, in this study, macro surface textures might not be filled with the relatively stiff material due to the absence of vibration and a limited squeezing pressure at the outlet, see case R2-M2 shown in Figure 8.9 (e). As a result, the tensile adhesion both in the fresh and hardened state would be compromised due to a relatively low contact area. In contrast, the fresh material

was more likely to have sufficient contact to the polished substrate with less rough textures and an improved tensile adhesion in the fresh state, as shown in Figure 8.9 (a). However, such a polished substrate failed to provide enough mechanical interlocking for hardened samples, where the tensile bond strength was merely 0.11 MPa at the age of 28 days. Fortunately, the negative influence of macro surface textures on the tensile adhesion in the fresh state can be reduced by coating the substrate beforehand, as verified by both the tack test and the large-scale 3D printing test, see Figure 8.9 (c). As such, sandblasted substrate with a fresh coating is recommended for the following experiments (see Chapter 9 and Chapter 10). Moreover, the tensile adhesion of hardened samples on the coated substrate was improved when compared with the uncoated substrate. Nevertheless, in comparison with the mold cast sample, as shown in Figure 8.9 (d), the tensile adhesion of the hardened layers on a coated substrate was still lower, due to the probable existence of voids at the interface between the coating and the first printed layer. Similar results were previously reported regarding the interlayer bond of 3D printed elements. For example, Rahul et al. [168] stated that the porosity was higher for the samples extracted from the interface position between two adjacent layers, as compared to the mold cast concrete and the bulk in the printed layer. A similar conclusion was also given by Le et al. [132] that more voids appeared at the interface between 3D printed layers. Further, Zareiyan et al. [148] pointed out that the interlayer bond strength was sensitive to interlocking where the observed increase in interlayer bond strength could be attributed to the increase in the contact area of layers.

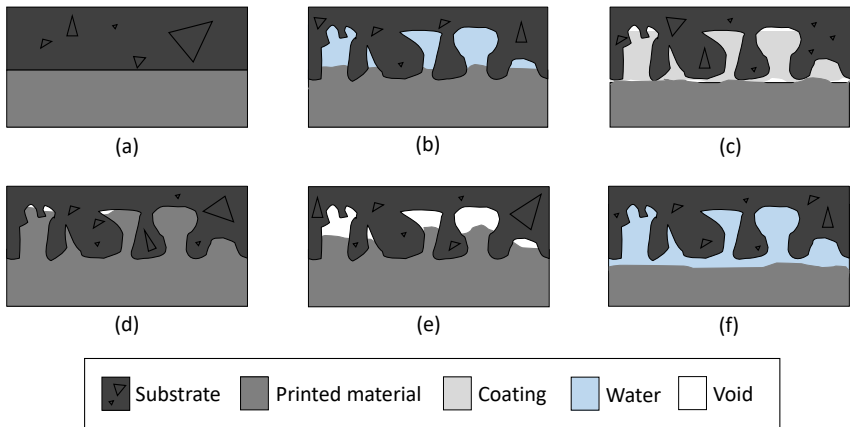


Figure 8.9 Schematic view of the contact zone with different substrate surface roughness levels and moisture contents, (a) R1-M3, (b) R2-M3, (c) R2-M3-CT, (d) R2-M3-MC, (e) R2-M2, and (f) R2-M4.

Although coating the substrate can enhance the tensile adhesion in the fresh and hardened state, such a manual intervention would reduce the construction efficiency and increase the cost accordingly. Some potential solutions can already

be found in the existing technologies. For example, in the context of concrete repair, Beushausen and Alexander [228] indicated that higher fluidity of repair materials led to better bond properties because more cement slurry can penetrate open pores and cavities and enhance the mechanical interlocking to the hardened substrate. However, the printed material for hard rock tunnel linings should be stiff enough to support the loose rock area and avoid any rebound [114]. Such a conflicting demand can be achieved by using a highly thixotropic material or adopting a stiffening control system at the nozzle position, where the material gains fast setting after full contact with the substrate [119, 124]. Alternatively, incomplete contact is expected to be avoided by applying additional pressure after extrusion. The influence of pressure levels on the tensile adhesion between the printed material and the substrate remains an interesting point for further study. It should also be noted that the authors failed to print at the lower surfaces of very rough substrates such as the hammered substrate (R3) and the water-jetted substrate (R4) with the printing path of a straight line. To assume complete contact with very rough substrates, the movement of the nozzle should be controlled according to the profile of the substrate surface (i.e. the internal surface of the excavated rock wall), rather than a pre-defined path. The shape of the substrate surface can also be scanned automatically, which can be derived from various robotic tunnel inspection systems [262].

Regarding the influence of the substrate surface moisture content on the tensile adhesion in the fresh and hardened state, experimental results showed that the saturated-surface-dry substrate (R2-M3) led to the highest tensile adhesion in the fresh state when compared to the air-dried substrate (R2-M2) and the wet substrate (R2-M4). In comparison with the air-dried substrate, as shown in Figure 8.9 (e), the rough texture and voids were filled with free water for a saturated-surface-dry condition, see Figure 8.9 (b). As a result, the tensile adhesion in the fresh state was improved due to the surface tension [176]. However, if the substrate was over-wetted such as the wet substrate, see Figure 8.9 (f), superfluous water would be present at the interface, which would compromise the shear resistance of the fresh material against the substrate and lead to a reduced lateral adhesion in the fresh state [244, 252]. Moreover, an increased surface moisture content resulted in a reduced tensile adhesion in the hardened state. Although the increased substrate surface moisture content would benefit from the migration of ions to the substrate with capillary absorption, such a high amount of water would increase the water-to-cement ratio at the near-to-interface area and generate a more porous structure in this area [176]. As a result, the tensile bond strength of hardened samples reduced as the surface moisture content increased.

## **8.4 Summaries**

In this chapter, the influence of the substrate surface roughness and moisture content on the adhesive properties of printed materials in the fresh and hardened

state was studied. Based on the experimental results, the following summaries are given:

(1) The macro surface textures of the rough substrate can not be filled by the stiff material for 3D concrete printing, leading to partial contact between the rough substrate and the printed layers. As a result, the tensile adhesion in the fresh and hardened state is compromised. A less rough substrate such as a polished substrate is beneficial for the tensile adhesion in the fresh state due to adequate contact while such a polished substrate fails to provide enough mechanical interlocking in the hardened state. Therefore, only sandblasted substrates will be used in the following studies (Chapter 9 and Chapter 10).

(2) By coating the rough substrate, the tensile adhesion in the fresh and hardened state is improved, as the macro textures are filled. Compared to the mold cast samples, the tensile adhesion of the hardened printed layers is still lower because of the presence of small voids at the interface between the coating and the printed overlays.

(3) As compared to the dried substrate, the substrate with a surface moisture content of saturated-surface-dry leads to higher tensile adhesion in the fresh state because the trapped water in the macro textures provides stronger dragging force by surface tension. While an over-wetted substrate results in reduced tensile adhesion due to the presence of superfluous water at the interface, which limits the shear resistance of printed layers against the substrate. Regarding the hardened state, an increased surface moisture content results in reduced tensile adhesion because higher amounts of water would increase the water-to-cement ratio at the near-to-interface area and generate a more porous inner structure at this zone.





## **Influence of polymer modification on adhesion**

### **9.1 Introduction**

This Chapter focuses on improving the adhesion properties of 3D printed concrete by polymer modification. Lessons could already be learned from the components of repair mortars. Commercially available repair mortars are usually modified with a redispersible polymer powder (RDP) and a cellulose ether (CE) [191, 263]. Although the working mechanism and application of redispersible polymer powder and cellulose ether have been widely explored for the application in repair mortars, the effect of these admixtures on the performance of 3D printable concrete for rock tunnel linings has not been studied yet. In this Chapter, the effect of admixtures including redispersible polymer powder and cellulose ether on the adhesive properties of 3D printable concrete for rock tunnel linings is evaluated. First, seven mixtures modified with different dosages of redispersible polymer powder and cellulose ether are formulated and a tack test with a loading control mode is performed to measure the adhesive strength of freshly printed materials. A stress growth test with a constant shear rate is used to measure the shear resistance of fresh materials for a better understanding of the adhesion performance. Moreover, an upside-down printing test against the lower face of a supported concrete slab is performed to measure the sag resistance and for comparison with the tack test results and stress growth test results. Finally, a pull-off test is performed to compare the tensile bond strength of printed materials in the hardened state.

### **9.2 Experimental program**

Sand, cement, superplasticizer, cellulose ethers including CE1 (MH300P2) and CE6 (MB60000P2), and redispersible polymer powder were used for the mixtures developed in this chapter. Seven mixtures were formulated including one reference mixture (REF), two redispersible polymer powder-modified mixtures (RDP-0.2% and RDP-0.6%), and four cellulose ether-modified mixtures (CE1-0.2%, CE6-0.2%, CE6-0.4%, and CE6-0.6%). The sand to binder ratio was fixed as 1 and the water-to-binder ratio was fixed as 0.35 for all mixtures. The dosage of superplasticizer was fixed as 0.1% by mass of binder. The addition levels of redispersible polymer powder were 0.2% and 0.6% by mass of binder respectively

for RDP-0.2% and RDP-0.6% mixtures. The addition level of CE1 was 0.2% for the CE1-0.2% mixture. From the evaluation of trials conducted at the dosage of 0.2%, it was observed that CE6 performs significantly better than CE1, which will be further explained in the following sections. This is also justified from the higher viscosity specified by the manufacturer for CE6 as compared to CE1. Therefore, the better performing cellulose ether, CE6 was selected for further evaluations at dosages of 0.4% and 0.6%. Summarily, the addition levels of CE6 were 0.2%, 0.4%, and 0.6% by mass of binder respectively for CE6-0.2%, CE6-0.4%, and CE6-0.6% mixtures.

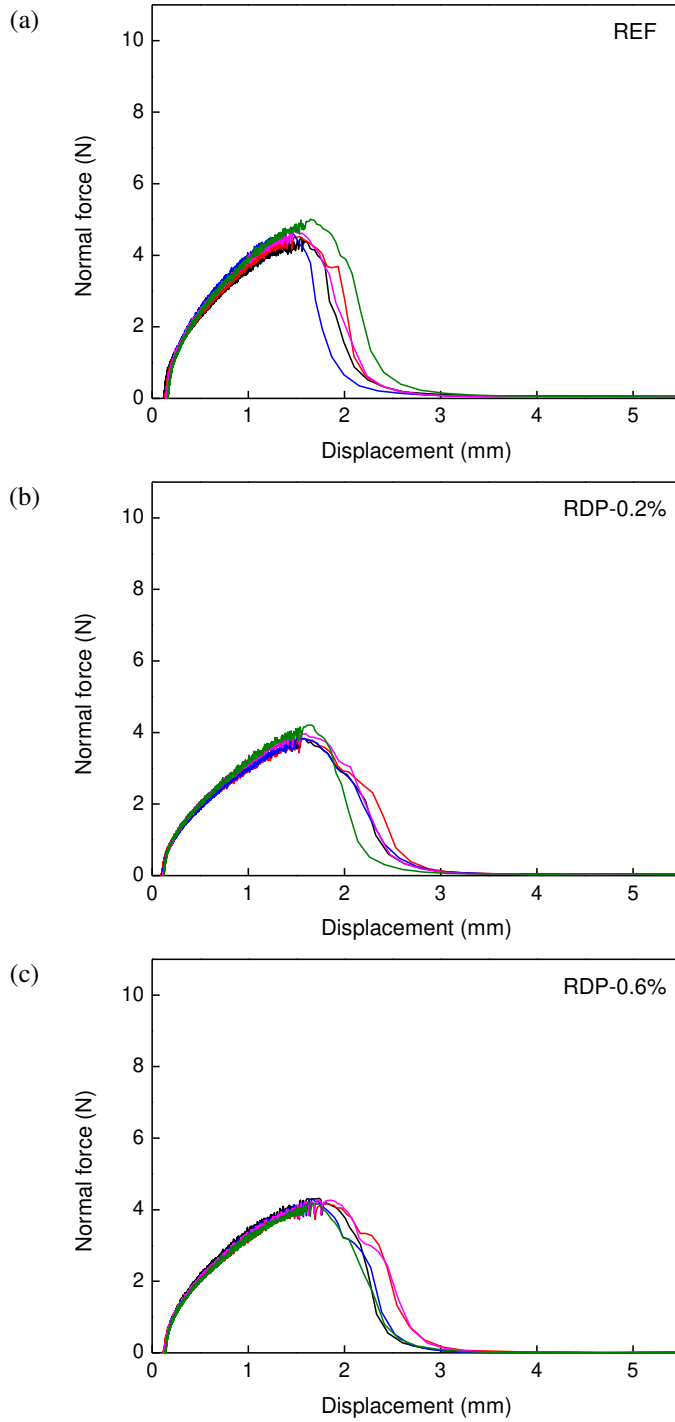
Small mixture batches (1.5 liters) were prepared in a conventional planetary mixer according to the following protocol: (1) manually mixing superplasticizer with water for 10 s, (2) adding water (and superplasticizer) to cement and rotating the paddle at 140 rpm for 30 s, (3) adding sand and rotating the paddle at 140 rpm for 30 s, (4) rotating the paddle at 285 rpm for 30 s, (5) scraping and resting for 90 s, (6) rotating the paddle at 285 rpm for 60 s, (7) adding redispersible polymer powder or cellulose ether and mixing at 285 rpm for 60 s. The total mixing period was 310 s.

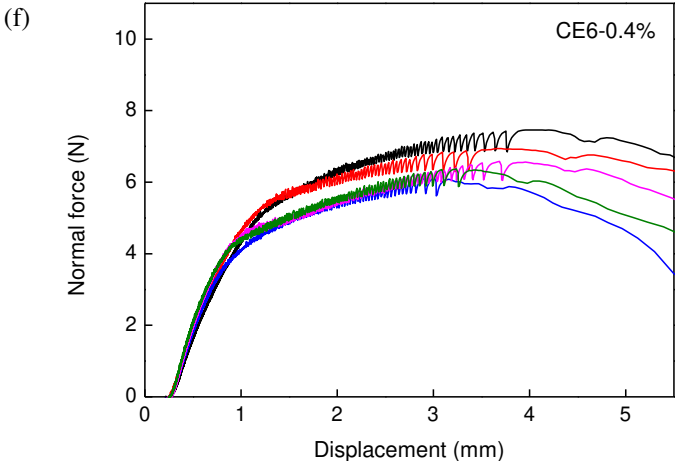
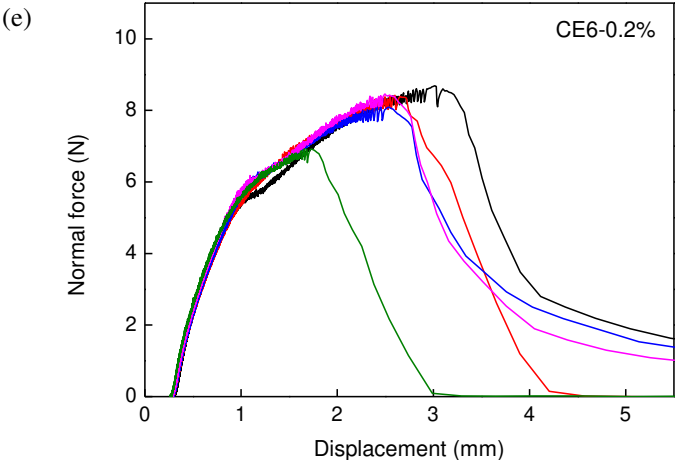
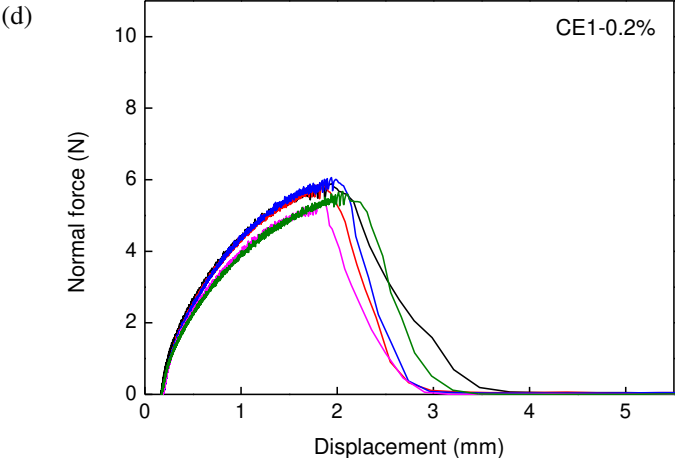
In addition, big mixture batches (20 liters) were prepared in a pan mixer for 3D printing experiments according to the following protocol: (1) manually mixing superplasticizer with water for 10 s, (2) mixing dry materials (sand and cement) for 30 s, (3) adding water (and superplasticizer) to the dry materials and mixing for 180 s, (4) scraping and resting for 60 s, (5) adding redispersible polymer powder or cellulose ether and mixing for 60 s. The total mixing period was 340 s.

## **9.3 Results and discussion**

### **9.3.1 Normal force versus displacement curves**

Normal force versus displacement curves were obtained from the tack test, as shown in Figure 9.1. The curves showed that the tested samples followed two main stages. In the first stage, the normal force increased from zero to a peak value, where an inward flow with a small displacement was observed. The second stage was characterized by a debonding behavior where the normal force dropped sharply from the peak value to zero and the displacement suddenly increased to a maximum value. It should be noted that cellulose ether-modified mixtures, especially for CE6 presented quite long increase stages, which will be explained in the following sections.





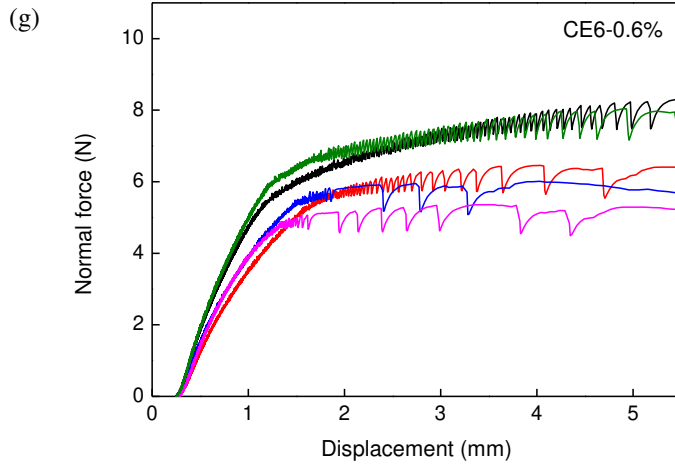


Figure 9.1 Normal force versus displacement curves obtained in the tack test.

The first issue to be discussed relates to the source of the tack effort which has to be exerted to separate the two surfaces, as well as the failure mode. The failure mode of the fresh sample in the tack test after debonding was recorded, as shown in Figure 9.2.

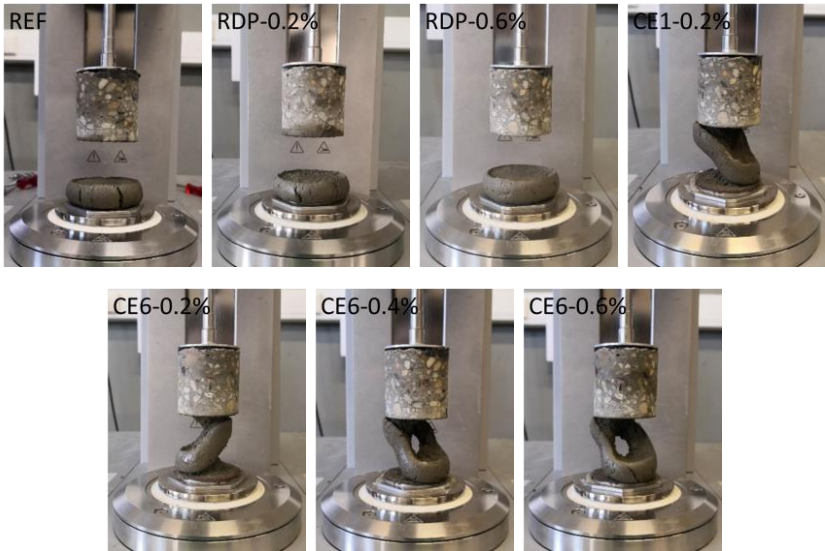


Figure 9.2 Failure modes of fresh samples in the tack test.

It was shown that the adhesive failure (i.e. failure occurring at the interface between the fresh sample and the concrete slab) occurred when we tested the reference mixture (REF) and the two redispersible polymer powder-modified mixtures (i.e. RDP-0.2% and RDP-0.6%). While cohesive failure (i.e. failure

occurring inside the fresh material) occurred when testing the four cellulose ether-modified mixtures (i.e. CE1-0.2%, CE6-0.2%, CE6-0.4%, and CE6-0.6%). In previous studies, Mohamed Abdelhay et al. [248] presented the tackiness of mud and pointed that the physical origin of the effort required to separate the plates could be the force required to overcome the Laplace depression (or capillary pressure) in the mud layer, generated by the curvature of the meniscus at the mud-plate interface as the mud layer was put in tension [264]. In addition, another physical explanation was that the effort required to lift the plates was the force required to force the inwards flow of the mud and the flow was almost entirely radial shear flow in the early stages of the lifting process [265]. A small increase in plate separation induced a large inward motion of the mud, which was the same phenomenon as was observed during the tack test of the mixtures formulated in this study.

In addition, Mohamed Abdelhay et al. [248] also pointed out that the failure associated with the effort required to separate the plates was either cohesive rupture in the mud layer or adhesive fracture at the mud-solid interface. Four types of failure profiles of mortars (i.e. cohesive rupture, adhesive rupture, liquid behavior, and mortar behavior) were described by Kaci et al. [266] while the failure mode of paste was always found to be cohesive, that is, occurring within the layer of paste, whatever the type of paste and the type of de-bonding experiment [251]. In this study, the failure occurred at the interface between the gritblasted concrete plate and fresh sample for the reference mixture and the redispersible polymer powder-modified mixtures, rather than inside the fresh mortar mixtures, indicating that the interface was a weak spot of the mixtures in the fresh stage. This result can be interpreted in terms of the presence of sand in the fresh sample which increased the overall shear stress and contributed a lot to the shear resistance [267]. The overall shear stress of a flowing mortar can be taken as the sum of the shear stress resulting from the yield stress of the cement paste, the flow of the cement paste, the interaction between cement paste and aggregates, and the shear stress resulting from the aggregate movement [267]. Therefore, it can be concluded that the flow resistance of the sample towards the center of the plates dominated the increasing stage (e.g. the evolution of deformation towards the critical displacement where the peak normal force occurred). The peak normal force was determined by the adhesion properties at the interlayer position when adhesive failure occurred, while the peak normal force was determined by the shear resistance of the fresh material when cohesive failure occurred. The reason why cellulose ether-modified mixtures presented a different normal force versus displacement profile was that a high dosage of cellulose ether enhanced the adhesion at the interface while it decreased the shear resistance, which will be further explained below.

To go one step further, the peak normal force is shown in Figure 9.3. A one-way ANOVA test was used to statistically analyze the influence of the addition of

redispersible polymer powder or cellulose ether on the peak normal force obtained in the tack test. A p-value less than 0.05 ( $p < 0.05$ ) was considered statistically significant. According to the one-way ANOVA test, the redispersible polymer powder-modified mixtures had no significantly different peak normal force compared to the reference mixture (REF) while all cellulose ether-modified mixtures presented a significant difference. It was also shown that the peak normal force was slightly decreased with the addition of redispersible polymer powder, compared to the reference mixture (REF). While all the cellulose ether-modified mixtures showed a higher peak normal force compared to the reference mixture (REF). In addition, the CE6-0.2% mixture showed a higher peak normal force than the CE1-0.2% mixture. For CE6-based mixtures, the increase in CE6 admixture addition level (i.e. 0.4% and 0.6%) did not result in a further enhancement of the peak normal force compared to the CE6-0.2% mixture, indicating that the adhesion enhancement of the CE6 admixture was limited.

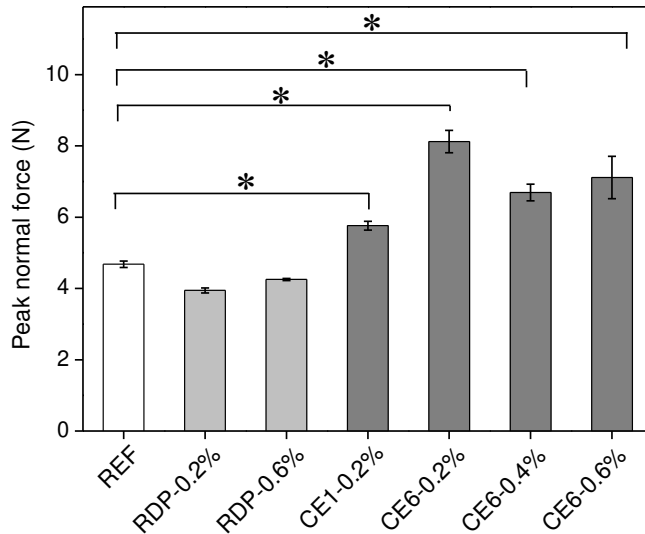


Figure 9.3 Peak normal force derived from the normal force versus displacement curves (error bars represent the standard error,  $n=5$ , symbol “\*” indicates a significant difference with a significance level of  $p < 0.05$ ).

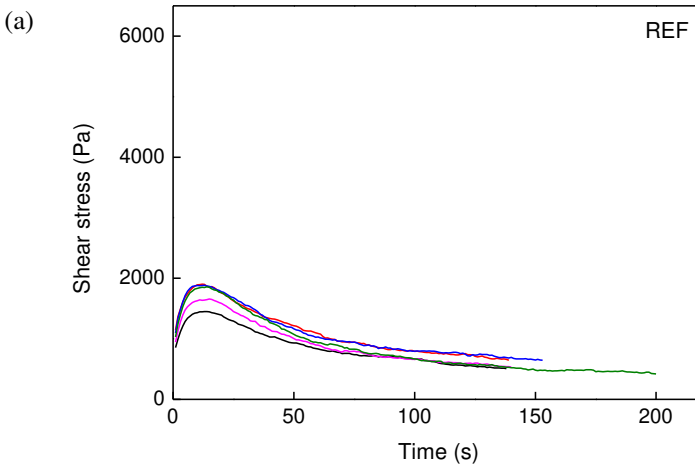
In previous studies, redispersible polymer powder has been demonstrated to improve the bond strength in the hardened state to various substrates [194]. Normally, it would take a long time for polymer particles to flocculate and form polymer films with the drainage of water between polymer particles [263]. However, the testing period of a tack test (normally less than 10 minutes) was too short to allow the formation of polymer films. Nevertheless, structural build-up of the tested material should also be considered if a very low loading rate is adopted. As already discussed above, the peak normal force measured in the tack test relates

to the shear of the material. As such, the shear resistance of the material can be improved due to the structural build-up, leading to enhanced adhesion in the fresh state. However, Zhang et al. [268] pointed out that adding redispersible polymer powder in the mixture would reduce the structural build-up rate. This is reflected by the lower values of the peak normal force for the two redispersible polymer powder-modified mixtures (RDP-0.2% and RDP-0.6%).

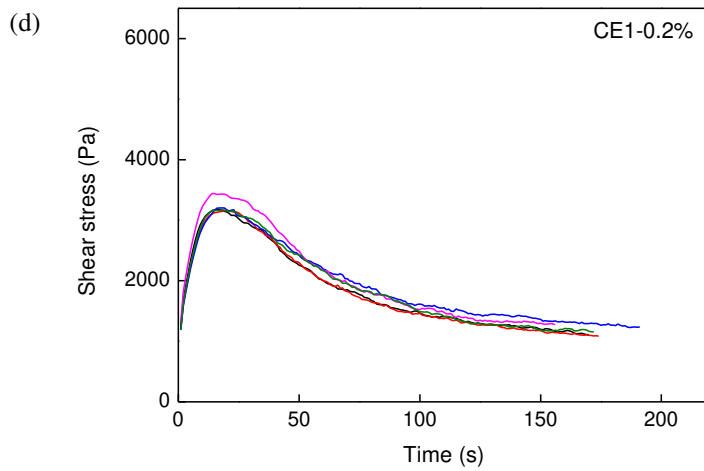
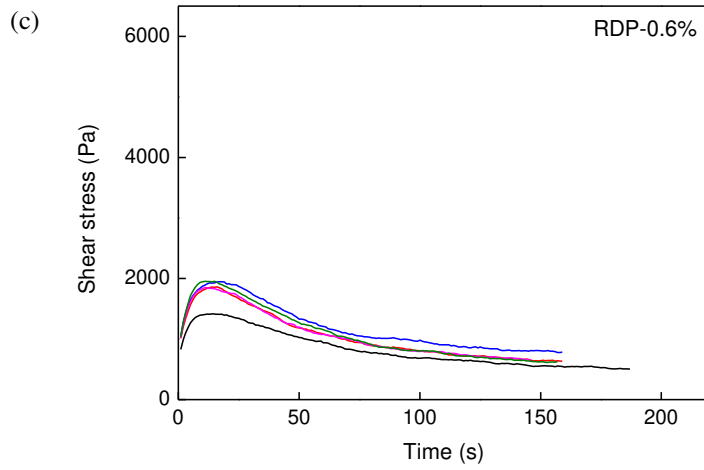
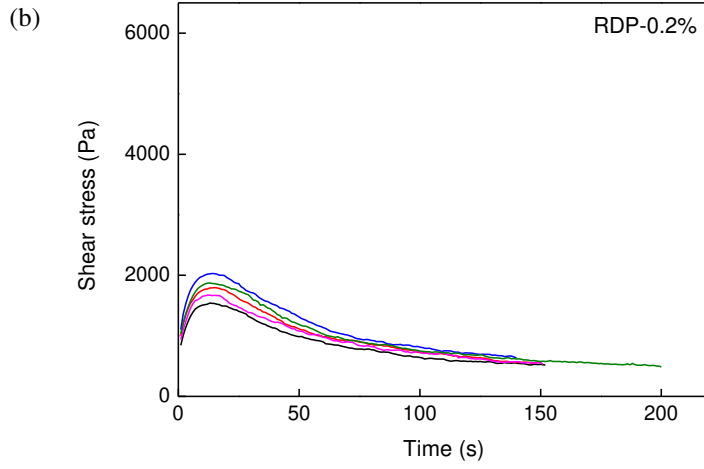
The addition of cellulose ether led to an increased peak normal force, which may be due to the migration of cellulose ether from the bulk of the fresh material to the interface with the hardened substrate. After coming into contact with the gritblasted concrete plate, cellulose ether can absorb on the concrete surface either by hydrogen bonding or by specific interaction involving the hydroxyl groups of cellulose ether and the concrete surface, resulting in a better adhesion performance [191]. Compared to CE1, CE6 possessed more functional groups and therefore resulted in a higher peak normal force.

### 9.3.2 Flow resistance

The shear stress versus time curves are shown in Figure 9.4. It was shown that the shear stress increased after the measurement started, followed by a decreasing stage. The peak shear stress was treated as the yield stress.







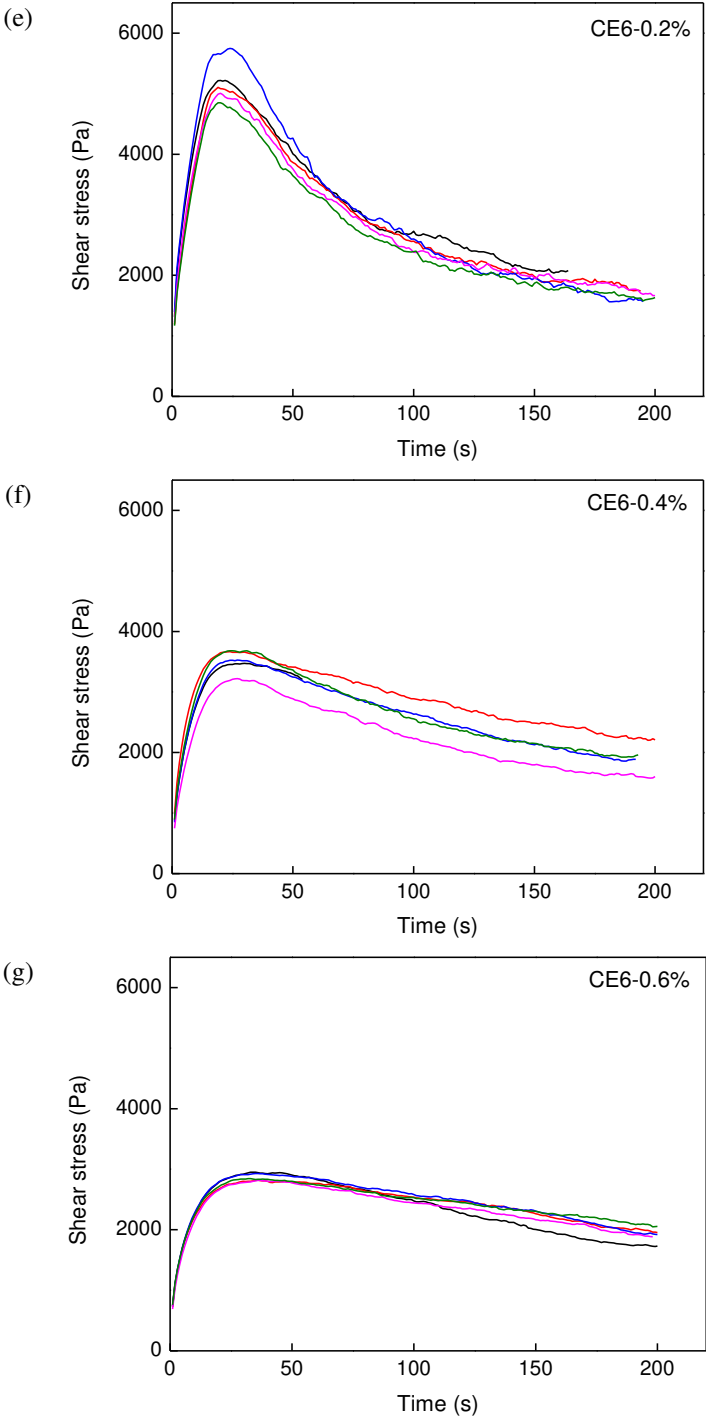


Figure 9.4 Shear stress versus time curves.

To better understand the results, the yield stresses of the mixtures are shown in Figure 9.5. A one-way ANOVA test was used to statistically analyze the influence of the addition of redispersible polymer powder or cellulose ether on the yield stress obtained in the stress growth test. According to the one-way ANOVA test, the redispersible polymer powder-modified mixtures had no significantly different yield stress compared to the reference mixture (REF) while all cellulose ether-modified mixtures presented a significant difference. The results showed that the mean yield stresses of the two redispersible polymer powder-modified mixtures (RDP-0.2% and RDP-0.6%) were 1781.8 Pa and 1806.3 Pa respectively, being almost the same as the mean value obtained for the reference mixture (1750.1 Pa). On the contrary, the yield stress of the four cellulose ether-modified mixtures (CE1-0.2%, CE6-0.2%, CE6-0.4%, and CE6-0.6%) was distinctly higher than the value obtained for the reference mixture. In addition, the increase in yield stress became less pronounced when the dosage of CE6 increased from 0.2% to 0.6%. The CE6-0.2% mixture possessed a maximum mean yield stress value of 5185.6 Pa.

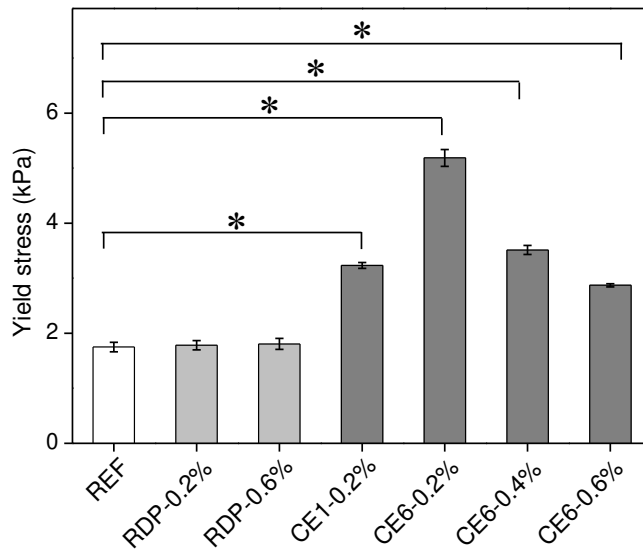


Figure 9.5 Yield stress derived from the shear stress curves (error bars represent the standard error,  $n=5$ , symbol “\*” indicates a significant difference with a significance level of  $p < 0.05$ ).

Previous studies pointed out that redispersible polymer powder decreased the yield stress because of the ball bearing action of polymer particles, the entrained air, and the dispersing effect of surfactants in redispersible polymer powder products [269]. Ohama et al. studied the influence of polymer-cement ratio on the fluidity by the slump test and showed that the water-cement ratio at a given slump is markedly reduced with an increase in the polymer-cement ratio [194]. It was also pointed

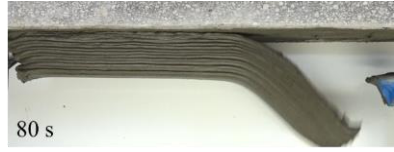
out that redispersible polymer powder had a relatively small dimension compared to that of cement particles [194] and therefore worked as a lubricant in the fresh cement-based materials, leading to smaller yield stress and higher workability. While in this study, there is no significant difference between the reference mixture and redispersible polymer powder-modified mixtures, which can be explained by the relatively low addition level (0.2% and 0.6%).

The function of cellulose ether in changing yield stress can be explained by a combination of different physicochemical phenomena that depend on the nature of the cellulose ether and its concentration [270]. An increase in yield stress involved a bridging flocculation mechanism, where the chain of cellulose ether would be adsorbed onto two or more cement particles, physically holding them together [271]. Therefore, with more functional groups, mixture CE6-0.2% obtained a much higher mean yield stress (5185.6 Pa) than mixture CE1-0.2% (3230.5 Pa).

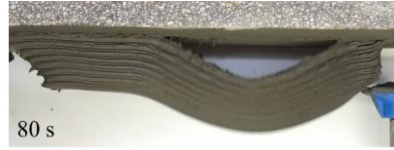
Regarding the impact of cellulose ether dosages on the yield stress, contradictory results have been found in the literature. Some authors held the opinion that a high dosage of cellulose ether would increase the yield stress because of depletion flocculation where non-absorbed polymers were depleted from a volume exclusion shell around large particles. The difference in polymer concentration in bulk solution concerning the depleted zone led to an increase of the osmotic pressure in the system, which caused the flocculation [49]. Some authors confirmed that cellulose ether would decrease the yield stress [272]. Jenni et al. investigated the role of cellulose ether on changes in mortar microstructures [195]. They proposed that the air entrapped during the mixing process was stabilized in the fresh mixture due to the decrease of the surface tension of water and the accumulation of cellulose ether at the air-void interfaces. It was also pointed by Wyrzykowski et al. [273] that a coarsening of the porosity and a slight increase in the total volume of pores occurs at a higher dosage of cellulose ether. This is likely due to the agglomeration of original subspherical pores, found to be more pronounced for the increased cellulose ether dosage. Therefore, the yield stress decreased due to the increased proportion of air content inside the fresh mixture where air acted as a lubricant [274]. Another explanation of this decrease was the steric hindrance induced by the cellulose ether adsorbed onto cement particles [275].

### **9.3.3 Sag resistance of printed layers**

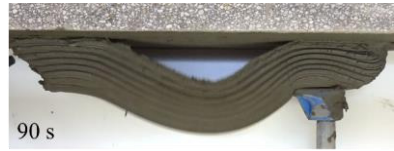
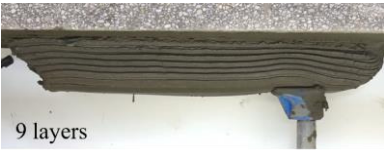
A 3D concrete printing test, involving printing upside down against the lower surface of a supported concrete slab, was performed. The tests were repeated twice for each mixture and only one of both experiments is shown in Figure 9.6.



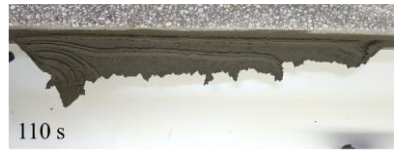
(a)



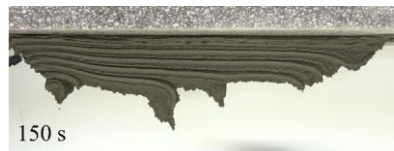
(b)



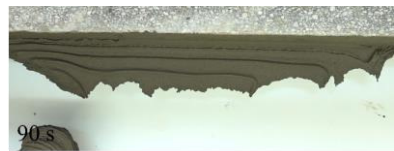
(c)



(d)



(e)



(f)



(g)

Figure 9.6 3D concrete printing test at the overhead position: left figures indicate the maximum amount of layers and right figures indicate failure modes, (a) REF, (b) RDP-0.2%, (c) RDP-0.6%, (d) CE1-0.2%, (e) CE6-0.2%, (f) CE6-0.4%, and (g) CE6-0.6%.

More details can be found in Table 9.1. Failure mode “adhesion” represents that failure occurred at the interface between the fresh material and the concrete slab, while failure mode “cohesion” represents that failure occurred at the interlayer position inside the fresh material.

Table 9.1 Maximum number of layers and failure modes (including adhesive failure and cohesive failure)

No.	Mixture	Maximum layers	Failure mode
1	REF	8/ 8	Adhesion
2	RDP-0.2%	8/ 9	Adhesion
3	RDP-0.6%	9/ 10	Adhesion
4	CE1-0.2%	9/ 11	Adhesion/ cohesion
5	CE6-0.2%	12/ 15	Cohesion
6	CE6-0.4%	9/ 10	Cohesion
7	CE6-0.6%	8/ 8	Cohesion

The reference mixture (REF) and the two redispersible polymer powder-modified mixtures (RDP-0.2% and RDP-0.6%) showed adhesive failure, indicating an insufficient adhesive strength. The cellulose ether-modified mixture (CE1-0.2%) presented adhesive failure in one test and cohesive failure in the other test. The other three cellulose ether-modified mixtures (CE6-0.2%, CE6-0.4%, and CE6-0.6%) only presented cohesive failure, indicating a strong adhesion at the position of the interface but relatively low shear resistance (i.e. low yield stress). The results of the upside-down printing tests follow the tack test results.

The maximum amount of layers  $n$  can be computed from the following equation:

$$n = \frac{\sigma_0}{\rho gh} \quad (9.1)$$

Where  $\sigma_0$  is the normal stress (Pa),  $\rho$  is the density of fresh material ( $\text{kg/m}^3$ ),  $g$  is the gravitational constant ( $9.81 \text{ m/s}^2$ ),  $h$  is the layer thickness (m).

For failure occurring at the interface,  $\sigma_0 = F/A$ , where  $F$  and  $A$  denote the normal force (N) and the plate area ( $\text{m}^2$ ). On the other hand, when the failure occurs inside

the fresh material,  $\sigma_0 = \sqrt{3}\tau_0$  based on the Von-Mises criterion [276], where  $\tau_0$  is the yield stress of the fresh material (Pa).

The maximum amount of layers for all mixtures predicted by the tack test, the stress growth test, and obtained from the upside-down printing test are shown in Figure 9.7. The results showed that the prediction from the tack test and the prediction from the stress growth test were qualitatively consistent with the results of the upside-down printing test. It should be noted that with the increase in CE6 dosage from 0% (REF) to 0.2%, the maximum number of layers predicted from the tack test increased from 12 layers to 21 layers, indicating an enhanced adhesion performance, as also confirmed by the upside-down printing test (from 8 layers to an average value of 13.5 layers). Furthermore, with the increase of CE6 dosage from 0.2% to 0.6%, the predicted number of layers from the tack test reached a plateau while the prediction from the stress growth test decreased from 21 layers to 18 layers, indicating that poor shear resistance played the key role, as also confirmed by the upside-down printing test, where the failure occurred inside the printed material and the maximum number of layers decreased from 13.5 (average value) to 8.

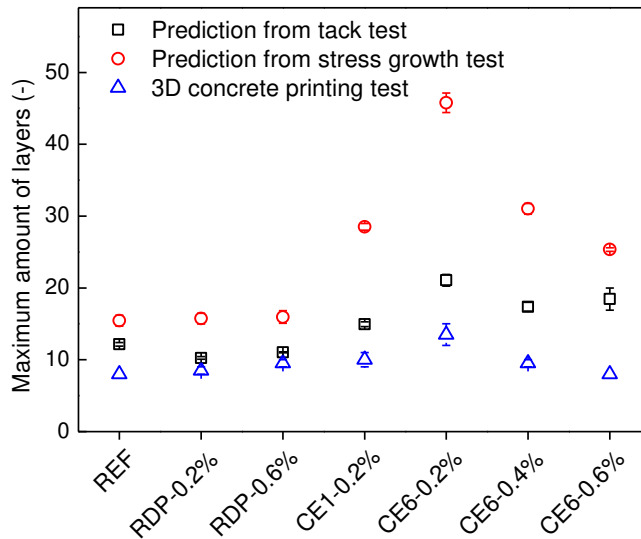


Figure 9.7 Comparison among the tack test, the stress growth test, and the 3D printing test (error bars represent standard error,  $n=5$  for the tack test and the stress growth test,  $n=2$  for the 3D concrete printing test).

In addition, we observed that the predictions based on tack test results were quantitatively closer to the outcome of the printing test, compared to those of the stress growth test. This can be interpreted by the envelop curve of Mohr criteria, as shown in Figure 9.8. In the figure, A represents the material without any normal stress, which can be reflected by yield stress measured by the stress growth test. B

represents the material in a tension state, which was related to either the tack test or the upside-down printing situation. C represents the material under compression, which is related to traditional 3D concrete printing situations. Without the consideration of normal stress, the predicted value provided by the stress growth test was higher than that provided by the tack test, which was also in good agreement with the obtained results (see Figure 9.7).

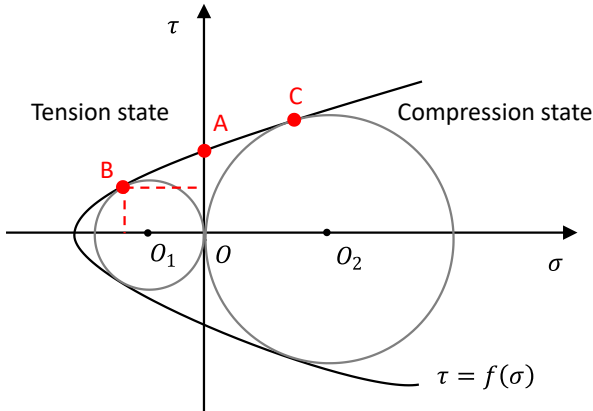


Figure 9.8 Envelop curve of Mohr criteria.

#### 9.3.4 Tensile bond of hardened samples

The tensile bond strength of the mixtures after curing for 7 days was measured, as shown in Figure 9.9. A one-way ANOVA test was used to statistically analyze the influence of the addition of redispersible polymer powder or cellulose ether on the bond strength obtained in the pull-off test. According to the one-way ANOVA test, the bond strength of the CE6-0.2% mixture presented a significant difference compared to that of the reference mixture (REF). Nevertheless, it was also shown that redispersible polymer powder enhanced the mean value of the bond strength while cellulose ether harmed the mean value of the bond strength. The improvement of redispersible polymer powder on the bond strength is discussed firstly. In this study, the redispersible polymer powder addition level was much lower than in other commonly adopted redispersible polymer powder-modified mixtures [171]. Still, the mean bond strength of the RDP-0.6% mixture (2.88 MPa) was increased by 52% compared to that of the REF mixture (1.89 MPa). It was pointed out that the redispersible polymer powder modification of cement mortar and concrete was governed by both cement hydration and polymer film formation processes in their binder phase. When redispersible polymer powder was mixed with fresh cement mortar, the polymer particles were uniformly dispersed in the cement paste phase. With drainage due to the development of the cement gel structure, the polymer particles were gradually confined [195] and the films or membranes bound the redispersible polymer powder-modified mixtures and the



gritblasted concrete slab to form an additional connection. Previous studies presented a nearly ten-fold increase in bond strength of redispersible polymer powder-modified mortar with a polymer-cement ratio of 20%, compared to unmodified mortar [194].

Palacios and Flatt [49] pointed out that cellulose ether is highly hydrophilic and has a high capacity to bind water molecules, increasing their effective volume in solution. This function led to an increase in the dynamic viscosity of the interstitial solution. Therefore, a high dosage of cellulose ether would prevent water to move into the porous substrate and prevent corresponding iron migration at the position of the interface, leading to impaired bond strength.

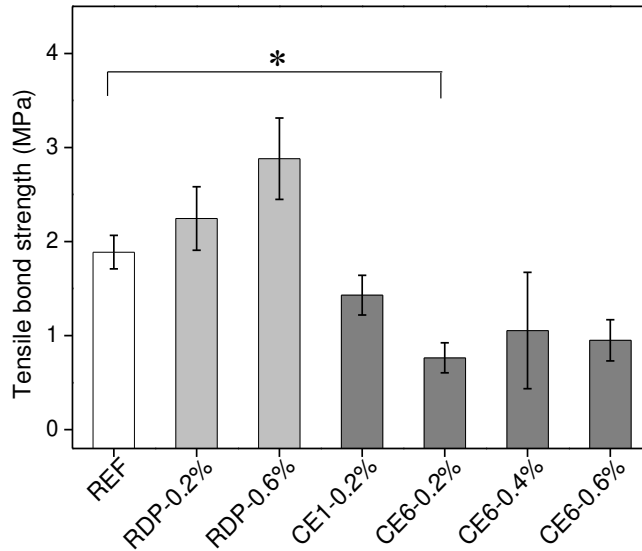


Figure 9.9 Tensile bond strength after curing for 7 days (error bars represent the standard error,  $n=3$ , symbol “\*” indicates a significant difference with a significance level of  $p < 0.05$ ).

## 9.4 Summaries

In this chapter, the effect of redispersible polymer powder and cellulose ether on the sag resistance and tensile bond strength of 3D printed cement-based materials for rock tunnel linings is studied. According to the results and the discussion, the following summaries are given:

- (1) The sag resistance of printed materials is related to two aspects including the adhesion at the interface and the shear resistance of the fresh material. The adhesion and shear resistance properties determine two different failure modes including adhesion failure (i.e. failure occurring at the interface) and cohesion failure (i.e. failure occurring in the fresh material).

(2) Redispersible polymer powder presents no significant effect on the sag resistance, while cellulose ether enhances adhesion at the interface because of its absorption onto the concrete substrate surface. However, a high addition level of cellulose ether reduces the shear resistance because of air entrainment, resulting in a transition from an adhesive failure to a cohesive failure.

(3) As already proven in Chapter 8, applying a fresh coating beforehand is beneficial to the adhesion of the freshly printed material. Instead of merely providing a cement-based coating, a polymer-based primer (e.g. cellulose ether-based slurry) can be applied on the excavated rock surface in advance, which has the potential for stronger adhesion.

(4) The maximum number of printed layers and failure modes in the upside-down printing test is more qualitatively predicted by the tack test, compared to the stress growth test. This is because the fresh material in the tack test and the printing test follows a similar tension state.

(5) Redispersible polymer powder improves the tensile bond strength of 3D printed cement-based material in the hardened state due to film formation. The tensile bond strength of cellulose ether-modified mixtures is lower than that of the reference mixture because the water is trapped by cellulose ether in the fresh material, leading to a dehydrated interface structure.

## Interaction between stiffening control and adhesion

### 10.1 Introduction

In the loose rock area, printed layers are easy to be sheared due to the punching of loose rock. Such a failure can be avoided by improving the shear resistance of printed layers. The developed twin-pipe pumping system can be used to drastically increase the shear resistance of fresh materials via dosing accelerator to cement-based flows at the printing head. As also presented in previous chapters, cellulose ethers can be added to improve the adhesion of freshly printed materials. As a result, another type of failure, namely that printed layers fall due to the lack of adhesion, can be avoided. In some specific cases, both cellulose ether and accelerator are required to avoid the two failure mechanisms mentioned above. However, the interaction of such two admixtures has not been described by other researchers. In this chapter, in total four types of hydroxyethyl methyl cellulose with different viscosity levels and pure aluminum sulfate were used to enhance the adhesion and accelerate the hydration reaction, respectively. First, the viscosifying property of the hydroxyethyl methyl cellulose in an aqueous solution with varying concentrations and temperatures was examined. Afterwards, the hydrodynamic diameter of cellulose ethers in the extracted pore solution was measured by dynamic light scattering (DLS), aiming at investigating the mobility of cellulose ether as influenced by the addition of aluminum sulfate. Finally, the adhesive properties of fresh materials were evaluated by using a tack test.

### 10.2 Experimental program

To avoid the possible influence of the organic component in commercial shotcrete accelerators such as ACC1, pure aluminum sulfate octadecahydrate (ACC2) was used. Four types of cellulose ethers including CE1 (MH300P2), CE2 (MH6000YP4), CE3 (MH15000YP4), and CE4 (MH30000YP4) were used. The viscosity levels increase gradually from CE1 to CE4. More details of these admixtures can be found in Chapter 3. To study the viscosifying property of cellulose ethers, aqueous solutions of cellulose ether with a dosage from 0.2% to 1% of cellulose ether by mass of water (including 0.2%, 0.4%, 0.6%, 0.8%, and 1.0%), were prepared using deionized water as solvent. For the analysis of the

extracted pore solution, cement pastes were prepared. In addition, mortars were prepared for the tack test and the concrete cylindrical sample R2-A (described in Section 3.3.2). The water-to-cement ratio was kept constant as 0.4 for all mixtures (both paste and mortar). The sand to cement ratio was 1 for mortar mixtures. The dosage of cellulose ether was 0.04% by the weight of cement except for the reference mixture (REF). The dosage of aluminum sulfate was 0% in the first series (REF, CE1, CE2, CE3, and CE4) and 3.5% by the weight of cement for the second series (REF-ACC, CE1-ACC, CE2-ACC, CE3-ACC, and CE4-ACC). The mix design is further indicated in Table 10.1.

Table 10.1 Mix design (kg/m<sup>3</sup>).

Mixture	Sand	Cement	Water	Accelerator	Cellulose ether
REF	918.62	918.62	367.45	0	0
CE1	918.62	918.62	367.45	0	0.37 (CE1)
CE2	918.62	918.62	367.45	0	0.37 (CE2)
CE3	918.62	918.62	367.45	0	0.37 (CE3)
CE4	918.62	918.62	367.45	0	0.37 (CE4)
REF-ACC	918.62	918.62	367.45	32.15 (ACC2)	0
CE1-ACC	918.62	918.62	367.45	32.15 (ACC2)	0.37 (CE1)
CE2-ACC	918.62	918.62	367.45	32.15 (ACC2)	0.37 (CE2)
CE3-ACC	918.62	918.62	367.45	32.15 (ACC2)	0.37 (CE3)
CE4-ACC	918.62	918.62	367.45	32.15 (ACC2)	0.37 (CE4)

The preparation of the aqueous solutions can be found in Section 3.4.5. The cement paste and mortar were mixed in a conventional planetary mixer according to the following mixing procedure: (1) mixing cement and cellulose ether (if any) at 140 rpm for 60 s, (2) adding water to the pre-mixed dry powders, and rotating the paddle at 140 rpm for 30 s, (4) adding sand (for mortar) and rotating the paddle at 140 rpm for 30 s, (5) rotating the paddle at 285 rpm for 30 s, (6) scraping and resting for 90 s, (7) rotating the paddle at 285 rpm for 60 s, (8) adding aluminum sulfate (if any) and mixing at 285 rpm for 30 s. The complete mixing sequence lasted around 300 s to 360s.

### 10.3 Results and discussion

#### 10.3.1 Viscosifying property

Generally, the viscosity of aqueous solutions or cement pore solutions can be increased with the addition of cellulose ethers. The viscosifying effect strongly relies on the concentration and the molecular weight of the polymers [191, 277]. In this study, taking cellulose ether CE4 as an example, the viscosity evolution of

the aqueous solutions at different concentrations is shown in Figure 10.1. Although the periodic discrimination was observed, the measured values of the variations in viscosity were still above the uncertainty of precision of the setup. Without considering the adsorption effect of cellulose ethers, the viscosity measured for the aqueous solution seems to be a relevant measurement for the understanding of viscosifying property of cellulose within cement paste. In addition, the viscosity of the aqueous solution with different cellulose ether types and concentrations is shown in Figure 10.2. The viscosity was quite small within the range from several to tens mPa·s in the case of a low concentration such as 0.2%. Once the concentration exceeded a specific value which was commonly called the overlapping concentration, the solution viscosity would increase significantly. The overlapping concentration roughly corresponded to the situation, in which the polymer coils occupy the entire volume [278]. The overlapping concentration of around 0.4% followed the previous researches [279]. It was pointed out by Graessley et al. [280] that five distinct states of polymeric solutions should be taken into consideration including ideally dilute particle solution, semi-dilute particle solution, semi-dilute network solution, concentrated particle solution, and concentrated network solution. The overlapping concentration is located between the dilute solution and the semi-dilute solution where the transition is determined by the molecular weight, the interaction between the polymer chains, and the interaction between polymer coils [281]. The interaction between polymer coils starts to dominate the viscosifying property of the solution when an overlapping concentration is reached. In such a situation, the polymer coils are considered to occupy the entire volume [191].

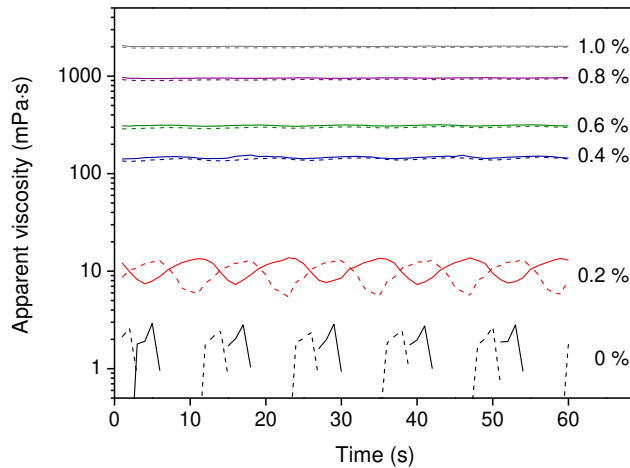


Figure 10.1 Viscosity evolution of the aqueous solution of cellulose ether CE4 with different concentrations, each series was repeated twice (solid and dashed lines).

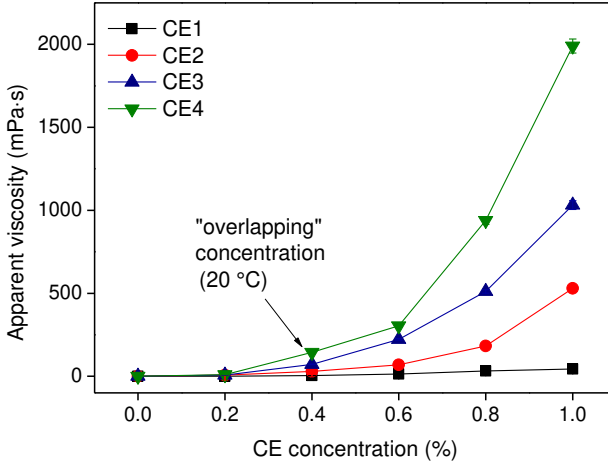


Figure 10.2 Viscosity of the aqueous solutions of cellulose ether as a function of concentration (error bars represent the standard error,  $n=2$ ).

Moreover, to specify the influence of raised temperature on the viscosifying effect of the cellulose ether, the viscosity of the aqueous solution with a concentration of 0.2% (below the overlapping concentration) and 1.0% (above the overlapping concentration) was measured for different temperatures ranging from 20 °C to 60 °C, as shown in Figure 10.3. It was shown that the viscosity reduced as the temperature increased. For example, the viscosity of CE1 solution with a concentration of 0.2% reduced by 70.7% when the temperature increased from 20 °C to 60 °C. In this study, a high dosage of aluminum sulfate would speed up the hydration process quite fast, in the meantime, release a lot of heat and increase the temperature inside the material [68, 282]. As a result, the rise of the temperature would limit the viscosifying effect, while facilitating the migration of interstitial solution due to a reduced viscosity [277].

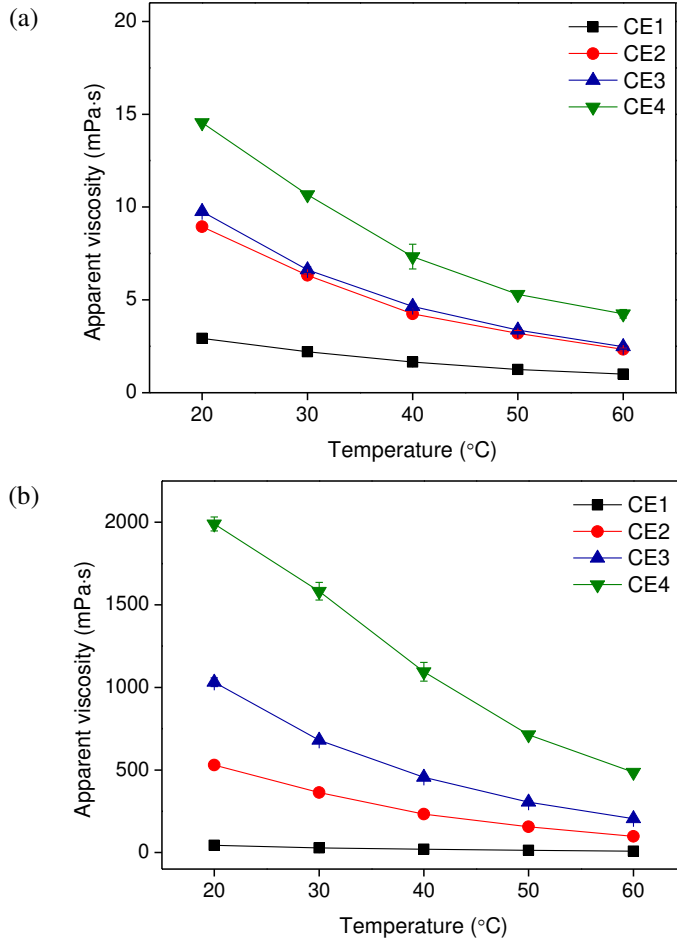


Figure 10.3 Viscosity of the solutions of cellulose ether as a function of temperature, (a) concentration 0.2% and (b) concentration 1.0% (error bars represent the standard error,  $n=2$ ).

### 10.3.2 Mobility of cellulose ether under pressure

In this section, only the low concentration (i.e. 0.2% by the mass of water) was taken into consideration as the pore solution of mixtures with a high dosage of cellulose ether (e.g. 1.0% by the mass of water) cannot be extracted in the static filtration test (an air pressure of 5 bars). The amount of water extracted for 5 mixtures by the static filtration process was measured. The proportion of the extracted water (the ratio of the extracted water amount to the total water amount in the cement paste) is shown in Figure 10.4. With the increase of the viscosity level of cellulose ether, the proportion of the extracted water reduced because more water was trapped by longer cellulose ether polymer chains. For example, the extracted water proportion was 22.6% and 9.3% for the reference mixture

(REF) and the mixture with CE4, respectively. The addition of aluminum sulfate further reduced the amount of extracted water due to the accelerated hydration of tricalcium aluminate and the consumption of water [49].

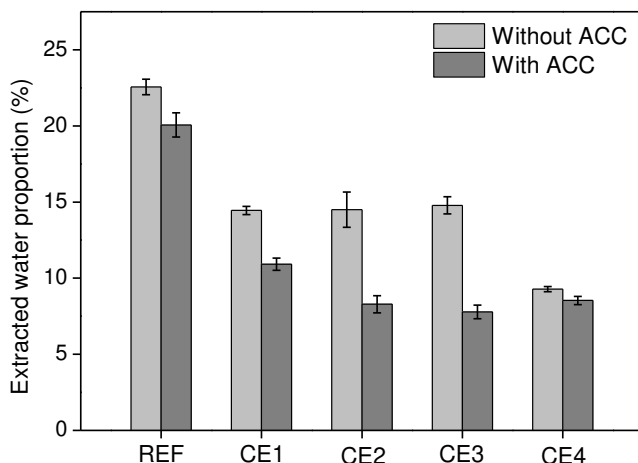
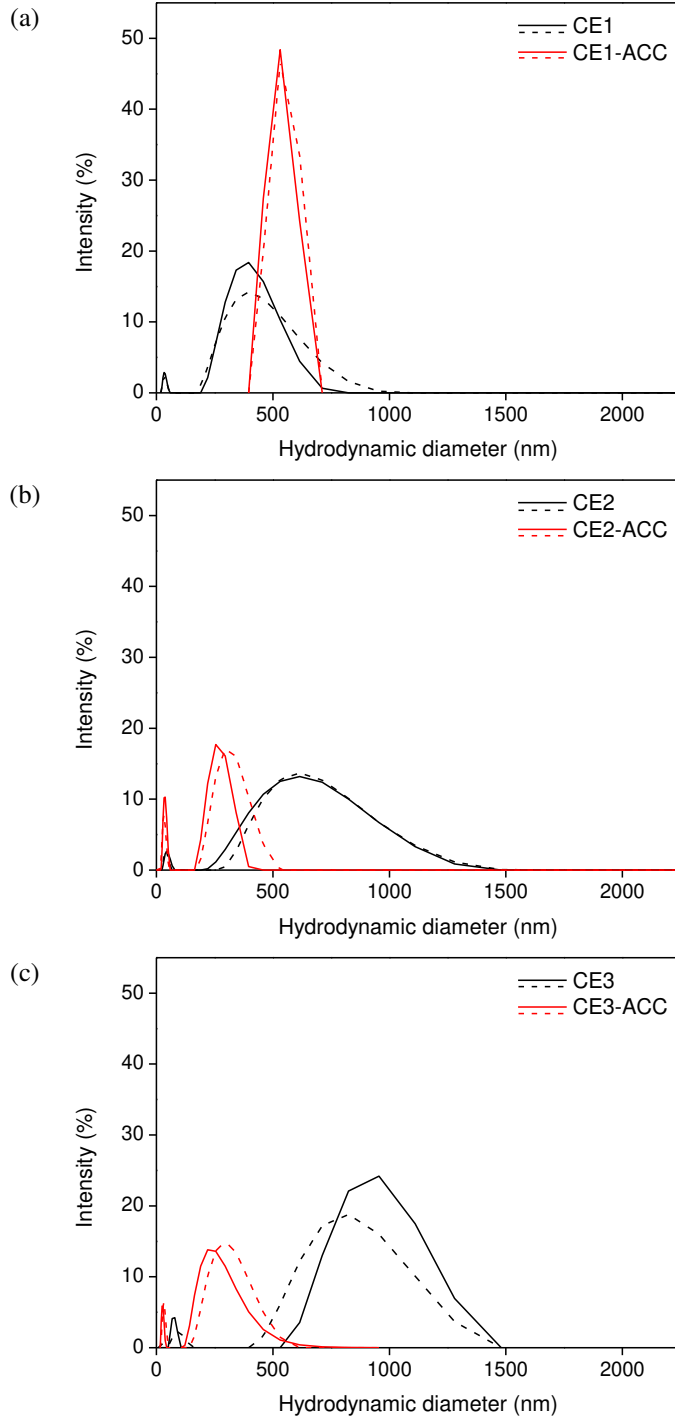


Figure 10.4 Proportion of the squeezed water (error bars indicate the standard error,  $n=2$ ).

To examine the mobility of cellulose ether, the hydrodynamic diameter of cellulose ether molecules dissolved in the extracted pore solution was determined by dynamic light scattering (DLS), as shown in Figure 10.5. The hydrodynamic diameter corresponding to the peak intensity was defined as the critical hydrodynamic diameter. For CE1 with a relatively low viscosity level, the critical hydrodynamic diameter was 396 nm and the value modestly increased to 531 nm with the addition of aluminum sulfate. For CE2, CE3, and CE4 with a relatively high viscosity level, the critical hydrodynamic diameters were 615, 955, and 615 nm, respectively. Different from the pore solution extracted from the mixture with CE1, the critical hydrodynamic diameter decreased to 237, 255, and 531 nm for the mixtures CE2-ACC, CE3-ACC, and CE4-ACC. With the addition of aluminum sulfate, the critical hydrodynamic diameter was significantly reduced, especially for the mixtures with CE2 and CE3. This can be interpreted that the pores were contracted and the mobility of cellulose ether with larger size was limited.





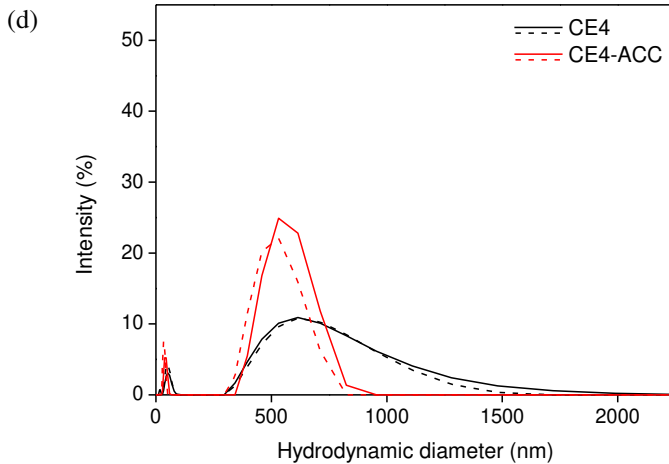


Figure 10.5 Relative contribution to the scattering light intensity as a function of the hydrodynamic diameter for the extracted pore solutions, each series was repeated twice (solid and dashed lines).

The concentration of cellulose ether in the extracted pore solution can be reflected by the amount of total organic carbon (TOC). The amount of total organic carbon, total carbon (TC), and inorganic carbon (IC) is shown in Table 10.2.

Table 10.2 The amount of total organic carbon, total carbon, and inorganic carbon (mg/L).

	Total organic carbon (TOC)	Total carbon (TC)	Inorganic carbon (IC)
REF	363	518	155
CE1	1582	1602	20.1
CE2	1018	1051	32.8
CE3	1003	1029	24.8
CE4	1138	1168	30.1
REF-ACC	461	472	10.9
CE1-ACC	2115	2120	5.03
CE2-ACC	1543	1568	25.3
CE3-ACC	1463	1470	7.73
CE4-ACC	1539	1565	26.1

The results are further depicted in Figure 10.6. The TOC values of mixture REF and REF-ACC were 363 and 461 mg/L, respectively. Since no cellulose ether was contained in the extracted pore solution, such low values can be attributed to the organic carbon contained in the cement, for instance, the cement grinding agents [191]. In addition, the TOC value of mixture CE1 with a low viscosity level

amounted to 1582 mg/L, while the three other mixtures CE2, CE3, and CE4 obtained lower values (i.e. 1018, 1003, and 1138 mg/L). In this work, the amount of cellulose ether was lower than the overlapping concentration, thus it can be predicted that no polymer chains were associated in the pore solution [283]. Nevertheless, cellulose ether coils with a higher viscosity level (e.g. CE2, CE3, and CE4) had a larger hydrodynamic diameter, as compared to that of cellulose ether CE1. As a result, the larger hydrodynamic diameter would hinder the mobility of cellulose ether coils, leading to a lower amount of total organic carbon in the extracted pore solution. Moreover, due to the very low charge, the adsorption of cellulose ether onto cement particles was not likely to occur [272]. Instead, the adsorption of the by-products in the industrial cellulose ethers might occur. For example, the by-products can be impurities (e.g. glycolates), thickeners (e.g. anionic polyacrylamides), or rheology modifiers (e.g. hydroxypropyl starch). Almost all these by-products present a high charge, leading to a high amount of adsorption onto the cement particles [277]. Unfortunately, this might also have an influence on the amount of total organic carbon but still remains unknown in this work. On the other hand, the addition of aluminum sulfate reduced the amount of extracted water due to the accelerated hydration process. In the meantime, free cellulose ether would remain in the pore solution and be extracted. As a result, the total organic carbon values of the mixtures with the addition of aluminum sulfate (i.e. CE1-ACC, CE2-ACC, CE3-ACC, and CE4-ACC) were higher, when compared to those without the addition of aluminum sulfate.

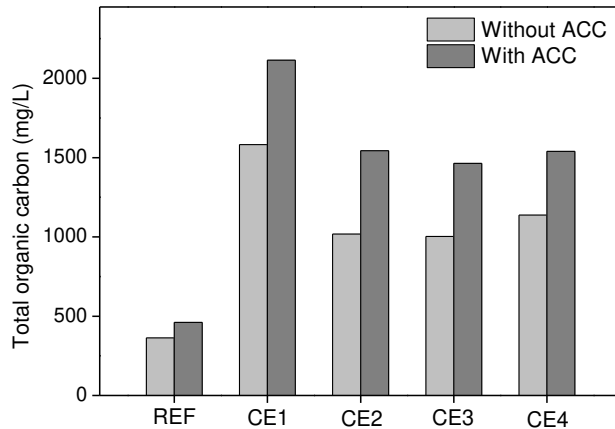


Figure 10.6 Total organic carbon (TOC) of extracted pore solution.

### 10.3.3 Adhesion in the fresh state

The influence of the viscosity level of cellulose ether and aluminum sulfate on the adhesive properties of fresh cement-based materials is evaluated by the tack test, where the normal force versus displacement curves were recorded, as shown in Figure 10.7. At the early stage, the samples presented elastic behavior, with an

inward flow (radial shear flow) towards the center of the sample. After reaching a critical displacement, the normal force started to reduce as the fresh sample separated from the top plate. A similar phenomenon was also observed in the results described in the previous chapters. Four parameters were derived from the normal force versus displacement curves including the peak normal force, the critical displacement, the total displacement, and the adhesion energy (the area formed by the normal force curve obtained in the test and the horizontal axis).

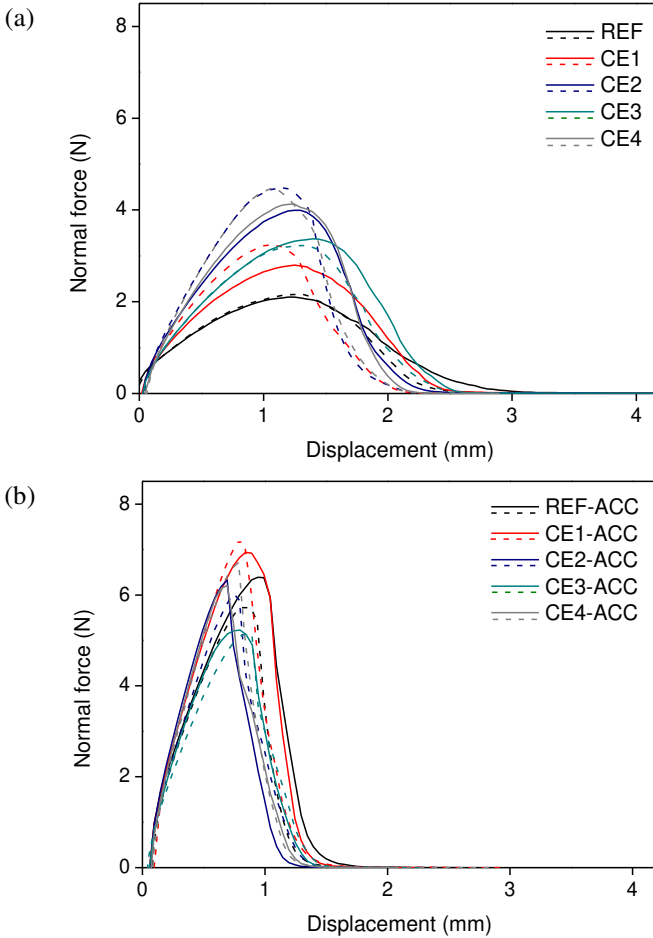


Figure 10.7 Normal force versus displacement curves of mixtures without and with aluminum sulfate, each series was repeated twice (solid and dashed lines).

The peak normal forces obtained from the normal force versus displacement curves were compared, as shown in Figure 10.8 (a). In the series of the mixtures without the addition of aluminum sulfate, the peak normal force generally increased with an increase in the viscosity level of cellulose ether. Specifically, the peak normal force of the reference mixture without cellulose ether (REF) was

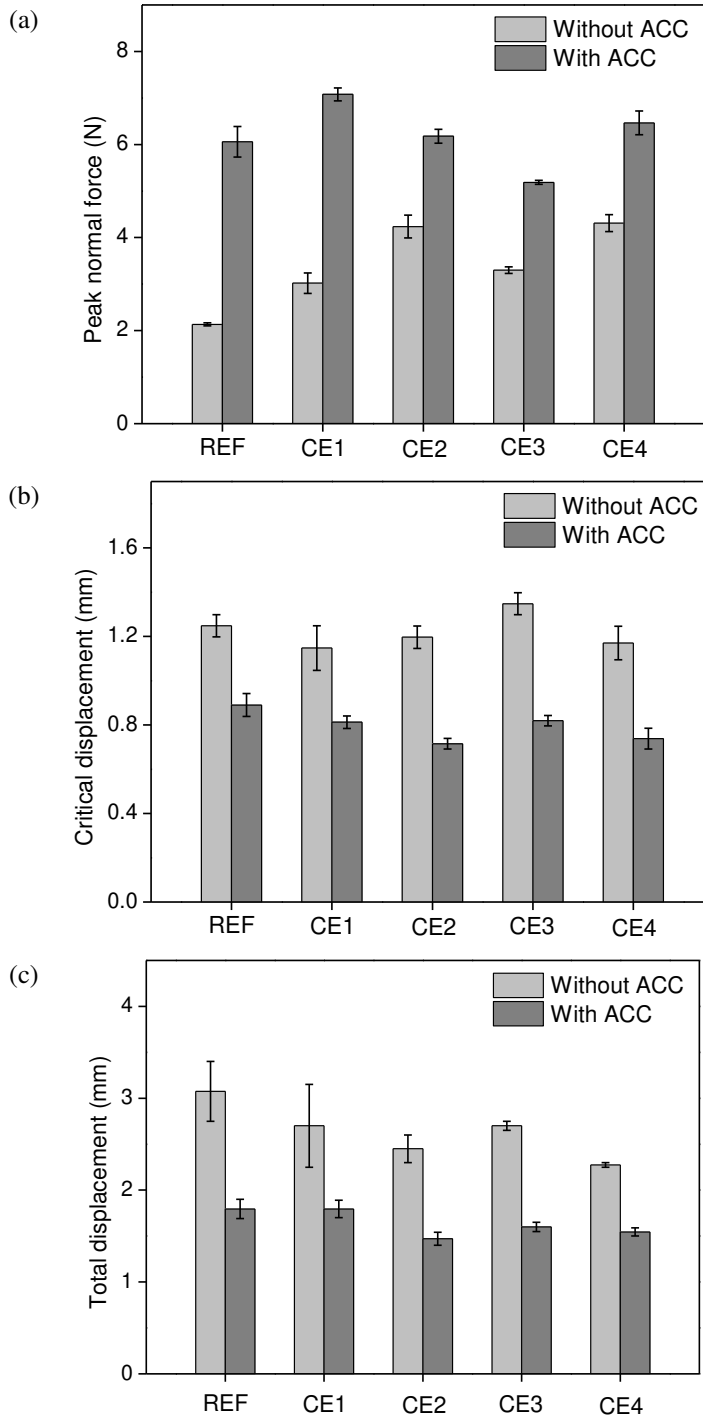
merely 2.1 N while the peak normal forces of the others were 3.0, 4.2, 3.3, and 4.3 N, respectively, which were much higher when compared with the reference mixture. As explained in the previous chapter, the value of the peak normal force was mainly controlled by two aspects including the resistance to flow due to the viscous energy dissipation of the material and the force at the interface between the lower surface of the concrete cylindrical sample and upper surface of the fresh sample, where the failure occurred [248]. On the one hand, the addition of cellulose ether enhanced separation-driven shear viscous flow of the fresh sample by increasing the macroscopic viscosity of the cement suspension [245], as already indicated by the increased dynamic viscosity of the aqueous solution. In addition, a bridging flocculation mechanism can occur involving the adsorption of a chain of the cellulose ether polymer onto two or more cement particles, and physically holding the particles together [49]. As a result, the yield stress of the sample was increased, which further improved the shear resistance of the fresh material. This phenomenon was more pronounced when the cellulose ether with a high viscosity level (i.e. high molecular weight with a long polymer chain) was added. On the other hand, the value of the peak normal force was also determined by the detaching force at the interface between the cylindrical sample-to-material interface. Mohamed et al. indicated that the force was required to overcome the Laplace depression or capillary pressure, which was generated by the curvature of the meniscus and linearly related to the surface tension as the fresh sample was placed in tension [248, 251]. However, it was also pointed out that the surface tension reduced from 0.072 N/m to around 0.065 N/m when several mg/L of cellulose ether was added to the solution [284]. Accordingly, the peak normal force of the mixtures with cellulose ether was expected to be slightly lower than the reference mixture, which was in contradiction with the results. The most physically sound explanation is that the cellulose ether introduced more functional groups and formed hydrogen bonding where the hydrogen atoms were attracted to an atom of oxygen [171]. As a result, the effort required to lift the top plate was improved and the value of the peak normal force was increased.

On the other hand, with the incorporation of aluminum sulfate in the mixture, the peak normal force was significantly increased. For example, the peak normal force of the reference mixture with the addition of 3.5% aluminum sulfate (REF-ACC) reached 6.1 N, which was about triple that of mixture REF. The raise in peak normal force was due to the increased shear resistance, as the hydration was promoted. It was illustrated by Dressler et al. [113] that the yield stress of the mixture with a 6% shotcrete accelerator was more than 10 times that of the mixture without accelerator. As a result, the force required for separation was higher for the mixture with the addition of aluminum sulfate because of the higher energy for the inward shear flow of the sample. However, the effect of cellulose ether was limited in the presence of aluminum sulfate, especially for the cellulose ether with

high viscosity levels. In the case of cellulose ether CE1, the peak normal force of the mixture with aluminum sulfate (CE1-ACC) was around 2.4 times that of the mixture without aluminum sulfate (CE1). While for other cellulose ethers including CE2, CE3, and CE4, the ratio was lower with a value of around 1.5. The limited facilitation of cellulose ether on the adhesion performance can be attributed to the constraint of the mobility of cellulose ether polymers, especially for the polymers with a higher viscosity level or molecular weight.

The critical displacement and the total displacement obtained from the normal force versus displacement curves are shown in Figure 10.8 (b) and Figure 10.8 (c), respectively. It is indicated that the displacement (either the critical displacement or the total displacement) of the mixtures with the addition of aluminum sulfate showed a significant reduction when compared to that without aluminum sulfate. From a microstructural point of view, two critical strains are described for cement paste which are derived from the network of colloidal interactions (in the order of a few percent) between cement particles and the formation of C-S-H connections (in the order of several hundredths of a percent) [179]. In this study, the critical displacement is mainly related to the later one, where destruction of the structure can be observed during the measurement. It was also pointed by Yi et al. [285] that very low elastic modulus and very high strain corresponding to the maximum stress were found at early ages of casting. As the age increased, however, elastic modulus increased rapidly and the strain corresponding to the maximum stress (critical strain) decreased rapidly. The addition of aluminum sulfate would dramatically promote hydrate precipitation in the pore space, leading a rapid decrease of the critical strain. As a result, from a macro perspective, the critical displacement decreased with the addition of aluminum sulfate, as well as the total displacement.

The calculated dissipated energy generally increased as the viscosity level of cellulose ether increased. For the reference mixture (REF) and the mixture with a low viscosity level (CE1), the addition of aluminum sulfate increased the dissipated energy due to the improvement of shear resistance of the fresh material. However, for mixtures with high viscosity level cellulose ether (e.g. CE2, CE3, and CE4), the dissipated energy of the mixtures with the addition of aluminum sulfate was lower than that of the reference mixtures (without the addition of aluminum sulfate). This can be interpreted that due to the less presence of cellulose ether and water at the interface for the mixture with aluminum sulfate, debonding occurred earlier and the adhesion energy for the shear of the material and the detaching at the interface was lower accordingly. However, it seems difficult to specify the respective contributions of these two aspects (i.e. shear of the fresh material and the debonding at the interface) to the dissipated energy, which needs further exploration.



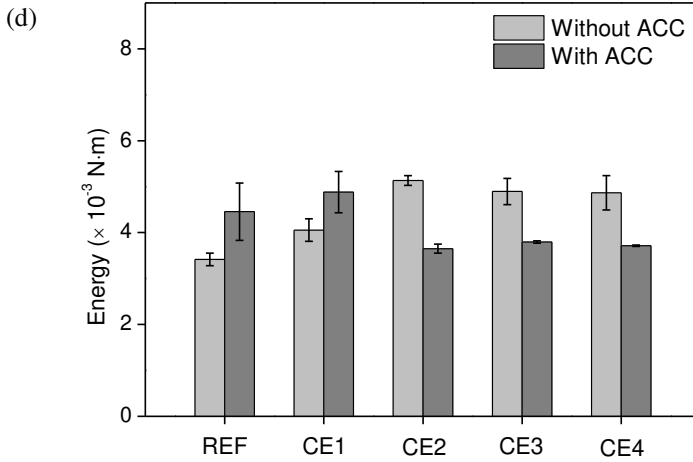


Figure 10.8 Peak normal force, critical displacement, total displacement, and dissipated energy of mixtures with and without the addition of aluminum sulfate (error bars represent the standard error,  $n=2$ ).

#### 10.4 Summaries

In this chapter, the influence of accelerator (i.e. aluminum sulfate) and the viscosity level of cellulose ethers on the adhesion performance of cement-based materials are explored. Based on the experimental results, the following summaries are given:

- (1) The addition of cellulose ether can enhance separation-driven shear viscous flow of the fresh materials. Such a phenomenon is more pronounced when adding a cellulose ether with a high viscosity level (i.e. high molecular weight with a long polymer chain).
- (2) The adhesion of the fresh material is also determined by the detaching force at the contact interface, where cellulose ether can introduce more functional groups such as forming hydrogen bonding, leading to an improved adhesion in the fresh state.
- (3) The adhesion in the fresh state can be improved by adding aluminum sulfate due to the increased shear resistance. However, the effect of cellulose ether is limited with the presence of aluminum sulfate, especially for the cellulose ether with high viscosity levels. The limited facilitation of cellulose ether on the adhesion performance can be attributed to the constraint of the mobility of polymers with contracted pore sizes.



## Conclusions and perspectives

### 11.1 General conclusions

To achieve the goal of stiffening control, a twin-pipe pumping (TPP) system with a helical static mixer is developed. In this way, a cement-based mixture (without accelerator) and a limestone powder-based mixture (with a high dosage of the accelerator) are transported separately and mixed within the helical static mixer just before extrusion. The stiffening rate of the mixture is then drastically modified inside the static mixer and the combined mixture extruded from the nozzle can reach a high green strength. It is indicated that limestone powder is suitable to be used as a carrier material for the accelerator. By regulating composition proportions in the cement-based mixture and the limestone powder-based mixture, both mixtures can reach long open time and high fluidity, which is beneficial for reducing the pumping pressure and extending the operation period. It is further proved that the helical static mixer is effective for mixing two separate flows with a division pattern. A good mixing homogeneity can be achieved by adopting a high amount of mixing baffles inside the static mixer. However, using too many mixing baffles would significantly increase the pumping pressure.

The helical static mixer introduced striation patterns in the 3D printed elements and the effect of such a heterogeneous phenomenon on the mechanical behavior is studied. During the mechanical (compressive, flexural, and tensile) tests, the cracks initiate within the limestone powder striation rather than at the interface area between two adjacent layers, which is expected to be the weakest link in a typical 3D printed element. Microstructure investigations based on mercury intrusion porosimetry (MIP) reveal that the pore size distribution is similar for the bulk and interface region in the 3D printed samples but distinct from that of mold cast samples. Although mold cast samples have a higher volume of finer micropores, the volume of macropores which is more detrimental to the compressive strength is found to be higher in 3D printed samples. Further, porosity analysis of micrographs shows that the macropores in 3D printed samples are primarily presented in limestone powder-based striations. Abundant ettringite forms at the contact zone between the cement-based striation and limestone powder-based striation in 3D printed samples. A small quantity of ettringite is also observed in the bulk of limestone powder-based striations, which is caused by ion

migration between the two regions after the inline mixing process by the static mixer.

The adhesion performance of printed materials at two representative positions, including the overhead position (inclination of  $180^\circ$ ) and the side position (inclination of  $90^\circ$ ), is investigated. Results indicate that the adhesion at the overhead position is limited by both the shear resistance of fresh materials and the property of the material-to-substrate interface, while the adhesion at the side position is mainly constrained by the shear resistance of fresh materials. As such, the printed layers at the overhead position suffer more risk of debonding, when compared to that at the side position. Moreover, the stress state analysis of printed layers at the overhead position and the side position indicates that the tack test and shear test give a good prediction about the printing capacity of fresh materials.

The influence of the substrate surface roughness and moisture content on the tensile adhesion of printed materials at the overhead position is studied. Results indicate that printed materials can not completely fill macro rough textures due to the stiff behavior of fresh materials and the limited pressure provided by the nozzle. As a result, less contact at the interface forms when the substrate surface roughness level increases, which subsequently limits the tensile adhesion both in the fresh and hardened state. By applying a coating onto the substrate beforehand, the tensile adhesion in the fresh and hardened state can be improved. On the other hand, increasing moisture content can enhance the tensile adhesion in the fresh state due to surface tension, while it would reduce the tensile adhesion of hardened samples, which can be attributed to a higher water-to-cement ratio at the contact zone.

The influence of different polymers including redispersible polymer powders and cellulose ethers on the tensile adhesion is investigated. The addition of cellulose ethers improves the adhesion of fresh materials as the cellulose ether at the interface introduces more functional groups such as formed hydrogen bonding. A high dosage of the cellulose ether limits the shear resistance of fresh materials, leading to a transition from an adhesive failure (i.e. failure occurs at the interface) to a cohesive failure (i.e. failure occurs in the bulk of fresh materials). Different from the cellulose ether, the addition of redispersible polymer powders does not improve the adhesion in the fresh state, while it increases the tensile bond strength of the hardened samples due to film formation.

The interaction of the cellulose ether (hydroxyethyl methyl cellulose) and accelerator (aluminum sulfate) on the adhesion performance of cement-based materials is studied. The separation-driven shear viscous flow of the fresh sample is improved with the addition of cellulose ethers due to the increased macroscopic viscosity of the cement suspension. On the other hand, the adhesion in the fresh state can be enhanced by adding aluminum sulfate due to the increased shear resistance. However, the effect of cellulose ethers is limited with the presence of

aluminum sulfate, especially for the cellulose ether with high viscosity levels (i.e. a high molecular weight with a long polymer chain). This is because the addition of aluminum sulfate accelerates the hydration and contracted pores, leading to the constraint of the mobility of cellulose ethers.

## **11.2 Main contributions**

The main contributions of this thesis can be summarized in the following aspects:

(1) This thesis devotes extending 3D concrete printing for the construction of hard rock tunnel linings, aiming at achieving a fully automated construction method. Based on this, the amount of rebound is reduced and the surface quality of tunnel linings can be improved, compared to that of shotcrete.

(2) An inline mixing system named twin-pipe pumping is developed. A cement-based flow and a limestone powder-based flow are pumped separately and combined in a helical static mixer right before extrusion. The conflict existing between a high flowability for the ease of pumping and a rapid stiffening rate required for holding surrounding rocks can be solved. The twin-pipe pumping system can also be used for common 3D concrete printings (from the bottom up) to achieve a high construction rate.

(4) The influence of surface inclinations, substrate properties, and polymer modification on the adhesion of 3D printed materials is systematically investigated. A tack test is introduced to evaluate the adhesion of fresh cement-based materials. Concrete cylindrical samples are used in the tack test and the substrate properties can be taken into consideration for the analysis of the adhesion mechanism in the tack test. An innovative 3D concrete printing method, i.e. printing at the lower surface of a horizontally supported concrete slab or against an upright concrete slab, is developed. In that way, the sag resistance of freshly printed materials can be evaluated on a large scale.

(5) The interaction between the cellulose ether for adhesion and aluminum sulfate for stiffening control is explored. This work can be a guidance in applying the twin-pipe pumping method for the construction of hard rock tunnel linings in practical applications.

## **11.3 Perspectives**

The current study reveals that, although the ion migration can enhance the formation of hydration products in limestone powder-based striations, strategies are still required to have printed elements with better mechanical integrity. For example, higher porosity was observed in the LP-based regions when compared to the PC-based regions. Further studies can be carried out to investigate the pore structure of printed materials with different limestone powder replacement rates.

The ion migration inside 3D printed elements can be facilitated by optimizing the rheological behavior of the two streams to be combined in the static mixer. The compositions of the mixtures used in the twin-pipe pumping system can be further optimized. For example, other types of inert fillers such as silica powders can be used as a carrier material for accelerators. Other types of accelerators introduced in Chapter 2 can also be tried. By using other types of accelerator (e.g. calcium nitrate, calcium chloride, and C-S-H seed), other supplementary cementitious materials (e.g. slag, fly ash, and silica fume) can also be used as a carrier material, which would not react with these specific types of accelerators but provide enough mechanical strength in the later stage. Instead of Portland cement, other types of cement such as calcium sulfoaluminate (CSA) cement are also applicable in the twin-pipe pumping system. One strategy is to borate the CSA cement-based mixture for a long open time and add calcium hydroxide in the inert filler-based mixture. When these two mixtures get combined in the static mixer, the borated phase rapidly destabilizes in the presence of calcium hydroxide, and the hydration reaction re-initiates. Alternatively, the twin-pipe pumping system can be used for the 3D printing of alkali-activated materials. The development of an appropriate mixture can also be based on the fundamental modeling considering particle packing (including the effect of fine powder particles). Furthermore, microstructural modeling can also be based on the potential effects of powder materials such as chemical (hydration), physical (nucleation), dilution (cement replacement), and filler (packing) effects.

The material developed for hard rock tunnel linings in this thesis is a kind of brittle material with almost no tensile capacity. Embedding reinforcement is a solution to increase the tensile strength of the printed tunnel linings. Many strategies have been proposed in the context of 3D concrete printing such as the mesh mold technology and introducing a steel cable into the concrete layer [286]. However, how to incorporate the reinforcement in an automated way and achieve full contact between printed material and reinforcement still needs further exploration. One solution is to capture the reinforcement profile by using an automated laser scanning equipment. As such, the printing nozzle can be moved in a real-time control way. Alternatively, the potential research direction is to investigate the tensile capacity based on a kind of multicomponent Engineered Cementitious Composite (ECC).

Although the tack test and the shear test can be used to accurately predict the printing capacity of 3D printed layers at the overhead position and the side position, the analysis of the stress field of fresh cement-based materials at the interface is still lacking and remains an interesting point for further investigation. In addition, the development of the failure criterion for fresh cement-based materials in a tension-shear state is certainly useful.

To achieve complete contact between the printed layers and the substrate, fresh cement-based materials should be fluid enough to penetrate the rough textures and

gain enough stiffness for the sag resistance in the meantime. Such a conflict can be avoided by using a highly thixotropic material or a stiffening control system where the stiffening rate gains a sudden increase after penetrating the voids. Adding additional pressure is also a potential way that can be applied after extrusion to compact fresh cement-based materials for better contact. Alternatively, an innovative design with two nozzles can be used where a first nozzle is used to spray a less viscous coating and a second one extrudes the printing material. As such, manually applying a coating can be left out and a fully automated printing process can be achieved.



## List of Figures

Figure 1.1 The application of shotcrete in tunnels, taken from [6].	2
Figure 1.2 Fire damage of the tunnel lining, taken from [7].	2
Figure 1.3 Factors influencing the amount of rebound, taken from [9].	3
Figure 1.4 Schematic view of extending 3D concrete printing to hard rock tunnel linings.	4
Figure 1.5 Basic types of failure modes of tunnel linings including (a) shearing of materials in the loose rock area, (b) detaching at the interface in the loose rock area, and (c) detaching at the interface under self-weight.	5
Figure 1.6 Schematic view of the twin-pipe pumping system.	8
Figure 1.7 Thesis outline.	10
Figure 2.1 Pressure $P$ (Pa), shear stress $\tau$ (Pa), shear rate $\dot{\gamma}$ ( $\text{s}^{-1}$ ), velocity $v$ (m/s), and flowrate $Q$ ( $\text{m}^3/\text{s}$ ) profiles of a concrete flow inside a pumping pipeline. The yield stress and plastic viscosity of concrete are $\tau_{0,B}$ (Pa) and $\mu_{P,B}$ (Pa·s), whereas the yield stress, plastic viscosity and the thickness of the lubrication layer are $\tau_{0,LL}$ (Pa), $\mu_{P,LL}$ (Pa·s), and $e_{LL}$ (m), taken from [29].	12
Figure 2.2 Setting or hardening effect represented by cumulative heat production [42].	15
Figure 2.3 Isothermal conduction calorimeter curves for $\text{C}_3\text{S}$ with various calcium salts. Dosage is 2% anhydrous salt by weight of $\text{C}_3\text{S}$ , taken from [52].	17
Figure 2.4 Schematic view of the two-fluid grouting system, taken from [102].	21
Figure 2.5 Representation of the shotcrete process with accelerators: (a) dry-mix shotcrete process, (b) wet-mix shotcrete process [107].	22
Figure 2.6 Nozzle used for the dry-mix shotcrete process, (a) nozzle structure, and (b) working principle of the nozzle used for the dry-mix shotcrete process, taken from [108].	23
Figure 2.7 Spray gun used for the wet-mix shotcrete process, taken from [109].	24
Figure 2.8 Example of spray-based 3D concrete printing, taken from [113].	25
Figure 2.9 Schematic overview of a 3D printing setup: (0) System command, (1) Robot controller, (2) Printing controller, (3) Robotic arm, (4) Print head, (5) Accelerator, (6) Peristaltic pump for accelerator, (7) Peristaltic pump for premix, (8) Premix mixer, (9) 3D printed object, taken from [119].	26
Figure 2.10 Mixing chamber used in ETH Zurich: a) a mixing reactor with a pin mixer type tool for smart dynamic casting; b) a mixing reactor with a pin mixer type tool for extrusion-based 3D printing, taken from [121].	27

Figure 2.11 A dynamic mixer consisting of blades and screw system, taken from [124].	27
Figure 2.12 Liquid additive injection device. Left: schematic drawing. Right: overview image of accelerator injection during printing, taken from [63].	28
Figure 2.13 Commercially available in-line static mixers, taken from [127].	29
Figure 2.14 Insufficient mixing homogeneity, taken from [63].	31
Figure 2.15 Principle of yield stress development over time with and without accelerator (alkali-free shotcrete accelerator) as well as the open window indicated by $t_{min}$ and $t_{max}$ , taken from [113].	33
Figure 2.16 Cohesion forces and adhesion forces.	35
Figure 2.17 (a) Uncross-linked polymers are somewhat free to diffuse across the interface, and (b) cross-linked polymers are not free enough to diffuse, where the dashed line indicates the interface.	37
Figure 2.18 (a) Liquid droplets with a high and low contact angle on a flat substrate, (b) no spreading of liquid on the substrate with a high contact angle, and (c) complete contact of liquid with a low contact angle, adapted from [171].	38
Figure 3.1 Particle size distribution of Portland cement, limestone powder, and silica sand.	44
Figure 3.2 X-ray diffractogram of the shotcrete accelerator.	48
Figure 3.3 Concrete cylindrical samples with different roughness levels: R1-A and R1-B: polished surface; R2-A and R2-B: gritblasted surface; R3-A and R3-B: hammered surface; R4-A and R4-B: water-jetted surface.	51
Figure 3.4 Example of a concrete cylindrical sample glued to a steel plate (left), the bottom surface and scanning paths (middle), and profile height along with evaluation position (right).	51
Figure 3.5 Root mean square deviation ( $R_q$ ) of the lower surface of concrete cylindrical samples (error bars represent the standard error, $n=4$ ).	52
Figure 3.6 (a) Setup equipped with the building material cell and the 4-blade vane rotor for the flow curve measurement, and (b) dimensions (mm).	53
Figure 3.7 Shearing regime in flow curve tests.	54
Figure 3.8 (a) Setup equipped with the building materials cell and the 6-blade vane rotor for the stress growth test, and (b) dimensions (mm).	54
Figure 3.9 (a) Setup equipped with the parallel plate geometry and the concrete cylindrical sample for the tack test, and (b) schematic view of the coated and uncoated concrete cylindrical sample.	56
Figure 3.10 Testing procedure of the tack test including (a) molding, (b) demolding, (c) squeezing, and (d) pulling off.	56
Figure 3.11 Linearly increasing loads during the tack test.	57
Figure 3.12 (a) Setup equipped with the concrete cylindrical sample for the shear test and (b) dimensions (mm).	59
Figure 3.13 (a) Setup equipped with coaxial cylinders for the viscosity measurement of aqueous solutions, and (b) dimensions (mm).	60
Figure 3.14 Four parts of static mixer.	62



Figure 3.15 Twin-pipe pumping system: A is the pump for the cement-based mixture, B is the pump for the limestone powder-based mixture, C and D are valves, E is the helical static mixer, F is the printed element, G is the controlling system. ....	63
Figure 3.16 3D concrete printing setup: (a) printing at the overhead position and (b) printing at the side position. ....	64
Figure 3.17 Schematic view of the printing paths: (a) continuous printing at the overhead position, (b) one-way printing at the overhead position, and (c) continuous printing at the side position. ....	65
Figure 3.18 Schematic view and dimensions (mm) of nozzles, (a) for the continuous printing and (b) for the one-way printing. ....	66
Figure 3.19 Extracting cubic samples from the printed wall element to test the compressive strength. ....	67
Figure 3.20 Compression test of 3D printed samples under three different loading directions including C-1, C-2, and C-3. ....	68
Figure 3.21 Extracting prismatic samples from the printed wall element to test the flexural strength. ....	69
Figure 3.22 Flexural test of 3D printed samples under three loading directions including D-1, D-2, and D-3. ....	70
Figure 3.23 Width and height of the 3D printed prismatic sample. ....	70
Figure 3.24 Extracting small prismatic samples from the wall element to test the tensile bond strength. ....	71
Figure 3.25 Pull-off test of 3D printed samples with an interface in the middle. ....	71
Figure 3.26 Schematic view of the pull-off test: (a) 3D printed samples on uncoated substrates and (b) mold cast samples prepared by sawing, (c) 3D printed sample on coated substrates, and (d) mold cast samples prepared by drilling. ....	74
Figure 3.27 Extracting small cubic samples from the bulk area inside one layer and the interface between two adjacent layers for microstructure assessment. ...	75
Figure 4.1 Schematic view of the cement-based mixture, the limestone powder-based mixture, and the combined mixture developed in the twin-pipe pumping system. ....	78
Figure 4.2 Compressive strength of samples with different limestone powder substitution rates (error bars represent the standard error, n=3). ....	81
Figure 4.3 Penetration resistance with time for combined mixtures with different levels of accelerator addition (symbols represent individual measurements). ....	82
Figure 4.4 Heat flow curves of combined mixtures with different levels of accelerator addition. ....	83
Figure 4.5 Energy released during the first 72 hours. ....	84
Figure 4.6 Compressive strength of samples with different accelerator dosages (error bar represents the standard error, n=3). ....	85
Figure 5.1 Flow diameters of PC-based mixtures and LP-based mixtures (symbols represent individual measurements). ....	89
Figure 5.2 Flow diameters of PC-based mixtures, LP-based mixtures, and combined mixtures. ....	90

Figure 5.3 Yield stress of PC-based mixtures and LP-based mixtures (symbols represent individual measurements). .....	91
Figure 5.4 Viscosity of PC-based mixtures and LP-based mixtures (symbols represent individual measurements). .....	91
Figure 5.5 Schematic view of the mechanism in twin-pipe pumping.....	93
Figure 5.6 Cross-sections of hardened samples obtained by the use of a static mixer with (a) 0 baffles, (b) 6 baffles, (c) 12 baffles, (d) 18 baffles, (e) 24 baffles, and (f) 30 baffles. ....	93
Figure 5.7 Binary images of the cross-sections of hardened samples obtained by the use of a static mixer with (a) 0 baffles, (b) 6 baffles, (c) 12 baffles, (d) 18 baffles, (e) 24 baffles, and (f) 30 baffles. ....	94
Figure 5.8 Schematic view of the striations with a division pattern, taken from [214]. .....	95
Figure 5.9 Percentage of white in function of the number of mixing baffles (error bars represent the standard error, n=3). .....	96
Figure 5.10 Pumping pressure in function of the number of mixing baffles. ....	97
Figure 5.11 3D concrete printing of a 3 meters high column, (a) column design, and (b) the column that was just printed. ....	98
Figure 6.1 Influence of the layer orientation on compressive strength (error bars represent the standard error, n=6). .....	103
Figure 6.2 Failure patterns and fracture planes of samples in the compression test: (a) C-1, (b) C-2, (c) C-3, and (d) mold cast samples. ....	104
Figure 6.3 Influence of layer orientation on flexural strength (error bars represent the standard error, n=3). .....	105
Figure 6.4 Failure patterns and fracture planes of samples in the flexural test: (a) D-1, (b) D-2, (c) D-3, and (d) mold cast samples. ....	106
Figure 6.5 Tensile bond strength results (error bars represent the standard error, n=5). .....	107
Figure 6.6 Failure patterns and fracture planes of 3D printed samples in the pull-off test: (a) side view and (b) red area indicates the light grey zone. ....	108
Figure 6.7 Pore size distribution of samples at the age of 28 days, measurements for each series were repeated twice (solid and dashed lines). ....	110
Figure 6.8 Cumulative pore volume of samples at the age of 28 days, measurements for each series were repeated twice (solid and dashed lines). ....	110
Figure 6.9 Secondary electron (SE) images of samples at the age of 28 days, (a) contact zone formation between two mixtures, (b) ettringite formation in LP-based mixture, and (c) limestone powder distribution in mold cast sample. ....	112
Figure 6.10 Ion migration between the striations of the PC-based mixture and the LP-based mixture. ....	113
Figure 6.11 (a) Backscattered electron (BSE) images and (b) binarized images of the samples at the age of 28 days. ....	114
Figure 6.12 Energy dispersive X-ray (EDX) spectrum obtained from the chosen point in Figure 6.11 (a). .....	114

Figure 7.1 Schematic view of 3D concrete printing for hard rock tunnel linings including the overhead position and the side position. ....	117
Figure 7.2 Tensile stress versus strain curves obtained in the tack test. ....	121
Figure 7.3 Effect of roughness levels and mixture types on peak tensile stress (error bars represent the standard error, n=2). ....	122
Figure 7.4 The shear stress evolution along with time obtained in the shear test. ....	125
Figure 7.5 Maximum shear stress measured for different concrete substrates (error bars represent the standard error, n=2). ....	126
Figure 7.6 Maximum shear stress measured in the shear test and the stress growth test (dots represent individual measurements). ....	127
Figure 7.7 3D concrete printing at the overhead position, (a) Mix1, (b) Mix2, and (c) Mix3. ....	128
Figure 7.8 3D concrete printing at the side position. ....	129
Figure 7.9 Maximum number of 3D printed layers (error bars represent the standard error, n=3). ....	130
Figure 7.10 Schematic view of the contact zone with different mixtures and different surface inclinations, where dashed yellow lines indicate the failure surface. ....	131
Figure 7.11 Stress state analysis of the first printed layer at the overhead position (i.e. crown), and the side position (i.e. axis) where the effect of the normal stress is ignored. ....	132
Figure 7.12 (a) Tensile stress derived from the tack test ( $\sigma_t$ ) and the 3D concrete printing test ( $\sigma_z$ ), (b) Shear stress derived from the shear test ( $\tau_s$ ) and the 3D concrete printing test ( $\tau_{yz}$ ). ....	133
Figure 8.1 Normal force versus displacement curves for the uncoated substrates with different surface roughness levels. ....	137
Figure 8.2 Normal force versus displacement curves for the coated substrates with different surface roughness levels. ....	137
Figure 8.3 Peak normal force (a), critical displacement (b), total displacement (c), and dissipated energy (d) of fresh samples measured with the coated and uncoated substrates (error bars represent the standard error, n=2). ....	140
Figure 8.4 Normal force versus displacement curves for substrates with different surface moisture contents. ....	140
Figure 8.5 Peak normal force (a), critical displacement (b), total displacement (c), and dissipated energy (d) of fresh samples measured with different surface moisture contents (error bars represent the standard error, n=2). ....	142
Figure 8.6 Effect of substrate surface roughness levels and moisture contents on the sag resistance of 3D printed layers, (a) R1-M3, (b) R2-M3, (c) R2-M3-CT, (d) R2-M2, and (e) R2-M4. ....	143
Figure 8.7 Effect of substrate surface roughness level and moisture content on tensile bond strength after curing for 28 days (error bars represent the standard error, n=6). ....	145

Figure 8.8 Failure patterns on fracture surface A (on the side of the printed layers) and fracture surface B (on the side of the substrate) of samples after the pull-off test (failure in red zone occurred in the substrate and failure in blue zone occurred in the printed layers), (a) R1-M3, (b) R2-M3, (c) R2-M3-CT, (d) R2-M3-MC, (e) R2-M2, and (f) R2-M4. ....	146
Figure 8.9 Schematic view of the contact zone with different substrate surface roughness levels and moisture contents, (a) R1-M3, (b) R2-M3, (c) R2-M3-CT, (d) R2-M3-MC, (e) R2-M2, and (f) R2-M4. ....	147
Figure 9.1 Normal force versus displacement curves obtained in the tack test. ....	155
Figure 9.2 Failure modes of fresh samples in the tack test. ....	155
Figure 9.3 Peak normal force derived from the normal force versus displacement curves (error bars represent the standard error, n=5, symbol “*” indicates a significant difference with a significance level of $p < 0.05$ ). ....	157
Figure 9.4 Shear stress versus time curves. ....	160
Figure 9.5 Yield stress derived from the shear stress curves (error bars represent the standard error, n=5, symbol “*” indicates a significant difference with a significance level of $p < 0.05$ ). ....	161
Figure 9.6 3D concrete printing test at the overhead position: left figures indicate the maximum amount of layers and right figures indicate failure modes, (a) REF, (b) RDP-0.2%, (c) RDP-0.6%, (d) CE1-0.2%, (e) CE6-0.2%, (f) CE6-0.4%, and (g) CE6-0.6%. ....	164
Figure 9.7 Comparison among the tack test, the stress growth test, and the 3D printing test (error bars represent standard error, n=5 for the tack test and the stress growth test, n=2 for the 3D concrete printing test). ....	165
Figure 9.8 Envelop curve of Mohr criteria. ....	166
Figure 9.9 Bond strength after curing for 7 days (error bars represent the standard error, n=3, symbol “*” indicates a significant difference with a significance level of $p < 0.05$ ). ....	167
Figure 10.1 Viscosity evolution of the aqueous solution of cellulose ether CE4 with different concentrations, each series was repeated twice (solid and dashed lines). ....	171
Figure 10.2 Viscosity of the aqueous solutions of cellulose ether as a function of concentration (error bars represent the standard error, n=2). ....	172
Figure 10.3 Viscosity of the solutions of cellulose ether as a function of temperature, (a) concentration 0.2% and (b) concentration 1.0% (error bars represent the standard error, n=2). ....	173
Figure 10.4 Proportion of the squeezed water (error bars indicate the standard error, n=2). ....	174
Figure 10.5 Relative contribution to the scattering light intensity as a function of the hydrodynamic diameter for the extracted pore solutions, each series was repeated twice (solid and dashed lines). ....	176
Figure 10.6 Total organic carbon (TOC) of extracted pore solution. ....	177
Figure 10.7 Normal force versus displacement curves of mixtures without and with aluminum sulfate, each series was repeated twice (solid and dashed lines). ....	178

Figure 10.8 Peak normal force, critical displacement, total displacement, and  
dissipated energy of mixtures with and without the addition of aluminum sulfate  
(error bars represent the standard error, n=2). ..... 182



## List of Tables

Table 1.1 Comparison between dry-mix shotcrete process, wet-mix shotcrete process, spray-based 3D concrete printing, and extrusion-based 3D concrete printing. ....	5
Table 2.1 Summary of the mechanism and effect of different accelerators.....	20
Table 2.2 Summary of recent studies on inline mixing systems.....	30
Table 3.1 Physical properties of cement. ....	43
Table 3.2 Chemical composition and loss on ignition (LOI) of cement (%). ....	43
Table 3.3 Chemical composition and loss on ignition (LOI) of limestone powder (%). ....	44
Table 3.4 Product data of superplasticizer. ....	45
Table 3.5 Product data of cellulose ether. ....	46
Table 3.6 Viscosity levels of cellulose ethers. ....	46
Table 3.7 Product data of redispersible polymer powder. ....	47
Table 3.8 Product data of shotcrete accelerator. ....	48
Table 3.9 Product data of aluminum sulfate octadecahydrate. ....	49
Table 3.10 Mixture design and characteristics for concrete substrates. ....	50
Table 3.11 An overview of the test conditions for the tack test. ....	58
Table 3.12 Technical data of the pumps used for the 3D concrete printing test. ....	61
Table 3.13 Technical data of the robotic arm. ....	62
Table 3.14 Technical data of the helical static mixer. ....	62
Table 3.15 Combinations of static mixer parts. ....	62
Table 3.16 Details of the printed elements. ....	63
Table 3.17 Test conditions for the 3D concrete printing (sag resistance) test. ...	66
Table 3.18 Test conditions for the pull-off test (overlay-to-substrate). ....	73
Table 4.1 Mix design of combined mixtures ( $\text{kg}/\text{m}^3$ ). ....	80
Table 4.2 Mix design of cement paste mixtures ( $\text{kg}/\text{m}^3$ ). ....	80
Table 5.1 Mix design of PC-based mixtures and LP-based mixtures ( $\text{kg}/\text{m}^3$ ). ...	88
Table 5.2 Initial and final setting times (min). ....	92
Table 6.1 Mixture compositions of the PC-based mixture, the LP-based mixture, and the combined mixture ( $\text{kg}/\text{m}^3$ ). ....	102
Table 6.2 Characteristics of the pore structure from mercury intrusion porosimetry. ....	110
Table 8.1 An overview of different conditions used in the tack test (column A), the 3D concrete printing test (column B), and the pull-off test (column C), where the star “*” indicates that the surface condition is tested within this study. ....	136

Table 9.1 Maximum number of layers and failure modes (including adhesive failure and cohesive failure) ..... 164

Table 10.1 Mix design ( $\text{kg/m}^3$ )..... 170

Table 10.2 The amount of total organic carbon, total carbon, and inorganic carbon (mg/L). .... 176



## References

- [1] K.G. Holter, S. Geving, Moisture transport through sprayed concrete tunnel linings, *Rock Mechanics Rock Engineering*, 49 (2016) 243-272.
- [2] J. Lai, J. Qiu, H. Fan, J. Chen, Y. Xie, Freeze-proof method and test verification of a cold region tunnel employing electric heat tracing, *Tunnelling and Underground Space Technology*, 60 (2016) 56-65.
- [3] Y. Shang, K. Li, W. He, C. Sheng, From the new Austrian tunneling method to the geoengineering condition evaluation and dynamic controlling method, *Journal of Rock Mechanics and Geotechnical Engineering*, 6 (2014) 366-372.
- [4] A.K. Agrawal, V.M.S.R. Murthy, S. Chattopadhyaya, Investigations into reliability, maintainability and availability of tunnel boring machine operating in mixed ground condition using Markov chains, *Engineering Failure Analysis*, 105 (2019) 477-489.
- [5] J. Armengaud, G. Casaux-Ginestet, M. Cyr, B. Husson, M. Jolin, Characterization of fresh dry-mix shotcrete and correlation to rebound, *Constr. Build. Mater.*, 135 (2017) 225-232.
- [6] Shotcrete: Systematically Sprayed Support, 2016, pp. <https://www.e-mj.com/features/shotcrete-systematically-sprayed-support/>.
- [7] F. Vuilleumier, A. Weatherill, B. Crausaz, Safety aspects of railway and road tunnel: example of the Lötschberg railway tunnel and Mont-Blanc road tunnel, *Tunnelling and Underground Space Technology*, 17 (2002) 153-158.
- [8] L. Soldo, M. Vendramini, A. Eusebio, Tunnels design and geological studies, *Tunnelling and Underground Space Technology*, 84 (2019) 82-98.
- [9] L. Malmgren, E. Nordlund, S. Rolund, Adhesion strength and shrinkage of shotcrete, *Tunnelling and underground space technology*, 20 (2005) 33-48.
- [10] B. Lu, Y. Qian, M. Li, Y. Weng, K.F. Leong, M.J. Tan, S. Qian, Designing spray-based 3D printable cementitious materials with fly ash cenosphere and air entraining agent, *Constr. Build. Mater.*, 211 (2019) 1073-1084.
- [11] H. Kloft, H.-W. Krauss, N. Hack, E. Herrmann, S. Neudecker, P.A. Varady, D. Lowke, Influence of process parameters on the interlayer bond strength of concrete elements additive manufactured by Shotcrete 3D Printing (SC3DP), *Cem. Concr. Res.*, 134 (2020) 106078.
- [12] T. Marchment, J. Sanjayan, Reinforcement method for 3D concrete printing using paste-coated bar penetrations, *Automat. Constr.*, 127 (2021) 103694.
- [13] B. Khoshnevis, Automated construction by contour crafting—related robotics and information technologies, *Automat. Constr.*, 13 (2004) 5-19.
- [14] G. De Schutter, K. Lesage, V. Mechtcherine, V.N. Nerella, G. Habert, I. Agusti-Juan, Vision of 3D printing with concrete — Technical, economic and environmental potentials, *Cem. Concr. Res.*, 112 (2018) 25-36.

- [15] T. Wangler, E. Lloret, L. Reiter, N. Hack, F. Gramazio, M. Kohler, M. Bernhard, B. Dillenburger, J. Buchli, N. Roussel, Digital concrete: opportunities and challenges, *RILEM Tech. Lett.*, 1 (2016) 67-75.
- [16] G. De Schutter, K. Lesage, Active control of properties of concrete: a (p)review, *Mater. Struct.*, 51 (2018) 123.
- [17] A. Perrot, Y. Mélinge, P. Estellé, C. Lanos, Vibro-extrusion: a new forming process for cement-based materials, 21 (2009) 125-133.
- [18] D. Jiao, K. El Cheikh, C. Shi, K. Lesage, G. De Schutter, Structural build-up of cementitious paste with nano-Fe<sub>3</sub>O<sub>4</sub> under time-varying magnetic fields, *Cem. Concr. Res.*, 124 (2019) 105857.
- [19] B. Lothenbach, F. Winnefeld, C. Alder, E. Wieland, P. Lunk, Effect of temperature on the pore solution, microstructure and hydration products of Portland cement pastes, *Cem. Concr. Res.*, 37 (2007) 483-491.
- [20] J.J. Thomas, D. Rothstein, H.M. Jennings, B.J. Christensen, Effect of hydration temperature on the solubility behavior of Ca-, S-, Al-, and Si-bearing solid phases in Portland cement pastes, *Cem. Concr. Res.*, 33 (2003) 2037-2047.
- [21] K.O. Kjellsen, R.J. Detwiler, Reaction kinetics of portland cement mortars hydrated at different temperatures, *Cem. Concr. Res.*, 22 (1992) 112-120.
- [22] K.O. Kjellsen, R.J. Detwiler, O.E. GjØrv, Development of microstructures in plain cement pastes hydrated at different temperatures, *Cem. Concr. Res.*, 21 (1991) 179-189.
- [23] D. Marchon, S. Kawashima, H. Bessaies-Bey, S. Mantellato, S. Ng, Hydration and rheology control of concrete for digital fabrication: Potential admixtures and cement chemistry, *Cem. Concr. Res.*, 112 (2018) 96-110.
- [24] L. Reiter, M. Palacios, T. Wangler, R.J. Flatt, Putting concrete to sleep and waking it up with chemical admixtures, *Special Publication*, 302 (2015) 145-154.
- [25] A. Szabo, L. Reiter, E. Lloret-Fritschi, F. Gramazio, M. Kohler, R.J. Flatt, Processing of Set on Demand Solutions for Digital Fabrication in Architecture, *Rheology and Processing of Construction Materials*, Springer2019, pp. 440-447.
- [26] M. Pfeuffer, W. Kusterle, Rheology and rebound behaviour of dry-mix shotcrete, *Cem. Concr. Res.*, 31 (2001) 1619-1625.
- [27] L. Reiter, T. Wangler, N. Roussel, R.J. Flatt, The role of early age structural build-up in digital fabrication with concrete, *Cem. Concr. Res.*, 112 (2018) 86-95.
- [28] R.A. Buswell, W.R. Leal de Silva, S.Z. Jones, J. Dirrenberger, 3D printing using concrete extrusion: A roadmap for research, *Cem. Concr. Res.*, 112 (2018) 37-49.
- [29] V. Mechtcherine, F.P. Bos, A. Perrot, W.R.L. da Silva, V.N. Nerella, S. Fataei, R.J.M. Wolfs, M. Sonebi, N. Roussel, Extrusion-based additive manufacturing with cement-based materials – Production steps, processes, and their underlying physics: A review, *Cem. Concr. Res.*, 132 (2020) 106037.
- [30] G. De Schutter, D. Feys, Pumping of fresh concrete: insights and challenges, *RILEM Tech. Lett.*, 1 (2016) 76-80.
- [31] V.N. Nerella, V. Mechtcherine, Virtual Sliding Pipe Rheometer for estimating pumpability of concrete, *Constr. Build. Mater.*, 170 (2018) 366-377.
- [32] D. Kaplan, F. de Larrard, T. Sedran, Design of concrete pumping circuit, *ACI materials journal*, 102 (2005) 110.
- [33] V. Mechtcherine, V.N. Nerella, K. Kasten, Testing pumpability of concrete using Sliding Pipe Rheometer, *Constr. Build. Mater.*, 53 (2014) 312-323.

- [34] V.N. Nerella, M.A.B. Beigh, S. Fataei, V. Mechtcherine, Strain-based approach for measuring structural build-up of cement pastes in the context of digital construction, *Cem. Concr. Res.*, 115 (2019) 530-544.
- [35] A. Perrot, C. Lanos, P. Estellé, Y. Meline, Ram extrusion force for a frictional plastic material: model prediction and application to cement paste, *Rheologica acta*, 45 (2006) 457-467.
- [36] A. Perrot, Y. Mélinge, P. Estellé, C. Lanos, Vibro-extrusion: a new forming process for cement-based materials, *Advances in Cement Research*, 21 (2009) 125-133.
- [37] P.F.G. Banfill, M.A.O.M. Teixeira, R.J.M. Craik, Rheology and vibration of fresh concrete: Predicting the radius of action of poker vibrators from wave propagation, *Cem. Concr. Res.*, 41 (2011) 932-941.
- [38] N. Roussel, Rheological requirements for printable concretes, *Cem. Concr. Res.*, 112 (2018) 76-85.
- [39] A.S.J. Suiker, R.J.M. Wolfs, S.M. Lucas, T.A.M. Salet, Elastic buckling and plastic collapse during 3D concrete printing, *Cem. Concr. Res.*, 135 (2020) 106016.
- [40] R.J.M. Wolfs, F.P. Bos, T.A.M. Salet, Early age mechanical behaviour of 3D printed concrete: Numerical modelling and experimental testing, *Cem. Concr. Res.*, 106 (2018) 103-116.
- [41] BS EN 934-2 Admixtures for concrete, mortar and grout. Concrete admixtures. Definitions, requirements, conformity, marking and labelling, 2011.
- [42] R. Myrdal, Accelerating admixtures for concrete. State of the art, (2007).
- [43] K. Lesage, Interactions between cement and combined concrete admixtures: the influence of cement paste rheology, Ghent University, 2014.
- [44] P. Hewlett, M. Liska, Lea's chemistry of cement and concrete, Butterworth-Heinemann 2019.
- [45] D. Lootens, P. Jousset, L. Martinie, N. Roussel, R.J. Flatt, Yield stress during setting of cement pastes from penetration tests, *Cem. Concr. Res.*, 39 (2009) 401-408.
- [46] H. Yang, Y. Yan, Z. Hu, The preparation of nano calcium carbonate and calcium silicate hardening accelerator from marble waste by nitric acid treatment and study of early strength effect of calcium silicate on C30 concrete, *Journal of Building Engineering*, 32 (2020) 101507.
- [47] R.P. Salvador, S.H.P. Cavalaro, I. Segura, A.D. Figueiredo, J. Pérez, Early age hydration of cement pastes with alkaline and alkali-free accelerators for sprayed concrete, *Constr. Build. Mater.*, 111 (2016) 386-398.
- [48] R.P. Salvador, S.H.P. Cavalaro, M.A. Cincotto, A.D.d. Figueiredo, Parameters controlling early age hydration of cement pastes containing accelerators for sprayed concrete, *Cem. Concr. Res.*, 89 (2016) 230-248.
- [49] P.-C. Aïtcin, R.J. Flatt, Science and technology of concrete admixtures, Woodhead publishing 2015.
- [50] S. Senft, S. Gallegos, D.P. Manson, C. Gonzales, Chemical admixtures for concrete, Crc Press 1999.
- [51] V.S. Ramachandran, Concrete admixtures handbook: properties, science and technology, William Andrew 1996.
- [52] V.H. Dodson, Concrete admixtures, Springer Science & Business Media 2013.

- [53] S. Popovics, Concrete materials: Properties, specifications, and testing, William Andrew 1992.
- [54] N. Tenoutasse, The Hydration Mechanism of C3A and C3S in the Presence of Calcium Chloride and Calcium Sulphate, CRIC 1969.
- [55] N. Shanahan, A. Sedaghat, A. Zayed, Effect of cement mineralogy on the effectiveness of chloride-based accelerator, *Cem. Concr. Comps.*, 73 (2016) 226-234.
- [56] J. Cheung, A. Jeknavorian, L. Roberts, D. Silva, Impact of admixtures on the hydration kinetics of Portland cement, *Cem. Concr. Res.*, 41 (2011) 1289-1309.
- [57] J. Sathya Narayanan, K. Ramamurthy, Identification of set-accelerator for enhancing the productivity of foam concrete block manufacture, *Constr. Build. Mater.*, 37 (2012) 144-152.
- [58] V.S. Ramachandran, Elucidation of the role of chemical admixtures in hydrating cements by DTA technique, *Thermochimica Acta*, 4 (1972) 343-366.
- [59] H. Justnes, Kalcijev nitrat kot mnogo-funkcionalni dodatek betonu ("Calcium Nitrate as Multifunctional Concrete Admixture" in Slovenian), 14th Slovenian colloquium on Concrete, Ljubljana, Slovenia, 2007, pp. 21-28.
- [60] H. Justnes, E. Nygaard, The mechanism of calcium nitrate as set accelerator for cement, *Proceedings of 10th International Congress on the Chemistry of Cement*, Gothenburg, Sweden, 1997, pp. 2-6.
- [61] T. Wise, V.S. Ramachandran, G.M. Polomark, The effect of thiocyanates on the hydration of portland cement at low temperatures, *Thermochimica Acta*, 264 (1995) 157-171.
- [62] B. Abdelrazig, D. Bonner, D. Nowell, P. Egan, J.J.T.a. Dransfield, Estimation of the degree of hydration in modified ordinary portland cement pastes by differential scanning calorimetry. Part II, 168 (1990) 291-295.
- [63] G.Y.G. Van der Meijde, Accelerating early strength and stiffness development of a Portland cement-based mortar for 3D printing, TU/E Eindhoven, 2019.
- [64] C. Maltese, C. Pistolesi, A. Bravo, F. Cella, T. Cerulli, D. Salvioni, A case history: Effect of moisture on the setting behaviour of a Portland cement reacting with an alkali-free accelerator, *Cem. Concr. Res.*, 37 (2007) 856-865.
- [65] Y. Qi, S. Li, Z. Li, J. Zhang, H. Li, Hydration effect of sodium silicate on cement slurry doped with xanthan, *Constr. Build. Mater.*, 223 (2019) 976-985.
- [66] S. Guo, Y. Zhang, K. Wang, Y. Bu, C. Wang, C. Ma, H. Liu, Delaying the hydration of Portland cement by sodium silicate: Setting time and retarding mechanism, *Constr. Build. Mater.*, 205 (2019) 543-548.
- [67] C. Paglia, F. Wombacher, H. Böhni, The influence of alkali-free and alkaline shotcrete accelerators within cement systems: I. Characterization of the setting behavior, *Cem. Concr. Res.*, 31 (2001) 913-918.
- [68] C. Paglia, F. Wombacher, H. Böhni, The influence of alkali-free and alkaline shotcrete accelerators within cement systems: Influence of the temperature on the sulfate attack mechanisms and damage, *Cem. Concr. Res.*, 33 (2003) 387-395.
- [69] C. Chen, Z. Sun, Influence of aluminum sulfate on hydration and properties of cement pastes, *Journal of Advanced Concrete Technology*, 16 (2018) 522-530.
- [70] D. Damidot, A. Rettel, Study of the interaction between the hydration of CA and of C3S at room temperature, *Proceedings of the 11th International Congress on the Chemistry of Cement (ICCC)*, 2003, pp. 1845-1854.

- [71] Z. Liu, B. Lou, D.M. Barbieri, A. Sha, T. Ye, Y. Li, Effects of pre-curing treatment and chemical accelerators on Portland cement mortars at low temperature (5 °C), *Constr. Build. Mater.*, 240 (2020) 117893.
- [72] M. Heikal, Effect of calcium formate as an accelerator on the physicochemical and mechanical properties of pozzolanic cement pastes, *Cem. Concr. Res.*, 34 (2004) 1051-1056.
- [73] T. Lee, J. Lee, Y. Kim, Effects of admixtures and accelerators on the development of concrete strength for horizontal form removal upon curing at 10 °C, *Constr. Build. Mater.*, 237 (2020) 117652.
- [74] H. Justnes, E.C. Nygaard, Technical calcium nitrate as set accelerator for cement at low temperatures, *Cem. Concr. Res.*, 25 (1995) 1766-1774.
- [75] Y.L. Yaphary, Z. Yu, R.H.W. Lam, D. Lau, Effect of triethanolamine on cement hydration toward initial setting time, *Constr. Build. Mater.*, 141 (2017) 94-103.
- [76] Z. Lu, X. Kong, D. Jansen, C. Zhang, J. Wang, X. Pang, J. Yin, Towards a further understanding of cement hydration in the presence of triethanolamine, *Cem. Concr. Res.*, 132 (2020) 106041.
- [77] Y. Zhang, L. Gao, X. Cai, Q. Li, X. Kong, Influences of triethanolamine on the performance of cement pastes used in slab track, *Constr. Build. Mater.*, 238 (2020) 117670.
- [78] S. Aggoun, M. Cheikh-Zouaoui, N. Chikh, R. Duval, Effect of some admixtures on the setting time and strength evolution of cement pastes at early ages, *Constr. Build. Mater.*, 22 (2008) 106-110.
- [79] J. Han, K. Wang, J. Shi, Y. Wang, Mechanism of triethanolamine on Portland cement hydration process and microstructure characteristics, *Constr. Build. Mater.*, 93 (2015) 457-462.
- [80] J.H.S.A. Luiz R. Prudencio, H. Paulo, Interaction between Accelerating Admixtures and Portland Cement for Shotcrete: The Influence of the Admixture's Chemical Base and the Correlation between Paste Tests and Shotcrete Performance, *ACI Materials Journal*, 93 (1996).
- [81] R.P. Salvador, S.H.P. Cavalaro, I. Segura, M.G. Hernández, J. Ranz, A.D.d. Figueiredo, Relation between ultrasound measurements and phase evolution in accelerated cementitious matrices, *Mater. Des.*, 113 (2017) 341-352.
- [82] E. Berodier, K. Scrivener, Understanding the Filler Effect on the Nucleation and Growth of C - S - H, *Journal of the American Ceramic Society*, 97 (2014) 3764-3773.
- [83] D. Marchon, R.J. Flatt, 12 - Impact of chemical admixtures on cement hydration, in: P.-C. Aïtcin, R.J. Flatt (Eds.) *Science and Technology of Concrete Admixtures*, Woodhead Publishing 2016, pp. 279-304.
- [84] J.J. Thomas, H.M. Jennings, J. Chen, Influence of nucleation seeding on the hydration mechanisms of tricalcium silicate and cement, *The Journal of Physical Chemistry C*, 113 (2009) 4327-4334.
- [85] L. Nicoleau, The acceleration of cement hydration by seeding: influence of the cement mineralogy, *ZKG international*, (2013) 40-49.
- [86] R.W. Balluffi, S.M. Allen, W.C. Carter, *Kinetics of materials*, John Wiley & Sons 2005.
- [87] L. Nicoleau, A. Nonat, D. Perrey, The di- and tricalcium silicate dissolutions, *Cem. Concr. Res.*, 47 (2013) 14-30.

- [88] S. Das, S. Ray, S. Sarkar, Early strength development in concrete using preformed CSH nano crystals, *Constr. Build. Mater.*, 233 (2020) 117214.
- [89] S. Leinitz, Z. Lu, S. Becker, D. Stephan, R. von Klitzing, W. Schmidt, Influence of Different Accelerators on the Rheology and Early Hydration of Cement Paste, in: V. Mechtcherine, K. Khayat, E. Secieru (Eds.) *Rheology and Processing of Construction Materials*, Springer International Publishing, Cham, 2020, pp. 106-115.
- [90] A. Quennoz, K.L. Scrivener, Interactions between alite and C3A-gypsum hydrations in model cements, *Cem. Concr. Res.*, 44 (2013) 46-54.
- [91] D. Marchon, Controlling cement hydration through the molecular structure of comb copolymer superplasticizers, *ETH Zurich*, 2016.
- [92] A. Favier, J. Hot, G. Habert, N. Roussel, J.-B.d.E. de Lacaillerie, Flow properties of MK-based geopolymer pastes. A comparative study with standard Portland cement pastes, *Soft Matter*, 10 (2014) 1134-1141.
- [93] P.L. Domone, The properties of low strength silicate/portland cement grouts, *Cem. Concr. Res.*, 20 (1990) 25-35.
- [94] W. Zhang, S. Li, J. Wei, Q. Zhang, R. Liu, X. Zhang, H. Yin, Grouting rock fractures with cement and sodium silicate grout, *Carbonates and Evaporites*, 33 (2018) 211-222.
- [95] W. Cui, J. Huang, H. Song, M. Xiao, Development of two new anti-washout grouting materials using multi-way ANOVA in conjunction with grey relational analysis, *Constr. Build. Mater.*, 156 (2017) 184-198.
- [96] M.R. Azadi, A. Taghichian, A. Taheri, Optimization of cement-based grouts using chemical additives, *Journal of Rock Mechanics and Geotechnical Engineering*, 9 (2017) 623-637.
- [97] H. Chen, Q. Wang, The behaviour of organic matter in the process of soft soil stabilization using cement, *Bulletin of Engineering Geology and the Environment*, 65 (2006) 445-448.
- [98] S. Kazemian, A. Prasad, B.B.K. Huat, J. Bolouri Bazaz, T.A. Mohammed, F.N. Abdul Aziz, Effect of aggressive pH media on peat treated by cement and sodium silicate grout, *Journal of Central South University*, 18 (2011) 840-847.
- [99] D. Ravikumar, N. Neithalath, An electrical impedance investigation into the chloride ion transport resistance of alkali silicate powder activated slag concretes, *Cem. Concr. Comps.*, 44 (2013) 58-68.
- [100] J. Funehag, Å. Fransson, Sealing narrow fractures with a Newtonian fluid: Model prediction for grouting verified by field study, *Tunnelling and Underground Space Technology*, 21 (2006) 492-498.
- [101] F. Sha, S. Li, R. Liu, Q. Zhang, Z. Li, Performance of typical cement suspension-sodium silicate double slurry grout, *Constr. Build. Mater.*, 200 (2019) 408-419.
- [102] Z. Yu, L. Yang, S. Zhou, Q. Gong, H. Zhu, Durability of cement-sodium silicate grouts with a high water to binder ratio in marine environments, *Constr. Build. Mater.*, 189 (2018) 550-559.
- [103] L.R. Prudêncio, Accelerating admixtures for shotcrete, *Cem. Concr. Comps.*, 20 (1998) 213-219.
- [104] C. Maltese, C. Pistolesi, A. Bravo, F. Cella, T. Cerulli, D. Salvioni, Effects of setting regulators on the efficiency of an inorganic acid based alkali-free

- accelerator reacting with a Portland cement, *Cem. Concr. Res.*, 37 (2007) 528-536.
- [105] I. Galobardes Reyes, Characterization and control of wet-mix sprayed concrete with accelerators, *Universitat Politècnica de Catalunya*, 2013.
- [106] J. Kaufmann, K. Frech, P. Schuetz, B. Münch, Rebound and orientation of fibers in wet sprayed concrete applications, *Constr. Build. Mater.*, 49 (2013) 15-22.
- [107] M. Jolin, Mechanisms of placement and stability of dry process shotcrete, *University of British Columbia*, 1999.
- [108] L. Chen, P. Li, G. Liu, F. Wang, Numerical simulation for optimizing the nozzle of moist-mix shotcrete based on orthogonal test, *Journal of Measurements in Engineering*, 5 (2017) 205-221.
- [109] R.P. Salvador, S.H.P. Cavalaro, R. Monte, A.D.d. Figueiredo, Relation between chemical processes and mechanical properties of sprayed cementitious matrices containing accelerators, *Cem. Concr. Comps.*, 79 (2017) 117-132.
- [110] S. Neudecker, C. Bruns, R. Gerbers, J. Heyn, F. Dietrich, K. Dröder, A. Raatz, H. Kloft, A New Robotic Spray Technology for Generative Manufacturing of Complex Concrete Structures Without Formwork, *Procedia CIRP*, 43 (2016) 333-338.
- [111] H. Lindemann, R. Gerbers, S. Ibrahim, F. Dietrich, E. Herrmann, K. Dröder, A. Raatz, H. Kloft, Development of a Shotcrete 3D-Printing (SC3DP) Technology for Additive Manufacturing of Reinforced Freeform Concrete Structures, in: T. Wangler, R.J. Flatt (Eds.) *First RILEM International Conference on Concrete and Digital Fabrication – Digital Concrete 2018*, Springer International Publishing, Cham, 2019, pp. 287-298.
- [112] E. Herrmann, J. Mainka, H. Lindemann, F. Wirth, H. Kloft, Digitally Fabricated Innovative Concrete Structures, *ISARC. Proceedings of the International Symposium on Automation and Robotics in Construction*, IAARC Publications, 2018, pp. 1-8.
- [113] I. Dressler, N. Freund, D. Lowke, The Effect of Accelerator Dosage on Fresh Concrete Properties and on Interlayer Strength in Shotcrete 3D Printing, *Materials*, 13 (2020) 374.
- [114] G. Pan, P. Li, L. Chen, G. Liu, A study of the effect of rheological properties of fresh concrete on shotcrete-rebound based on different additive components, *Constr. Build. Mater.*, 224 (2019) 1069-1080.
- [115] P. Wu, J. Wang, X. Wang, A critical review of the use of 3-D printing in the construction industry, *Automat. Constr.*, 68 (2016) 21-31.
- [116] T.T. Le, S.A. Austin, S. Lim, R.A. Buswell, A.G. Gibb, T. Thorpe, Mix design and fresh properties for high-performance printing concrete, *Mater. Struct.*, 45 (2012) 1221-1232.
- [117] J. Zhang, S. Xu, W. Li, High shear mixers: A review of typical applications and studies on power draw, flow pattern, energy dissipation and transfer properties, *Chemical Engineering and Processing: Process Intensification*, 57-58 (2012) 25-41.
- [118] R.K. Thakur, C. Vial, K.D.P. Nigam, E.B. Nauman, G. Djelveh, Static Mixers in the Process Industries—A Review, *Chem. Eng. Res. Des.*, 81 (2003) 787-826.

- [119] C. Gosselin, R. Duballet, P. Roux, N. Gaudillière, J. Dirrenberger, P. Morel, Large-scale 3D printing of ultra-high performance concrete—a new processing route for architects and builders, *Mater. Des.*, 100 (2016) 102-109.
- [120] V. Esnault, A. Labyad, M. Chantini, F. Toussaint, Experience in online modification of rheology and strength acquisition of 3D printable mortars, *RILEM International Conference on Concrete and Digital Fabrication*, Springer, 2018, pp. 24-38.
- [121] L. Reiter, T. Wangler, A. Anton, R.J. Flatt, Setting on demand for digital concrete – Principles, measurements, chemistry, validation, *Cem. Concr. Res.*, 132 (2020) 106047.
- [122] T. Wangler, F. Scotto, E. Lloret-Fritsch, R.J. Flatt, Residence Time Distributions in Continuous Processing of Concrete, *Rheology and Processing of Construction Materials*, Springer2019, pp. 448-456.
- [123] E. Lloret Fritsch, *Smart Dynamic Casting-A digital fabrication method for non-standard concrete structures*, ETH Zurich, 2016.
- [124] Y. Yuan, Y. Tao, Mixing and Extrusion of printing concrete, *Computational modelling of concrete and concrete structures*Bad Hofgastein, Austria, 2018.
- [125] P. Kuhn, A. Brühwiler, R. Bourquin, D. Lootens, L. Oblak, Mixer, system for applying a building material and method for producing a structure from building material, Google Patents, 2019.
- [126] A. Jovanović, M. Pezo, L. Pezo, L. Lević, DEM/CFD analysis of granular flow in static mixers, *Powder technology*, 266 (2014) 240-248.
- [127] A. Ghanem, T. Lemenand, D. Della Valle, H. Peerhossaini, Static mixers: Mechanisms, applications, and characterization methods—A review, *Chem. Eng. Res. Des.*, 92 (2014) 205-228.
- [128] Y. Tao, K. Lesage, K.V. Tittelboom, Y. Yuan, G.D. Schutter, Twin-pipe pumping strategy for stiffening control of 3D printable concrete: from transportation to fabrication, *Cem. Concr. Res.*
- [129] M.D. Das, A.N. Hrymak, M.H.I. Baird, Laminar liquid–liquid dispersion in the SMX static mixer, *Chemical Engineering Science*, 101 (2013) 329-344.
- [130] E.L. Paul, V.A. Atiemo-Obeng, S.M. Kresta, *Handbook of industrial mixing: science and practice*, John Wiley & Sons2004.
- [131] J. Xiao, C. Zou, M. Liu, G. Zhang, G. Delaplace, R. Jeantet, X.D. Chen, Mixing in a soft-elastic reactor (SER) characterized using an RGB based image analysis method, *Chemical Engineering Science*, 181 (2018) 272-285.
- [132] T.T. Le, S.A. Austin, S. Lim, R.A. Buswell, R. Law, A.G. Gibb, T. Thorpe, Hardened properties of high-performance printing concrete, *Cem. Concr. Res.*, 42 (2012) 558-566.
- [133] R.J.M. Wolfs, F.P. Bos, T.A.M. Salet, Hardened properties of 3D printed concrete: The influence of process parameters on interlayer adhesion, *Cem. Concr. Res.*, 119 (2019) 132-140.
- [134] B. Panda, S.C. Paul, L.J. Hui, Y.W.D. Tay, M.J. Tan, Additive manufacturing of geopolymer for sustainable built environment, *Journal of Cleaner Production*, 167 (2017) 281-288.
- [135] B. Panda, S.C. Paul, N.A.N. Mohamed, Y.W.D. Tay, M.J. Tan, Measurement of tensile bond strength of 3D printed geopolymer mortar, *Measurement*, 113 (2018) 108-116.



- [136] Y.W.D. Tay, G.H.A. Ting, Y. Qian, B. Panda, L. He, M.J. Tan, Time gap effect on bond strength of 3D-printed concrete, *Virtual and Physical Prototyping*, 14 (2019) 104-113.
- [137] J.G. Sanjayan, B. Nematollahi, M. Xia, T. Marchment, Effect of surface moisture on inter-layer strength of 3D printed concrete, *Constr. Build. Mater.*, 172 (2018) 468-475.
- [138] J. Van Der Putten, G. De Schutter, K. Van Tittelboom, Surface modification as a technique to improve inter-layer bonding strength in 3D printed cementitious materials, *RILEM Tech. Lett.*, 4 (2019) 33-38.
- [139] T. Marchment, J. Sanjayan, M. Xia, Method of enhancing interlayer bond strength in construction scale 3D printing with mortar by effective bond area amplification, *Materials and Design*, 169 (2019) 107684.
- [140] E. Hosseini, M. Zakertabrizi, A.H. Korayem, G. Xu, A novel method to enhance the interlayer bonding of 3D printing concrete: An experimental and computational investigation, *Cem. Concr. Comps.*, 99 (2019) 112-119.
- [141] G. Ma, N.M. Salman, L. Wang, F. Wang, A novel additive mortar leveraging internal curing for enhancing interlayer bonding of cementitious composite for 3D printing, *Constr. Build. Mater.*, 244 (2020) 118305.
- [142] T. Marchment, J. Sanjayan, M. Xia, Method of enhancing interlayer bond strength in construction scale 3D printing with mortar by effective bond area amplification, *Mater. Des.*, 169 (2019) 107684.
- [143] L. Wang, Z. Tian, G. Ma, M. Zhang, Interlayer bonding improvement of 3D printed concrete with polymer modified mortar: Experiments and molecular dynamics studies, *Cem. Concr. Comps.*, 110 (2020) 103571.
- [144] J. Van Der Putten, D. Snoeck, K. Van Tittelboom, 3D Printing of cementitious materials with superabsorbent polymers, *Durable Concrete for Infrastructure under Severe Conditions-Smart Admixtures, Self-responsiveness and Nano-additions*, Magnel Laboratory for Concrete Research, 2019, pp. 86-89.
- [145] C. Schröfl, V.N. Nerella, V. Mechtcherine, Capillary water intake by 3D-printed concrete visualised and quantified by neutron radiography, *RILEM International Conference on Concrete and Digital Fabrication*, Springer, 2018, pp. 217-224.
- [146] J. Van Der Putten, M. Azima, P. Van den Heede, T. Van Mullem, D. Snoeck, C. Carminati, J. Hovind, P. Trtik, G. De Schutter, V. Tittelboom, Neutron radiography to study the water ingress via the interlayer of 3D printed cementitious materials for continuous layering, *Constr. Build. Mater.*, 258 (2020) 119587.
- [147] N. Ukrainczyk, A. Rogina, Styrene-butadiene latex modified calcium aluminate cement mortar, *Cem. Concr. Comps.*, 41 (2013) 16-23.
- [148] B. Zareiyan, B. Khoshnevis, Effects of interlocking on interlayer adhesion and strength of structures in 3D printing of concrete, *Automat. Constr.*, 83 (2017) 212-221.
- [149] Q. Xu, J. Stark, Early hydration of ordinary Portland cement with an alkaline shotcrete accelerator, *Advances in cement research*, 17 (2005) 1-8.
- [150] I. Galobardes, S.H. Cavalaro, A. Aguado, T. Garcia, Estimation of the modulus of elasticity for sprayed concrete, *Constr. Build. Mater.*, 53 (2014) 48-58.

- [151] H.-G. Park, S.-K. Sung, C.-G. Park, J.-P. Won, Influence of a C12A7 mineral-based accelerator on the strength and durability of shotcrete, *Cem. Concr. Res.*, 38 (2008) 379-385.
- [152] J.-P. Won, U.-J. Hwang, S.-J. Lee, Enhanced long-term strength and durability of shotcrete with high-strength C12A7 mineral-based accelerator, *Cem. Concr. Res.*, 76 (2015) 121-129.
- [153] S.T. Lee, D.G. Kim, H.S. Jung, Sulfate attack of cement matrix containing inorganic alkali-free accelerator, *J KSCE Journal of Civil Engineering*, 13 (2009) 49-54.
- [154] C. Paglia, F. Wombacher, H. Böhni, M. Sommer, An evaluation of the sulfate resistance of cementitious material accelerated with alkali-free and alkaline admixtures: Laboratory vs. field, *Cem. Concr. Res.*, 32 (2002) 665-671.
- [155] D.P. Bentz, A review of early-age properties of cement-based materials, *Cem. Concr. Res.*, 38 (2008) 196-204.
- [156] G. De Schutter, M. Vuylsteke, Minimisation of early age thermal cracking in a J-shaped non-reinforced massive concrete quay wall, *Engineering Structures*, 26 (2004) 801-808.
- [157] T. Meagher, N. Shanahan, D. Buidens, K.A. Riding, A. Zayed, Effects of chloride and chloride-free accelerators combined with typical admixtures on the early-age cracking risk of concrete repair slabs, *Constr. Build. Mater.*, 94 (2015) 270-279.
- [158] H. Mihashi, J. Leite, atilde, B. o Paulo de, State-of-the-Art Report on Control of Cracking in Early Age Concrete, *Journal of Advanced Concrete Technology*, 2 (2004) 141-154.
- [159] E. Holt, Contribution of mixture design to chemical and autogenous shrinkage of concrete at early ages, *Cem. Concr. Res.*, 35 (2005) 464-472.
- [160] E. Holt, M. Leivo, Cracking risks associated with early age shrinkage, *Cem. Concr. Comps.*, 26 (2004) 521-530.
- [161] B. Klemczak, A. Knoppik-Wróbel, Early age thermal and shrinkage cracks in concrete structures—description of the problem, *Architecture-Civil Engineering-Environment*, 4 (2011) 35-48.
- [162] O.M. Jensen, P.F. Hansen, Influence of temperature on autogenous deformation and relative humidity change in hardening cement paste, *Cem. Concr. Res.*, 29 (1999) 567-575.
- [163] D.A. Buidens, Effects of Mix Design Using Chloride-Based Accelerator on Concrete Pavement Cracking Potential, University of South Florida, 2014.
- [164] A. Kronlöf, M. Leivo, P. Sipari, Experimental study on the basic phenomena of shrinkage and cracking of fresh mortar, *Cem. Concr. Res.*, 25 (1995) 1747-1754.
- [165] R. Combrinck, W.P. Boshoff, Typical plastic shrinkage cracking behaviour of concrete, *J Magazine of Concrete Research*, 65 (2013) 486-493.
- [166] A. Leemann, P. Nygaard, P. Lura, Impact of admixtures on the plastic shrinkage cracking of self-compacting concrete, *Cem. Concr. Comps.*, 46 (2014) 1-7.
- [167] B. Lagerblad, L. Fjällberg, C. Vogt, Shrinkage and durability of shotcrete, *J Shotcrete: Elements of a System*, (2010) 173-180.

- [168] A.V. Rahul, M. Santhanam, H. Meena, Z. Ghani, Mechanical characterization of 3D printable concrete, *Constr. Build. Mater.*, 227 (2019) 116710.
- [169] J. Van Der Putten, M. Azima, P. Van den Heede, T. Van Mullem, D. Snoeck, C. Carminati, J. Hovind, P. Trtik, G. De Schutter, K. Van Tittelboom, Neutron radiography to study the water ingress via the interlayer of 3D printed cementitious materials for continuous layering, *Constr. Build. Mater.*, 258 (2020) 119587.
- [170] M.K. Mohan, A.V. Rahul, G. De Schutter, K. Van Tittelboom, Extrusion-based concrete 3D printing from a material perspective: A state-of-the-art review, *Cem. Concr. Comps.*, 115 (2021) 103855.
- [171] V.-T. Phan, Relationship between the adhesive properties and the rheological behavior of fresh mortars, *École normale supérieure de Cachan-ENS Cachan*, 2012.
- [172] H. Sasse, R.T. Comm, Adhesion between polymers and concrete/Adhésion entre polymères et béton: Bonding· Protection· Repair/Revêtement· Protection· Réparation, Springer 2013.
- [173] L.-H. Lee, Fundamentals of adhesion, Springer Science & Business Media 1991.
- [174] N. Maeda, N. Chen, M. Tirrell, J.N. Israelachvili, Adhesion and Friction Mechanisms of Polymer-on-Polymer Surfaces, *Science*, 297 (2002) 379.
- [175] R.T.L. Allen, S.C. Edwards, D. Shaw, Repair of concrete structures, CRC Press 1992.
- [176] B. Bissonnette, L. Courard, A. Garbacz, Concrete surface engineering, CRC Press 2015.
- [177] K. Kendall, Adhesion: molecules and mechanics, *Science*, 263 (1994) 1720-1725.
- [178] M.B. Amar, D. Bonn, Fingering instabilities in adhesive failure, *Physica D: Nonlinear Phenomena*, 209 (2005) 1-16.
- [179] N. Roussel, G. Ovarlez, S. Garrault, C. Brumaud, The origins of thixotropy of fresh cement pastes, *Cem. Concr. Res.*, 42 (2012) 148-157.
- [180] R. Tadmor, P. Bahadur, A. Leh, H.E. N'guessan, R. Jaini, L. Dang, Measurement of Lateral Adhesion Forces at the Interface between a Liquid Drop and a Substrate, *Physical Review Letters*, 103 (2009) 266101.
- [181] R. Tadmor, R. Das, S. Gulec, J. Liu, H. E. N'guessan, M. Shah, P. S. Wasnik, S.B. Yadav, Solid-Liquid Work of Adhesion, *Langmuir*, 33 (2017) 3594-3600.
- [182] M.A. Yazdi, E. Dejager, M. Debraekeleer, E. Gruyaert, K. Van Tittelboom, N. De Belie, Bond strength between concrete and repair mortar and its relation with concrete removal techniques and substrate composition, *Constr. Build. Mater.*, 230 (2020) 116900.
- [183] K. Shito, Y. Kamihigashi, S. Nojima, A. Yoshida, The Application of Water Jet Technology to Surface Preparation and Removal on Concrete Structures, *Concrete Journal*, 38 (2000) 40-54.
- [184] E.K. Tschegg, M. Ingruber, C.H. Surberg, F. Munger, Factors influencing fracture behavior of old-new concrete bonds, *ACI Materials Journal*, 97 (2000) 447-453.
- [185] L. Czarnecki, L. Courard, Garbacz, Application of surface engineering methods towards evaluation of concrete repair efficiency, *Engineering and Construction*, 12 (2007) 630-634.

- [186] B. Bissonnette, L. Courard, H. Beushausen, D. Fowler, M. Trevino, A. Vaysburd, Recommendations for the repair, the lining or the strengthening of concrete slabs or pavements with bonded cement-based material overlays, *Mater. Struct.*, 46 (2013) 481-494.
- [187] L. Courard, T. Piotrowski, A. Garbacz, Near-to-surface properties affecting bond strength in concrete repair, *Cem. Concr. Comps.*, 46 (2014) 73-80.
- [188] H. Beushausen, B. Höhlig, M. Talotti, The influence of substrate moisture preparation on bond strength of concrete overlays and the microstructure of the OTZ, *Cem. Concr. Res.*, 92 (2017) 84-91.
- [189] E.K. Schrader, Mistakes, misconceptions, and controversial issues concerning concrete and concrete repairs, Part 3, *J Concrete International*, 14 (1992) 54-59.
- [190] M.K. Mohan, A.V. Rahul, K. Van Tittelboom, G. De Schutter, Rheological and pumping behaviour of 3D printable cementitious materials with varying aggregate content, *Cem. Concr. Res.*, 139 (2021) 106258.
- [191] C. Brumaud, H. Bessaies-Bey, C. Mohler, R. Baumann, M. Schmitz, M. Radler, N. Roussel, Cellulose ethers and water retention, *Cem. Concr. Res.*, 53 (2013) 176-184.
- [192] J.-Y. Petit, E. Wirquin, Evaluation of various cellulose ethers performance in ceramic tile adhesive mortars, *International Journal of Adhesion and Adhesives*, 40 (2013) 202-209.
- [193] J. Pourchez, B. Ruot, J. Debayle, E. Pourchez, P. Grosseau, Some aspects of cellulose ethers influence on water transport and porous structure of cement-based materials, *Cem. Concr. Res.*, 40 (2010) 242-252.
- [194] Y. Ohama, Handbook of polymer-modified concrete and mortars: properties and process technology, William Andrew 1995.
- [195] A. Jenni, L. Holzer, R. Zurbruggen, M. Herwegh, Influence of polymers on microstructure and adhesive strength of cementitious tile adhesive mortars, *Cem. Concr. Res.*, 35 (2005) 35-50.
- [196] NEN-EN 12390-3, Testing hardened concrete — Part 3: Compressive strength of test specimens, 2019.
- [197] NBN EN 1542, Products and systems for the protection and repair of concrete structures - Test methods - Measurement of bond strength by pull-off, (1999).
- [198] BS 1134, Assessment of surface texture. Guidance and general information, 2010.
- [199] N.M. Alderete, Microstructure of Mortar and Concrete with Supplementary Cementitious Materials: Relation with the Capillary Imbibition Phenomenon, Ghent University, 2018.
- [200] R.P. Chhabra, J.F. Richardson, Non-Newtonian flow and applied rheology: engineering applications, Butterworth-Heinemann 2011.
- [201] NBN EN 1015-3, Methods of test for mortar for masonry-Part 3: Determination of consistence of fresh mortar (by flow table), European code, 1999.
- [202] EN 196-9, Methods of Testing Cement- Part 9: Heat of Hydration- Semi-adiabatic Method, British Standard, 2010.
- [203] ASTM C403/C403M-16, Standard Test Method for Time of Setting of Concrete Mixtures by Penetration Resistance, ASTM International, 2016.

- [204] NEN EN 12390-5, Testing hardened concrete. Flexural strength of test specimens, (2019).
- [205] N. Alderete, Y. Villagrán, A. Mignon, D. Snoeck, N. De Belie, Pore structure description of mortars containing ground granulated blast-furnace slag by mercury intrusion porosimetry and dynamic vapour sorption, *Constr. Build. Mater.*, 145 (2017) 157-165.
- [206] E.W. Washburn, The dynamics of capillary flow, *Physical review letters*, 17 (1921) 273.
- [207] N. Ghafoori, R. Spitek, M. Najimi, Influence of limestone size and content on transport properties of self-consolidating concrete, *Constr. Build. Mater.*, 127 (2016) 588-595.
- [208] G. İnan Sezer, Compressive strength and sulfate resistance of limestone and/or silica fume mortars, *Constr. Build. Mater.*, 26 (2012) 613-618.
- [209] L.G. Li, A.K.H. Kwan, Adding limestone fines as cementitious paste replacement to improve tensile strength, stiffness and durability of concrete, *Cem. Concr. Comps.*, 60 (2015) 17-24.
- [210] D. Wang, C. Shi, N. Farzadnia, Z. Shi, H. Jia, A review on effects of limestone powder on the properties of concrete, *Constr. Build. Mater.*, 192 (2018) 153-166.
- [211] J. Han, K. Wang, Y. Wang, J. Shi, Study of aluminum sulfate and anhydrite on cement hydration process, *Mater. Struct.*, 49 (2016) 1105-1114.
- [212] J.W. Bullard, H.M. Jennings, R.A. Livingston, A. Nonat, G.W. Scherer, J.S. Schweitzer, K.L. Scrivener, J.J. Thomas, Mechanisms of cement hydration, *Cem. Concr. Res.*, 41 (2011) 1208-1223.
- [213] L. Duan, Y. Zhang, J. Lai, Influence of Ground Temperature on Shotcrete-to-Rock Adhesion in Tunnels, *Advances in Materials Science and Engineering*, 2019 (2019) 8709087.
- [214] S. Wang, Y. Jian, X. Lu, L. Ruan, W. Dong, K. Feng, Study on load distribution characteristics of secondary lining of shield under different construction time, *Tunnelling and Underground Space Technology*, 89 (2019) 25-37.
- [215] Z. Zhao, H. Xu, G. Liu, F. Liu, G. Wang, A robust numerical method for modeling ventilation through long tunnels in high temperature regions based on 1D pipe model, *Tunnelling and Underground Space Technology*, 115 (2021) 104050.
- [216] G. Liu, J. Zhao, Z. Zhang, C. Wang, Q. Xu, Mechanical Properties and Microstructure of Shotcrete under High Temperature, *Applied Sciences*, 11 (2021).
- [217] S.M. Peker, S.S. Helvacı, Solid-liquid two phase flow, Elsevier 2011.
- [218] CHAPTER 2 - Flow Drilling: Underbalance Drilling with Liquid Single-Phase Systems, in: B. Rehm, A. Haghshenas, A. Paknejad, A. Al-Yami, J. Hughes, J. Schubert (Eds.) *Underbalanced Drilling: Limits and Extremes*, Gulf Publishing Company 2012, pp. 39-108.
- [219] Inline static mixers and blenders for low shear processing, 2019, pp. <https://www.admix.com/wp-content/uploads/2019/2006/Admix-Datasheet-Admixer.pdf>.
- [220] F. Grosz-Roll, Assessing homogeneity in motionless mixers, *Int. Chem. Eng.*, 20 (1980) 542-549.

- [221] H.E.H. Meijer, M.K. Singh, P.D. Anderson, On the performance of static mixers: A quantitative comparison, *Prog. Polym. Sci.*, 37 (2012) 1333-1349.
- [222] W.-M. Lu, H.-Z. Wu, M.-Y. Ju, Effects of baffle design on the liquid mixing in an aerated stirred tank with standard Rushton turbine impellers, *Chemical Engineering Science*, 52 (1997) 3843-3851.
- [223] J. Ye, C. Cui, J. Yu, K. Yu, J. Xiao, Fresh and anisotropic-mechanical properties of 3D printable ultra-high ductile concrete with crumb rubber, *Compos. Part. B-Eng*, 211 (2021) 108639.
- [224] B. Panda, S.C. Paul, M.J. Tan, Anisotropic mechanical performance of 3D printed fiber reinforced sustainable construction material, *Materials Letters*, 209 (2017) 146-149.
- [225] G. Ma, Z. Li, L. Wang, F. Wang, J. Sanjayan, Mechanical anisotropy of aligned fiber reinforced composite for extrusion-based 3D printing, *Constr. Build. Mater.*, 202 (2019) 770-783.
- [226] B. Nematollahi, P. Vijay, J. Sanjayan, A. Nazari, M. Xia, V. Naidu Nerella, V. Mechtcherine, Effect of Polypropylene Fibre Addition on Properties of Geopolymers Made by 3D Printing for Digital Construction, *Materials*, 11 (2018).
- [227] J. Van Der Putten, M. Deprez, V. Cnudde, G. De Schutter, K. Van Tittelboom, Microstructural Characterization of 3D Printed Cementitious Materials, *Materials*, 12 (2019) 2993.
- [228] H. Beushausen, M.G. Alexander, Bond strength development between concretes of different ages, 60 (2008) 65-74.
- [229] L. Cui, J.H. Cahyadi, Permeability and pore structure of OPC paste, *Cem. Concr. Res.*, 31 (2001) 277-282.
- [230] B.B. Das, B. Kondraivendhan, Implication of pore size distribution parameters on compressive strength, permeability and hydraulic diffusivity of concrete, *Constr. Build. Mater.*, 28 (2012) 382-386.
- [231] S. Wild, M. Arabi, G.O. Rowlands, Relation between pore size distribution, permeability, and cementitious gel formation in cured clay–lime systems, *Materials science and technology*, 3 (1987) 1005-1011.
- [232] R. Kumar, B. Bhattacharjee, Porosity, pore size distribution and in situ strength of concrete, *Cem. Concr. Res.*, 33 (2003) 155-164.
- [233] B. Kondraivendhan, B. Bhattacharjee, Effect of age and water-cement ratio on size and dispersion of pores in ordinary portland cement paste, *ACI Materials Journal*, 107 (2010) 147.
- [234] J. Li, L. Gao, D. Hou, P. Wang, Y. Zhou, Q. Ding, C. Xiong, Insights on the ion migration throughout the nano-channel of ettringite under an external electric field: Structure, dynamics, and mechanisms, *Constr. Build. Mater.*, 262 (2020) 120074.
- [235] T. Senga Kiese, S. Bonnet, O. Amiri, A. Ventura, Analysis of corrosion risk due to chloride diffusion for concrete structures in marine environment, *Marine Structures*, 73 (2020) 102804.
- [236] Z. Toutou, N. Roussel, C. Lanos, The squeezing test: a tool to identify firm cement-based material's rheological behaviour and evaluate their extrusion ability, *Cem. Concr. Res.*, 35 (2005) 1891-1899.
- [237] W. Franus, R. Panek, M. Wdowin, SEM Investigation of Microstructures in Hydration Products of Portland Cement, in: E.K. Polychroniadis, A.Y. Oral, M.

- Ozer (Eds.) 2nd International Multidisciplinary Microscopy and Microanalysis Congress, Springer International Publishing, Cham, 2015, pp. 105-112.
- [238] E. Gallucci, K. Scrivener, Crystallisation of calcium hydroxide in early age model and ordinary cementitious systems, *Cem. Concr. Res.*, 37 (2007) 492-501.
- [239] A. Souid, M. Esaker, D. Elliott, O. Hamza, Experimental data of bio self-healing concrete incubated in saturated natural soil, *Data in Brief*, 26 (2019) 104394.
- [240] S. Divya Rani, A.V. Rahul, M. Santhanam, A multi-analytical approach for pore structure assessment in historic lime mortars, *Constr. Build. Mater.*, 272 (2021) 121905.
- [241] H.S. Wong, M.K. Head, N.R. Buenfeld, Pore segmentation of cement-based materials from backscattered electron images, *Cem. Concr. Res.*, 36 (2006) 1083-1090.
- [242] M. Fathima Suma, M. Santhanam, A.V. Rahul, The effect of specimen size on deterioration due to external sodium sulphate attack in full immersion studies, *Cem. Concr. Comps.*, 114 (2020) 103806.
- [243] C. Li, L. Jiang, N. Xu, S. Jiang, Pore structure and permeability of concrete with high volume of limestone powder addition, *Powder Technology*, 338 (2018) 416-424.
- [244] A. Kaci, R. Bouras, V.T. Phan, P.A. Andréani, M. Chaouche, H. Brossas, Adhesive and rheological properties of fresh fibre-reinforced mortars, *Cem. Concr. Comps.*, 33 (2011) 218-224.
- [245] S. Kawashima, M. Chaouche, D.J. Corr, S.P. Shah, Influence of purified attapulgite clays on the adhesive properties of cement pastes as measured by the tack test, *Cem. Concr. Comps.*, 48 (2014) 35-41.
- [246] Y. He, X. Zhang, R.D. Hooton, X. Zhang, Effects of interface roughness and interface adhesion on new-to-old concrete bonding, *Constr. Build. Mater.*, 151 (2017) 582-590.
- [247] K. Gadri, A. Guettala, Evaluation of bond strength between sand concrete as new repair material and ordinary concrete substrate (The surface roughness effect), *Constr. Build. Mater.*, 157 (2017) 1133-1144.
- [248] Y.O. Mohamed Abdelhay, M. Chaouche, H. Van Damme, The tackiness of smectite muds. 1. The dilute regime, *Applied Clay Science*, 42 (2008) 163-167.
- [249] Ł. Sadowski, *Adhesion in Layered Cement Composites*, Springer 2019.
- [250] Y. Shen, Y. Wang, Y. Yang, Q. Sun, T. Luo, H. Zhang, Influence of surface roughness and hydrophilicity on bonding strength of concrete-rock interface, *Constr. Build. Mater.*, 213 (2019) 156-166.
- [251] Y.O. Mohamed Abdelhay, M. Chaouche, J. Chapuis, E. Charlaix, J. Hinch, S. Roux, H. Van Damme, Tackiness and cohesive failure of granular pastes: Mechanistic aspects, *The European Physical Journal E*, 35 (2012) 45.
- [252] Y. Tao, G. Vantghem, K. Lesage, Y. Yuan, W.D. Corte, K.V. Tittelboom, G.D. Schutter, Adhesion properties of printable polymer-modified concrete for rock tunnel linings, *ACI Materials Journal*, (2020).
- [253] A. Valikhani, A.J. Jahromi, I.M. Mantawy, A. Aziznamini, Experimental evaluation of concrete-to-UHPC bond strength with correlation to surface roughness for repair application, *Constr. Build. Mater.*, 238 (2020) 117753.
- [254] S. Austin, P. Robins, C. Goodier, The performance of hardened wet-process sprayed mortars, *Magazine of Concrete Research*, 52 (2000) 195-208.

- [255] J. Silfwerbrand, Shear bond strength in repaired concrete structures, *Mater. Struct.*, 36 (2003) 419-424.
- [256] H. Beushausen, The influence of concrete substrate preparation on overlay bond strength, *Magazine of Concrete Research*, 62 (2010) 845-852.
- [257] M.G. Grantham, *Concrete Repair: A practical guide*, CRC Press 2011.
- [258] M. Luković, B. Šavija, H. Dong, E. Schlangen, G. Ye, Micromechanical study of the interface properties in concrete repair systems, *Journal of Advanced Concrete Technology*, 12 (2014) 320-339.
- [259] X. Feng, L. Jiang, Design and creation of superwetting/antiwetting surfaces, *Advanced Materials Interfaces*, 18 (2006) 3063-3078.
- [260] L. Courard, Parametric study for the creation of the interface between concrete and repair products, *Mater. Struct.*, 33 (2000) 65.
- [261] T. Bharathidasan, S.V. Kumar, M.S. Bobji, R.P.S. Chakradhar, B.J. Basu, Effect of wettability and surface roughness on ice-adhesion strength of hydrophilic, hydrophobic and superhydrophobic surfaces, *Applied Surface Science*, 314 (2014) 241-250.
- [262] R. Montero, J.G. Victores, S. Martínez, A. Jardón, C. Balaguer, Past, present and future of robotic tunnel inspection, *Automat. Constr.*, 59 (2015) 99-112.
- [263] J.J. Assaad, Development and use of polymer-modified cement for adhesive and repair applications, *Constr. Build. Mater.*, 163 (2018) 139-148.
- [264] K.R. Shull, C.M. Flanigan, A. Crosby, Fingering instabilities of confined elastic layers in tension, *Physical review letters*, 84 (2000) 3057.
- [265] D. Derks, A. Lindner, C. Creton, D. Bonn, Cohesive failure of thin layers of soft model adhesives under tension, *Journal of applied physics*, 93 (2003) 1557-1566.
- [266] A. Kaci, R. Bouras, M. Chaouche, P. ani, H. Brossas, Adhesive and rheological properties of mortar joints, *Applied rheology*, 19 (2009) 51970.
- [267] G. Lu, K. Wang, T.J. Rudolphi, Modeling rheological behavior of highly flowable mortar using concepts of particle and fluid mechanics, *Cem. Concr. Comps.*, 30 (2008) 1-12.
- [268] Y. Zhang, Z. Jiang, Y. Zhu, J. Zhang, Q. Ren, T. Huang, Effects of redispersible polymer powders on the structural build-up of 3D printing cement paste with and without hydroxypropyl methylcellulose, *Constr. Build. Mater.*, 267 (2021) 120551.
- [269] M. Wang, R. Wang, H. Yao, S. Farhan, S. Zheng, Z. Wang, C. Du, H. Jiang, Research on the mechanism of polymer latex modified cement, *Constr. Build. Mater.*, 111 (2016) 710-718.
- [270] N. Roussel, *Understanding the rheology of concrete*, Elsevier 2011.
- [271] C.M. Fellows, W.O. Doherty, *Insights into bridging flocculation, Macromolecular symposia*, Wiley Online Library, 2005, pp. 1-10.
- [272] L. Patural, P. Marchal, A. Govin, P. Grosseau, B. Ruot, O. Devès, Cellulose ethers influence on water retention and consistency in cement-based mortars, *Cem. Concr. Res.*, 41 (2011) 46-55.
- [273] M. Wyrzykowski, R. Kiesewetter, B. Münch, R. Baumann, P. Lura, Pore structure of mortars with cellulose ether additions – Study of the air-void structure, *Cem. Concr. Comps.*, 62 (2015) 117-124.



- [274] D. Jiao, C. Shi, Q. Yuan, X. An, Y. Liu, H. Li, Effect of constituents on rheological properties of fresh concrete-A review, *Cem. Concr. Comps.*, 83 (2017) 146-159.
- [275] L. Patural, J.-P. Korb, A. Govin, P. Grosseau, B. Ruot, O. Devès, Nuclear magnetic relaxation dispersion investigations of water retention mechanism by cellulose ethers in mortars, *Cem. Concr. Res.*, 42 (2012) 1371-1378.
- [276] G.H. Meeten, Yield stress of structured fluids measured by squeeze flow, *Rheologica Acta*, 39 (2000) 399-408.
- [277] D. Bülischen, J. Kainz, J. Plank, Working mechanism of methyl hydroxyethyl cellulose (MHEC) as water retention agent, *Cem. Concr. Res.*, 42 (2012) 953-959.
- [278] C. Brumaud, R. Baumann, M. Schmitz, M. Radler, N. Roussel, Cellulose ethers and yield stress of cement pastes, *Cem. Concr. Res.*, 55 (2014) 14-21.
- [279] D. Bülischen, J. Plank, Water retention capacity and working mechanism of methyl hydroxypropyl cellulose (MHPC) in gypsum plaster — Which impact has sulfate?, *Cem. Concr. Res.*, 46 (2013) 66-72.
- [280] W.W. Graessley, R.L. Hazleton, L.R. Lindeman, The Shear - Rate Dependence of Viscosity in Concentrated Solutions of Narrow - Distribution Polystyrene, *Transactions of the Society of Rheology*, 11 (1967) 267-285.
- [281] R. Kniewske, W.M. Kulicke, Study on the molecular weight dependence of dilute solution properties of narrowly distributed polystyrene in toluene and in the unperturbed state, *Die Makromolekulare Chemie*, 184 (1983) 2173-2186.
- [282] Y. Tang, G. Xu, J. Lian, H. Su, C. Qu, Effect of temperature and humidity on the adhesion strength and damage mechanism of shotcrete-surrounded rock, *Constr. Build. Mater.*, 124 (2016) 1109-1119.
- [283] N. Roussel, A. Lemaître, R.J. Flatt, P. Coussot, Steady state flow of cement suspensions: a micromechanical state of the art, *Cem. Concr. Res.*, 40 (2010) 77-84.
- [284] P.L. Nasatto, F. Pignon, J.L. Silveira, M.E.R. Duarte, M.D. Nosedá, M. Rinaudo, Interfacial properties of methylcelluloses: The Influence of molar mass, *Polymers*, 6 (2014) 2961-2973.
- [285] S.-T. Yi, J.-K. Kim, T.-K. Oh, Effect of strength and age on the stress-strain curves of concrete specimens, *Cem. Concr. Res.*, 33 (2003) 1235-1244.
- [286] D. Asprone, C. Menna, F.P. Bos, T.A.M. Salet, J. Mata-Falcón, W. Kaufmann, Rethinking reinforcement for digital fabrication with concrete, *Cem. Concr. Res.*, 112 (2018) 111-121.



# Curriculum vitae

## Personal information

Name: Yaxin Tao

Date of birth: March 18<sup>th</sup>, 1993

Place of birth: Hefei, Anhui, China

Email: Yaxin.Tao@UGent.be; taoyaxin@hotmail.com

## Education

2018-2021      Doctor in Civil Engineering  
  
Department of Structural Engineering and Building  
Materials, Faculty of Engineering and Architecture,  
Ghent University, Belgium

2015-2018      Master in Architectural and Civil Engineering  
  
Department of Geotechnical Engineering, College of  
Civil Engineering, Tongji University, China

2011-2015      Bachelor in Road and Bridge Engineering  
  
School of Transportation, Southeast University, China

## Journal papers

1. **Yaxin Tao**, A.V. Rahul, Karel Lesage, Yong Yuan, Kim Van Tittelboom, Geert De Schutter. Stiffening control of cement-based materials using accelerators in inline mixing processes: Possibilities and challenges. *Cement and Concrete Composites*, 2021, 119: 103972.
2. **Yaxin Tao**, Gieljan Vantghem, Karel Lesage, Yong Yuan, Wouter De Corte, Kim Van Tittelboom, Geert De Schutter. Adhesion properties of printable polymer-modified concrete for rock tunnel linings. *ACI Materials Journal*, accepted.
3. **Yaxin Tao**, Karel Lesage, Kim Van Tittelboom, Yong Yuan, Geert De Schutter. Twin-pipe pumping strategy for active stiffening control of 3D printable concrete: from transportation to fabrication. *Cement and Concrete Research*, under review (2020.06).
4. **Yaxin Tao**, A.V. Rahul, Karel Lesage, Kim Van Tittelboom, Yong Yuan, Geert De Schutter. Mechanical and microstructural properties of 3D printable concrete in the context of the twin-pipe pumping strategy. *Cement and Concrete Composites*, minor revision (2021.04).
5. **Yaxin Tao**, Karel Lesage, Kim Van Tittelboom, Yong Yuan, Geert De Schutter. Influence of substrate surface roughness and moisture content on adhesion performance of 3D printable concrete. *Cement and Concrete Composites*, minor revision (2021.05).
6. **Yaxin Tao**, Qiang Ren, Gieljan Vantghem, Karel Lesage, Kim Van Tittelboom, Yong Yuan, Wouter De Corte, Geert De Schutter, Extending 3D concrete printing to hard rock tunnel linings: adhesion of fresh concrete at different working faces. *Automation in Construction*, major revision (2021.06).
7. **Yaxin Tao**, Qiang Ren, Karel Lesage, Kim Van Tittelboom, Yong Yuan, Geert De Schutter. Shape stability of printable concrete with river and manufactured sand characterized by squeeze flow. *Cement and Concrete Composites*, under review (2021.09).
8. **Yaxin Tao**, Karel Lesage, Kim Van Tittelboom, Yong Yuan, Geert De Schutter. Effect of hydroxyethyl methyl cellulose and aluminum sulfate on the adhesion performance of cement-based materials. *Cement and Concrete Composites*, under review (2021.10).
9. **Yaxin Tao**, A.V. Rahul, Manu K. Mohan, Kim Van Tittelboom, Yong Yuan, Geert De Schutter. Blending performance of the helical static mixer used for

twin-pipe 3D concrete printing. To be submitted to *Cement and Concrete Research*.

10. **Yaxin Tao**, A.V. Rahul, Manu K. Mohan, Kim Van Tittelboom, Yong Yuan, Geert De Schutter. Mixing homogeneity of 3D printable concrete via twin-pipe pumping: Experimental test and numerical simulation. In preparation.
11. Qiang Ren, **Yaxin Tao**, Dengwu Jiao, Zhengwu Jiang, Guang Ye, Geert De Schutter. Plastic viscosity of cement mortar with manufactured sand as influenced by geometric features and particle size. *Cement and Concrete Composites*, 2021, 122: 104163.
12. Manu K. Mohan, A. V. Rahul, **Yaxin Tao**, Geert De Schutter, Kim Van Tittelboom. Two-stage mixing strategy using borated CSA cement systems: Application in extrusion-based concrete 3D printing. *Cement and Concrete Research*, under review (2021.05).
13. Yubo Sun, **Yaxin Tao**, A.V. Rahul, Guang Ye, Geert De Schutter. Effect of conventional superplasticizers on rheology and strength development of alkali-activated slag concrete. *Cement and Concrete Composites*, under review (2021.10).
14. Yubo Sun, Shizhe Zhang, A.V. Rahul, **Yaxin Tao**, Filip Van Bockstaele, Guang Ye, Geert De Schutter. Rheology of alkali-activated slag: New insight from microstructure perspectives. *Cement and Concrete Research*, under review (2021.10).

### Patents

1. **Yaxin Tao**, Karel Lesage, Kim Van Tittelboom, Geert De Schutter. Method to provide extrudable concrete, EP 20171258.5, Europe.
2. Yong Yuan, **Yaxin Tao**, Wei Jiang, Xupeng Yao, Xiaoyun Wang. A 3D concrete printing nozzle with ready-mixed function, ZL201721850190.1, China.
3. Yong Yuan, **Yaxin Tao**, Wei Jiang, Xupeng Yao, Xiaoyun Wang. A 3D concrete printing device with microwave curing function, ZL 201721848638.6, China.

### Proceedings

1. **Yaxin Tao**, Karel Lesage, Kim Van Tittelboom, Yong Yuan, Geert De Schutter. Using limestone powder as the carrier material. *3rd RILEM International Conference on Digital Fabrication with Concrete (Digital Concrete 2022)*. 2022.

2. **Yaxin Tao**, Karel Lesage, Kim Van Tittelboom, Yong Yuan, Geert De Schutter. Adhesive properties of fresh cement paste as measured by the tack test. *fib Congress 2022*. 2022.
3. **Yaxin Tao**, Karel Lesage, Kim Van Tittelboom, Yong Yuan, Geert De Schutter. Influence of accelerator on the pore structure of 3D printable concrete. *2nd Symposium on Concrete and Concrete Structures*. 2022.
4. **Yaxin Tao**, Karel Lesage, Kim Van Tittelboom, Yong Yuan, Geert De Schutter. Adhesion performance of cement-based materials in the fresh state. *International conference on advances in sustainable construction materials and structures*. 2021.
5. **Yaxin Tao**, Karel Lesage, Kim Van Tittelboom, Yong Yuan, Geert De Schutter. Squeeze flow test for measuring the shape stability of 3D printable mortar. *Concrete structures for resilient society*. 2020.
6. **Yaxin Tao**, Karel Lesage, Kim Van Tittelboom, Yong Yuan, Geert De Schutter. Effect of limestone powder substitution on fresh and hardened properties of 3D printable mortar. *Second RILEM international conference on concrete and digital fabrication*. Springer, Cham, 2020.
7. **Yaxin Tao**, Karel Lesage, Kim Van Tittelboom, Yong Yuan, Geert De Schutter. Stiffening control of printable cement paste with flash setting admixture. *Rheology and processing of construction materials*. Springer, Cham, 2019.
8. Yong Yuan, **Yaxin Tao**, Xiaoyun Wang. Rheological analysis of printable concrete during transportation process. *Life Cycle Analysis and Assessment in Civil Engineering: Towards an Integrated Vision*. CRC Press, 2018.
9. Yong Yuan, **Yaxin Tao**, Weijiu Cui. Numerical Simulation of Pumping Pressure Loss. *Proceedings of the 12th fib International PhD Symposium in Civil Engineering*. 2018.
10. Yong Yuan, **Yaxin Tao**. Mixing and Extrusion of Printing Concrete. *Computational Modelling of Concrete Structures*. CRC Press, 2018.
11. Yong Yuan, Xiaoyun Wang, **Yaxin Tao**. Bond properties between printable concrete and rock. *5th fib Congress in Melbourne, Australia (2018) proceedings*. 2018.







Striation pattern in fluid acrylic painting, modern art.